Scalable spintronics devices with reduced Pt and Ru content

Alvaro Palomino

To cite this version:

Alvaro Palomino. Scalable spintronics devices with reduced Pt and Ru content. Micro and nanotechnologies/Microelectronics. Université Grenoble Alpes [2020-..], 2022. English. NNT : 2022GRALT049 . tel-03889377

HAL Id: tel-03889377
https://theses.hal.science/tel-03889377v1

Submitted on 8 Dec 2022

THÈSE

Pour obtenir le grade de

DOCTEUR DE L'UNIVERSITÉ GRENOBLE ALPES

Spécialité : NANO ELECTRONIQUE ET NANO TECHNOLOGIES

Arrêté ministériel : 25 mai 2016

Présentée par

Alvaro PALOMINO

Thèse dirigée par **Bernard DIENY**
et codirigée par **Blandine AGERON**, Université Grenoble Alpes

préparée au sein du **Laboratoire Spintronique et Technologie des Composants**
dans **l'École Doctorale Electronique, Electrotechnique, Automatique, Traitement du Signal (EEATS)**

« Dispositifs spintroniques aux noeuds technologiques avancés contenant des quantités réduites de Pt et de Ru ».

« Scalable spintronics devices with reduced Pt and Ru content ».

Thèse soutenue publiquement le **7 juin 2022**,
devant le jury composé de :

Monsieur Bernard DIENY
INGENIEUR HDR, CEA CENTRE DE GRENOBLE, Directeur de thèse
Madame Blandine AGERON
PROFESSEUR DES UNIVERSITES, Université Grenoble Alpes, Co-directrice de thèse
Monsieur Michel HEHN
PROFESSEUR DES UNIVERSITES, Université de Lorraine, Rapporteur
Madame Myriam PANNETIER-LECOEUR
INGENIEUR HDR, CEA CENTRE DE PARIS-SACLAY, Rapporteure
Monsieur Gilles PACHE
PROFESSEUR DES UNIVERSITES, AIX-MARSEILLE UNIVERSITE, Examinateur
Monsieur Ahmad BSIESY
PROFESSEUR DES UNIVERSITES, Université Grenoble Alpes, Président

Abstract

In the field of information and communication technologies (ICT), the development of non-volatile memories is crucial to reduce the amount of energy required to store and process data. Spin transfer-torque Magnetic Random-Access Memory (STT-MRAM) is already used as an alternative to embedded flash (e-flash) memory and envisioned for static RAM (static random-access memory) replacement due to its high performance and easy integration with complementary metal oxide semiconductor (CMOS) technology. However, MRAM contains several materials classified as critical, in particular by the European Union (EU), with a high supply risk. Platinum (Pt) is used in combination with cobalt (Co) to form a synthetic antiferromagnet structure that provides the required stability for reference layer of the magnetic tunnel junction (MTJ), the main component of MRAM. Due to the tiny amounts of Pt present in the initial ore (few ppm), the energy (2000 MJ/kg), the carbon emissions (12500 kg.eq/kg) and the price (25000 euro/kg) associated to the extraction and subsequent refinement of such metal are very high.

The purpose of this work is to realize spintronic devices, without the use of critical Pt and Ru. In a first approach, we analyzed the possibility of using perpendicular shape anisotropy for the p-MRAM reference layer, which allows the use of more common ferromagnetic materials such as FeCoB or NiFe. In a second approach, we study the possibility of substituting platinum with more common nickel (Ni) whose requirements are some orders of magnitude lower (200 MJ/kg, 6.5 kg.eq/kg, 12 euro/kg) but which still provides perpendicular magnetic anisotropy (PMA) when combined with cobalt (Co). In addition, a copper-based seed layer has been used, since it is a common metal classified as non-critical, to induce the fcc (111) texture required for the PMA of the Co/Ni multilayers, instead of the more critical hafnium used in other works. The conclusions we draw from our studies is that the use of nickel or more common ferromagnetic elements can provide good performance and strong reductions in terms of energy, price or carbon emissions. However, due to the tiny amounts of critical metals used in MRAM, the benefits of these substitutions remain small compared to the requirements for manufacturing the silicon wafers on which these types of devices are grown. Therefore, more emphasis should be placed on reducing the environmental impact of manufacturing the silicon wafers themselves. Nevertheless, the presence of alternative materials to the use of Pt or Pd remains positive for the development of the technology in the event of supply disruptions, since four mining companies, one Russian and the other three South African, ensure 80% of the World production. Finally, we propose an innovative vortex based magnetic sensor sensitive to a perpendicular field with large scalability down to sub-100 nm nodes. The electrical measurements performed demonstrate linear field ranges up to more than 0.2 T. In addition, the diameter or the material used for the sensing layer can control the linear field range. This device has the particular advantage that it does not require an in-plane magnetized reference layer, as in conventional vortex-based sensors that often comprise an antiferromagnetic layer containing critical metals such as Ir or Pt. A perpendicular reference layer, based on Co/Ni multilayer can be used avoiding the use of Pt. A certain residual stray field can help to stabilize the vortex polarity in a single direction so that the use of a synthetic antiferromagnetic structure containing critical ruthenium can also be avoided.

Résumé

Dans le domaine des technologies de l'information et de la communication (ICT), le développement des mémoires non volatiles est crucial pour réduire la quantité d'énergie nécessaire au stockage et au traitement des données. La mémoire à accès aléatoire STT-MRAM est déjà utilisée comme alternative à la mémoire flash intégrée (e-flash) et envisagée pour le remplacement de la RAM statique (mémoire à accès aléatoire statique) en raison de ses hautes performances et de sa facilité d'intégration avec la technologie semi-conducteur à oxyde métallique complémentaire (CMOS). Cependant, la MRAM contient plusieurs matériaux classés comme critiques, notamment par l'Union européenne (UE), avec un risque d'approvisionnement élevé. Le platine (Pt) est utilisé en combinaison avec du cobalt (Co) pour former une structure antiferromagnétique synthétique (SAF) qui fournit la stabilité requise pour la couche de référence de la jonction tunnel magnétique (MTJ), le composant principal de la MRAM. En raison des quantités infimes de Pt présentes dans le minerai initial (quelques ppm), de l'énergie (2000 MJ/kg), des émissions de carbone (12500 kg.eq/kg) et du prix (25000 euro/kg) associés à l'extraction et le raffinement ultérieur de ce métal sont très élevés. Le but de ce travail est de réaliser des dispositifs spintroniques, sans l'utilisation de Pt et Ru critiques. Dans une première approche, nous avons analysé la possibilité d'utiliser l'anisotropie de forme perpendiculaire pour la couche de référence p-MRAM, ce qui permet l'utilisation de matériaux ferromagnétiques plus courants tels que FeCoB ou NiFe. Dans une deuxième approche, nous étudions la possibilité de substituer le Pt par du nickel (Ni) plus commun dont les besoins sont inférieurs de quelques ordres de grandeur (200 MJ/kg, 6,5 kg.eq/kg, 12 euro/kg) mais qui fournit tout de même des anisotropie magnétique (PMA) lorsqu'il est combiné avec du cobalt. De plus, une couche de germination à base de cuivre a été utilisée, puisqu'il s'agit d'un métal courant classé comme non critique, pour induire la texture fcc (111) nécessaire au PMA des multicouches Co/Ni, au lieu du hafnium plus critique utilisé dans d'autres travaux. La conclusion de nos études est que l'utilisation du nickel ou d'éléments ferromagnétiques plus courants peut apporter de bonnes performances et de fortes réductions en termes d'énergie, de prix ou d'émissions de carbone. Cependant, en raison des quantités infimes de métaux critiques utilisés dans la MRAM, les avantages restent faibles par rapport aux exigences de fabrication des tranches de silicium sur lesquelles ces types de dispositifs sont développés. Par conséquent, il convient de mettre davantage l'accent sur la réduction de l'impact environnemental de la fabrication des tranches de silicium elles-mêmes. Néanmoins, la présence de matériaux alternatifs à l'utilisation du Pt ou du Pd reste positive pour le développement de la technologie en cas de rupture d'approvisionnement, puisque quatre sociétés minières, l'une russe et les trois autres sud-africaines, assurent 80% de la production mondiale. Enfin, nous proposons un capteur magnétique innovant à base de vortex sensible à un champ perpendiculaire avec une grande évolutivité jusqu'aux nœuds inférieurs à 100 nm. Les mesures électriques effectuées démontrent des plages de champs linéaires jusqu'à plus de 0,2T. De plus, le diamètre ou le matériau utilisé pour la couche de détection peut contrôler la plage de champ linéaire. Ce dispositif présente notamment l'avantage de ne pas nécessiter de couche de référence aimantée dans le plan, comme dans les capteurs conventionnels à base de vortex qui utilisent souvent une couche antiferromagnétique contenant des métaux critiques tels que Ir ou Pt. Une couche de référence perpendiculaire peut être utilisée, basée sur une multicouche Co/Ni, évitant l'utilisation de PGM. Nous voyons qu'un certain champ parasite résiduel peut aider à stabiliser la polarité du vortex dans une seule direction, de sorte que l'utilisation d'une structure antiferromagnétique synthétique critique contenant du ruthénium pourrait ne pas être nécessaire non plus.

Contents

APPENDIX

Acknowledgments

This thesis is dedicated to those who left, Marco, Steven, Aurelien, Luis, Dali, Federica, Caroline, Cécile, Romeo, Arnaud, Jay, Vincenzo, Haozhe, Daniel.S, Oji, Rafael, Leonardo, Qiang, Odilia, Michael, Rana, Sabrina, Artem, Neha and those yet to leave, Daniel, Joseba, Louis, David, Laura, Bruno, Nuno, Andrea, Ariam, Neha, Charles, Ahmed, Javi, Khasan, Miiiina, Pedro, Kamal, Samuel, Arijit, Philippe, Sambit, Eline, Floris, Michael, Libor, Javi, Mario, Rodri, Aurélie, Johanna... Because you gave me the daily drive to pursue this work.

I will miss all those times we went for beers, lakes, hiking, skying, snowboarding, bouldering, crossfit... yeah even we started a crossfit cult.

I would also like to thank my thesis jury: first of all Michel Hehn and Myriam Pannetier-Lecoeur who accepted to be rapporteurs. I also thank Gilles Pachi for coming to my thesis defence in such a good mood, and finally Ahmad Bsiesy for chairing it and following me during all the ISCs.

Thanks to all the PTA staff, Christophe best volleyball referee ever. Thanks to the secretary team, Lea, Sabrina, Adriana and Celine. Thanks to Trevor and David for the sharp observations.

Thank you Bernard to help me during all this time, for your gentleness, it was a pleasure to work with you and learn from you. Thanks to Ricardo to take care of the team, big demanding task. Merci Liliana to discuss with me, specially during COVID times and your encouragement. And the BBQ of course. Thanks Lucian who allowed me to join the team at first. Thanks Blandine for our discussions. Robert to help me with AFM. Gracias Kevin por ayudarme a usar tu prober y charlar de rato en rato ;) y Laurent, puedes beber todas las cervezas que te debo en el pot, si eres capaz. Many thanks to Stephane, even if we did not take coffee together, it felt like it during the ordinary event of asking for a sample. Maybe this is why I end up asking for so many samples.

It is always good to start into something new with someone else, it is much better if it happens to be with a friend, thanks Daniel, time here without you would have been like a tortilla without onion. From the subway with Sebas the first day to the last tacos.

Special thanks to Marco to let me see that sometimes, everything can go wrong. And for the crudo of course. Thanks Steven for teaching me from the beginning how to process in the clean room, I survived the fire and the water, when the sand arrived I was writing. Thanks Mr. Aurelien O. for the assistance in the clean room and the Filipino food. Less thanks for buying that heavy furniture that we had to move. Laura and Josebita, transmitiendome siempre buen rollo, se os quiere diablos.

Thanks to all the team of NEED for IoT, we might have not save the world, but we did our bit.

I don't want to forget to thank also Guillaume and Marc, who supervised me during my master thesis and were so cool with me, it was a great pleasure, and probably a big reason of why I started a PhD.

Many thanks to all the people that crossed my path during this time, Julia, Laure, Baptiste, Pablito, Jana, Martina, Anais. Vincent, Gaëtan et Mathilde that passed through the writting period with me avec que du love, merci la belle et les bêtes. Chloe(s), Pauline, Lisa, Amélie, Camille, Montsecita, Denise, Biagio, Marco P., Kelly, the biologist... all the solides du crossfit that make me wake up in a good mood, Alex and Gaëtan that force me to finish the wod to go to write, Lionel that has been there from day 1 and all others of the team.

To my family, friends and my parents, who have gave me the opportunity to enjoy all this.

"We don't abandon our pursuits because we despair of ever perfecting them" #WDQ
EPICTETUS, Discourses, 1.2.37b

List of Abbreviations

ACEA	European Automobile Manufacturers Association
AF(M)	Antiferromagnet(ic) material
AFM	Atomic force microscopy
Al	Aluminium
As	Share of raw material
AMR	Anisotropic Magneto-Resistive
AP	Anti-parallel
B	Boron
bcc	Body centered cubic
BEOL	Back-End-of-Line
CIP	Current in plane
CMP	Chemical-mechanical polishing
CMOS	Complementary metal oxide semiconductor
Co	Cobalt
COVID-19	Coronavirus disease 2019
Cr	Chromium
CT	Current transformers
Cu	Copper
DOS	Density of states
DRAM	Dynamic Random Access Memory
e-beam	Electron beam litography
EDX	Energy-dispersive X-ray spectroscopy
EH	Electron holography
EI	Economic Importance
$\mathbf{EoL_{RIR}}$	End of life recycling input rate
EU	European Union
fcc	Face centered cubic
Fe	Iron
FeRAM	Ferroelectric Random Acess Memory
FIB	Focus Ion Beam
FL	Free layer
FM	Ferromagnet(ic)
FMR	Ferromagnetic resonance
Ga	Gallium
Ge	Germanium
GHG	Global greenhouse gas
GMR	Giant magnetoresistance
GWP	Global warming potential
HAADF	High-angle annular dark-field
HDD	Hard disk drive
Hf	Hafnium
HHI	Herfindahl-Hirschman Index
HM	Heavy metal
IBE	Ion beam etching

ICs	Integrated circuits
ICT	Information and communication technologies
IEC	Interlayer exchange coupling
IPA	Isopropanol
i-PMA	Interfacial perpendicular magnetic anisotropy
Ir	Iridium
ITO	Indium tin oxide
LED	Light emitting diode
LLG	Landau-Lifshitz-Gilbert
MBE	Molecular Beam Epitaxy
MFM	Magnetic force microscopy
MgO	Magnesium oxide
MIBK	Methyl isobutyl ketone
Mn	Manganese
Mo	Molybdenum
MOKE	Magneto-optical Kerr effect
MRAM	Magnetic random access memory
MTJ	Magnetic tunnel junction
Nd	Neodymium
Ni	Nickel
NM	Non-magnetic
NVM	Non-volatile memories
OOMMF	Object Oriented MicroMagnetic Framework
Ox	Oxide
P	Parallel
PC	Poly-crystal
PCM	Phase change memory
Pd	Palladium
PGMs	Platinum group metals
PMA	Perpendicular magnetic anisotropy
PMMA	Poly(methyl methacrylate)
ppm	part per million
PSA	Perpendicular shape anisotropy
Pt	Platinum
PVD	Physical vapor deposition
Qs	Total added value of a sector
REEs	Rare earth elements
RF	Radio-frequency
RIE	Reactive ion etching
RKKY	Ruderman-Kittel-Kasuya-Yosida
RMS	Root mean square
RRAM	Resistive random access memory
RT	Room temperature
RTN	Random telegraph noise
Ru	Ruthenium
SAF	Synthetic antiferromagnet
SEM	Scanning electron microscopy
Sc	Single-crystal
SIA	Structural inversion asymmetry
SNR	Signal to noise ratio
SOI	Spin-orbit interaction
SOT	Spin-orbit torque
sp	Superparamagnetic

SR	Supply Risk
SRAM	Static Random Access Memory
STEM	Scanning transmission electron microscopy
STT	Spin-transfer torque
SSM	Supply chain management
S	Sample number
TA	Thermally Assisted
Ta	Tantalum
Te	Tellurium
TEM	Transmission electron microscopy
TMR	Tunnel magnetoresistance
TSP	Tunneling spin polarization
UV	Ultraviolet
VCMA	Voltage controlled magnetic anisotropy
VNA-FMR	Vector network analyzer ferromagnetic resonance
VSM	Vibrating sample magnetometry
W	Tungsten
WER	Write error rate
WTO	World Trade Organisation
XRD	X-ray diffraction

List of Symbols

A_{ex}	Exchange constant	J·m^{-1}
A_R	in-plane aspect ratio	
$\vec{B}_R$	Rashba field	A·m^{-1}
D	Diameter	m
e	Electron charge	$1.6 \times 10^{-19} C$
E	Energy	J
E_F	Fermi Energy	J
E_{tot}	Gibbs energy	J
E_{ex}	Exchange energy	J
E_{anis}	Magnetoscrystalline anisotropy energy	J
E_{dem}	Demagnetizing energy	J
E_{Zeeman}	Zeeman energy	J
g	Landé factor	$\lvert g \rvert \approx 2$
G	Conductance	S
G_{amp}	Amplifier gain	
H	Magnetic field	A·m^{-1}
H_{eff}	Effective field	A·m^{-1}
H_c	Coercive field	A·m^{-1}
H_{ex}	Exchange field	A·m^{-1}
H_{off}	Offset field	A·m^{-1}
H_d	Demagnetizting field	A·m^{-1}
H_{app}	Applied external field	A·m^{-1}
H_n	Nucleation field	A·m^{-1}
H_a	Annihilation field	A·m^{-1}
I_{C0}	Critical switching current	A
J	Current density	A·m^{-2}
k_F	Wave vector	
K_u	Bulk anisotropy constant	J/m^3
K_s	Interfacial anisotropy constant	J/m^3
K_{eff}	Effective anisotropy constant	J/m^3
l_{ex}	Exchange length	m
$\vec{m}$	Reduced magnetization vector	
M_s	Saturation magnetization	A·m^{-1}
N	Demagnetizing tensor	
P	Spin polarization	
R	Resistance	Ω
t	Thickness	m
t_{eff}	Effective thickness	m
T	Temperature	K
w	Width	m
Z	Impedance	Ω
κ	Decay coefficient	
Δ_n	Bloch state n	

μ_B	Bohr magneton	J·T^{-1}
α_R	Rashba constant	
ρ	Resistivity	Ω·m
τ	Retention time	s
Δ	Thermal stability factor	
θ_K	Kerr rotation angle	rad
ϵ_K	Kerr ellipticity	
α	Gilbert damping	
γ	Gyromagnetic ratio	Hz·T^{-1}
$\hbar$	Plank constant	$1.05457 \times 10^{-34} J \cdot s$
μ_0	Vacuum magnetic permeability	$4\pi \times 10^{-7}$ T·A^{-1}·m

Chapter 1

Introduction to spintronics

This chapter introduces the main spintronic phenomena commonly used in spintronics that serves to the functioning of memory devices and magnetic sensors, as those developed during this thesis. It also explains the main material developments that have led to the current highly efficient magnetic stacks followed by a brief review of some state of the art spintronic devices.

1.1 Spintronics phenomena

In this section, spin dependent electronic transport is first introduced in particular the different spintronic phenomena such as giant magnetoresistance (GMR) and tunneling magnetoresistance (TMR), used for the reading of magnetic random access memories (MRAM) and the spin transfer torque (STT) effect used for the writing process. Finally spin orbit torque (SOT) used in novel generation of MRAM is introduced.

1.1.1 Spin dependent electronic transport

Ferromagnetic materials are the main building block of many spintronic devices such as magnetic random access memory (MRAM) or magnetic sensors. The ferromagnetic response characteristic of such materials is a consequence of their electronic band structure. In ferromagnetic transition metals, such as Fe, Co, Ni and their alloys, the conduction bands splits in two subbands, i.e. 3d is splitted into 3d↑ and 3d↓ and 4s into 4s↑ and 4s↓, corresponding to each spin configuration. The resulting spontaneous magnetization of ferromagnetic materials arises from the difference in energy ΔE between the 3d↑ and 3d↓ subbands, due to the exchange energy. Exchange energy is further explained later in Section 1.2.1. For now, it is sufficient to know that the exchange energy is lowered when the spin magnetic moments of two electrons are aligned leading to an asymmetry of the number of electrons populating each subband. As a result, the density of states at the Fermi energy E_F is different in the two subbands as illustrated in Figure 1.1 for the d-orbital. The s-band is filled up to the Fermi energy E_F and there is almost the same number of electrons with spin magnetic moments up and down as seen in Figure 1.1. Therefore, the ferromagnetic response results essentially from the splitting in the d-band.

The mobility of electrons in magnetic materials is influenced by their spin. Such spin dependence in the transport properties of ferromagnetic materials was already predicted by N.Mott in 1936 [1].

In a simple approximation, it can be considered that 4s electrons are those who carry most of the current. The electron effective mass in the s-band is very small, since this band is very wide as compared to the d-band, leading to a larger mobility of the electrons in the s-band [2].

At the Fermi level, the two s and d bands overlap. This leads the 4s electrons to be scattered into the more localized 3d states, of same spin.

Since the 4s↑ have no 3d↑ states in which they can be scattered (Figure 1.1), they are highly mobile and carry lot of current. On the contrary, the 4s↓ have lot of 3d↓ states available into which they can be scattered. Therefore they are strongly scattered and carry little current.

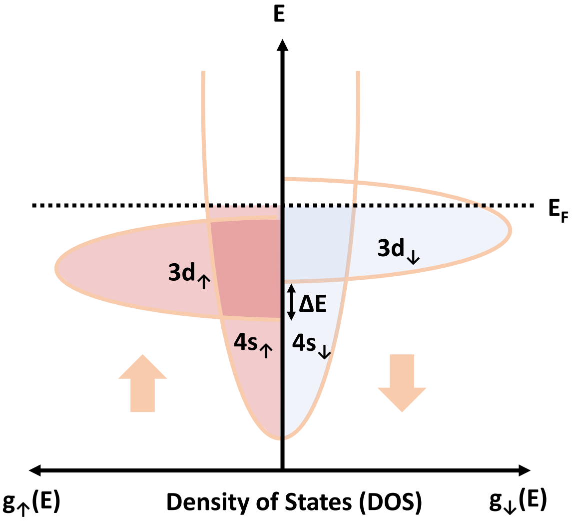

Fig. 1.1: Energy band structure representation of a transition metal with strong ferromagnetic properties.

The two categories of spins carry the current in parallel with different resistivities, resulting into a spin polarized current flowing in the ferromagnetic material. The total resistivity (ρ) of a ferromagnetic metal at low temperature proposed by this two-current model is given by equation 1.1 [3] as described in the parallel conduction channels of Figure 1.2.

$$\frac{1}{\rho} = \frac{1}{\rho_\uparrow} + \frac{1}{\rho_\downarrow}, i.e. \quad \rho = \frac{\rho_\uparrow \rho_\downarrow}{\rho_\uparrow + \rho_\downarrow} \tag{1.1}$$

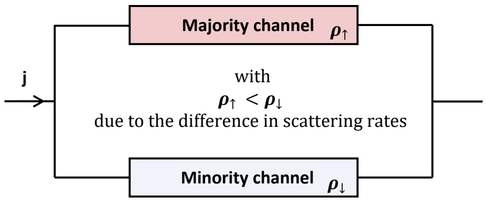

Fig. 1.2: Equivalent circuit for the electronic subbands in the “two-current model”. Resisitivity (ρ) is smaller for the majority spin channel, as the electron mobility is larger in the s-majority subband since majority s-electrons cannot scatter to the majority d-band as no empty 3d↑ states exist at Fermi energy as illustrated in Figure 1.1.

1.1.2 Giant Magnetoresistance (GMR)

Following the “two-channel model” the giant magnetoresistance effect (GMR) can be understood. The GMR appears in systems based on non-magnetic materials, such as Cr, sandwiched between two ferromagnetic materials, FM/NM/FM as in Figure 1.3. In such systems, if both FMs are magnetically oriented in a parallel configuration as depicted in Figure 1.3 a , the current can be considered short-circuited by the spin majority channel. Most of the current will flow through the majority channel of smaller resistivity $\rho_\uparrow$, resulting in a low resistance, $r_P = r$. However, in the antiparallel configuration, the electrons will traverse both majority and minority spin channels as seen in Figure 1.3 b. Therefore, the electrons will behave alternatively as majority or minority electrons, passing from one FM layer to another, resulting into a larger and identical resistance $r_{AP} = (r + R)/2$ for both cases.

The relative difference in resistance between both parallel and antiparallel configurations depicted in 1.3 is known as the GMR ratio and can thus be expressed as in Equation 1.2 [4]:

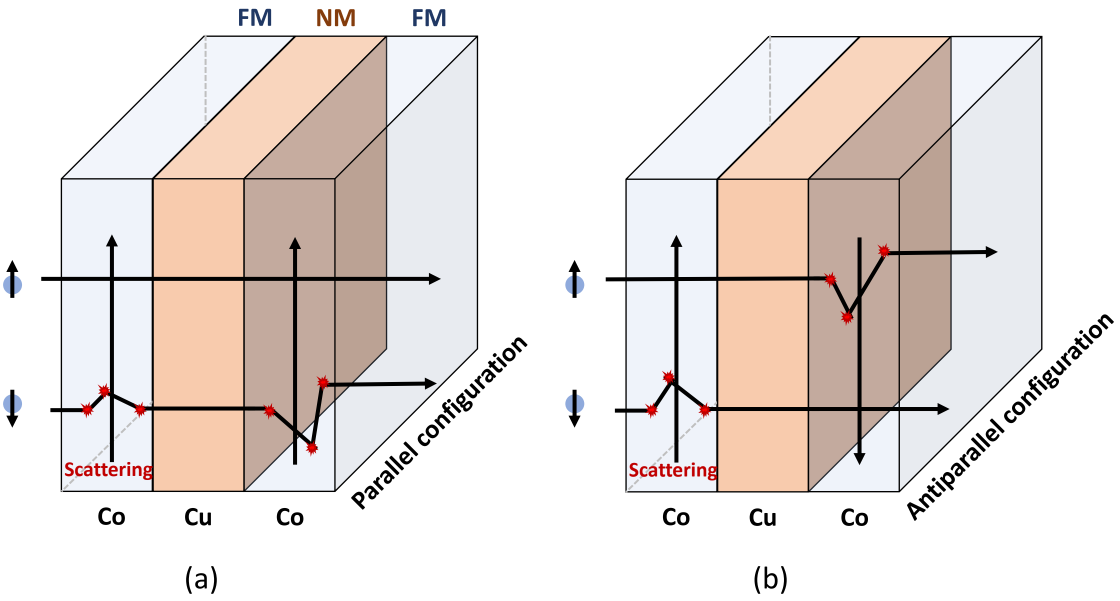

Fig. 1.3: Illustration of the two-current model displaying the conduction paths of the majority and minority electrons in a trilayer structure FM / NM / FM where FM denotes ferromagnetic metal and NM denotes non-magnetic metal, such as Co/Cu/Co. The minority 4s↓ conduction electrons can be scattered into 3d↓ bands as the density of states is not zero ($g_{\uparrow}(E_F) \neq 0$) leading to scattering events in those channels.

$$GMR = \frac{r_{AP} - r_P}{r_P} = \frac{(R-r)^2}{4Rr} \tag{1.2}$$

This GMR effect was first observed by the groups of Albert Fert and Peter Grünberg in 1988 [5, 6]. Dieny et al. developed spin valves systems (FM/NM/FM) in 1991 [7] with the particular advantage of the reduced fields required to observe the GMR effect, of only few milliteslas compared to the few teslas of other previous systems as Fe/Cr [4]. Such spin valve systems were later introduced by IBM in 1998 for the magnetoresistive reading heads in hard disk drives (HDD). The GMR sensor used for HDD readout exhibits a resistance change of roughly 10 percent in response to an applied field. The introduction of GMR sensors in HDD allowed high magnetic data storage capacity as it can probe a much smaller region of the magnetic medium than conventional inductive read heads and provides a larger sensitivity. Also, it enabled the integration of a more compact read/write head [8].

1.1.3 Tunneling Magnetoresistance (TMR)

Another crucial event for the development of spintronic devices was the discovery of tunneling magnetoresistance (TMR). Tunneling magnetoresistance is observed in systems similar to spin valves, but where the non magnetic metallic spacer layer is substituted by an insulating layer. In these systems called magnetic tunnel junctions (MTJ), the current flows from one ferromagnetic layer to the other passing through the insulating thin layer constituting a tunnel barrier. A particular advantage of such system with an insulating barrier is the resulting larger impedance compared to spin valves based on GMR. Such larger resistance of typically few kΩ makes MTJs easier to integrate with transistors, an important requirement for MRAM applications.

Julliere first observed TMR at low temperatures in magnetic tunnel junctions in 1975, in a Fe/Ge/Co system [9]. In 1995, Moodera et al. and Myazaki et al. observed TMR in amorphous AlOx based junctions at room temperature [10, 11] .

A second advantage of MTJs is the large magnetoresistance values reported when using a monocrystalline magnesium oxide (MgO) barrier predicted to be larger than 1000% by Butler and Mathon in

2001 [12, 13]. In 2004, S.Parkin et al. and S.Yuasa et al. observed giant TMR values of 220%[14] and 180%[15] respectively in crystalline MgO based tunneling barriers at room temperature. The largest TMR value experimentally observed is 604% by Ikeda et al. in 2008, in a CoFeB/MgO/CoFeB system [16]. The difference in TMR between the experimental values and those predicted experimentally are due to imperfections at the interfaces and defects during the crystal growth of the materials [17, 18]. However, the TMR values are still much larger than those given by using an amorphous AlOx barrier, typically ranging between 20% and 80% [19].

In order to obtain such giant TMR values, very well textured MgO barriers are required. They can be grown either by Molecular Beam Epitaxy (MBE) on bcc CoFe or Fe magnetic electrodes or on amorphous CoFeB electrodes followed by annealing to recrystallize the electrode with the same texture as the crystalline barrier.

The fact of using a crystalline barrier makes an important difference since in MTJs the transport mechanism relies on quantum mechanical tunneling effect. The tunneling current can be expressed as in Equation 1.3, being proportional to the number of occupied states in 1 (injector) at energy E, $D_1(E)f_1(E)$ and the probability of having an unoccupied state in the electrode 2 at energy (E+eV), $D_2(e+eV)(1-f_2(E+eV))$.

$$I_{1\rightarrow 2}(E) \propto D_1(E)f_1(E)T(E)D_2(E+eV)(1-f_2(E+eV)) \tag{1.3}$$

The term T(E) is a transmission coefficient, that depends on the barrier thickness as given in equation 1.4.

$$T(E) \propto e^{-2\kappa d} \tag{1.4}$$

A first approach to explain TMR was used by Julliere in 1975. For a ferromagnetic material, the density of states at Fermi energy for the majority and minority electrons are different: D↑ and D↓ respectively. The spin polarization of a ferromagnet can then be defined as in equation 1.5:

$$P_0 = \frac{D^{\uparrow}(E_F) - D^{\downarrow}(E_F)}{D^{\uparrow}(E_F) + D^{\downarrow}(E_F)} \tag{1.5}$$

In the parallel configuration case, majority spin ↑ electrons from the injector can tunnel towards majority states in the collector and minority spin electrons can tunnel towards minority spin states.

In the antiparallel configuration, majority spin electrons from the injector can tunnel towards the minority states of the collector and vice versa. Therefore, a difference conductance appears between both configurations, characterized by the TMR ratio, as expressed in equation 1.6.

$$TMR = \frac{G_P - GAP}{G_{AP}} = \frac{R_{AP} - RP}{R_P} = \frac{2P_1P_2}{1-P_1P_2} \tag{1.6}$$

In the case of an amorphous barrier, such as AlOx, there is no crystallographic symmetry in the barrier. Therefore, incoherent tunneling takes place, leading to TMR values not larger than 100% at room temperature, as every electron symmetry contributes equally to the tunneling as observed in Figure 1.4 a. For such case, the TMR can still be explained by Julliere model, that assumes equal tunneling probabilities for all electrons regardless of their Bloch states. As the coherency of the Bloch states is lost in such amorphous tunneling barrier the model is still valid.

The model of Julliere fails to explain the very large TMR of magnetic tunnel junctions based on epitaxial barriers such as MgO barriers. In the case of a crystalline barrier, such as MgO with a bcc (001) crystalline texture, the electrons are able to tunnel coherently from the magnetic electrodes with the same texture. The electron's wave-functions in the FM layer are coupled with the evanescent wave-functions having the same symmetry in the barrier and the orbital symmetry is maintained as the electrons tunnel. Slonczewski was able to develop a more complex model in 1989, where the band structure effects in the barrier and the magnetic electrodes are included. In this model, the wave vector k_F of the electrons is also included. This allows to understand the large TMR values observed in MgO based MTJs. It is demonstrated by Slonczewski that the equivalent spin polarization of the ferromagnet/barrier couples is given by

$$P = \frac{(k_{F,\uparrow} - k_{F,\downarrow})(\kappa^2 - k_{F,\uparrow}k_{F,\downarrow})}{(k_{F,\uparrow}+k_{F,\downarrow})(\kappa^2+k_{F,\uparrow}k_{F,\downarrow})} = P_0\frac{\kappa^2 - k_{F,\uparrow}k_{F,\downarrow}}{\kappa^2 + k_{F,\uparrow}k_{F,\downarrow}} \tag{1.7}$$

where $k_{F,\uparrow}$ and $k_{F,\downarrow}$ are the wave vectors for the majority and minority electrons at the Fermi level. κ defines the decay coefficient of the electron tunneling probability traversing the tunneling barrier. P_0 is given by the polarization of the ferromagnet in Julliere's model.

An important consequence of this expression is the fact that the polarization is different for the type of electron considered. Each band has a different polarization, which means that the tunneling probability of the electron is strongly dependent on its orbital symmetry as seen in Figure 1.4 b. Therefore, the tunneling current is filtered as function of the electrons orbital symmetry.

The tunneling decay is strongly influenced by the Bloch state type as observed in Figure 1.4 c, for the case of 8 MgO tunneling barrier atomic monolayers. Bloch states Δ_2 and Δ_5 have a much stronger exponential decay than for Δ_1 states. So mostly electrons which have a Δ_1 wave function symmetry tunnel through the MgO barrier. Moreover, for bloch states Δ_2 and Δ_5 , both majority and minority states can be found at the Fermi level as observed in Figure 1.4 d but their contribution to the tunneling process is weaker. However, for Δ_1 , only majority electrons are filled at the Fermi level, resulting in a full polarization, 100%. In the antiparallel configuration, there are no minority states $\Delta_{1\downarrow}$ to tunnel from or to. Therefore, only in the parallel configuration, there is a significant conduction through this channel. The effect is even stronger in Co since there is no Δ_2 nor Δ_5 states at Fermi energy.

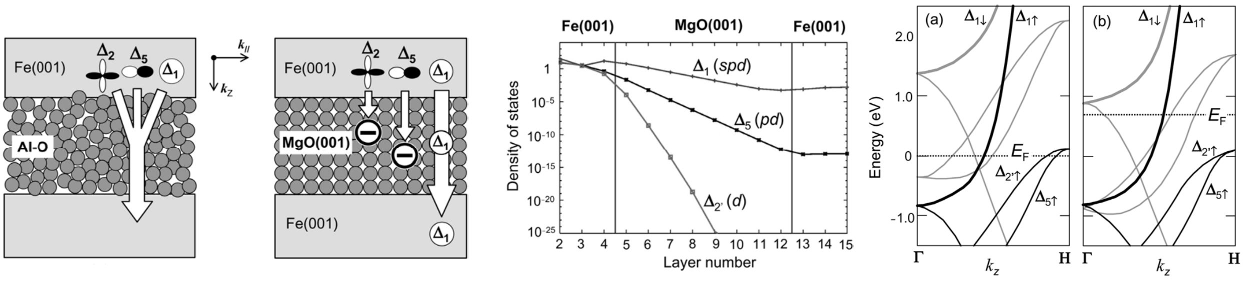

(a) (b) (c) (d) (e)

Fig. 1.4: Illustration of electrons tunneling through an amorphous (Al_2O_3) (a) and a crystalline (MgO) barrier (b). Density of states (DOS) variation for majority electrons tunneling ($k_{\|}$=0) in a MTJ system Fe/MgO/Fe with bcc (001) symmetry in the parallel configuration obtained by first-principle calculations (c). Band dispersion of bcc Fe (d) and bcc Co (e) in the [0 0 1] (–H) direction. From [18].

The resulting TMR here described allows to have two well differentiated resistance states that are read as the '0' and '1' bits during the information reading process in MRAM applications. Now that the mechanism of reading has been explained, we follow with an introduction to the physical phenomena that is used for the writing of MRAM devices.

1.1.4 Spin Transfer Torque (STT)

The magnetic state of a ferromagnet can be modified by using a spintronic phenomenon known as spin transfer torque (STT). STT is based on the transfer of spin angular momentum between two parallel ferromagnetic films connected by a non-magnetic metallic spacer (FM/NM/FM) when a current transverses the multilayer system as proposed by Slonczewski and Berger in 1996 [20, 21].

Current-driven excitations in magnetic multilayers were first observed by Tsoi et al. in 1998 [22]. In 2000, Katine et al. demonstrated the switch of the magnetization alignment of Co layers in a Co/Cu/Co system [23] induced by spin torque. Few years later, STT in MTJs was reported. First in 2004 in MTJs based on an AlO_x barrier [24] and one year later in MgO based MTJs [25, 26, 27]. In those early studies, critical switching currents between $0.78 - 6 \cdot 10^6 A/cm^2$ were observed, and the influence of the pulse duration into the switching current started to be analyzed, attributed to a thermally activated process for pulses longer than 20 ns.

In Figure 1.5, the spin transfer torque phenomenon in a ferromagnet (FM1)/ non-magnetic metal (NM) / ferromagnet (FM2) system is illustrated, while the NM layer can also be an insulator as in MTJs. When the current transverses the first ferromagnetic material, the delocalized conducting electrons 4s responsible of the current transport tend to align in the direction of the local magnetization, given by the 3d electrons due to exchange interaction as explained in the previous Section 1.1.1. The current becomes spin polarized, transverse the NM layer until it reaches the NM/FM2 interface. In the FM2, the local magnetization is differently oriented as seen in Figure 1.5 a. The electrons traversing this second interface NM/FM2 tends to align in the direction of the local magnetization which implies a transfer of spin angular momentum $(\vec{m_\perp})$. The electrons become aligned into the direction of the local magnetization in typically less than a nanometer. As a result, this transfer of spin angular momentum can modify the local magnetization direction, which is used for the writing operation of MRAM.

For the opposite current polarity, the electrons flow from FM2 to FM1 as in Figure 1.5 c. The same effect as described above takes place in FM1, there is a transfer of spin angular momentum from the electrons coming from FM2 with a different magnetization. However, there is a certain amount of electrons whose spin is antiparallel to the local magnetization M1. Those electrons are strongly scattered or do not find states into which to propagate through the FM1/NM interface so that they are reflected back to the FM2. The transfer of spin angular momentum of the backscattered electrons into the local magnetization M2 results in a torque $(\vec{m_\perp})$ which pulls the magnetization away from M1 as observed in Figure 1.5 d.

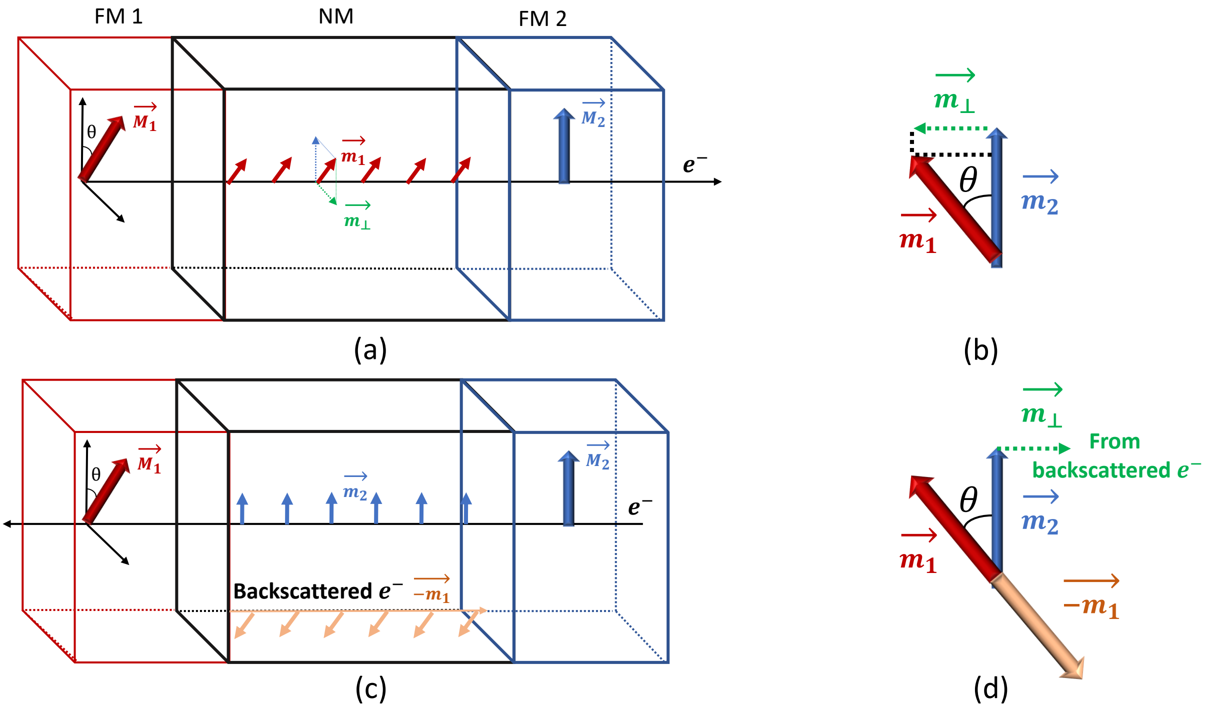

Fig. 1.5: Illustration of spin-transfer torque in a ferromagnet (FM) / non magnetic metal (NM) / ferromagnet (FM) system for a positive current (a). The resulting torque $\vec{m_\perp}$ tends to align the local magnetization $\vec{M_2}$ in the direction of $\vec{M_1}$ (b). For a negative current, the back-scattered electrons from the interface FM1/NM travel back to FM2 (c), the resulting torque tends to push $\vec{M_2}$ away from $\vec{M_1}$ (d).

In MRAM, a magnetic tunnel junction is used in which one ferromagnetic layer is more stable than the other by means that will be later described in Section 1.2. Therefore, there is a 'fixed' reference layer and a 'free' layer[1] that is used to store the information, as its orientation with respect to the

---

[1] The terms free layer and storage layer are used interchangeably in this manuscript.

first layer modifies the resulting resistance due to the TMR phenomenon previously explained [28]. For the writing operation, if both layers are oriented antiparallel, a positive current will make spin polarized electrons flow from the reference (FM1) to the free layer (FM2) and the spin transfer torque described above will turn the magnetization of the free layer (FM2) in the same direction as that of the reference layer (FM1), resulting into a parallel configuration. The back-scattered electrons from the free layer (FM2) towards the reference layer (FM1) will have little effect due to the larger stability of this layer. However, for the transition from parallel to antiparallel, P → AP, a negative current is required, so that the electrons flow from the free layer (FM2) towards the reference layer (FM1) and those back-scattered electrons will be responsible of the spin transfer torque into the free layer that will reverse its magnetization. Therefore, by using different current polarities, it is possible to switch between both configurations.

The expression of the spin transfer torque is given in Equation 1.8, where ST stands for Slonczewski torque [29].

$$(\frac{d\vec{m}_2}{dt})_{ST} = \frac{J}{t \cdot e} P_{spin} \frac{-|g|\mu_B}{2} (\vec{m}_2 \times (\vec{m}_2 \times \vec{m}_1)) \tag{1.8}$$

where $\frac{-|g|\mu_B}{2}(\vec{m}_2 \times (\vec{m}_2 \times \vec{m}_1))$ represents the torque contribution of each electron flowing from M_1 to M_2. The cross-product $-(\vec{m}_2 \times (\vec{m}_2 \times \vec{m}_1))$ defines the torque direction $\vec{m}_\perp$ depicted in Figure 1.5 b, g is the electron Landé factor and μ_B is the Bohr magneton. In order to account for the total current of electrons flowing towards the free layer, the injected current density J is included while t is the thickness of the free layer. The spin polarization previously introduced is also accounted. P_{spin} is the spin polarization at the NM/FM interface. It can be tuned by selecting different materials [30] and it also depends on the barrier quality and the presence of imperfections.

This 'Slonczewski torque' is also known as 'in-plane torque', since the resulting torque lies in the plane defined by the magnetization of both free layer $\vec{M}_2$ and reference layer $\vec{M}_1$. However, another type of torque exists known as 'perpendicular torque', since it is directed in the perpendicular direction of both magnetizations$-(m_2 \vec{\times} \vec{m}_1)$. This term is often neglected in spin valves but can be larger in MTJs (from 10 to 30% of the $\vec{\tau}_{||}$)[31, 32, 33] and depend on the bias voltage [34], leading to some undesired back-switching of the free layer magnetization [35]. In contrast to in-plane MTJ systems, for p-MTJs as the ones studied in this manuscript, the perpendicular torque contribution does not affect the switching mechanism [36].

1.1.5 Spin Orbit Torque (SOT)

About a decade ago, in 2011, a different mechanism of transferring spin angular momentum to a ferromagnetic layer, by using Spin-Orbit-Interaction (SOI) was reported [37]. The resulting torque known as spin orbit torque (SOT) appears in metallic samples with structural inversion asymmetry (SIA).

Two main mechanisms are responsible for the SOT effect:

1. The Spin-Hall effect
2. The Rashba effect

The Rashba effect is an interfacial effect. By sandwiching the ferromagnetic free layer (FM) between two dissimilar interfaces, e.g. a heavy metal and an oxide layer as in Figure 1.6) an effect known as Rashba effect can appear [38, 39]. Due to the SIA (i.e., the potential $V(-\mathbf{r}) \neq V(+\mathbf{r})$) a net electric field appears. As a consequence, the electrons that are flowing in the plane of a conductor experience a magnetic field (Rashba field) given by Equation 1.9.

$$\mathbf{B}_R = \alpha_R(\hat{\mathbf{z}} \times \mathbf{j}) \tag{1.9}$$

where α_R is the Rashba constant, $\hat{\mathbf{z}}$ a unit vector in the direction perpendicular to the plane and $\mathbf{j}$ the vector current density [37].

The second mechanism, called Spin-Hall-Effect, is a bulk effect that originates in the heavy metal layer. When an in-plane charge current is applied to a heterostructure with broken inversion symmetry and large spin-orbit coupling, the spin polarized electrons are accumulated in the adjacent ferromagnet. These accumulated spins can transfer angular momentum and exert a torque on the magnetization. For a better understanding of the resulting torques, their nature and symmetry was studied by Garello et al in 2013. [40].

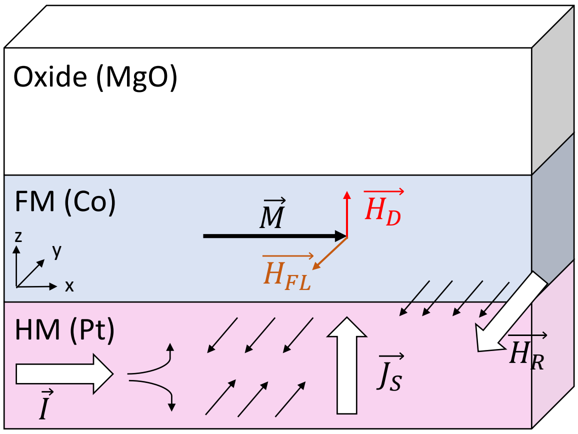

Fig. 1.6: Stack structure of a typical heavy metal(HM)/ferromagnetic layer (FM)/oxide layer (Ox) used for inducing SOT in the FM due to Spin-Hall-effect and Rashba interaction, where H_R denotes Rashba field while H_D and H_{FL} denote damping-like and field-like effective fields both resulting from the spin Hall effect.

The use of SOT for switching the ferromagnetic free layer of a MTJ has several advantages such as separate write and read current paths yielding improved write endurance in memory cells, low writing current and possibility of fast (sub-ns) switching.The disadvantage is the larger cell footprint of SOT-MRAM compared to STT-MRAM due to the fact that SOT-MRAM are three terminal devices while STT-MRAM are two terminal devices. Nevertheless, the advantages of SOT writing mechanism makes this approach very attractive particulary for fast MRAM such as those intended for SRAM type of applications. Such advantages are explained in Section 1.3.

1.2 Spintronic materials

In order to build a magnetic memory element with two possible bit states “0” and “1”, a uniaxial magnetic anisotropy is required in both ferromagnetic layers composing the three layer structure previously introduced (FM/MgO/FM). We explained in the previous sections that such trilayer structure possesses large TMR for the reading process and is written by the application of STT from a spin polarized current.

In the first generation of MRAM based on in-plane magnetized MTJs, such uniaxial anisotropy was obtained by giving to the cell an elliptical shape thus providing a shape anisotropy of the free layer, with easy-axis along the long axis of the ellipse. All more recent generations of MRAM are based on out-of-plane magnetized tunnel junctions which exhibit larger anisotropy and better trade-off between retention and writability. In these junctions, an interfacial anisotropy contribution is used which exists at the interface between the magnetic metallic electrodes and the tunnel barrier, leading to advantages such as lower writing current or larger scalability. Recently, a combination of both shape anisotropy and interfacial anisotropy has been used to improve the scalability of p-STT-MRAM [41, 42, 43, 44].

In order to understand the nature of such uniaxial anisotropy, the different contributions to the total free energy of a ferromagnet are first explained. An introduction to in-plane magnetized MTJs and out-of plane magnetized MTJs (p-MTJs) follows.

1.2.1 Free energy of a ferromagnet

The total free energy of a ferromagnetic element is given by several contributions, mainly exchange energy, magnetocrystalline anisotropy energy, demagnetizing energy and Zeeman energy, as given in Equation 1.10 [45].

$$E_{tot} = E_{ex} + E_{anis} + E_{dem} + E_{Zeeman} \tag{1.10}$$

Exchange energy

In localized magnetism, as for rare earths, for which the f-bands are partially filled, the exchange interaction is a short range interaction between electron spins. From Pauli exclusion principle, two electrons parallel their spins to reduce their electrostatic interaction energy, what results in Hund's rule in an atom.

In a crystal, the outer electrons will no longer be confined to the atoms. In this case, the nature of the exchange interaction will depend on the interatomic distance although crystallinity is not a requirement for ferromagnetism [46], i.e. it does not require a geometrical regularity of atoms position.

The Hamiltonian of the exchange interaction in a localized magnetism model is given by equation 1.11.

$$\mathcal{H}_{ex} = -\sum_{i<j} \mathbf{J_{ij}} \vec{s_i} \cdot \vec{s_j} \tag{1.11}$$

$\mathbf{J_{ij}}$ stands for the Heisenberg exchange constant between neighboring spins $\vec{s_i}$ and $\vec{s_j}$ and its sign determines if the interaction is positive, favoring a parallel alignment of the spins, resulting into a ferromagnetic response or negative resulting into an antiferromagnetic material.

For transition metals, for which the d-bands are partially filled, the ferromagnetic character is given by delocalized electrons. Therefore, an itinerant magnetism model (Stoner model) can be considered as a better description for the exchange energy. In this case, the exchange energy is given in equation 1.12:

$$E_{ex} = \int_V A_{ex}[(\nabla m_x(\mathbf{r}))^2 + (\nabla m_y(\mathbf{r}))^2 + (\nabla m_z(\mathbf{r}))^2] dV \tag{1.12}$$

where A_{ex} is the exchange stiffness constant that depends on the material lattice parameter and is typically on the order of $10^{-11} J/m$ [45].

Magnetocrystalline anisotropy energy

The exchange interaction previously introduced can be understood as a spin-spin interaction that depends on the relative orientation between spins but is isotropic, it does not depend on the relative orientation between the spin axis and the crystal lattice. However, there is also a coupling between the spin and the orbital motion of each electron that depends on the crystalline lattice, i.e. spin-orbit coupling. In a crystal, the distribution of charges generates an electrostatic field that modifies the angular momentum of the electron orbitals, generating preferential directions for the alignment of the magnetic moments of the electrons called easy directions of magnetization.

In order to rotate the spin away from its easy directions, an associated energy due to the spin-orbit coupling needs to be provided, which is the magnetocrystalline anisotropy energy. The energy expression of the magnetocrystalline anisotropy energy depends on the symmetry of the crystalline structure and is given in equation 1.13 for the most common case of uniaxial anisotropy along the direction $\vec{u}$ [45].

$$E_{anis} = \int_V K_u[1 - (\vec{u} \cdot \vec{m})^2] dV \tag{1.13}$$

where K_u is the anisotropy constant, expressed in (J/m^3) units.

Interfacial anisotropy energy

For the case of thin multilayers, an additional source of anisotropy called interfacial anisotropy can be present, as in Pt/Co, Co/Ni or Fe/MgO systems. Such interfacial anisotropy can arise due to interfacial electron hybridization or interfacial stress [47]. In such cases, an effective anisotropy constant $K_{eff} = K_u + K_s/t$ is defined as the sum of bulk K_u and interface anisotropy K_s constants, where t is the layer thickness. In Section 1.2.3 we discuss how such interfacial anisotropy is exploited for perpendicularly magnetized MTJs.

Zeeman energy

Under the action of an external field, the energy of a magnetic element is minimized when the magnetization $\mathbf{m}(\mathbf{r}, t)$ is oriented in the direction of the applied external field $\mathbf{H_{app}}(\mathbf{r}, t)$.

The interaction of a magnetic element with an external magnetic field can be expressed as given in Equation 1.14.

$$E_{Zeeman} = -\mu_0 \int_V M_s \mathbf{m}(\mathbf{r}, t) \cdot \mathbf{H_{app}}(\mathbf{r}, t) d\mathbf{r} \tag{1.14}$$

where $\mu_0 = 4\pi \times 10^{-7}$ is the vacuum permeability [45].

Demagnetizing energy

A magnetic body generates a magnetic field by itself. This generated magnetic field tends to align the magnetization along the long axis of the magnetic element and favors a local alignment of the magnetization in the element boundaries. Such generated magnetic field is labeled as “demagnetizing field” when considered inside the volume of the magnetic body itself, and “stray field” when considered in the external region of the magnetic body. The resulting demagnetizing energy is given by equation 1.15 [48]

$$E_{dem} = -\frac{1}{2} \int_V \mathbf{H}_d \cdot \mathbf{J} dV \tag{1.15}$$

where $\mathbf{J} = \boldsymbol{M}/\mu_0$ is the magnetic polarization and $\mathbf{H}_d$ is given in Equation 1.16.

$$\mathbf{H}_d = -\mathbf{N} \cdot \mathbf{J}/\mu_0 \tag{1.16}$$

where $\mathbf{N}$ is the demagnetizing tensor. In a general case, numerical computation is required to obtain the values of the demagnetizing coefficients. For the case of uniform magnetization, the demagnetizing tensor is diagonal as given in Equation 1.17.

$$\mathbf{N} = \begin{bmatrix} N_{xx} & 0 & 0 \\ 0 & N_{yy} & 0 \\ 0 & 0 & N_{zz} \end{bmatrix} \tag{1.17}$$

where the trace of $\mathbf{N}$ equals 1. For simple geometries such as the sphere $N_{xx} = N_{yy} = N_{zz} = 1/3$, the slab (or infinite thin film) $N_{xx} = N_{yy} = 0$ $N_{zz} = 1$ or a cylinder of infinite thickness ($L_z = \infty$), $N_{xx} = N_{yy} = 1/2$ $N_{zz} = 0$ the demagnetizing coefficients are well known. An analytical expression is given by Aharoni for the rectangular prism [49]. Approximate expression exists for cylinders [50]. Rigorously speaking, only elements with ellipsoidal shape can have a uniform demagnetizing field and therefore a uniform magnetization.

The competition between all terms of energy and particularly exchange energy and demagnetizing energy determines whether a magnetic element presents a uniform magnetization or not, such as for instance a flower state in cylindrical sample with out-of-plane anisotropy or a vortex state in a cylindrical sample with easy-plane anisotropy [51].

1.2.2 In plane magnetized MTJ

Now that the main contributions to the total energy of a ferromagnetic element have been introduced, the sources of in-plane and out-of-plane anisotropy used in MRAM MTJs can be better understood.

In the early days of MRAM development, the magnetic tunnel junction structures were developed with in-plane configuration for the ferromagnetic electrodes as previously used in spin valves. The in-plane MTJs are typically patterned with an elliptical shape in order to define an uniaxial anisotropy.

In order to induce a unidirectional anisotropy, i.e. a specific in-plane preferred direction, in the ferromagnetic reference layer (F), F is typically pinned in a certain direction by using an antiferromagnetic layer(AF), as $\mathrm{I}r_{20}\mathrm{M}n_{80}$ or $\mathrm{P}t_{50}\mathrm{M}n50$ in the configuration AF/F as in Figure 1.7. The MTJ needs to be annealed at a temperature larger than the antiferromagnetic layer blocking temperature (T_N) and cooled down in the desired magnetic field direction. An interfacial exchange coupling exists between the AF and the F material that favors a parallel alignment between the spins of the F and AF at the interface [52, 53] leading to a unidirectional anisotropy instead of a uniaxial anisotropy.

A single reference layer polarizer magnetization creates a net stray field on the free layer that hinders a bi-stable parallel/anti-parallel configuration of the MTJ. To avoid this, a synthetic antiferromagnetic structure (SAF) is often used as in Figure 1.7 to reduce the resulting stray field from the reference layer. Since both magnetic components of the SAF, FM_1 and FM_2 are antiferromagnetically coupled, the total stray field on the free layer can be compensated leading to a net zero field into the free layer. The SAF structure is based on an antiparallel interlayer exchange coupling (IEC) between two ferromagnetic layers separated by a non-magnetic layer (NM). Metals conventionally used for providing such antiferromagnetic coupling are ruthenium (Ru) or iridium (Ir). The strength and sign of the IEC vary with the NM thickness in an oscillatory way [54, 55].

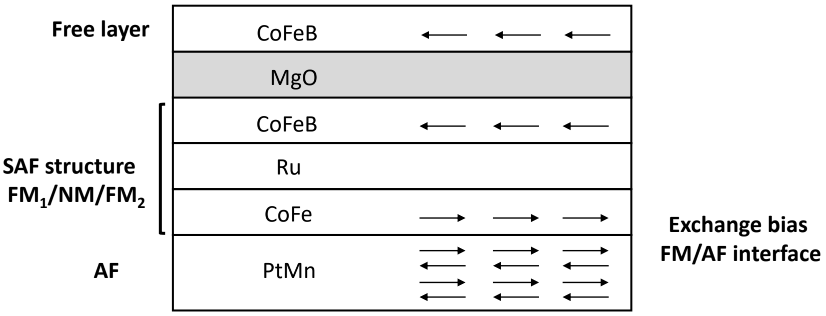

Fig. 1.7: Stack representation of a conventional in-plane MTJ, including a AF layer to induce exchange bias on the reference layer that comprises a SAF structure to reduce the resulting stray field on the free layer.

Different variants of the initial stack structure have been investigated in order to reduce the switching current. A faster switching mechanism based on the precessional motion of the free layer by using an out-of plane polarizer was proposed [56]. The introduction of a source of perpendicular anisotropy into the free layer led to switching currents as low as $\sim 2MA/cm^2$ [57]. The presence of such source of PMA helps to counteract the large out-of plane demagnetizing field that inhibits current induced switching.

1.2.3 Out of plane magnetized MTJ based on i-PMA

Beyond the advances made in the stack developments of in-plane MTJs, nowadays most of the developments in MRAM are based on magnetic tunnel junctions with perpendicular anisotropy (PMA), i.e. p-MTJs. There are several reasons that make p-MTJs advantageous. First, in the case of in-plane MTJs, an elliptical shape is required in order to provide uniaxial shape anisotropy. This increases the cell footprint and introduce more device variability due to the patterning process. In p-MTJs, there is no need to have such elongated shape. The perpendicular anisotropy is by itself uniaxial, so that a cylindrical MTJ can be used allowing an easier down-size scalability.

Several material systems can exhibit perpendicular anisotropy [47] such as Co/Pt, Co/Pd or Co/Ni multilayers, alloys presenting a L10 order (FePt, FePd, CoPt ou CoPd), semiconductor ferromagnets such as Ga_xMn or recently reported $L1_0MnAl$. Nonetheless, as we have seen in the previous Section 1.1, the MgO/CoFeB system exhibits large TMR and STT and thereby constitutes the ideal candidate for the tunnel junction itself, as it also presents PMA.

Perpendicular magnetic anisotropy originates at the interface between the FeCoB layers and the MgO tunneling barrier [58]. Such PMA at magnetic metal/oxide interface was discovered in 2002 at SPINTEC and its use for out-of-plane STT-MRAM cell was demonstrated at Tohoku Univ. in 2010 [59, 47, 58]. By reducing the CoFeB storage layer thickness, the interfacial anisotropy can overcome the demagnetizing energy and stabilize a stable perpendicular magnetic state, as seen in Figure 1.8 a.

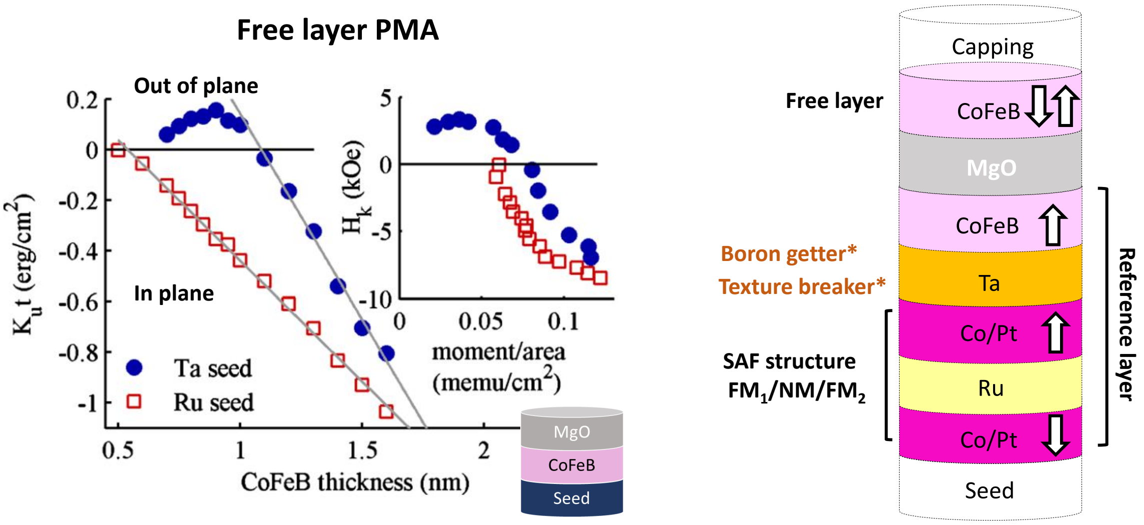

(a) (b)

Fig. 1.8: Perpendicular anisotropy energy of thin films with composition Seed/CoFeB/MgO, for both Ta and Ru seed layers. A transition between the in-plane ($K_ut < 0$) and out-of-plane region ($K_ut > 0$) is observed as a function of the CoFeB layer thickness for Ta seed layer (blue dots). The inset shows anisotropy versus moment area of the same samples (a). Figure redrawn from [60]. A typical structure of a p-MTJ (CoFeB/MgO/CoFeB) with a CoFeB reference layer coupled to a SAF element by a thin Ta lamination (typically 0.2-0.3 nm) that acts both as boron getter during annealing of the MTJ and texture breaker between the SAF and CoFe/MgO/CoFe miss-matching crystallographic structures (b).

It can also be highlighted in Figure 1.8 a that the PMA disappears for all CoFeB thickness if the seed layer used is a ruthenium layer. It was demonstrated by Nistor et al. [61] that a boron getter layer is required to absorb the diffusing boron after annealing of the MTJ. Otherwise, boron diffuses towards the MgO barrier leading to a deterioration of the MgO barrier properties, both in terms of PMA and TMR. It turns out that Ta is a boron getter element (as also tungsten (W) or molybdenum (Mo)) and that is the reason why in Figure 1.8 a, the PMA is maintained when using a Ta seed layer.

Moreover, the use of a tantalum thin layer also serves as a texture breaker. A particular problem of using two ferromagnetic electrodes (reference and free layer), is that the reference layer produces a stray field on the free layer that disturbs its functioning, as for in-plane MTJs. A synthetic antiferromagnetic reference layer structure (SAF) has also become a standard in p-MTJs as in Figure 1.8 b, since the use of two oppositely magnetized components allow a resulting null field on the free layer. Such reference layer is typically built with Co/Pt or Co/Pd multilayers with large interfacial anisotropy antiferromagnetically coupled by a thin Ru layer (typically 0.4nm or 0.9nm, due to the oscillatory nature of the RKKY coupling [54]), leading to an increased stability of the reference layer. However, the previous SAF structure has a threefold symmetry fcc (1 1 1), different from the fourfold crystallographic symmetry bcc (0 0 1) of the oxide tunneling barrier. Therefore, a texture breaker thin lamination as Ta is essential to grow the bcc (0 0 1) MTJ correctly.

As will be discussed later in Section 1.3.1, besides a larger areal density, p-MTJs result into lower switching currents when compared to in-plane magnetized MTJs, making them the most used structure in STT-MRAM applications nowadays.

1.3 Spintronic devices

Several types of spintronic devices are used today for different applications such as memories, magnetic sensors, RF devices, logic devices or neuromorphic devices among others [62, 63, 64]. They are based on the control of the spin angular momentum of the electrons, in contrast with conventional electronic devices in which only control over the electron charge is exploited.

In the case of memory applications, STT-MRAM is especially suitable for density, while SOT-MRAM seems to be more appropriate when faster switching is required, as for cache applications. A combination of both phenomena has also led to promising results [65, 66] and other effects such as voltage controlled magnetic anisotropy (VCMA) are attracting a lot of interest [67] to further reduce the power consumption.

1.3.1 Magnetic random access memory (MRAM)

Different classifications of MRAM devices can be possibly made but we classify them into two main groups: a first generation of MRAM whose writing mechanism was performed by generating a field to switch the magnetization of the storage layer and a more recent generation of devices where the switching is performed by a current passing through the MTJ (or spin-valve).

MRAM written by field

In the early days of MRAM development, between 1996 and 2004, the writing of the MTJs was performed by applying a magnetic field as for Stoner Wolfarth MRAM [68] or Toggle MRAM [69], the latter being the first commercialized MRAM [70, 71, 72]. However, field induced switching technologies required large currents of few mA. Moreover, the scalability is limited due to electromigration in the conducting lines that create the magnetic field by pulses of current, as illustrated in Figure 1.9 a, leading to reliability issues. Thermally assisted MRAM (TA-MRAM), based on the local heating of the MTJs partially improved those issues, but the writing mechanism itself remained also by magnetic field [73, 74].

MRAM written by current

The drawbacks encountered by field-driven MRAM namely large switching current and electromigration between the conducting lines generating magnetic field were overcome by the introduction of STT switching. STT enables very good write selectivity, since the current used for the writing process flows through the selected MTJ. In addition, the same path is used for reading and writing processes as seen in Figure 1.9 b, which enables a better scalability.

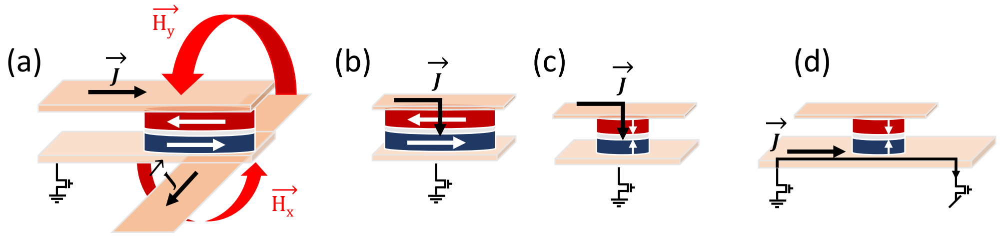

Fig. 1.9: Integration scheme of Toggle MRAM (a), in-plane STT-MRAM (b), p-STT-MRAM (c) and p-SOT-MRAM (d).

In the first generation of in-plane MRAM previously discussed in Section 1.2.2, the thermal stability factor (Δ) is limited by the aspect ratio of the ellipsoidal MTJ. The thermal stability factor, is given by the energy barrier between the parallel “P” and antiparallel “AP” states between the reference and storage layer as seen in Figure 1.10.

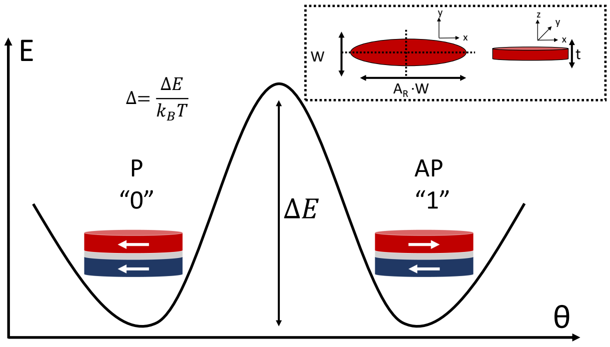

Fig. 1.10: The energy barrier between the parallel and antiparallel states in the MTJs defines the thermal stability factor (Δ) of the MTJ, as $\Delta = \Delta E/k_B T$. The inset shows the elliptical free layer dimensions, as used in in-plane MTJs, where t is the layer thickness, w width, $A_R \cdot w$ length and A_R the in-plane aspect ratio.

The resulting thermal stability factor for in-plane magnetized storage layer, with relatively weak magnetocrystalline anisotropy, as it is often the case is given by Equation 1.18 [75].

$$\Delta = \frac{\Delta E}{k_B T} = \frac{\mu_0}{2} \frac{M_s^2 t^2 (A_R - 1) w}{k_B T} \tag{1.18}$$

As observed in Equation 1.18, the thermal stability for in-plane magnetized storage layers scales with the aspect ratio. As a result, the requirement of a sufficiently high thermal stability factor limits the downsize scalability. In order to fulfill the industrial standards of retention, Δ should be between 60 and 100. For an in-plane magnetized MTJ, to keep $\Delta > 70$ the minimal dimensions allowed are about 60 nm x 150 nm, for a conventional CoFeB storage layer 2.5nm thick [75].

A different approach was explored by using a perpendicular configuration of the magnetization in the MTJ, as explained in Section 1.2.3 [60]. A first advantage of p-MTJs is its lower switching current compared to in-plane MTJs. For in-plane MTJs, the barriers for retention and writing are different. Retention is given by the in-plane shape anisotropy of the free layer while for writing the large out-of plane demagnetizing energy has to be surmounted as observed in the switching trajectory of Figure 1.11 a. In contrast, for p-MTJs both barriers are the same, given by the perpendicular direction as seen in Figure 1.11 b, which results in lower switching currents for the same thermal stability.

The thermal stability in macrospin approximation for a cylindrical perpendicularly magnetized free layer, with diameter w, is given by Equation 1.19 [75].

$$\Delta = \frac{\Delta E}{k_B T} = \frac{[(K_V - (1/4)\mu_0(3N_z - 1)M_s^2)t + K_s]\frac{\pi}{4}w^2}{k_B T} \tag{1.19}$$

As explained in Section 1.2.3, in p-MTJs the main source of perpendicular anisotropy is interfacial and results into a $\Delta = 77$ for w=25nm, for the case of a CoFeB storage layer 1.2 nm thick and interfacial anisotropy $1.2 \times 10^{-3}\ J/m^2$ [75]. The storage layer thickness is reduced as compared to the in-plane case in order to reduce the demagnetizing energy that tends to favor an in-plane orientation. However, the storage layer thickness reduction is limited by a decrease of the spin polarization that can affect the TMR of the MTJ.

Conventional p-MTJs of around 25nm diameter can keep a sufficiently large thermal stability. To further reduce the cell size, one possibility is to add a second MgO oxide barrier on top of the storage layer to provide an extra source of interfacial anisotropy [76, 77].

Another innovative approach consists in significantly increasing the thickness of the storage layer, to an aspect ratio (t/D) close to 1, so that the demagnetizing energy favors the perpendicular orienta-

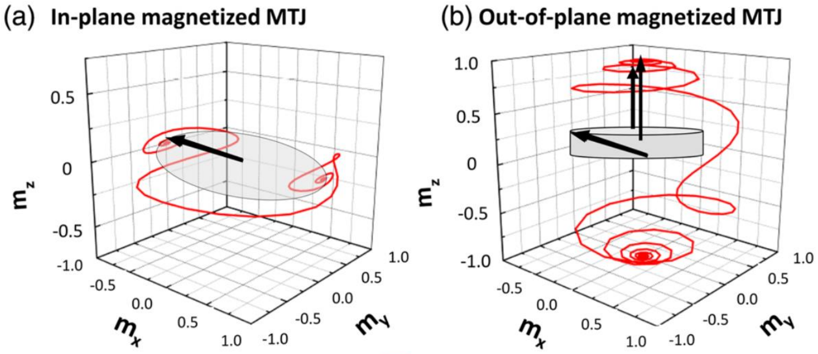

$$j_c^{in-plane} = \left(\frac{4e}{\hbar}\right)\frac{\alpha k_B T}{\eta A}\left(\Delta + \boxed{\frac{\mu_0 M_s^2 V}{2k_B T}}\right) \qquad j_c^{perp} = \left(\frac{4e}{\hbar}\right)\frac{\alpha k_B T}{\eta A}\Delta$$

Fig. 1.11: Scheme of the switching trajectories for in-plane storage layer (a) and perpendicularly magnetized storage layer (b). The respective switching currents are given by the respective equations below the figure. The highlighted term in red shows the “extra” demagnetizing energy that needs to be overcome by STT switching of in-plane magnetized MTJs that does not contribute to the overall thermal stability. Figure from [47].

tion of the magnetization, providing perpendicular shape anisotropy (PSA). PSA-STT-MRAM uses a combination of both interfacial anisotropy and shape anisotropy and allows the scaling down to very small nodes (sub-10 nm) [41, 42]. In Chapter 4 we exploit the use of perpendicular shape anisotropy to develop a reference layer of a p-MTJ, in order to get rid of critical metals typically present in the SAF structure.

Finally, SOT-MRAM has emerged as a promising technology in recent years since it allows a fast switching (reliable sub-ns write), virtual “unlimited” endurance and negligible read disturb since the reading and writing paths are separated, as seen in Figure 1.9 d. There are three schemes of SOT switching, with different storage magnetic layer easy-axis directions. The first, with the easy-axis in the perpendicular direction [37, 78, 79, 80] as in Figure 1.12 a while the other two are based on in-plane MTJs, one with the the easy-axis orthogonal to the current [81] as in Figure 1.12 b, while the last has [82, 83] easy-axis collinear with the current as in Figure 1.12 c.

The first, with perpendicular magnetization, benefits from high speed and is the best in terms of scaling, as discussed previously for the STT case. However, it requires an external in-plane field for deterministic switching. Innovative solutions have been proposed to circumvent such problem, as using a magnetic layer on top of the hard mask to generate the required field [84]. The second, with in-plane magnetization orthogonal to the current is field free but the incubation time is larger. The latest, with the easy-axis collinear to the current, is also fast but requires an out-of-plane field.

A possible drawback of SOT-MRAM compared to STT-MRAM is in any case the requirement of two transistors instead of the single one used in STT-MRAM, which limits the areal density of the technology.

Field free switching in p-MTJs at 10 ns by combining both STT and SOT has also been recently demonstrated with high yield on 300 mm scale [85].

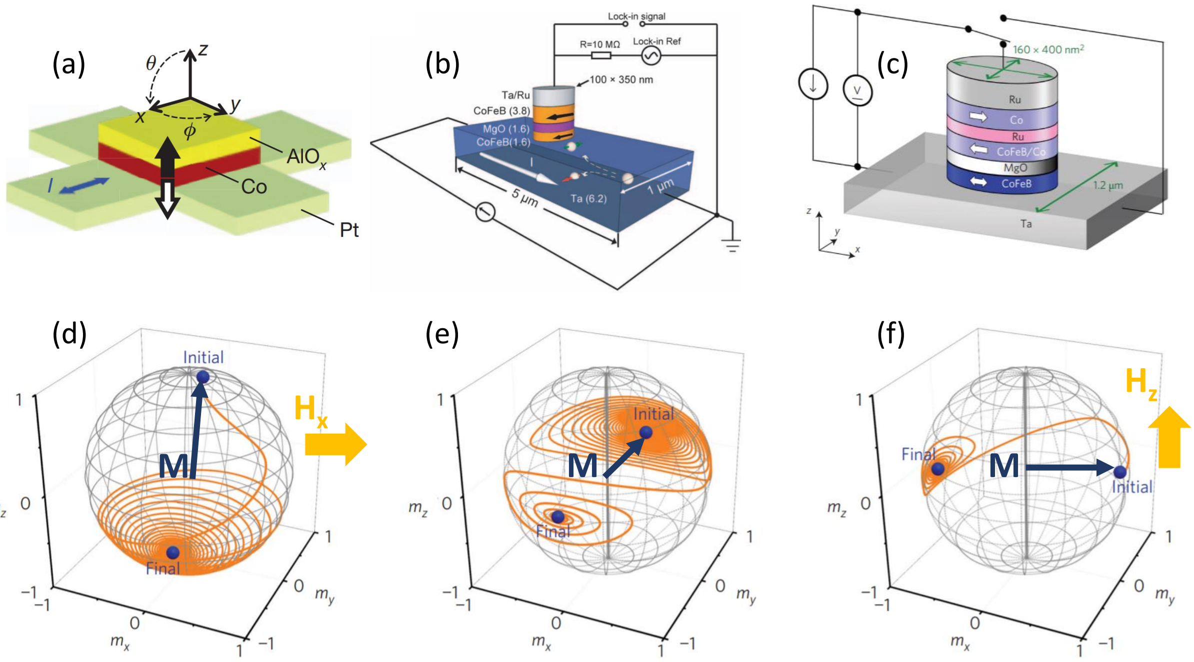

Fig. 1.12: Different reported SOT writing schemes, with different storage magnetic layer easy-axis. The easy-axis of the free layer can be perpendicular to the applied writing current (a), orthogonal (b) or collinear (c), leading to different magnetization dynamics (d,e,f) respectively. Image redrawn from [81]. Other images from: Miron et al. [37] (a) and Liu et al. [82] (b).

A comparison between different memory technologies together with MRAM is given in Table 1.1.

	Mature Memory Technologies			**Emerging Memory Technologies**			
	SRAM	**DRAM**	**FLASH**	**PCM**	**RRAM**	**FeRAM**	**MRAM**
Non-volatile	No	No	Yes	Yes	Yes	Yes	Yes
Endurance (# of cycles)	10^{16}	10^{16}	10^{5}	10^{8}	10^{6}	$10^{10} - 10^{14}$	$>10^{15}$
Read speed (ns)	1-100	30	50	20-50	10	20-80	2-20
Write speed (ns)	5-10	10	10^{4}	75	5-20	50	2-20
Write power	Low	Low	Very high	Medium	Low	Low	Low to medium
Cell size (F^2)	50-120	6-10	4	6-12	6-12	15-34	6-12
Scalability	Limited	Limited	Yes	Yes	Yes	Under research	Yes

Table 1.1: Performance indicators for existing stand-alone memory technologies. Strengths are highlighted in green while limiting factors are given in orange and red. Table redrawn from [86].

For the case of MRAM and resistive random access memory (RRAM[2]) the write and read speeds can be as fast as for solid state memories like Dynamic Random Access Memory (DRAM) and Static Random Access Memory (SRAM). However, RRAM is limited by its endurance [87] that can nevertheless be sufficient for Flash applications. For MRAM a larger number of cycles $> 10^{15}$ can be supported, necessary condition for use as working memory in microprocessors.

Several big microelectronic companies such as Samsung, TSMC, Intel or Global Foundries have started to commercialized MRAM products, highlighting the importance of this type of non-volatile memory technology. Commercialization started in 2012 with 64Mbit in-plane STT-MRAM by EVERSPIN technologies. In 2019 Everspin also demonstrated a 28 nm 1Gb STT-MRAM and it is now commercially available [88, 89].

---

[2] RRAM relies on the formation and the rupture of conductive filaments corresponding to low and high resistance states, respectively, in the insulator between two electrodes

1.3.2 Magnetic field sensors

Magnetic tunnel junctions or spin valves can be used as sensing elements, as they provide a resistance variation as a function of an applied external field with a dc bias supply [28]. Spintronic sensors based on magnetoresistance variation (AMR, GMR and TMR sensors) are nowadays used in a wide range of automotive, industrial or biomedical applications [90, 63, 91]. They present several benefits compared to other devices such as Hall sensors, current transformers (CT), shunt resistors or fluxgates due to their high sensitivity, compact size, low power consumption, compatibility with CMOS integration and low cost[92].

The conventional MTJ or spin valve structures, as described in Section 1.2.2 for in-plane magnetized MRAM are typically used, as observed in Figure 1.13 a. Under the action of an external field in the direction parallel to the reference layer, the MTJ experiences a variation of TMR, so called sensor transfer curve as observed in Figure 1.13 b.

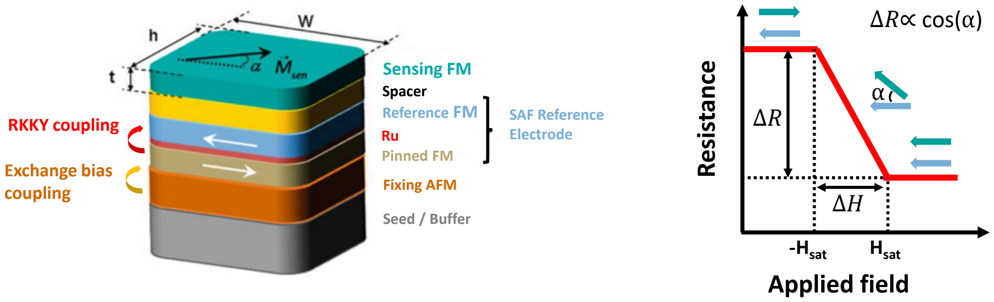

(a) (b)

Fig. 1.13: Scheme of the typical magnetic tunnel junction (spin valve) configuration used in TMR (GMR) sensors (a). A linear variation of resistance ΔR is obtained with an external applied field, with linear range ΔH (b). The sensor transfer curve shows the resistance variation from the change in the orientation of the sensing layer with respect to the reference layer by a certain angle (α). At zero field, the system is designed so that the magnetization of reference and free layer are orthogonally oriented with an intermediate resistance value. Image redrawn from [93].

The field range of response of the sensor is given by ΔH and corresponds to the field values between a fully parallel and antiparallel configuration between the reference and sensing layer. The ideal sensor exhibits a linear transfer curve with no hysteresis as in Figure 1.13 b.

The main characteristic of a magnetic sensor is its sensitivity, i.e. the variation of magnetoresistance with applied magnetic field ($\Delta R/\Delta H$).

The linear field range is given in this case by the anisotropy field of the sensing layer. Different linearization strategies can be used as given in Figure 1.14. At equilibrium reference and sensing layer would be parallelly oriented if not any extra other source of anisotropy is introduced, so that a non-linear MR response would result under an external orthogonal field as in 1.14 a. Several solutions are proposed to set the magnetization of the sensing layer orthogonal: crossed anisotropies upon material deposition (a), use of in-plane shape anisotropy for the sensing layer (b), use of an external permanent magnet (c) use of a superparamagnetic sensing layer (d) or finally the use of exchange bias also in the sensing layer, orthogonally to the pinning direction of the reference layer by a second antiferromagnetic (AFM) material (e).

Another type of sensor device, sensitive to in-plane field, has emerged in which the sensing layer presents a vortex state. Magnetoresistive sensors including a magnetic vortex free layer is a promising approach, due to their linear response, large linear range with low magnetic noise [94, 95, 96]. Typical vortex based sensors are based on the linear variation of resistance by the displacement of the out-of-plane magnetized vortex core in a orthogonal direction to the in-plane applied field as shown in Figure 1.15.

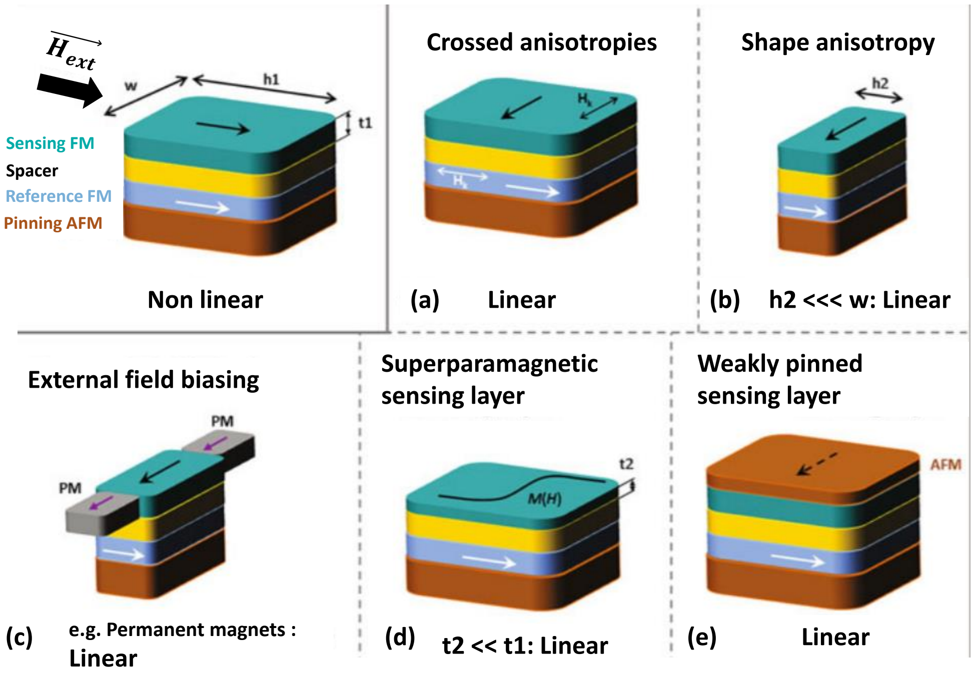

Fig. 1.14: Scheme of different linearization strategies used in MR sensors. Image redrawn from [93].

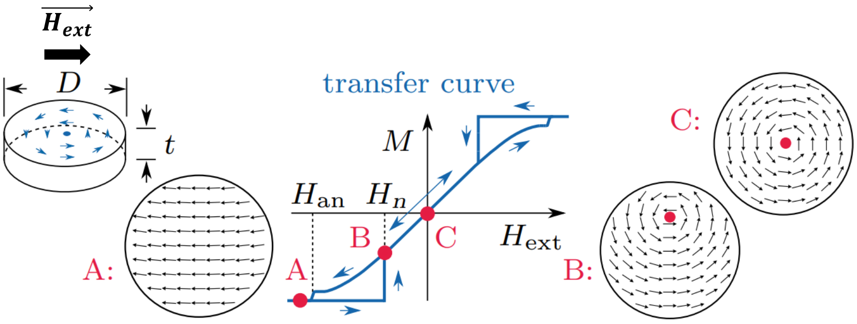

Fig. 1.15: Scheme of the transfer curve of a vortex based sensor, where H_n and H_{an} are the vortex nucleation and annihilation fields respectively. Figure from [95].

We have developed an innovative magnetoresistive sensor concept, sensitive to out-of-plane field, based also on the use of a vortex state in the sensing layer but with an out-of-plane magnetized reference layer, explained in Chapter 6. The sensing mechanism of this innovative device is based on the vortex core expansion/shrinkage in the sensing layer under the effect of an external perpendicular field allowing scalability to smaller nodes and a larger sensing field range as compared to conventional vortex based sensors.

Chapter 2

Why substitute critical materials in STT-MRAM?

Since the COVID-19 pandemic, there has been a significant shortage of chips as only few actors are in charge of chip manufacturing. February 8th 2022, the European Commission presented the "Chips Act", « a comprehensive set of measures to ensure the EU's security of supply, resilience and technological leadership in semiconductor technologies and applications ».

The chips act is born as a result from the need of Europe to be capable of manufacture semiconductor products without relying on the main industrial big fabrication facilities overseas. As stated in the act[1]: « Europe has an overall global semiconductors market share of only 10% and largely relies on third-country suppliers. In case of disruption of the supply chain, Europe's chips' reserves in some industrial sectors, such as automotive, may run out in a few weeks, forcing many European industries to slow down or halt production ».

Besides the importance of being able to manufacture the products inside the EU, another problematic needs to be regarded. Nowadays the main key components of most of the advanced technology, not only in the semiconductor sector, contain critical materials.

Reliable access to certain critical raw materials is a growing concern for the development of strategic technologies and sectors aiming for a more sustainable future. Critical materials are beyond the popularly known rare earths, whose supply is mainly concentrated in China. Many other metals are considered critical and there is a fear of shortage in their supply as their concentration in the earth is limited, as is the case of platinum group metals[2] (PGMs).

In this thesis, we target the substitution of certain critical materials (Pt, Ru) used in the most mature and commercialized Magnetic Random Access memory (MRAM) technology, p-STT-MRAM. We propose two alternatives which are detailed in Chapter 4 and Chapter 5. In addition, a new concept of magnetic sensor that might avoid the use of certain critical metals, such as iridium or platinum is proposed in Chapter 6.

In this Chapter, we first introduce some examples of critical materials used in emerging technologies. We follow by an introduction to the different parameters used by the EU methodology[3] for assessing criticality, for the specific case of Pt. Finally, we evaluate the particular impact of the use of platinum in p-STT-MRAM and more generally in spintronic devices.

---

[1] The European Chips Act: https://digital-strategy.ec.europa.eu/en/library/european-chips-act-communication-regulation-joint-undertaking-and-recommendation

[2] The six platinum-group metals are iridium, osmium, palladium, platinum, rhodium and ruthenium.

[3] Methodology for Establishing the EU List of Critical Raw Materials - Guidelines [97]

2.1 Critical materials in green technologies

In recent decades, concern about climate change has increased and solutions for the demanding energy scenarios of the future are being investigated. Batteries, fuel cells, wind turbines or photovoltaics are examples of such renewable energy technologies.

Similarly, in the information and communication technologies (ICT) sector, alternative approaches are investigated in order to reduce the energy consumption of traditional devices.

Figure 2.1 shows the expected exponential increase of energy consumption up to 2030.

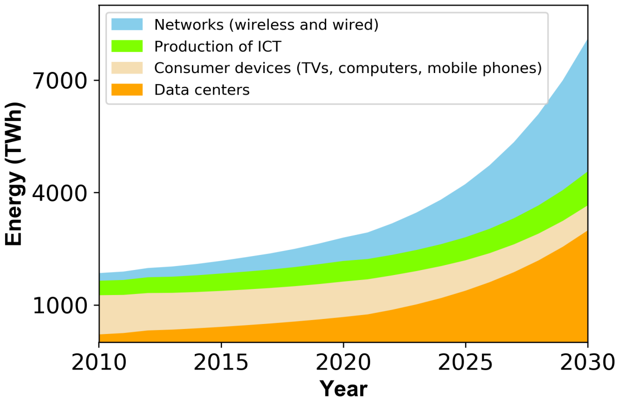

Fig. 2.1: Energetic forecast of information and communication technologies (ICT) for 2030 (Data from [98]).

The total amount of data globally produced is expected to reach 175 zettabytes by 2025 [99].

According to Belkhir [100], the global greenhouse gas (GHG) emissions from ICT could rise from 1.6% of the total in 2007 to 14% in 2040, taking the 2016 global production level as a reference.

New technologies and computer architectures are under development to reduce the power consumption. The use of non-volatile memory (NVM[4]) is a very attractive solution for ultra-low-power systems for the IoT [101]. Perpendicularly magnetized STT-MRAM is a promising technology among other non-volatile memories as it combines low power consumption, fast switching, high endurance and scalability [63, 102].

Although all these green technologies are promising, in many cases they contain critical raw materials that hinders their potential advantages. In some cases, the environmental benefit is not as important as initially predicted due to the elevated impact of the critical material extraction and further refining [103]. In addition, the production of those metals is often concentrated in the hands of a few countries, making the supply risk of such products a potential problem for the development of those green technologies.

China, Africa, and Latin America provide 74% of all battery raw materials. Rare earths for permanent magnets contained in wind turbines are mainly produced by China. In the case of the fuel cell industry, platinum is a key component of catalysts. Platinum production is mainly concentrated in South Africa [104].

As for the case of renewable energy technologies, in the information and communication technologies (ICT) sector, a large number of materials with high supply risk are present. For example, REEs in several applications including magnets, HDDs, displays, LED, lasers, circuit boards, or memories. Gallium, in GaAs alloy for semiconductors, LEDs, mobile phones, etc. Palladium is used for capacitors, ICs and circuit boards [104].

For the case of emerging data storage technologies, Ku et al. analyzed potential supply chain constraints [105]. They infer that increasing HDD production could put stress on Nd and PGM supply chains. Furthermore, if phase-change memory (PCM) or Resistive RAM (RRAM) become more important, Ge, Te or Hf supply chains could be stressed in the next decade.

---

[4] Non-volatile memory (NVM) can retain stored information even after power is removed.

In the case of Ferroelectric RAM (FeRAM) and MRAM devices, they concluded that the use of platinum group metals (PGMs) for gate layers can be problematic in terms of supply due to the small annual production of Pt and Ir, and that alternative solutions must be found.

The European Commission included in 2020 such conclusions in its report on raw materials for strategic technologies and sectors [104]. Nonetheless, the materials analyzed by Ku et al. correspond to the first generation of MRAM, using in-plane anisotropy developed in the early 2000s, as explained in Chapter 1.2.2. However, state-of-the-art MRAM uses spin transfer torque writing, in out-of-plane magnetized magnetic tunnel junctions (MTJ) [106, 102]. In perpendicular MTJs, materials that exhibit perpendicular magnetic anisotropy (PMA) are required, as previously explained in Chapter 1.2.3. Unlike in-plane MTJs, p-MTJs require the use of PGMs such as platinum or palladium for the reference layer SAF. Ruthenium is typically used in both configurations since it is responsible of the strong antiferromagnetic coupling that enables a SAF configuration.

The SAF is intended to provide thermal stability to the reference layer magnetization and to reduce the stray field exerted by the reference layer on the storage layer magnetization, as previously explained in Chapter 1.2.3.

Figure 2.2 a shows the stack composition of a typical p-STT-MRAM. In this case, multilayers comprising (Pt 0.25/Co 0.5 nm) repeats provide a strong perpendicular magnetic anisotropy (PMA) to the reference layer while a Ru layer 0.9 nm thick is used to obtain antiferromagnetic coupling between the top and bottom SAF components.

Platinum and ruthenium are part of a group of elements, known as PGM, whose mineral reserves are highly concentrated in a few locations, mainly in South Africa. Their low initial ore concentration, of only a few ppm[5] makes their mining and posterior processing complex, resulting into a very significant environmental impact.

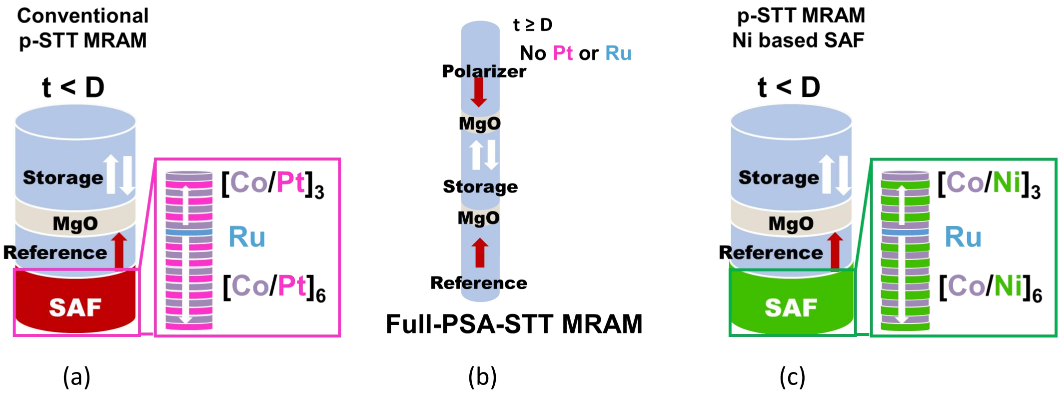

Fig. 2.2: Typical stack structure of p-STT-MRAM with a Co/Pt based SAF (a). Full-PSA-STT-MRAM alternative based on perpendicular shape anisotropy (PSA) (b). p-STT-MRAM alternative with a Co/Ni based SAF (c).

Figure 2.2 b shows one of the alternatives we propose that is based on the use of perpendicular shape anisotropy (PSA). Further details are given in Chapter 4. In this case, more common ferromagnetic materials (Fe, Co, Ni) or their alloys can be used for the reference and top polarizer. The high thermal magnetic stability is obtained by varying the geometrical aspect ratio of the reference and top polarizer layers. This second alternative is a novel approach that completely avoids the use of PGMs. Nonetheless, it requires a strict dimensional control of the pillar diameter in the 10-20 nm range, since the layer properties are defined by the pillar aspect ratio.

Figure 2.2 c shows the second alternative we propose, that is based on the use of Co/Ni multilayers. The optimization of such SAF structure is explained in Chapter 5. In this case, platinum layers can be substituted by non-critical nickel layers.

---

[5] ppm: parts per million

2.2 Criticality indicators: the case of Pt

Raw materials criticality evaluation usually focuses on supply risk, economic importance, and in some cases, environmental aspects [107]. Figure 2.3 shows a critically assessment for some typical materials used in MRAM technology, together with heavy and light rare earth elements and non-critical nickel and copper, used in the alternative proposed in Figure 2.2 c.

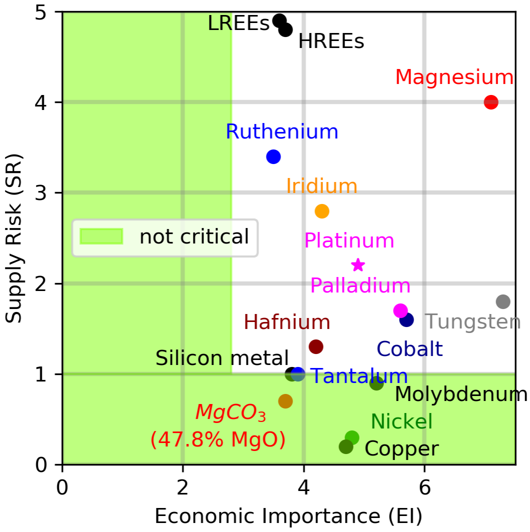

Fig. 2.3: Material criticality assessment for typical metals contained in spintronic memory together with HREEs and LREEs (heavy/light rare earth elements respectively). Green region defines the limits of the non-critical zone (SR $\leqslant 1$ and EI $\leqslant 2.8$). Source: data from European Commission [108, 109].

Figure 2.3 shows that PGMs (in particular Platinum, Ruthenium and Palladium) lie high in the critical region of supply risk and economic importance. However, materials as Nickel or Copper lie in the non-critical region, highlighted in green, due to their lower supply risk. In the following, we introduce both economic importance and supply risk indicators, and other factors that determine them as the material recyclability, sustitutability and HHI[6].

2.2.1 Economic importance

Economic importance (EI) is defined, in the EU assessment, as the importance of a material for the EU economy in terms of end-use applications and the added value (VA) of the corresponding manufacturing sectors according to the NACE rev.2, 2-digit level statistical classification of economic activities in the European Community [97]. It is given by Equation 2.1:

$$\text{Economic importance} = \sum_{S} (A_S \cdot Q_S) SI_{EI} \tag{2.1}$$

The parameters, As and Qs define the share of raw material and the total added value of that sector respectively. The substitution index, SI_{EI}, indicates the feasibility of finding an alternative material. Equation 2.1 shows that the presence of possible substitution strategies can lower the economic criticality assigned to a certain material.

---

[6] Herfindahl-Hirschman Index (HHI) is an indicator of the market concentration and the political stability of the producers.

2.2.2 Supply risk

Supply risk (SR) reflects the risk of supply disruptions, based on the concentration of primary supply of raw material producing countries, considering their governance and trade policies.

It is calculated as shown in Equation 2.2:

$$\text{Supply risk} = (1 - EoL_{RIR}) \cdot SI_{SR} \cdot \text{weighted HHI} \tag{2.2}$$

- EoL_{RIR} = end of life recycling input rate
- SI_{SR} = substitution index related to supply risk
- HHI = Herfindahl-Hirschman Index

A detailed description of these parameters is given in the reference work of Blengini et al. [97]. We follow the discussion of each of them for the case of platinum.

2.2.3 Recyclability

Large recycling rates translate into a reduction of the supply risk of a material, as it can provide a secondary flow of the element. While for industrial or automotive applications the platinum recycling rate can be as high as 80-90% or 50-60% respectively, it drops to a low 5-10% for electronic components [110].

The importance of the Chinese platinum jewelry sector is highlighted in Figure 2.4, that shows the main contributors of platinum recycling from the auto catalyst (a) and jewelry sector (b) respectively.

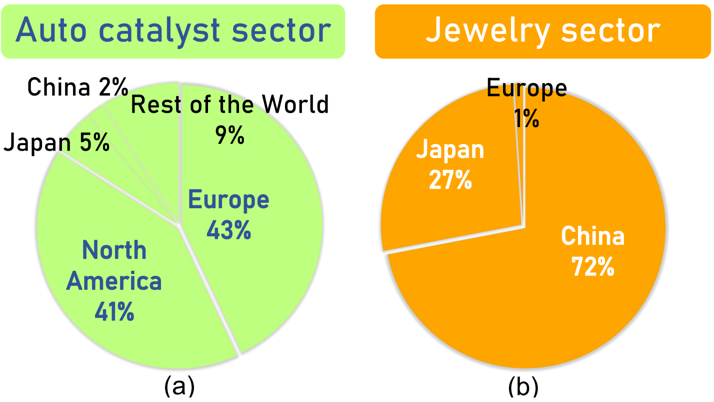

Fig. 2.4: Recycling leaders of platinum in the auto catalyst sector(a) and the jewelry sector(b) respectively, in 2018. Data from [111].

For the auto catalyst sector, Europe and North America are leaders in PGM recycling with a total of 40.25 tons recovered in 2019. For the jewelry sector, Asia is leader with 14.45 tons.

The low recycling rates for electronic components, of 5-10%, could be ascribed to the intermixing of materials in those elements. For instance, for microelectronic chips or the case of MRAM, nanometer thin layers of a large variety of metals are combined, making recycling much more challenging and costly. Nonetheless, Hagelüken claims that gold and precious metals contained in electronic scrap can be recovered very efficiently when they enter state-of-the-art metallurgical plants [110, 112]. According to Hagelüken, the recycling rate for waste electronic and electrical equipment remains low because it end up exported to developing countries where they only focus on few valuable metals, practice known as 'cherry-picking', and even so the recovery rate is not very high for those precious metals. Therefore, the challenge remains on the collection and monitoring of those billions of small objects containing tiny amounts of scarce materials rather than technical reasons [110, 112].

The interest in PGMs recycling has increased in the last decades, as seen in Figure 2.5 which shows a three fold growth in the number of patents related to PGM recycling from the period 1970-1979 to 2000-2009.

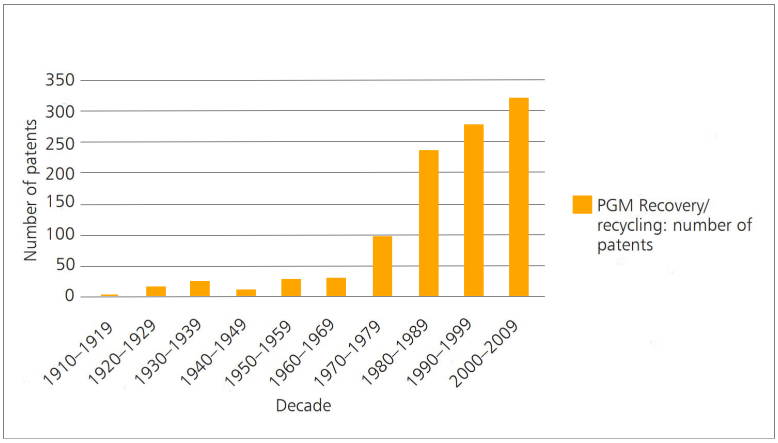

Fig. 2.5: Number of patents related to PGM recovery/recycling in the 1910-2009 period (a). From [110].

Accordingly, the fraction of platinum recovered from recycling has risen from 10% of the total global supply in 2003 up to 25% in 2019 [113, 114].

2.2.4 Substitutability

The supply risk of a material is also linked to the substitutability of such element for a given application. The substitution index (SI) in Equation 2.2 will be lowered if alternatives to such material exist, reducing the total supply risk. Ideally, the substitute material is produced in large quantity, has a low criticality and is mined as a primary product rather than a co/by-product, as is the case for nickel, the material we propose as alternative in Figure 2.2 c.

In the case of p-STT-MRAM, Pt is sometimes replaced by palladium (Pd) that also provides PMA when combined with Co in the form of Co/Pd multilayers. Nonetheless, Pd world production of 209 tons remains in the same order of the 187 tons of Pt [108]. Moreover, Pd is also classiffied as critical and it is a by-product of Pt, Ni, and Cu mining. Consequently, the substitution of Pt by Pd is not an ideal option.

Pt and Pd are key components of the car catalytic converters, that are used to reduce pollution emissions. Pt is more suitable for diesel engines while Pd is better for gasoline combustion engines.

Figure 2.6 shows that Pd price has been historically lower than that of Pt, which represented the main driver for its substitution.

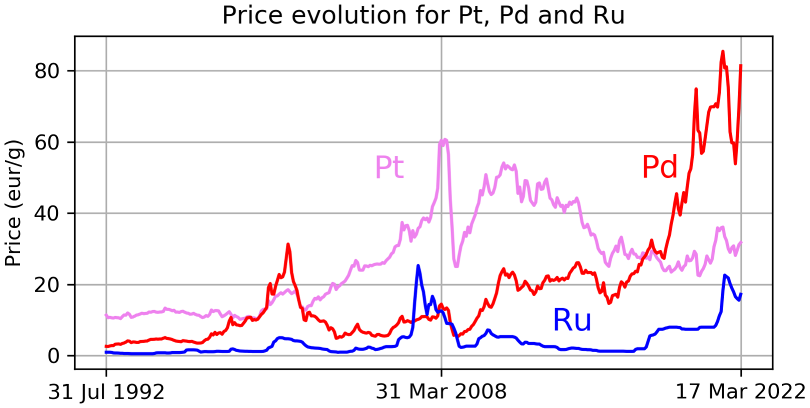

Fig. 2.6: Price evolution (€/g) between Jan 2000 and Mar 2022 for Platinum (pink), Palladium (red) and Ruthenium (blue). Source: Johnson Matthey [115].

However, in the last years the price of Pd has surpassed that of Pt. This can be explained by the increase of gasoline cars reported by the European Automobile Manufacturers Association (ACEA[7]) accounting now for 59.5% of the EU market against 29.1% diesel share in the third quarter of 2019[8]. The gasoline share increased by 6.1% while the diesel share reduced by 14.1%, as a result from governmental pressure to reduce fine particle emissions. The drop on PGM prices observed in Figure 2.6 in 2008 followed the price fall of most commodities following the financial crisis of 2007-2009. Large price volatility is observed during the last two years due to the impact of reduced economic activity and supply disruptions following the breakout of the COVID-19 pandemic.

Given the factors stated above, it is preferable to use Ni rather than the substitution by Pd for p-STT-MRAM, as long as the required magnetic specifications can be achieved.

World nickel production in 2010-2014 was four orders of magnitude greater than that of platinum, 1750 kilotons versus 187 tons of platinum [108, 109]. Moreover, nickel is classified as non-critical material, as seen in Figure 2.3, in contrast to critical platinum. Finally, both Ni and Pt are mined as primary products and co-products of other metals, as seen in Figure 2.7.

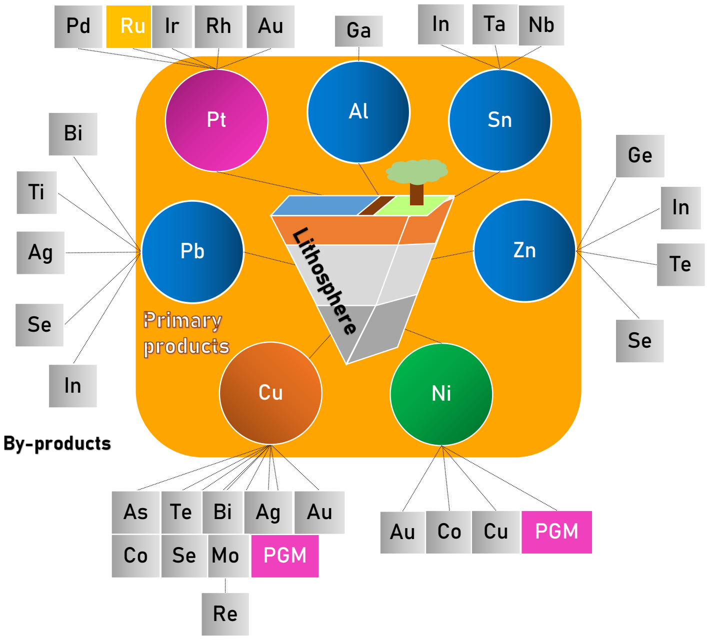

Fig. 2.7: Metal mining primary products (into the orange area) and their respective by-products. Re-draw from UK Energy Research Center [116].

By-product materials are often undesirable, since their production depends directly on the production of the primary material from which they are obtained, as in the case of Pd.

2.2.5 Herfindahl-Hirschman Index

Herfindahl-Hirschman Index (HHI) is an indicator of the market concentration and the political stability of the producers. Figure 2.8 shows that the world Ni production is much more diversified than that of Pt.

South Africa is the main worldwide Pt producer with 66.8% share, followed by Russia with 12.8%, a country that is known to apply dual pricing for strategic resources, as is the case already for natural gas exports [117]. Moreover, Russia invasion of Ukraine in the February 2022 has increased the geopolitical tension. Temporary closure of Europe's airspace to flights from Russia can lead to PGMs supply disruptions [118, 119]. Major shipping companies, such as Maersk, have already announced

---

[7] The European Automobile Manufacturers' Association (ACEA) represents the 16 major Europe-based car, van, truck and bus makers: BMW Group, DAF Trucks, Daimler Truck, Ferrari, Ford of Europe, Honda Motor Europe, Hyundai Motor Europe, Iveco Group, Jaguar Land Rover, Mercedes-Benz, Renault Group, Stellantis, Toyota Motor Europe, Volkswagen Group, Volvo Cars, and Volvo Group.

[8] Fuel types of new cars: petrol +6.1%, diesel -14.1%, electric +51.8% in third quarter of 2019

temporary suspension of shipments from and to Russia of goods other than food and medicine [120, 121].

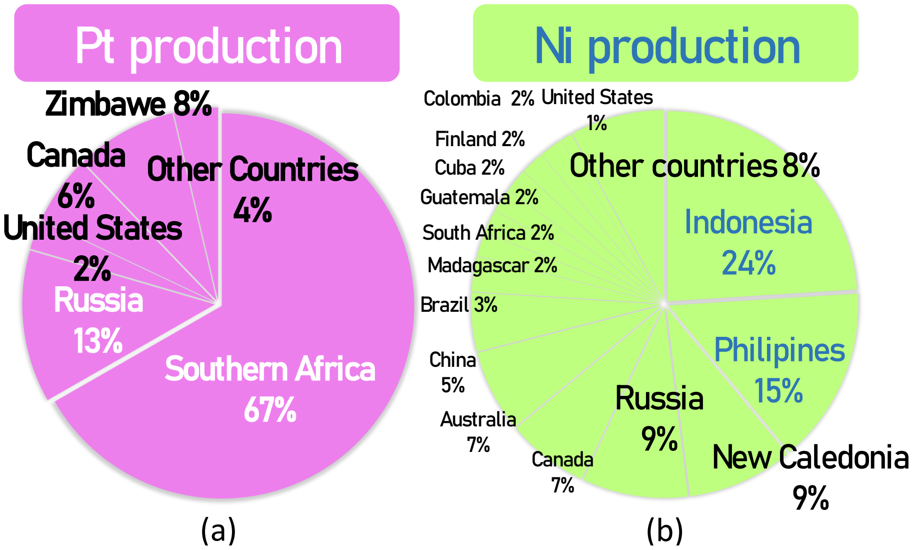

Fig. 2.8: Pt (a) and Ni (b) world production of 2018 by country. U.S. Geological Survey, 2019 [122].

Four mining companies are responsible of 80% of the PGM market production, integrating the whole process from mining to refining: Anglo Platinum, Impala Platinum, and Lonmin Platinum from South Africa and Norilsk in Russia [123].

One of the alternatives to replace (Co/Pt) multilayers in STT-MRAM we propose is to use (Co/Ni) multilayers. However, some previous studies have used a hafnium (Hf) seed layer for the growth of the Co/Ni multilayers [124, 125, 126]. Unfortunately, Hf is also classified as critical material.

Figure 2.9, shows that Hf production is largely concentrated in US and France, with 41% and 43% of the global production respectively in the period 2010-2014. The large share of production of these two countries results from its use in nuclear industry. In our study, we use much more common copper as seed layer for the growth of the (Co/Ni) multilayers. Cu still provides large PMA to the (Co/Ni) multilayers due to its (111) texture. More details are given in Chapter 5.

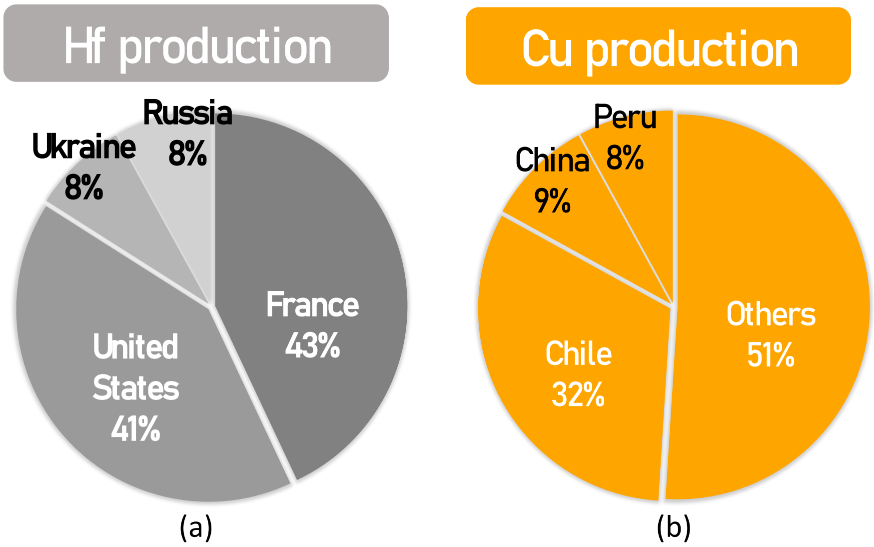

Fig. 2.9: Hf (a) and Cu (b) world production of 2010-2014 from EU Commission, 2017 [108, 109].

Even if France is a large supplier of Hf, it is classified as a material with relatively high supply risk for the EU since the EU relies on a single company for its supply [127]. Moreover, the other two larger suppliers of Hf are Russia and Ukraine. Therefore, production and shipment from those countries could be affected by the current geopolitical situation as previously mentioned for the case of PGMs.

Copper supply is much more diversified. Chile (26%) and Peru (23%) are the two main producers while the rest was sourced from at least 12 other countries in the 2010-2014 period [109].

Import reliance

The import reliance is used when calculating the HHI index.

The European import reliance of platinum is as high as 98%, meaning that only around one ton of this material is produced in Europe. Finland is the main responsible of this production with 90% of the share while Poland is responsible for the remaining 10%. The European import reliance of nickel drops to 59%, sufficiently low to ensure that demand can be covered even in the event of supply disruptions [108].

The US import reliance of Pt is 73%, mainly from South Africa 44%, Germany 15%, United Kingdom 10% and Italy 7%, while for Nickel the import reliance is lower than for the case of EU, 52%. For the case of Nickel, the major supply sources are Canada, Norway, Australia and Russia (U.S. Geological Survey, 2019 [122]).

2.3 Environmental implications of the use of PGMs

In this section, to better understand the high embodied energy of PGMs, a brief introduction to the extraction and processing of these materials is given first, followed by a comparison of the energy and water required for the production of PGMs and other more common metals.

2.3.1 PGMs extraction and processing

As Cole and Ferron mention, published information is rather limited compared to other metals due to the competitiveness of the PGM market [128]. Due to the precious nature of these metals, they are recovered from low grade ores (few grams per ton). In addition, PGM elements (plus gold) are often found together. As they have rather similar chemical properties, separation is difficult.

The main stages from extraction to final refining are shown in Figure 2.10.

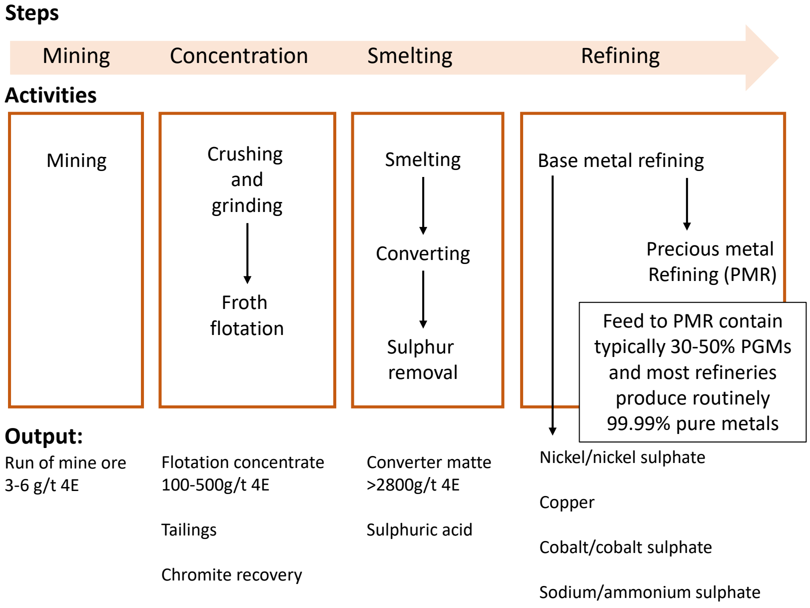

Fig. 2.10: Simplified PGM processing chain. From Sinsalo et al. (2018) [123].

In terms of the cost of operations, 72% comes from mining, with ore concentration accounting for 10% and smelting and refining responsible for the remaining 18% (9% each). [129].

PGMs are obtained as primary products or by-products of nickel and copper, depending on their relative concentration in the ore [123]. They are usually associated with nickel-copper sulphides in magmatic rocks [130].

The first step in the extraction process is crushing and grinding. The ore is reduced to small particles of less than about 100 μm.

The resulting crushed powder is mixed with water to form a slurry, in which the desired mineral is rendered hydrophobic by a surfactant or collector chemical. This slurry is then introduced into flotation cells that are aerated to produce bubbles, which rise to the surface to form a froth. The froth is then removed to produce a concentrate of the target mineral (in Figure 2.10, the flotation concentrate). Several flotation stages are usually performed to maximize the extraction yield [131].

Smelting removes most gangue minerals as molten slag. Converting removes most iron and sulfur by oxidation with air and oxygen. Thanks to these two stages, the concentration of the converter matte is much higher, as shown in Figure 2.10 (few kg per ton).

Finally, the converter matte can be further processed to high purity PGMs, nickel, copper and cobalt [132]. Sherrit-Gordon's sulphuric acid pressure leach process is the common process chosen by PGM base metal refineries in the western world, as in Figure 2.11. [128].

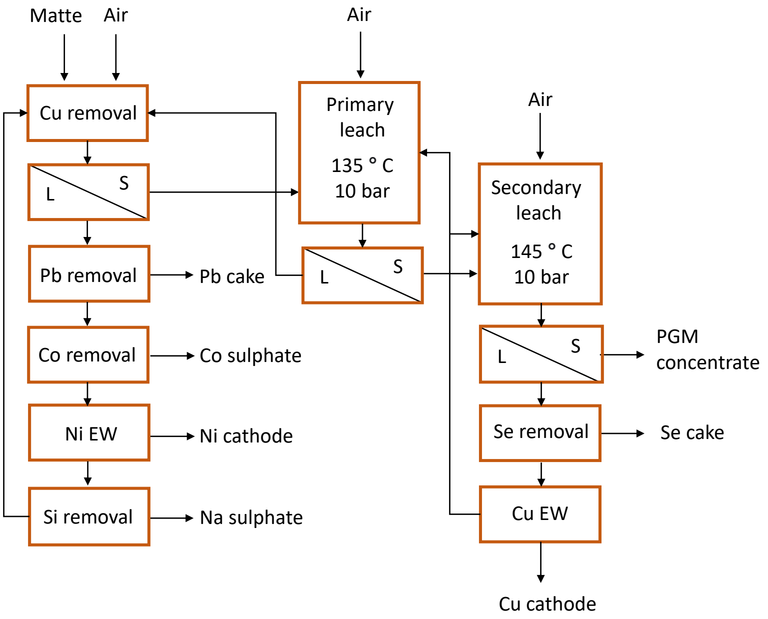

Fig. 2.11: Simplified refining process for Rustenburg Base Metals Refinery. From Sinsalo et al. (2018) [123].

Cu removal is carried out under mild conditions to leach some nickel and cobalt with the objective of precipitating copper from the nickel sulphate solution with fresh matte. The primary leach aims to dissolve all the nickel and some of the copper from the matte. The secondary leach aims to dissolve all remaining copper and some iron from the matte [123].

The different concentrations of platinum group metals (PGMs) at each stage of the process are given in Tables 2.1 and 2.2. We can see that, although the initial concentrate appears to be similar for the South African companies (Table 2.1), it diverges when processed. The values reported from Stillwater are higher in concentration as shown in Table 2.2 which is attributed to a different composition of the ore body.

Alternatives such as the Kell Process proposed by Liddell et al. in which they estimate a significant reduction in energy and CO2 emissions (50% and 70% respectively) compared to smelting and refining are interesting for a more sustainable production [134].

COMPANY	Typical South African Concentrate Analyses PGM g/t	Typical South African Furnace Matte Analyses PGM g/t	Typical South African Converter Matte Analyses PGM g/t
Amplats: Waterval	143	640	2100
Amplats: Union	142	830	
Impala	138	1050	3430
Lonmin: Merensky	130	1000	6000
Lonmin: UG2 blend	340	2500	
Northam	132	724	2570

Table 2.1: Typical South African Analyses for different companies. From Cole et al. [128].

ELEMENTS	SMELTER			CONVERTER	
	CONC .	GREEN MATE	SLAG	WHITE MATE	SLAG
PGM's (Pt+Pd) g/t	2500	7300	15	24000	260

Table 2.2: Chemical Analyses of various Streams in the Stillwater Smelter [133].

2.3.2 Energy and water related to PGMs production

One main driver for the substitution of PGMs, apart from their high price, is their large environmental impact. Figure 2.12 shows the energy (a) and water (b) required for the production of a variety of metals. The energetic requirements in the case of PGMs production are from 1 to 3 orders of magnitude larger compared to the other metals, and up to 5 in terms of water requirements, when comparing PGMs with nickel.

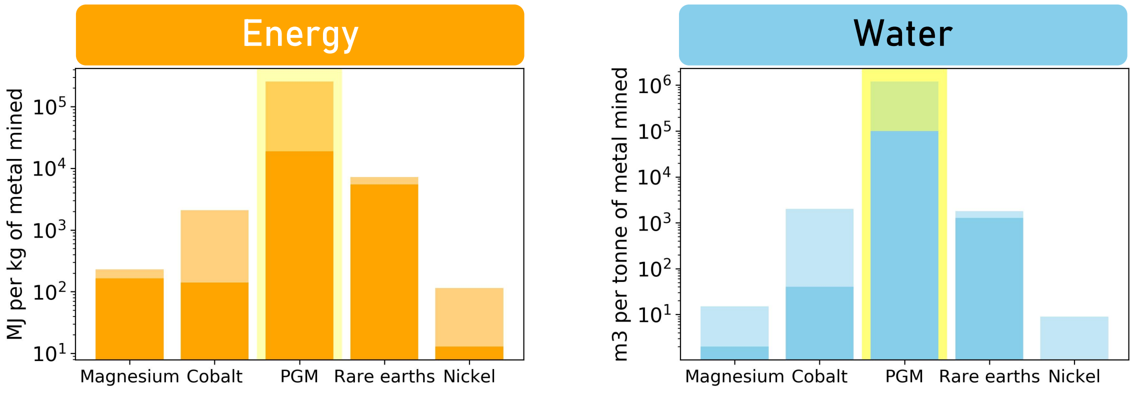

(a) (b)

Fig. 2.12: Energy and water requirements for the production of metals from the ore (high grade-pale colour, low grade-dark colour) in logarithmic scale. From European Commission, Report on Critical Raw Materials in the Circular Economy (2018). Energy data for nickel from [135] and water from [136].

The large difference in embodied energy and water requirements between PGMs and the other metals results from the low concentration of PGMs in the ore from which they are mined (few g/Ton) [123]. PGMs are usually found together with gold and have very similar chemical properties, such that their separation become difficult.

In the case of spintronic applications and microelectronics, small amounts of those metals are used, so that a specific evaluation needs to be performed. However, a correct analysis must not only take into account the amount of metal used in the final product, but also the amount of metal that is lost during the processing of the device, which is discussed in the next section.

2.4 Losses related to the PVD deposition of metal thin films.

Microelectronics is considered an example of radical « dematerialization » as the products usually provide high value and utility while having a negligible weight.

For Williams et al., this affirmation might not always be correct, if the amount of materials required in the whole fabrication process is considered, as they concluded in their article: 'The 1.7 Kilogram Microchip: Energy and Material Use in the Production of Semiconductor Devices' whose title is self-explanatory [137].

In some cases, the quantities of materials required for a specific technology are calculated using the amount of material contained in the final device [105]. However, this approach omits the total amount of material lost in the device fabrication related to the deposition and etching processes to nanopattern the device. Therefore, the real amount of material required is much higher than that contained in the final devices.

Microelectronic circuits are built up from integrated components, e.g., transistors, memory dots, vias, interconnects, with characteristic dimensions in the nanometer range. For the case of MRAM technology, each memory cell is a patterned element of diameter in the 20 to 50 nm range. In order to fabricate the MTJs used in these devices, several layers, each one 2–3 atoms thick, are deposited on 300 mm diameter wafers. Then all elementary components are nanopatterned through a sequence of lithography, etch and deposition operations.

The sputtering deposition process of thin films is further explained in Chapter 3.1. During deposition, a significant proportion of the sputtered material does not reach the substrate and is wasted on the inner walls of the deposition chamber.

To meet industrial requirements, the wafer must be homogeneous in thickness with sub-nm accuracy over the entire surface. This is achieved by different strategies such as rotation or linear motion of the substrate, increasing the distance between the target and the wafer, or the use of low deposition rates.

The efficiency of material deposition is highly dependent on the tool geometry, the material to be deposited and the conditions necessary for optimum uniformity of the deposited layer, as the gas pressure during deposition.

Strategies to reduce the losses during the sputtering process are investigated for instance in the patent of Walter H. et al., using a particular cathode assembly [138].

The particular assembly consists of two elongated target segments, made of the same material, inclined towards each other, with a resulting reduction in sputtering losses.

The substrate is linearly translated to ensure an appropriate film homogeneity.

Since the length and width of the cathode exposed to the magnetic field are longer than the corresponding lengths on the substrate, a certain amount of material ends up aside of the substrate during the deposition which results into the so-called target end loss. A second source of material loss is related to the sweeping motion of the substrate and is known as overscan loss. In this patent, they report that overscan losses for a planar target can be of 33% and by using the tilted faced target, they can be reduced to 20%. However, this type of geometry requires an extra target for each material.

For the case of indium tin oxide (ITO), deposition of only 15% of the target sputtered material onto the substrate has been reported [139].

Rossnagel reported deposition fractions on the substrate from 22% to 80% as a function of different parameters as the sputtered material, argon pressure and throw distance of a sputtering process at 1000 W in 200 mm diameter planar magnetron [140]. We estimated the sputtering losses of our own sputtering deposition tool for the case of Pt. Figure 2.13 shows the amount of Pt deposited in the period 13 Apr 2013 to 19 Jul 2019.

During magnetron sputtering, the material target erosion does not occur over the complete target but is concentrated over an 'etching track', due to a larger plasma density in that region.

Due to the elevated cost of PGMs, the targets are commonly recycled by refilling the eroded region. Indeed, in our case the full target weights around 800 gr, but the weight and size of the target depends on the size of the wafer on which the metal is deposited, to ensure a good homogeneity.

The target recycling is less common for other less expensive metals. In this sense, 'end of life target' recovery is ensured for PGMs targets.

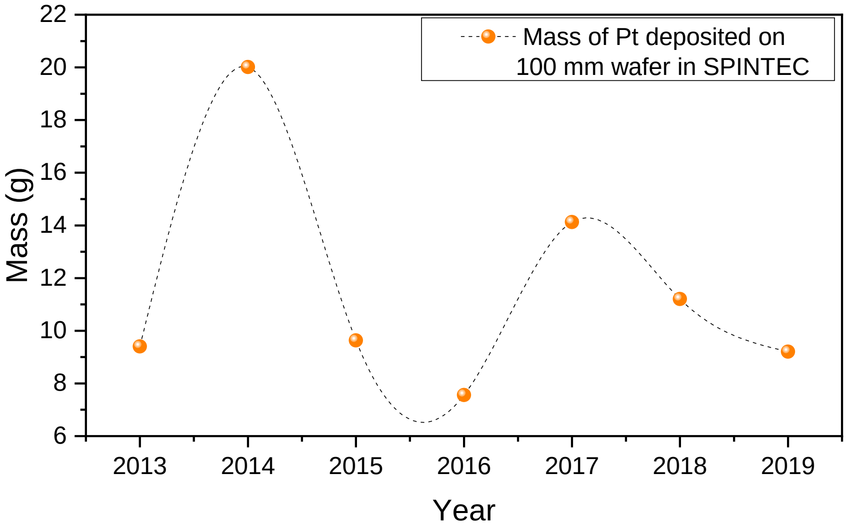

Fig. 2.13: Amount of Pt demanded to be deposited in SPINTEC for the period 13 Apr 2013 to 19 Jul 2019.

In our case, in total, 81 grams were deposited prior to the Pt target refill that required 294 gr of Pt.

Therefore, we estimate that 72.5% of the sputtered material is lost during the deposition process, calculated as the fraction of Pt deposited on the wafer over the Pt refilled in the target. In the next section, we consider different deposition efficiency scenarios, as industrial tools are optimized to reduce these losses.

2.5 Evaluating the impact of Pt substitution in p-STT-MRAM.

We have seen in the previous sections that the environmental cost of PGMs extraction and their price is very large. Nevertheless, in spintronic applications and microelectronics in general, only very small amounts of these materials are used.

We evaluate the energy, price and global warming potential (GWP) for the material production of Pt in the case of a conventional p-STT-MRAM, or the two alternatives we propose. The ferromagnetic elements used for the reference and top polarizer in the Full-PSA-STT-MRAM alternative, as in Figure 2.2 b, or the nickel layers that play the role of Pt in the second alternative of Figure 2.2 c.

Figure 2.14 shows the results of such evaluation where we used a 72.5% percentage of losses during sputtering deposition, as in our previous estimation.

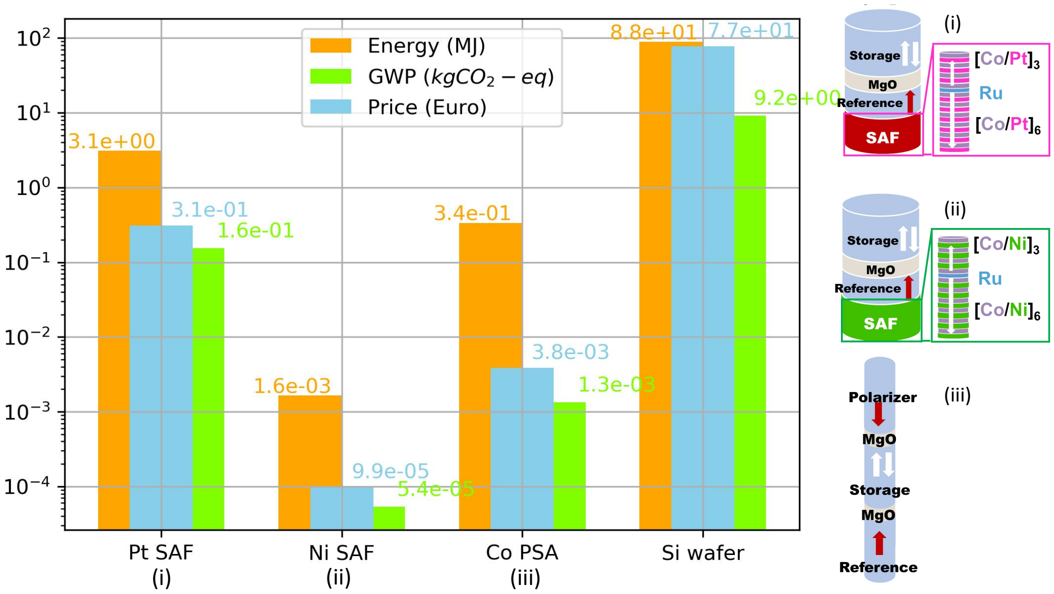

Fig. 2.14: Energy (orange), GWP (green) and price (blue), in logarithmic scale, required to produce the Pt used in a conventional SAF, the Co in the PSA based substitution, the Ni in the case of (Co/Ni) based SAF alternative and for the production of a 300 mm bare Si wafer. The sources for its calculation are given in Appendix A

The estimated percentage of losses determines the final conclusions drawn, such that a more accurate estimation is necessary for each particular scenario, especially if smaller losses can be achieved. The reported numbers in Figure 2.14 are given for the extraction of Pt present in conventional SAF and for Ni and Co in the proposed solutions as indicated in Figure 2.2. This comparison is made based on the amount of material deposited on a 300 mm wafer. For the case of PSA, cobalt was used as ferromagnetic material, but other options could be suitable such as NiFe or FeCoB, which are less critical than Co. The PSA approach increases the mass of material used but the final amount of energy required and global warming potential are strongly decreased, respectively by 89% and 99% with respect to the conventional approach based on a synthetic antiferromagnet comprising (Pt/Co) multilayers. The Pt-free alternative, based on Co only PSA allows for a hundred times smaller carbon footprint. This is evident from the difference in global warming potential between the two materials [141].

Figure 2.14 shows that in the case of (Co/Pt) substitution by a (Co/Ni) based SAF, even stronger reductions can be achieved, where GWP is reduced up to a factor of 10^4.

However, when comparing the overall requirements to obtain the amount of Pt used in the SAF, with those needed to produce the Si wafer itself, on top of which all these devices are grown, the benefits associated with Pt replacement appear negligible, regardless of the substitution approach. For example, PSA substitution saves 2.8 MJ per 300 mm wafer, which is an 89% reduction over the Pt SAF alternative. However, the energy requirements for the Si wafer fabrication itself amounts to hundreds of MJ, according to recent data [137, 142, 143, 144]. The same trend is observed for price and carbon footprint, where the requirements for the Si wafer are two and one orders of magnitude higher respectively.

Figure 2.15 shows the energy, price and GWP required for Pt production depending on the Pt thin film thickness deposited and compared to that of the bare Si wafer, represented by the reference black line. For the case of 72.5% losses during Pt sputtering deposition (solid line), the energy equivalent to produce the Si wafer would equal that to produce the Pt required for STT-MRAM fabrication only if the Pt thickness would exceed 50 nm, which is more than an order of magnitude larger than what it is used in the current SAF implementation. For GWP and price, it moves to even higher thicknesses.

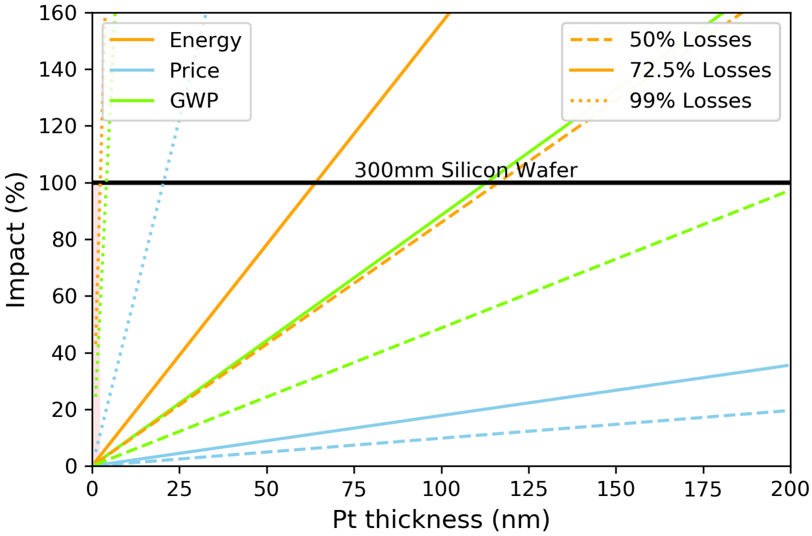

Fig. 2.15: Pt layer thickness on a 300 mm wafer that would result in similar requirements (energy in orange, price in pink and GWP in green) as manufacturing a 300 mm bare silicon wafer used as a substrate for this technology (assuming different sputter losses, 50%, 75% and 99%, corresponding to dashed, solid and dotted lines respectively). From [145].

Only in the case of 99% losses (dotted lines) during deposition, the requirements for Pt would be on the same order than those for the Si substrate, i.e., a Pt thickness of 2.25 nm. However, such high losses do not occur in thin film deposition tools. As mentioned earlier, deposition losses depend on the tool used. In industrial production, equipment suppliers strive to minimize these losses. As can be seen in Figure 2.15, further reduction in losses during deposition would further decrease the energy, price, and GWP requirements associated with the use of Pt, thereby reducing the benefits of Pt substitution by using a PSA reference or (Co/Ni) based SAF in place of the current (Co/Pt) SAF in the MRAM reference layer.

Considering the importance of the energy and environmental impact of the manufacturing of silicon wafers, it is important to specify the contribution of each step of the manufacturing process, measured per kg of Si. This contribution is detailed in Table 2.3.

Table 2.3 shows that even adding only the energy used up to the polysilicon stage, the requirements correspond to 143 MJ (Williams) and 73.5 MJ (Takiguchi) for a wafer mass of 127 g, which is well above the calculated 3.1 MJ required for Pt in the SAF reference layer. Even higher requirements are reported by Ashby [144], 6017 MJ per m2 for mono-crystalline Si wafers used as microelectronic substrates, which leads to 425 MJ for a 300 mm wafer.

A previous life cycle impact assessment of solar cell fabrication reached a similar conclusion. Indeed, the authors concluded that the upstream process of silicon wafer manufacturing has a greater environmental impact than the manufacturing of the solar cells themselves [146].

In that study, it was argued that an improvement in the wafer production process would be much more beneficial for solar cell fabrication. Improvements in the microelectronics technology process steps have a much higher degree of complexity to be implemented, compared to upstream process

Fabrication step	**Electrical energy (MJ/kg Si output)**		**Si yield (%)**	
	Williams (2002) [137]	***Takiguchi (2011) [143]***	***Williams (2002) [137]***	***Takiguchi (2011) [143]***
Refining silica to mg-Si	46.8	39.6	90%	79%
mg-Si to trichlorosilane	180	539.64	90%	76%
Trichlorosilane to polysilicon	900		42%	
PC-Si to sc-Si ingot	900	111.6	50%	100%
Sc-Si ingot to Si wafer	864	153	56%	37%
Process chain from silica to wafers	7657.2	-	9.5%	-

Table 2.3: Energy requirements and yield during the silicon wafer fabrication. The electricity requirements for Si wafer fabrication have been converted to energy for direct comparison with the other raw materials requirements. (3.6 MJ/kWh). Losses related to power plants efficiency have been neglected.

improvements.

In fact, our present study related to the impact of Pt substitution in MRAM yields a similar conclusion. The fabrication of silicon wafers has a greater energy and environmental impact than the use of energy-intensive materials such as PGMs in the device manufacturing process. The main cause is the significant mass difference between the 127 g silicon wafer and the 3.4 mg of Pt required to fabricate the device.

Boyd [142] already evaluated the GWP associated with the fabrication of silicon wafers compared to other phases of the CMOS device life cycle. The GWP given for the fabrication of a 300 mm silicon wafer is of the same order as the GWP of the chemicals required during the CMOS fabrication process. However, the main contribution of the GWP in the device life cycle of the device remains, in most cases, the actual use phase.

2.5.1 Supply disruption, is it going to occur?

Although the economic and environmental impact of Pt use is low in perpendicular STT-MRAM memory, its potential supply risk remains a concern and substitution strategies are still attractive in this regard. High prices for certain resources can lead to technological innovation through research towards alternatives. For example, higher gasoline prices in Europe compared to the United States can explain a more developed public transport system and lower per capita consumption. However, as mentioned by Buijs and Sievers, in the case of technology industries, the availability of mineral resources is a greater concern than price, as the cost of these raw materials is often a small part of the final price [147]. As early as 1979, during the Nixon administration, the US government feared a possible disruption of the platinum supply: “There is a possibility of disruption of supplies from Rhodesia as a result of internal disorders, and a more remote one in the case of South Africa. This would seriously affect US, European, and Japanese imports of two critical materials—platinum and chromium. There is also a possibility of sudden changes in export availability of these two materials from our other major supplier, the Soviet Union, because of our limited advance knowledge of political and economic factors determining its export plans” [148].

Studies on possible future material bottlenecks do not predict future Pt shortages [149, 150].

Figure 2.16 a shows that Valero et al. predict that both Pt reserves[9] and resources[10] will be below the cumulative demand until 2050 [150].

However, Grandell et al. predicted an increase in Pt mining, as for them consumption is well above the reserves as seen in Figure 2.16 b, which is undesirable due to its high environmental impact [149]. Nonetheless, reserves consumption remains around 50% what denotes foreseeable sources of Pt available.

Even if both studies do not predict global shortages of Pt from a resource perspective, other factors need to be considered. Zientec et al. declared that the availability and accessibility of PGMs could be disrupted by economic, environmental, political and social events [152]. Previous disruptions have been observed for Pd in 1999 and 2000 due to the blockade of exports from Russia, or for the disruption in Pt supply in 1986, 2011 and 2012 due to miner strikes in South Africa [153].

Ku. A (2018) concluded that the use of PGMs for gate layers in some FeRAM and MRAM device structures may be problematic in terms of future supply due to the small annual production of Pt and Ir [105].

In terms of production, 765 kg of Pt were required in Western Europe in 2019 for electronic devices such as hard disk drives (HDDs) [154]. This could be covered by European platinum production of about 1 ton. However, a total ≈ 56 tons of Pt were required in the EU for various applications, 41 tons of which are required for automotive needs, well above its own production.

If we focus on perpendicular STT-MRAM, to meet the December 2019 global wafer production dedicated to memory corresponding to 7.47 million wafers [155] and assuming all wafers are dedicated to STT-MRAM and contain a SAF comprising Co/Pt multilayers, which is an unrealistic upper limit, 436 kg of Pt would be required for this annual production.

This is of the same order as the EU’s Pt needs for electrical applications and would represent around 10% of the world’s Pt needs for electrical applications in 2019 (≈4.1 tons) [154], highlighting an increased demand for other technologies such as hard disk drives (HDDs).

What this tells us is that, although the supply risk is high for the PGM group of metals, and production is highly concentrated, as shown in Figure 2.8, the Pt supply needs for the STT-MRAM are minor compared to the total production.

It is important to note that the about 5 g contained in every catalytic converter of diesel cars are much easier to recycle than the Pt present in MRAM devices. Nevertheless, the Pt lost during deposition because being deposited aside of the wafers in the sputtering unit can be at least partially recovered. However, the Pt which is etched away of the wafer during the memory cell nano-patterning process will always be difficult to recover. A fully closed loop of Pt seems difficult to achieve. Therefore, trying to substitute Pt by less critical materials seems to be the best option.

---

[9] Reserves are the estimated amount of a mineral that can be economically mined under current conditions [151].

[10] Resources can become reserves if high demand or other factors such as technological developments or discovery of new deposits justify extraction [116].

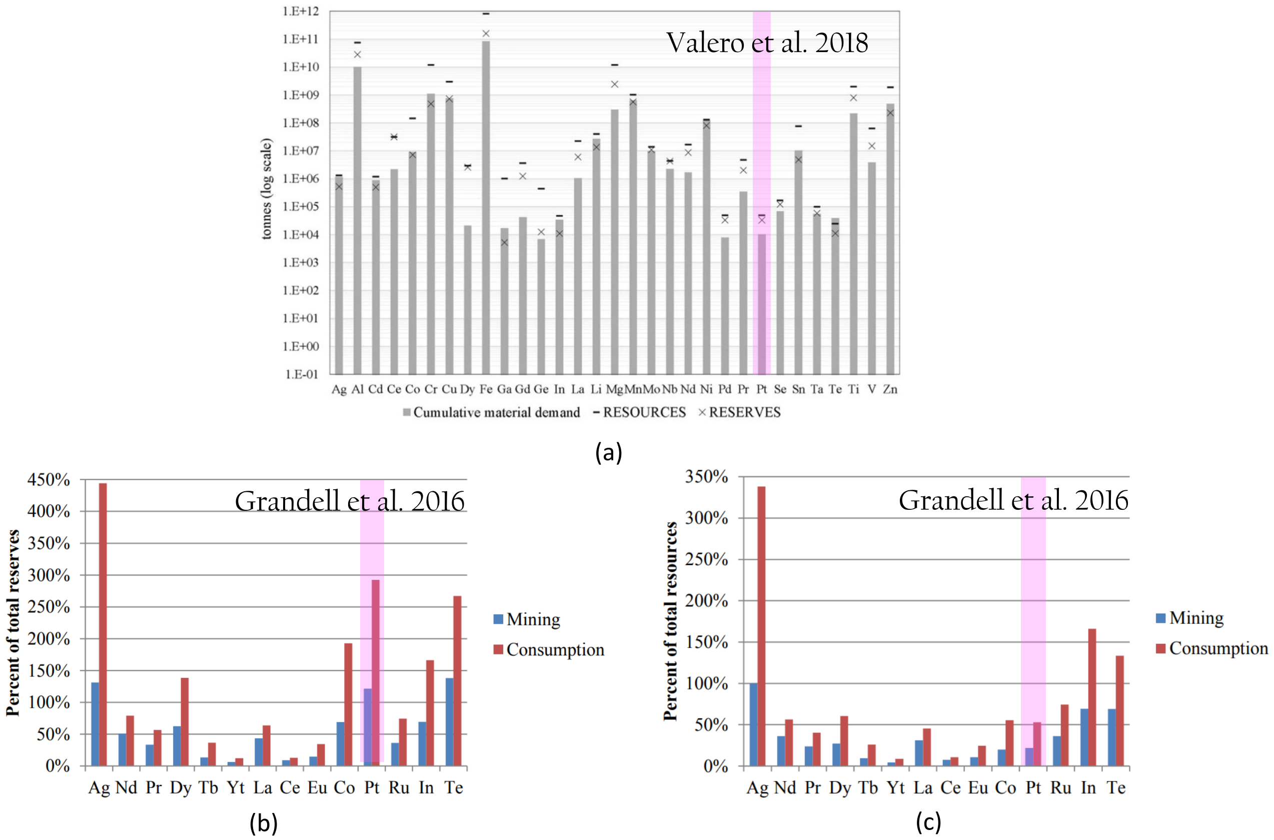

(a)

(b)

(c)

Fig. 2.16: Cumulative material demand for green technologies by element from 2016 to 2050 with material reserves and resources data (vertical axis in logarithm scale) (a). From [150]. Material cumulative need for clean energy technology until 2050 in relation to global mineral reserves (b) and resources (c). From [149]. Pt is highlighted.

In addition, the COVID-19 pandemic has shown that supply can be quickly affected, and the event of a conflict between Western countries and Russia following the invasion of Ukraine could put additional strain on supply chains, of which PGMs are part [118, 119].

2.6 Other material concerns

Magnesium is a key material for STT-MRAM, as its oxide form provides outstanding TMR properties, so far not reproduced by any other type of metal oxide. Despite its abundance in nature, its worldwide production is highly concentrated in China (87%), leading it to be identified as a “high supply risk” material by the European Commission [108]. China has already imposed certain measures affecting magnesium exports, which the EU, the US and Mexico have already claimed are contrary to World Trade Organisation (WTO) rules [156].

However, the oxide barrier can also be deposited directly from its oxide form, magnesia (MgO). Magnesite ($MgCO_3$) is processed into natural magnesia:

$$MgCO_3 = MgO + CO_2(\Delta H = +118kJ/mol) \tag{2.3}$$

Magnesite is considered non critical by the European Union as seen in Figure 2.3. The import reliance of magnesite is very close to zero. Several EU countries are producers of MgO, such as Slovakia, Austria, Spain, Greece or Poland, with a significant average production of 1.160 kt of MgO per year [109].

Two other important components for STT-MRAM are Ta and W, both of which are used as boron getters. Boron is adsorbed from the FeCoB interfacial layer. The amorphous electrode is used to promote the bcc (001) nanostructuration of the magnesium oxide tunnel barrier, which is difficult to achieve above the fcc crystalline structure that maximizes the PMA properties of Co/Ni or Co/Pt multilayers. This bcc crystallization is in fact responsible for the high TMR value of MgO-based magnetic tunnel junctions, as described previously in Chapter 1.6.

The introduction of the EU’s new Conflict Minerals Regulation in January 2021 addresses the case of both Ta and W [157]. The main goal of this regulation is to end the trade and usage of conflict minerals and metals by global smelters and refiners, as well as the abuse of mine workers. Therefore, the objective of this regulation is to force EU companies to import those metals only from responsible sources. Ta is mainly produced by Rwanda (31%), the Democratic Republic of Congo (19%), and Brazil (14%) while W primary producers are China (84%) and Russia (4%). Although W has been demonstrated to yield higher annealing tolerance and effective PMA [158], a Ta getter provides acceptable performance.

Initiatives such as the one adopted by the EU can lead to a more sustainable supply chain management (SSM), as mentioned by Ageron et al., “suppliers aware of sustainable issues will naturally be more involved in SSM” [159].

2.7 Conclusions

In this chapter we have seen that improvements in the Si wafer fabrication process can generate the most beneficial environmental impact, rather than the PGMs substitution, not only for STT-MRAM but more generally for most microelectronic components that use small amounts of those metals.

Nonetheless, due to the high risk of supply disruptions in the highly concentrated PGM production, the substitution is crucial as a risk mitigation measure.

Possible alternatives to the use of Pt are studied in Chapter 4 and Chapter 5.

In Chapter 6, we developed an alternative sensor sensitive to out-of-plane field based on the expansion/contraction of a vortex core in the sensing layer of an MTJ. This type of sensor has the potential advantage of avoiding the use of platinum or iridium, which are typically used in planar MTJ-sensors for the pinning layers. The same conclusion as for the case of STT-MRAM can be extended to the case of this spintronic sensor device. The substitution of PGMs remains a risk mitigation measure to the high supply risk of such metals.

In the following Chapter 3, the means of fabrication of such nano-devices are explained in detail, together with the characterization tools we have used during this thesis.

Chapter 3

Nanofabrication and characterization of spintronic devices

This chapter explains the different steps followed for the fabrication of spintronic devices.

We first present the sputtering process that is used for the deposition of each layer of the magnetic tunnel junctions (MTJ).

Prior to the nanofabrication of spintronic devices in small diameters, various techniques are used at the thin-film level:

- **Structural characterization**: Atomic force microscopy (AFM).
- **Annealing tools**: with and without applied magnetic field (ANNEALSYS).
- **Magnetic properties characterization**: Vibrating Sample Magnetometer (VSM) and Magneto-optical Kerr effect (MOKE).

Once the structural and magnetic properties have been optimized, the nanofabrication process proceeds down to nanometric nodes in the Upstream Technological Platform (PTA) [160]. During the process, various nano-fabrication tools are used:

- **Material deposition tools:** Physical vapor deposition (PVD) and evaporation tools.
- **Etching tools:** Ion beam etching (IBE) and reactive ion etching (RIE).
- **Lithography tools:** e-beam lithography and ultraviolet (UV) lithography.
- **Observation tools:** profilometer, optical microscope and scanning electron microscope (SEM).

An electrical wafer tester is used for electrical characterization. The tester is already built and has been in development for several years.

Finally, the development of a buffer layer based on tantalum (Ta) of low roughness, which does not contain platinum (Pt) in its structure, is described.

3.1 MTJ thin film deposition

All samples described in this manuscript have been deposited at SPINTEC by Stéphane Auffret. The technique used for deposition is magnetron sputtering.

In the early days of MRAM development, the growth of crystalline tunneling barriers motivated by their predicted high tunneling spin polarization (TSP) and TMR values compared to amorphous barriers, was investigated. Molecular beam epitaxy (MBE) deposition was used for the growth of such crystalline oxide barriers. However, in 2004 Parkin et al. reported large TMR values of up to 220% at room temperature using a much simpler sputter deposition technique followed by an annealing at 350°C [161]. Djayaprawira et al. also reported 230% TMR for MgO based tunnel junctions with amorphous CoFeB electrodes, deposited by a Canon ANELVA commercial 200-mm production sputter deposition system [162]. These early works showed that large TSPs and TMRs could be obtained in MTJs with sputter-deposited MgO tunnel barriers, highly advantageous compared to epitaxial growth techniques for the industrial development of MRAM technology due to their higher throughput. Sputtering is also widely used for film deposition on semiconductor wafers, magnetic media and a number of other applications [140].

In our case, for the deposition of the thin layers, we used an ACTEMIUM magnetron sputtering tool, at room temperature under very high vacuum, 10^{-8} mbar. Magnetron sputtering uses a static magnetic field at the cathode location which makes the sputtering faster. An electric field is created between the grounded anode and the negatively biased cathode as illustrated in Figure 3.1 a. Sputter deposition is performed using a gaseous argon (Ar) plasma, where high-energy Ar ions within the plasma directed towards the cathode erode the target surface, stripping atoms from its surface. The ions transfer physical momentum and kinetic energy to the target atoms, large enough to break the bonds and dislodge the atoms. The sputtered target atoms are partially deposited on the substrate, creating a thin film as seen in Figure 3.1 a.

The secondary electrons produced during the sputtering process follow what is known as a drift path, which follows $\boldsymbol{E} \times \boldsymbol{B}$ and can close on itself. These trapped secondary electrons eventually lose their kinetic energy due to collision with gas atoms or other electrons and form a highly dense plasma near the cathode. Such a high plasma density produces faster etching in that region, known as the etching track, and forms deep grooves in the cathode, as seen in Figure 3.1 b, for a circular target.

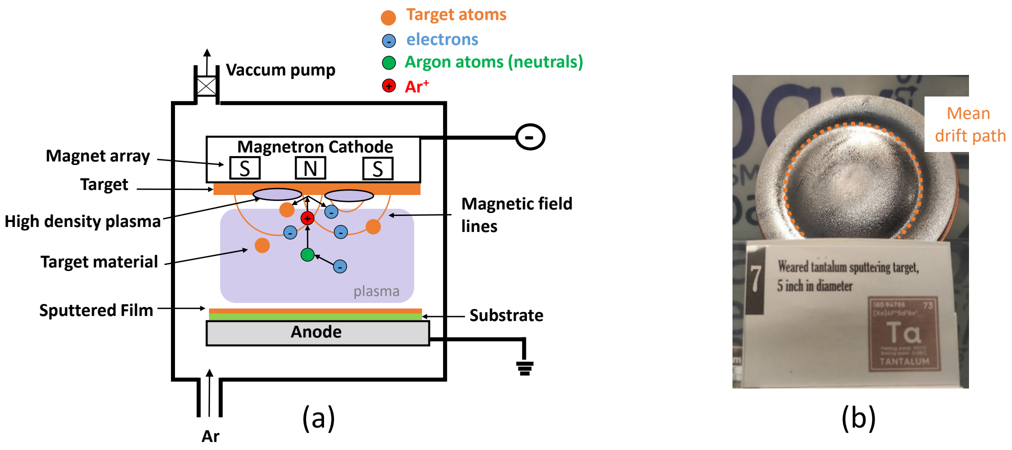

(a) (b)

Fig. 3.1: Schematic of the magnetron sputtering process (a). Eroded circular tantalum target sputtered in our tool with a magnetron cathode, showing the resulting deep grooves of the etching track (b).

The deposition tool is also equipped with a treatment chamber for the oxidation and sputtering steps. In our case, the MgO barrier is formed by the natural oxidation of metallic Mg in the treatment chamber. The magnetic stack grows without breaking the vacuum due to the high importance of interface properties. The uniformity of the deposited thin film is achieved by rotating the substrate, with 10% to 15% non-uniformity at the edges of the 100mm wafers, as shown in Figure 3.2 a.

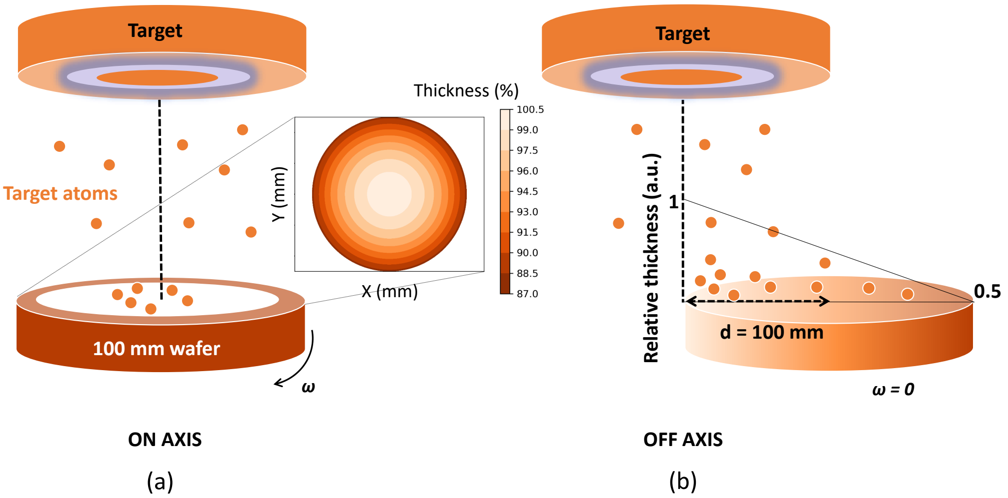

Fig. 3.2: On-axis magnetron sputtering deposition scheme. The inset shows the thickness deposition profile of the tool in this configuration (a). Off-axis deposition scheme for thickness wedges (b).

Thickness wedges deposition is achieved by offsetting the substrate wafer from the target axis as shown in Figure 3.2 b and stopping the rotation. This off-axis configuration allows us to create material thickness gradients of up to a factor of 2 along the wedge. The resulting thickness is individually characterized for each specific material by X-ray reflectivity.

Deposition systems based on the rotation of the substrate are preferred in R&D applications as they allow for smaller and cheaper targets. However, they cause greater material losses on the walls of the chamber. For industrial production, uniformity is achieved by linear motion of the wafer at a short distance between the target and the substrate, which reduces sputtering losses but requires larger, more expensive targets.

3.2 MTJ characterization at thin-film level

In this section, the tools used for characterization at the thin-film level are briefly introduced.

3.2.1 Atomic Force Microscopy

Atomic force microscopy (AFM) is a powerful technique for mapping the topography of a sample at the nanometer scale, with sub-nm vertical resolution. It was demonstrated in 1986 by Binning, Quate and Gerber [163]. Surface mapping is based on the interaction forces between the probe tip and the sample. If the tip and the sample are in close proximity, an attractive force appears that deflects the tip towards the sample. If the tip and the sample are in contact, a repulsive force appears. The tip-sample interaction is controlled by reflecting a laser off the cantilever in a photo-diode detector, as illustrated in Figure 3.3 a. A feedback system controls the cantilever deflection. There are different modes of operation, such as contact mode or dynamic mode. In the former, the dominant interactions between the tip and the sample are repulsive, while in the latter they can be attractive or repulsive depending on the amplitude of the vibration. In contact mode, the tip and sample can be damaged due to lateral forces. However, in dynamic tapping mode, the tip and specimen are in contact for only short periods, solving the problem of lateral forces.

In dynamic mode, the amplitude or frequency of the cantilever vibration is measured and the frequency is held at or near the resonant frequency (commonly 300kHz). A feedback loop monitors changes in these parameters to maintain a constant tip-to-sample distance.

In our case, roughness measurements were made on Bruker's Dimension Icon® tool using the PeakForce Tapping® (PFT) mode, introduced in 2010 by Bruker. In this mode, the cantilever vibrates at a frequency well below the resonance frequency (between 1kHz and 10kHz). It combines the advantages of contact mode and tapping mode: direct force control and avoidance of damage due to lateral forces. In addition, pico newton level interaction forces can be measured, allowing for the highest resolution [164].

3.2.2 Vibrating Sample Magnetometry

This technique, credited to Foner in 1959 [165], is based on the vibrating motion of a magnetized sample in the vertical direction as illustrated in Figure 3.3 b. The motion creates an oscillating magnetic flux that induces an alternating electromotive force (emf) in the pick-up coils, according to Faraday's law of induction. The emf is proportional to the magnetic moment of the sample and is amplified by a lock-in amplifier [166]. A magnetic field sweep allows measurements of full magnetic hysteresis loops.

The tool used during this thesis is a VSM from MicroSense ®. The high tool sensitivity (10^{-6} emu or 10^{-9} $A.m^2$ in SI units) allows for accurate determination of magnetic properties as coercive field, anisotropy field or saturation magnetization.

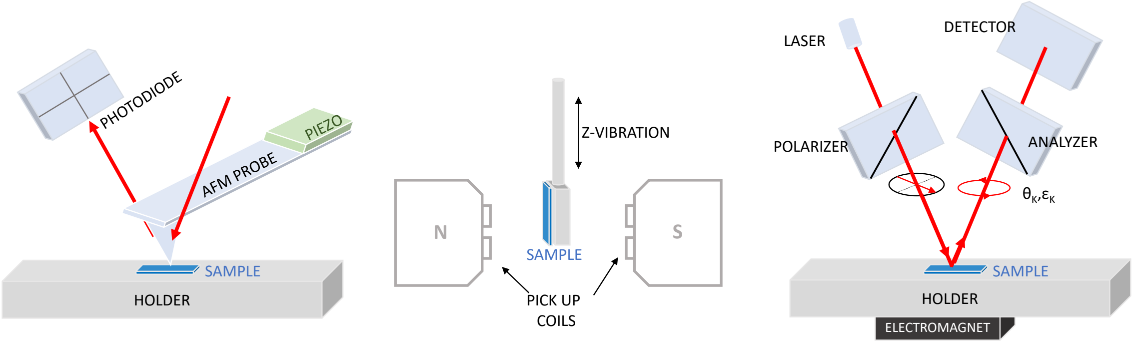

(a) (b) (c)

Fig. 3.3: AFM (a) VSM (b) and MOKE (c) set-up schematic representation.

3.2.3 Magneto-optical Kerr effect

For faster measurements of magnetic properties, a magneto-optical Kerr effect (MOKE) tool is preferred. Unlike VSM, MOKE measures the magnetic moment of a specific region of the sample, allowing rapid mapping of deposited wafers with material wedges.

When a linearly polarized light beam from a laser is reflected from a magnetic sample, as in Figure 3.3 c, several effects can take place on its polarization that are related to the magnetic properties of the sample: the direction of polarization of the sample can rotate (i), a certain ellipticity can be introduced in the beam (ii) or the intensity of the beam can be changed (iii) [167]. The Kerr rotation angle, θ_K, and the Kerr ellipticity, ϵ_K, are linearly dependent on the magnetization.

Three geometries can be used depending on the direction of the magnetic field with respect to the plane of incidence and the sample surface: polar, longitudinal, and transverse.

The laser used has a wavelength of 660nm which results in a 300µm spot and the maximum applied field is 400mT. The tool used during this thesis is a NanoMOKE3® from Durham Magneto Optics. The fact that the maximum field is limited to 400 mT makes the study of some SAF properties in Chapter 5 not possible with this tool, due to their larger reversal fields in many cases. The VSM is the tool used for those cases in which fields of more than 400 mT are required.

3.3 Process flow for the nanofabrication of patterned MTJs

Once characterization at the thin-film level has been performed, a metallic hard mask of tantalum (Ta), typically 150 nm thick, is deposited by magnetron sputtering. Before the Ta hard mask, a 3 nm ruthenium (Ru) layer is deposited, which will serve as an etching stop layer during the hard mask etching process.

3.3.1 MTJ patterning

The first step in the MTJ patterning process is the RIE of the Ta hard mask. To define circular structures with a small diameter, down to 20 nm, electron beam lithography (e-beam) is used.

A poly(methyl methacrylate) (PMMA) polymer is spin-coated onto the wafer, baked at 180° for 300 seconds, and then exposed by electron beam lithography, as illustrated in Figure 3.4 a, b and c respectively. After the development step, which is performed by using a mixture of Methyl isobutyl ketone (MIBK) and isopropanol (IPA) in a 1:3 ratio, holes are created in the resin, as illustrated in Figure 3.4 d.

The holes in the PMMA resin are filled with 20 nm of chromium (Cr), which will serve to define the previously deposited hard Ta mask.

Cr deposition is performed in a PLASSYS MEB550 physical vapor deposition (PVD) tool at 0.1nm/s.

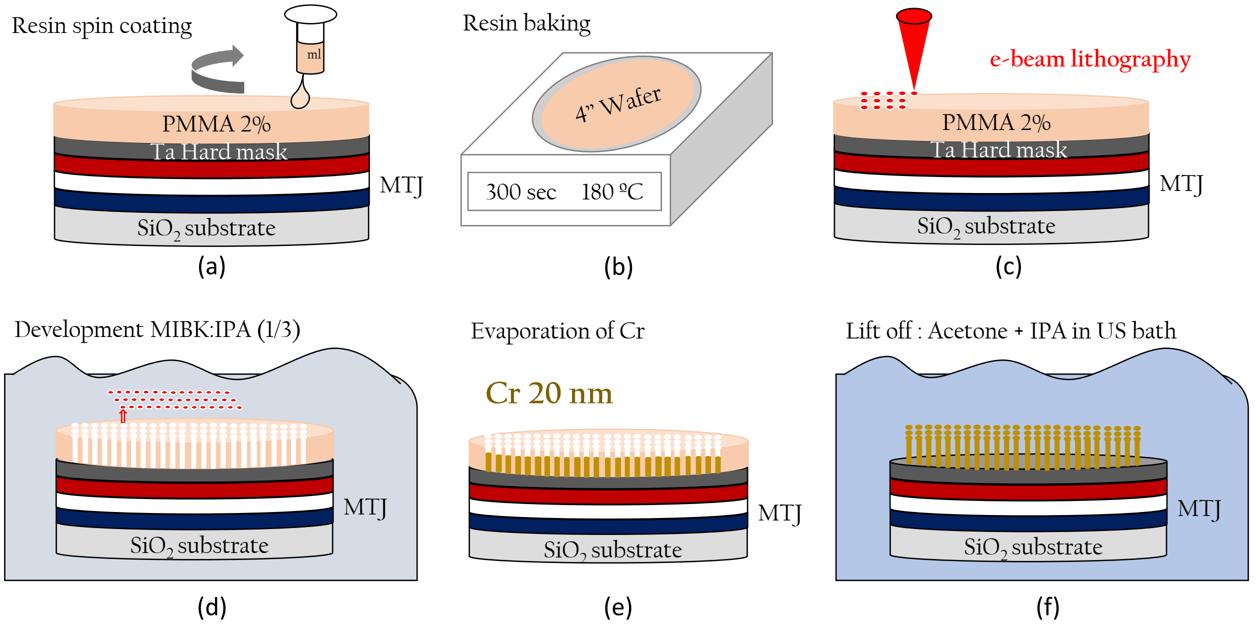

Fig. 3.4: Schematic representation of the first steps prior to the etching of the hard mask, where the Cr dots that will locally prevent etching of the hard mask are defined by electron beam lithography.

During the lift-off process, PMMA is removed and the Cr remains only on top of the Ta hard mask as small dots of the size defined during the e-beam lithography, as illustrated in Figure 3.5 a.

Figure 3.5 d shows a scanning electron microscopy (SEM) observation using a ZEISS ULTRA +, of a single Cr dot of 34 nm diameter. The deposited Cr will serve for the RIE of the Ta hard mask, since Ta will be etched everywhere except in the regions below the Cr dots which protect the Ta underneath. An interferometry system is used to control the etching process as shown in the inset of Figure 3.5 a. The etching endpoint needs to be properly selected, shortly after the signal flattening that indicates the complete removal of the hard mask material. Deviations from an optimal endpoint can lead to an underetched or overetched situation as shown in Figure 3.6 a and b respectively. The former will result in local nano-masking during the IBE process and short-circuits after bottom contact definition, while the latter may result in the falling of the pillar and resulting in an uncontacted pillar.

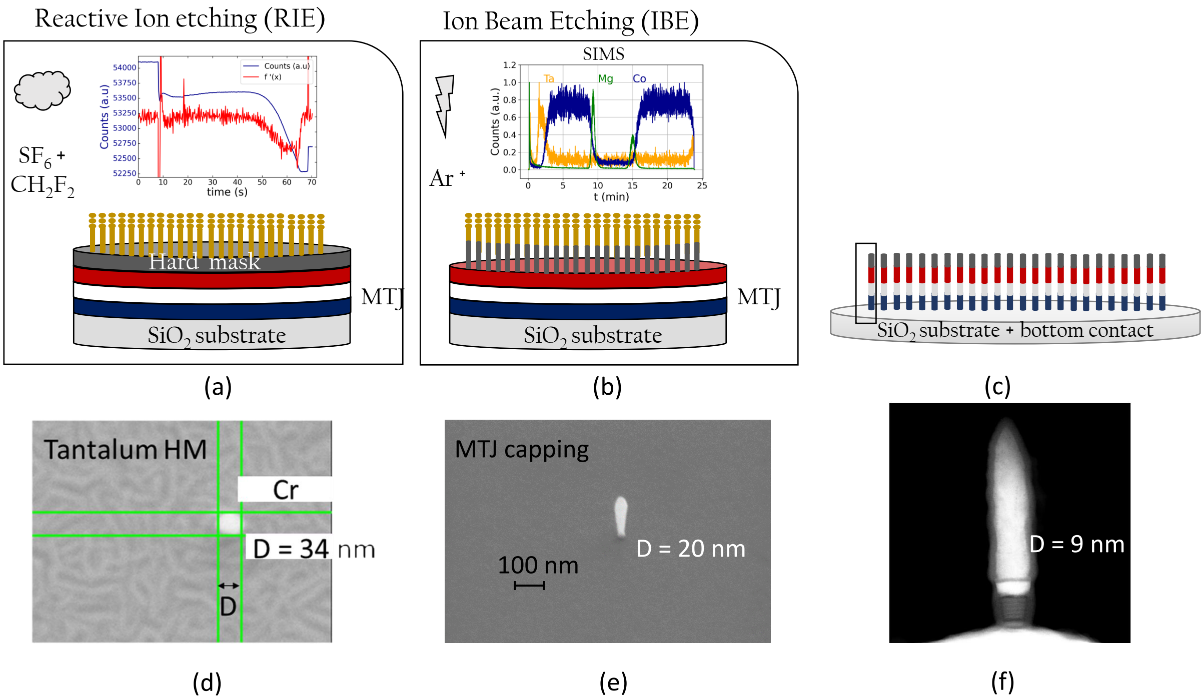

Fig. 3.5: Schematic representation of the reactive ion etching of the hard mask, with an example of interferometry system signal (a) and ion beam etching of the MTJ (b). The IBE is stopped at the bottom contact metallic layer (c). SEM observation of a circularly shaped Cr dot of 34nm diameter after deposition by evaporation and the subsequent lift-off process. The Ta hard mask characteristic texture is observed underneath (d). SEM observation of the hard mask after RIE (e). High-angle annular dark-field scanning transmission electron microscopy (STEM-HAADF) observation of the MTJ after IBE (f).

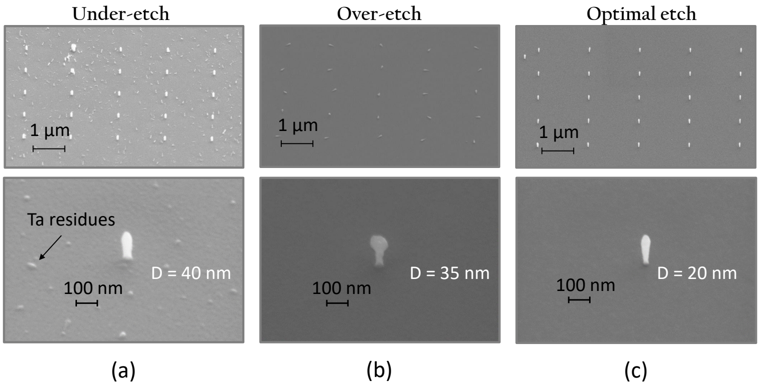

Fig. 3.6: SEM observation after RIE of the Ta hard mask resulting in under-etching (a), over-etching (b) and optimal etch (c) respectively.

During this thesis, three different inductively coupled plasma (ICP) etching tools have been used. Two of them were previously widely used by the team: PLASMALAB100 FROM OXFORD and the STS MULTIPLEX FROM SPTS. During the course of this thesis, a new tool, a SENTECH SI 500-324, was introduced and some calibration was required for optimal etching. Apart from an optimal etching time, other parameters like a correct balance between etching gases are crucial. The etching process is isotropic [168], since the etching rate is the same in all directions, because the SF_6 etching atoms have an isotropic velocity distribution, as observed in Figure 3.7 a. However, by introducing a passivating gas, as CH_2F_2, a passivating layer is formed on the walls, as seen in Figure 3.7 b, resulting in an anisotropic etching process, which creates a slope in the etching profile [169, 168]. The ratio of fluorine to carbon (F/C) of the gas phase etching species is essential for the control of the etching process. Experimental observations of the hard mask after etching with insufficient flow of CH_2F_2, or a larger amount, are shown in Figures 3.7 c and d respectively.

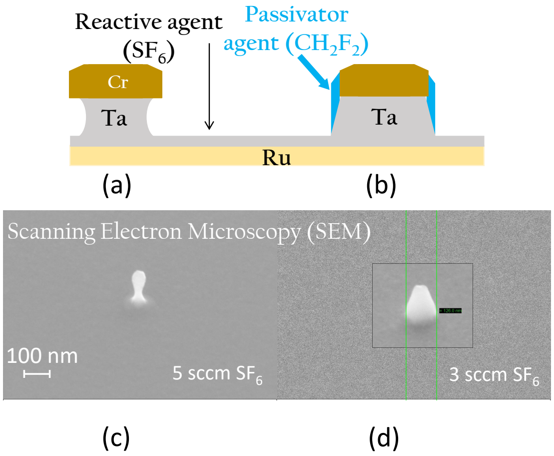

Fig. 3.7: Schematic representation of reactive ion etching of the hard mask with insufficient passivating gas flow (or excess reactive gas), resulting in isotropic etching (a). A higher amount of passivator ratio results in a more anisotropic etching (b). Experimental SEM images for the case of an excessive flow of SF_6 (c) and a lower flow (d) during the optimization process of the tool. The only difference between both tests shown in c and d is the SF_6 flow, decreased from 5 to 3 sccm. The rest of the parameters were kept constant: ICP 150W, 3sccm of CH_2F2, 10 sccm of Ar, RF power 30W, 0.44 Pa and 20ºC.

Once the etching conditions were optimized, pillars with a satisfactory straight shape were obtained as shown in Figure 3.5 e, in this case with a diameter as small as 20 nm.

Once the Ta hard mask has been etched, the rest of the magnetic stack is etched by IBE. In high-volume MRAM production, RIE is preferred, as IBE has larger difficulties to obtain short etching times, tight-pitch device arrays and high aspect ratio structures for additional top electrode wiring, especially for 300 mm wafers [106].

The magnetic stack is etched at a certain angle which helps prevent redeposition of conductive sidewalls, but vertical enough to ensure the diameter does not become too large, resulting in a tapered shape. After etching the magnetic stack, a second grazing incidence (10°) etching is performed to clean the tunneling barrier of possible conductive redeposits on the sidewalls and, in the case of perpendicular shape anisotropy (PSA) devices fabrication, to reduce the diameter of the MTJ. The etched elements are detected in-situ by a SIMS detector, enabling to follow the etching process as observed in the inset of Figure 3.5 b. The IBE is stopped at the bottom metallic contact layer. Figure 3.5 f shows a high-angle annular dark-field scanning transmission electron microscopy (STEM-HAADF) image of a pillar with a diameter as low as 9 nm, after ion milling and the reduction of the diameter with grazing incidence.

3.3.2 Bottom contact definition

The next step is the etching of the bottom metal electrode in certain regions, in order to isolate the different devices that make up the entire wafer. An AZ1512HS resin is spin coated and further baked, followed by a UV lithography step and further development, as illustrated in Figure 3.8 a,b,c and d respectively. By using UV lithography, the gap between the different devices where the metal contact should be etched is defined.

The etching of the buffer layer is performed by RIE and creates the contact pads for further device characterization, as seen in the optical microscopy Figure 3.8 f. In the next step, a polymer encapsulation is deposited which serves to separate the lower and upper contact pads.

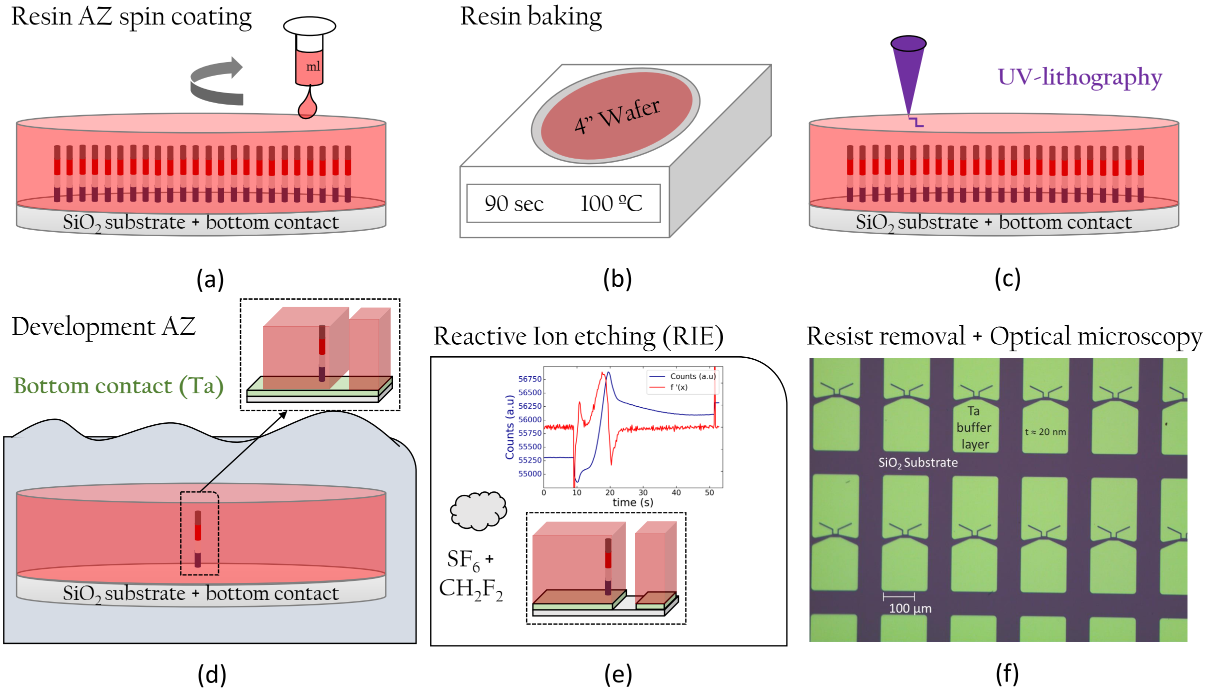

Fig. 3.8: Schematic representation of the AZ resin spin coating used for bottom contact definition (a) resin baking (b) and UV-lithography process (c). After exposure, the resin develops in a specific chemistry (d) followed by RIE of the lower contact (Pt or Ta). The non-contacting pad (represented by the right green rectangle in the figure), will serve for the top contact in a further step (e). Optical microscopy is used to inspect the quality of the etching (f). Each set of two pads corresponds to a device, all devices being electrically isolated from each other.

3.3.3 MTJ Encapsulation

Accuflo organic polymer is used for pillar encapsulation [170]. After Accuflo is baked, an AZ resin is spin coated and baked again to define the regions where Accuflo will be etched. The steps are illustrated in Figure 3.9 a-d. After resin development, a protective square is located on top of Accuflo as seen in the inset in Figure 3.9 d. After the RIE process controlled by the interferometer signal, all of the Accuflo is etched except around the pillars in a region separating the top and bottom contacts. The height of Accuflo is measured by profilometry, as seen in Figure 3.9 f, using a DEKTAK DXT "E" tool. The Accuflo height corresponds to the initially deposited thickness, around 500nm. In the inset of Figure 3.9 f, a SEM observation of the contact region is given. The Accuflo can be distinguished as the shaded region at the top of the bottom contact. Comparison between the RIE time and the thickness measured here gives the Accuflo etching speed. Knowing the etching speed is important to create the top contact. For that, a hole is created in the Accuflo insulating polymer, above the pillar. The hole should be deep enough to reach the hard Ta mask, but not too deep, otherwise etching below the MgO oxide barrier would create a short circuit between the MTJ electrodes.

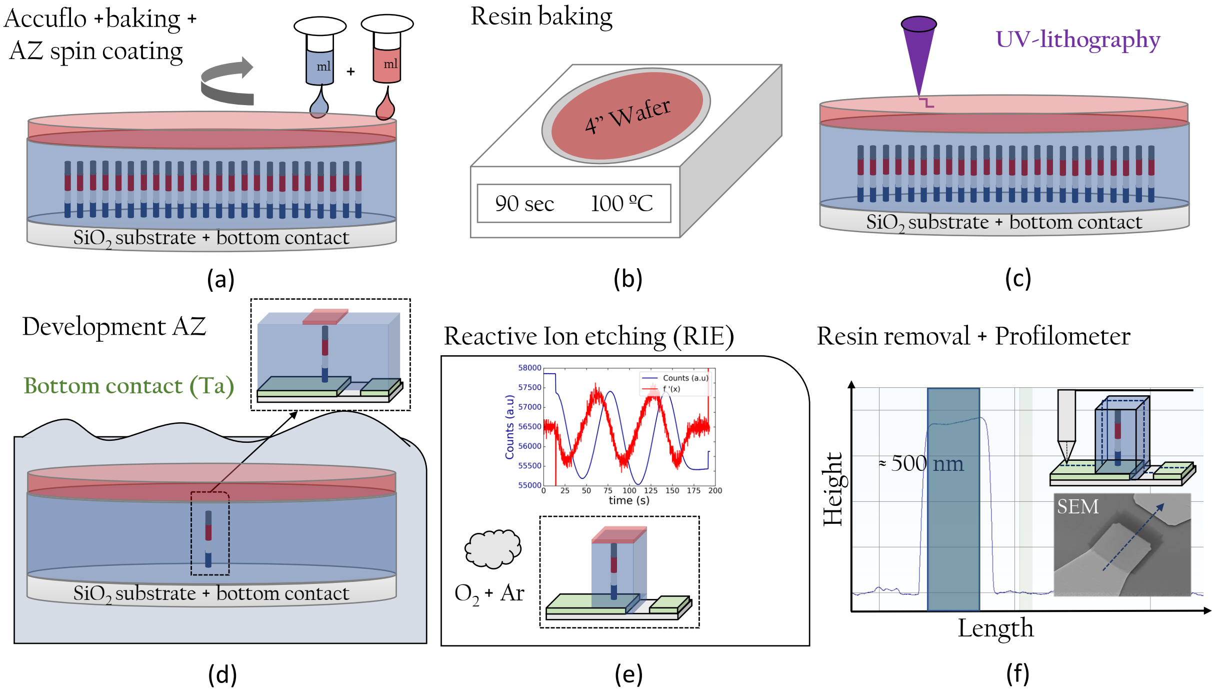

Fig. 3.9: Schematic representation of Accuflo spin coating and AZ resin used for the encapsulation definition. An Accuflo bake step up to 250ºC is required prior to AZ resin deposition (a). Resin baking (b) and UV-lithography process (c). After exposure, the resin is developed in a specific chemistry (d) followed by RIE of the Accuflo insulator. The encapsulation covers the MTJ pillar and separates the lower and upper contact pads (e). After RIE, Accuflo height is measured to inspect deposition uniformity and to facilitate further analysis of short-openings in the final wafer yield. It also allows calculating the etching speed versus RIE time for the subsequent 'hole opening' step to create the top contact (f). The inset shows SEM observation of the region where the profilometer scan is performed, with the arrow indicating the direction of the scan.

To open the hole, a new lithography cycle is performed as illustrated in Figure 3.10 a-d. After the RIE (Figure 3.10 e), a hole is opened in the Accuflo region as seen in the inset of Figure 3.10 f. The height of the Accuflo hole can be measured with the profilometer and it should be up to half the height of the hard mask to achieve good electrical contact. This hole is then filled with a metal in the following step.

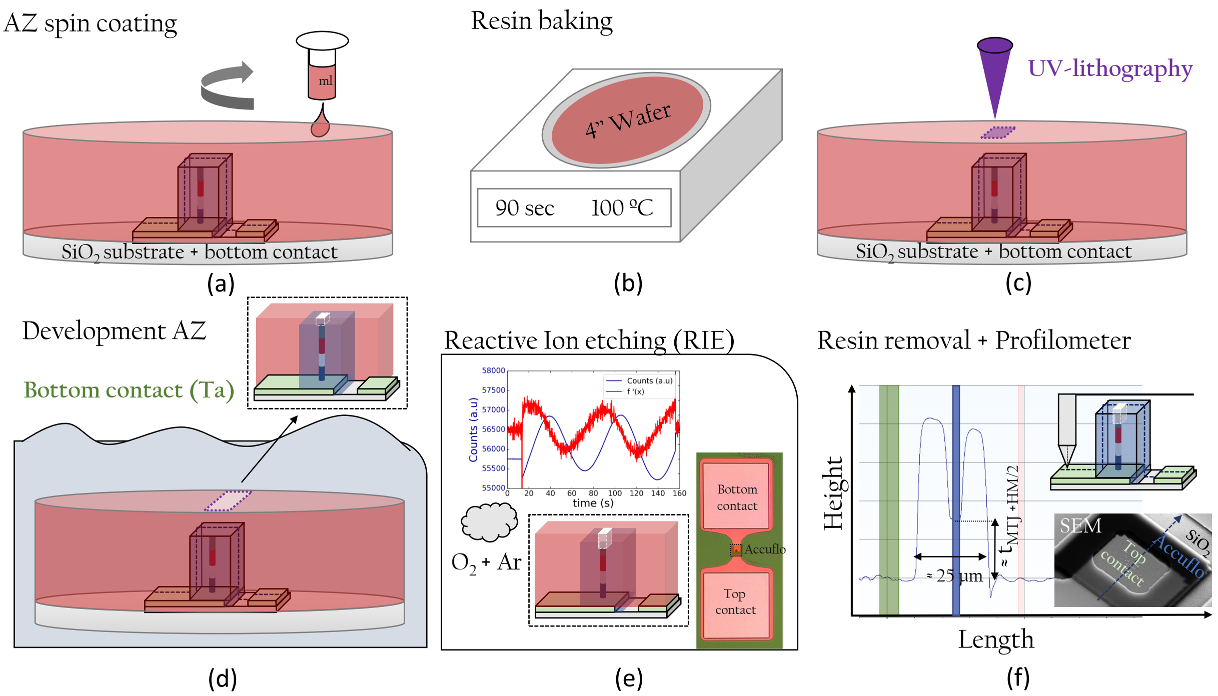

Fig. 3.10: Schematic representation of AZ resin spin coating used to define an opening in the encapsulation to deposit the top metal contact (a) resin baking (b) and UV-lithography process (c). After exposure, the resin develops in a specific chemistry (d) followed by RIE of the Accuflo insulator only exposed to chemical etching in the opening region. The etching time is calculated to reach the thickness of Accuflo that covers half of the hard mask, to have a good contact but to avoid a short circuit. The inset shows an optical microscopy image of the pad region where the etching in the Accuflo (hole in the dark contrast) can be observed (e). After RIE, the hole in the Accuflo encapsulation can be controlled by profilometry(f).

3.3.4 Top contact definition

Once the hole in the insulating polymer has been made, the last steps consist of depositing the upper metal contact. A new lithography cycle is performed as illustrated in Figure 3.11 a-f. In this case, the AZ resin is rendered negative by a double exposure cycle. (Figure 3.11 c and e), once with mask and the second in flood exposure mode. The resulting pattern allows us to deposit a metallic layer of 10 nm of Cr followed by 300 nm of Al (represented in yellow in Figure 3.11 g) only on the pads with a certain space to avoid contact between them. Finally, after the lift-off process, the fabrication process ends.

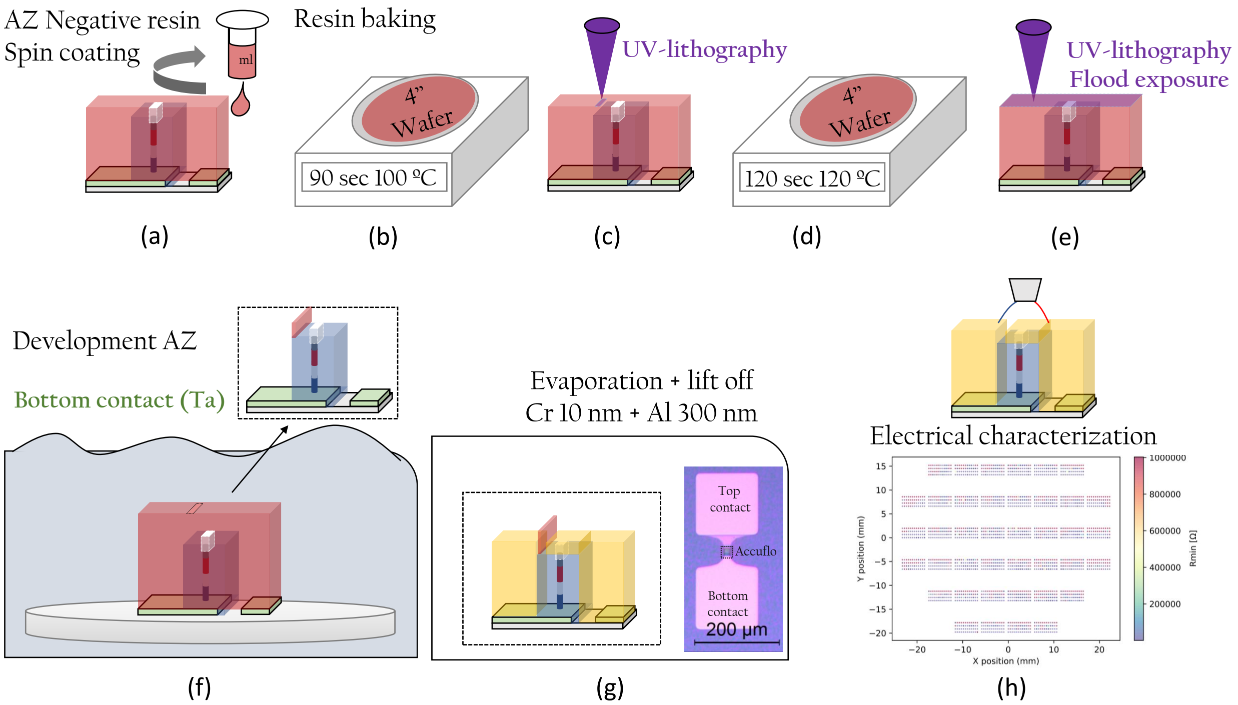

Fig. 3.11: Schematic representation of AZ resin spin coating used to define an opening in the encapsulation to deposit the top metal contact (a) resin baking (b) and UV-lithography process (c). After exposure, the resin develops in a specific chemistry (d) followed by RIE of the Accuflo insulator only exposed to chemical etching in the opening region. The etching time is calculated to achieve a thickness of Accuflo that covers half of the hard mask, to have a good contact but to avoid a short circuit. The inset shows an optical microscopy image of the region of the pads where the small opening in the middle of Accuflo can be seen. (e). After RIE, the hole height in the Accuflo encapsulation can be controlled by profilometry (f).

3.4 MTJ characterization at patterned level

The wafer is electrically characterized with an electrical prober optimized over several years at SPINTEC. An electromagnet is used to apply a magnetic field through two coils connected to a KEPCO generator. To get hysteresis loops, it is necessary to sweep the magnetic field. A waveform generator (Agilent 33500B) monitors the KEPCO power supply. For reading the resistance state of the MTJ, a Keithley 2401 current generator sends the current through an RF probe to the contact pads, while a digital multimeter (Agilent 34411A) measures the voltage, resulting in the resistance of the MTJ directly by Ohm's law.

To add a write current to switch the device over STT, a pulse generator (HP 8110A) connected to the RF probes in conjunction with the digital multimeter via a bias tee is used. As a result, a DC (read) and RF (write) input is used to generate a mix signal. This configuration allows us to make a phase diagram, like the one seen later in Figure 4.17 b. A schematic of the experimental setup is illustrated in Figure 3.12.

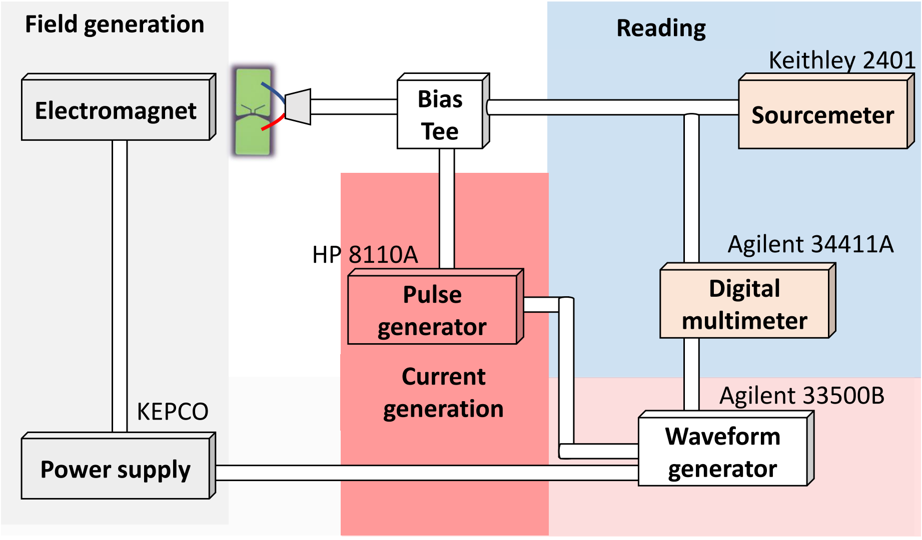

Fig. 3.12: Electrical prober set-up for MTJ characterization at patterned level.

3.5 Buffer layer development

The main objective of this thesis is to replace the critical metals (especially Pt and Ru) contained in STT-MRAM cells. However, SPINTEC conventionally uses a 3nm Ta/25nm Pt buffer layer for MTJ growth. This thick Pt buffer layer is used to promote an appropriate fcc 111 texture for the Co/Pt multilayers that make up the SAF to which the reference layer is magnetically coupled. Previous studies have reported the influence of Pt buffer layer thickness on the coercivity and perpendicular anisotropy of Co/Pt multilayers [171, 172]. The stability of the reference layer coupled to the SAF structure could be compromised if much thinner Pt buffer layers are used. Therefore, an essential step for us to get rid of the use of platinum was to find an alternative material. Initially, a Ta-based buffer was investigated, as Ta has also been shown to provide high PMA to Co/Pt multilayers. [173].

For the conventional case of a Ta3nm/Pt25nm buffer layer structure, RMS roughness values of 0.37nm were measured by atomic force microscopy (AFM), as seen in Figure 3.13 b and e, in the as-deposited state and after a 400°C anneal for 10 minutes respectively. In the case of using a 25 nm Ta buffer layer alone, the RMS roughness increased to values of 0.49 nm and 0.44 nm, respectively for the as-deposited and after annealing cases as observed in Figure 3.13 a,d. Such an increase in roughness is detrimental for the proper functioning of STT-MRAM cells. Defects in the thin tunnel barrier can lead to reliability issues and therefore a smooth substrate is an essential requirement for MTJ growth. In many cases, chemical-mechanical polishing (CMP) is used to reduce roughness prior to magnetic stack deposition.

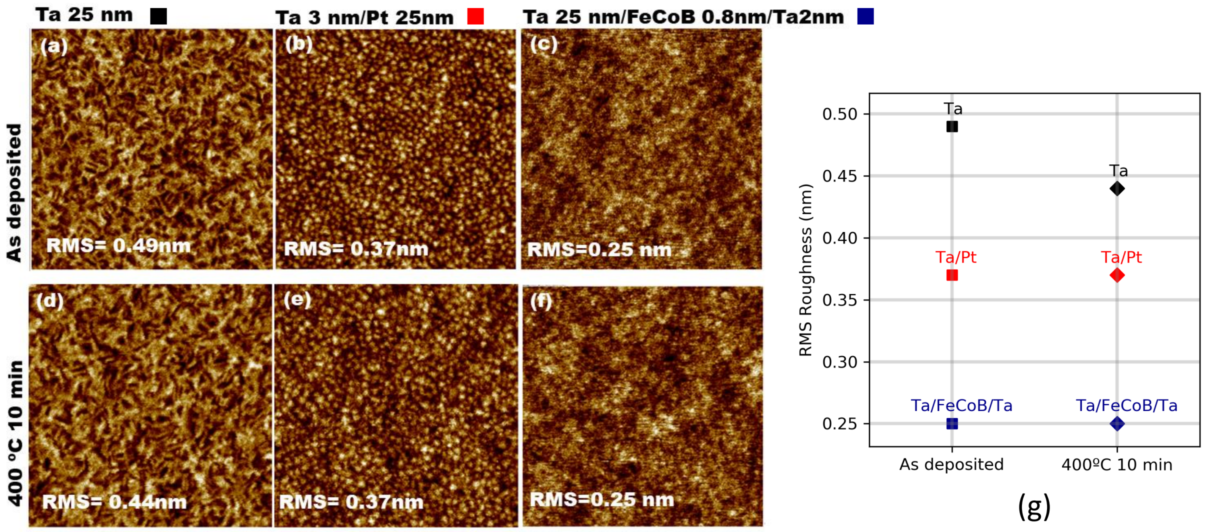

Fig. 3.13: AFM scans (500 nm x500 nm) for different buffer layers: Ta 25nm (a) Ta 3nm/Pt 25nm (b) Ta 25nm/FeCoB 0.8nm/Ta 2nm (c) as-deposited and after 400C annealing for 10 minutes (d,e,f) respectively. RMS roughness values of the scans shown in a-f.

However, we managed to find a solution for reducing the Ta buffer roughness, even without CMP treatment. By inserting a thin amorphous layer of FeCoB in the last few nanometers of the Ta buffer layer, a smoother top surface could be achieved. The insertion of this thin amorphous FeCoB layer reduces the RMS roughness of the 25 nm Ta buffer layer by almost half, both after deposition and after annealing at 400°C for 10 minutes as shown in Figure 3.13 c and f respectively. The RMS roughness achieved with the FeCoB insertion is even smaller than that of a Ta 3nm/Pt 25nm buffer layer, which was our standard for Co/Pt multilayer growth. The roughness values for all different cases are given in Figure 3.13 g. The texture developed in the buffers Ta (Figure 3.13 a, d) and Pt (Figure 3.13 b, e) as a result of the growth of the grains is clearly broken by the insertion of the 0.8 nm amorphous layer of FeCoB (Figure 3.13 c, f). Due to its low thickness and intermixing with Ta after the annealing process, this FeCoB layer is not magnetic at room temperature.

Therefore, we demonstrate how a platinum-free, low-roughness buffer layer can be achieved by adding a thin (sub-nm) FeCoB insertion.

Chapter 4

Perpendicular shape anisotropy for the reference layer of STT-MRAM

In this chapter, we first give an introduction to perpendicular shape anisotropy (PSA) and its use for the STT-MRAM storage layer.

We propose an All-PSA-STT-MRAM structure, consisting of a lower reference layer, a storage layer and an top polarizing layer whose magnetization is set antiparallel to the reference layer to compensate for the stray field in the storage layer, all elements being designed with PSA to avoid the use of platinum group metals.

The selection of the dimensions and materials used is based on macrospin calculations to achieve an optimal hierarchy in the stability of all layers and a reduced stray field in the storage layer. We have minimized the roughness increase by using Ta laminations. Due to the small diameters targeted, obtaining these small MTJs is not trivial and the process to achieve this is also explained. Finally, we show off-axis electron holography observations of the magnetization of the All-PSA-STT-MRAM structure and electrical results of the patterned MTJs.

4.1 Introduction to perpendicular shape anisotropy (PSA).

Innovative concepts are being explored to improve MRAM scalability, such as depositing MTJs on pre-patterned pillars [174]. This avoids the difficult etching process of magnetic tunnel junction stacks with very small diameters (sub-30 nm) and small pitch. However, apart from manufacturing difficulties, the main problem of MTJ downscaling is the loss of thermal stability of the storage layer element.

The thermal stability factor is a dimensionless parameter characterized by the energy E_B required to switch the storage layer between its two stable states ‘1’ and ‘0’, at a temperature T, which is given by Equation 4.1, in macrospin approximation [41]:

$$\Delta = \frac{E_b}{k_B T} = (\frac{\mu_0 M_s^2}{2} t(N_{xx} - N_{zz}) + K_u t + K_s)\frac{\pi D^2}{4 k_B T} \tag{4.1}$$

.

In Equation 4.1, k_B and μ_0 are respectively the Boltzmann constant and the vacuum magnetic permeability. D and t denote the cylindrical storage layer diameter and thickness respectively. The other parameters are related to the magnetic properties of the used material: M_S is the saturation magnetization, K_s is the interfacial anisotropy at the interface between the tunnel barrier and the magnetic storage layer (most often a MgO/FeCoB interface) and K_u stands for a possible uniaxial magnetocristalline or magnetoelastic anisotropy. N_{xx} and N_{zz} are respectively the in-plane and out-of-plane demagnetizing factors.

The thermal stability factor determines data retention. The retention time τ follows an Arrhenius's law [175]:

$$\tau = \tau_0 \; exp(\Delta) \tag{4.2}$$

where τ_0 is an attempt time of the order of 1ns.

In conventional STT-MRAM, interfacial anisotropy causes the magnetization to be in the out-of-plane direction, resulting in an energy barrier $E_B = \Delta \cdot k_B T$, which should be in the range 60–100 $\mathrm{k_B T}$ at room temperature to meet industrial memory retention requirements[1]. For conventional p-MTJs, the thickness of the free layer is much smaller than the MTJ diameter, $t << D$, so that the demagnetizing factors $N_{zz} > N_{xx}$. Even if the shape anisotropy term $\frac{\mu_0 M_s^2}{2}(N_{xx} - N_{zz})$ is negative, the interfacial anisotropy, $\mathrm{k_s}$, is large enough to overcome this contribution. However, Equation 4.1 shows that the overall anisotropy depends directly on the cell area $(\frac{\pi D^2}{4})$, which means that the thermal stability decreases with the diameter of the MTJ. Below a certain diameter of the order of 20 nm, the retention requirements can no longer be met in ordinary p-MTJs.

Figure 4.1 a shows calculations of the thermal stability Δ as a function of MTJ diameter and free layer thickness. Thermal stability decreases below 60 at diameters below 15 nm for the conventional thickness used in the p-STT-MRAM. New approaches have been described to maintain higher Δ down to lower diameters, such as Double-MTJ, which uses an MgO capping on the free layer, providing an additional source of perpendicular anisotropy [76], or the use of an assistance layer [176, 177]. Experimental results for the thermal stability of double MTJs for varying diameters are given in Figure 4.1 b. For diameters below 20 nm, the thermal stability drops below 60. In addition, multiple MgO laminations can be used to further increase the perpendicular anisotropy of the free layer and, consequently, the thermal stability at small diameters [178, 179], as seen in the experimental results in Figure 4.1 c, for the case of a Quad-MTJ using four MgO interfaces.

To scale STT-MRAM below 20 nm, one possibility is that the magnetostatic shape anisotropy energy of density $\frac{\mu_0 M_s^2}{2}(N_{xx} - N_{zz})$ contributes to the total out-of-plane anisotropy. As the aspect ratio (t/D) of the storage layer increases near 1[2], the in plane demagnetizing factor becomes larger than the out of plane factor, $N_{xx} > N_{zz}$, and consequently the shape anisotropy term, which is usually negative, becomes positive and adds to the interfacial anisotropy. As a result, thermally stable memory cells of diameters as small as 4 nm are possible, provided that the storage layer is sufficiently thick, as shown in Figure 4.1 a for the case of PSA-STT-MRAM [41, 42, 43]. PSA has recently been implemented in the storage layer of the STT-MRAM to improve its downsizing scalability [41, 42, 43]. In these earlier studies, the thickness of the storage layer was increased to enhance thermal stability down to diameters below 10 nm, where conventional STT-MRAM based on interfacial anisotropy is no longer stable. Multilayered ferromagnetic structures, with MgO insertions in the PSA storage layer have also been reported to increase the thermal stability of PSA-STT-MRAM [182].

An additional advantage of PSA-MTJs is that their properties are less sensitive to temperature fluctuations than p-MTJs, which makes them a good candidate for applications with a wide operating temperature range (e.g. automotive -40°C/+150°C) [44, 183].

We have recently reported the observation by off-axis electron holography of the stability of PSA-STT-MRAM up to 225°C, as seen in Figure 4.2.

A schematic representation of the characterized MTJ structure is shown in Figure 4.2. Figures 4.2 b and c show a STEM image of an MTJ with $\sim$ 20 nm diameter and 60 nm free layer thickness and the associated energy-dispersive X-ray spectroscopy (EDX) chemical map respectively. The out-of-plane magnetization of the storage layer is maintained from 20°C to 225°C, as seen in Figures 4.2 d-f. The same strategy can be applied to the reference layer in the context of Pt substitution. The Co/Pt based SAF with high perpendicular ansisotropy can be replaced by a more common ferromagnetic material with a high enough aspect ratio (t/D) so that its shape anisotropy is large enough to ensure stability.

---

[1] The required value of Δ depends on the specific application, memory or logic, and the memory capacity, as larger memory capacities require larger thermal stability factors to avoid accidental failures.

[2] More precisely t/D $>$ 0.89, according to the analytical expressions for the demagnetizing factors N_{xx} and N_{zz} proposed by Sato and Ishii [181].

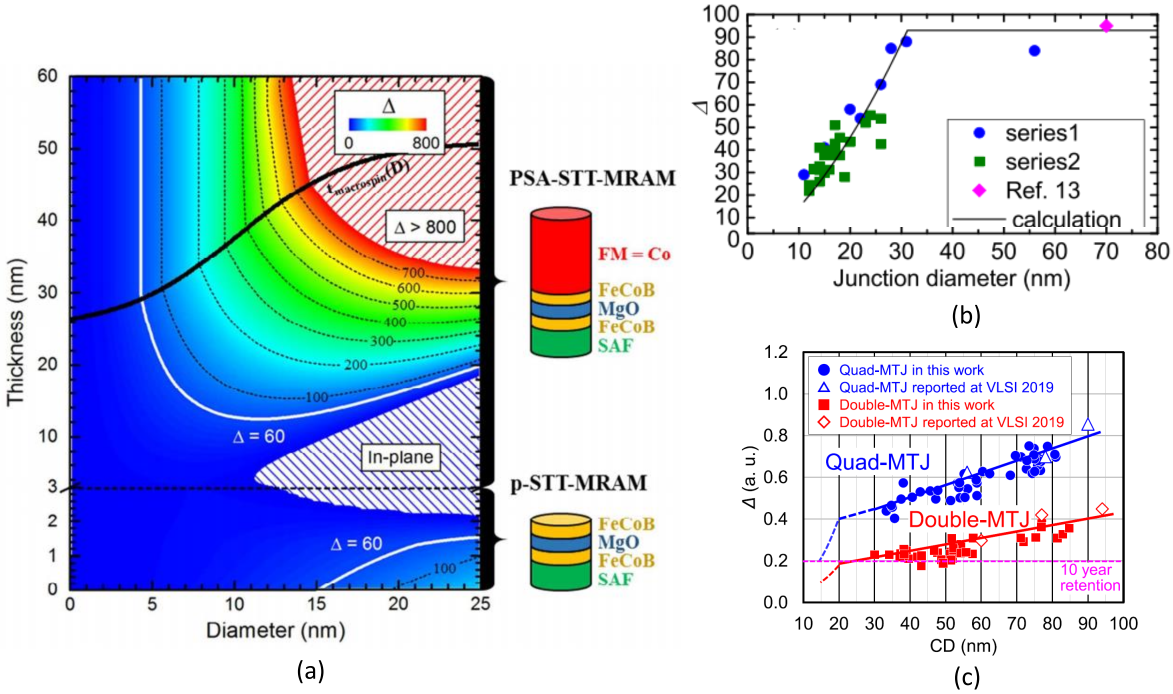

Fig. 4.1: Stability diagram of a cylindrical storage layer made of FeCoB for the p-STT-MRAM case and FeCoB(1.4 nm)/Co(t-1.4 nm) for the PSA-STT-MRAM case versus its total thickness (t) and diameter (D) at room temperature (300 K). From Perrisin et al. [41] (a). Experimental thermal stability of MgO/CoFeB/Ta/CoFeB/MgO Double-MTJs with respect to junction diameter. Series 1 and 2 refers to identical Double-MTJ samples. From Sato et al. [180] (b). Experimental results of Δ at room temperature for both Quad-MTJs and Double-MTJs. From Miura et al. [179] (c).

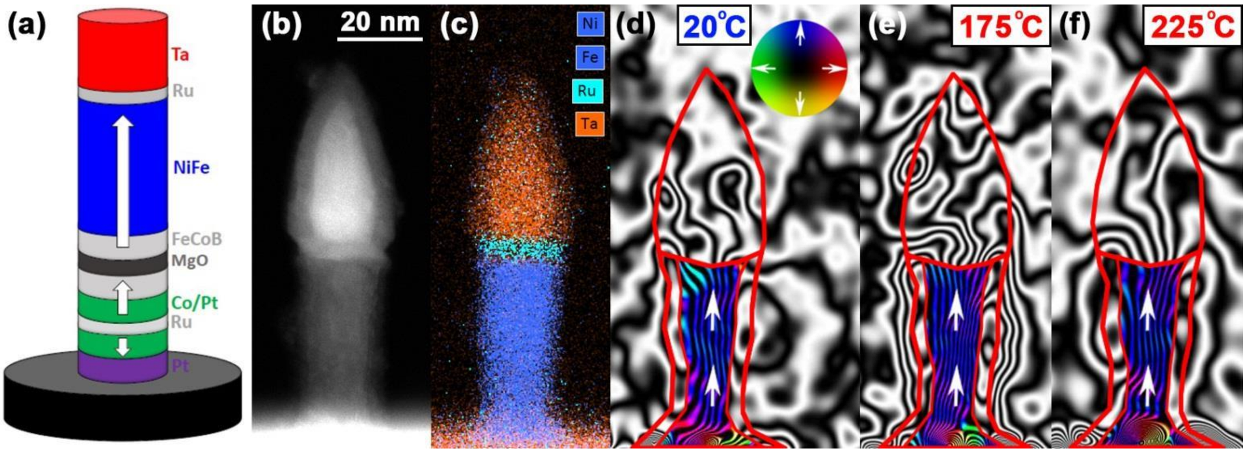

Fig. 4.2: Schematic of a PSA-STT-MRAM MTJ cell with a 60 nm thick NiFe free layer (a). STEM image of a PSA pillar with a diameter of ∼ 20nm (b); and the associated EDX chemical map showing the elemental distribution of Ta (hard mask-red), NiFe (storage layer-blue), and Ru (RIE etch stop layer-turquoise) (c). Magnetic induction maps reconstructed from electron holograms acquired during in-situ heating at (d) 20°C; (e) 175°C; and (f) 225°C. The magnetization direction is shown using white arrows, as depicted in the color wheel. From [184].

4.2 Optimization of All-PSA-STT-MRAM

Perpendicular shape anisotropy can also be used for the STT-MRAM reference layer. Instead of employing the anisotropy arising in Co/Pt multilayers, PSA can alternatively be used. The advantage of this approach is that, in principle, any magnetic material can be used for such a proposal, since perpendicular anisotropy will arise due to the shape of the magnetic element. Therefore, conventionally used metals such as FeCoB or Co can be selected, but also less critical metals such as NiFe. The only restriction to be met is that the reference layer must be more stable than the free layer, as is usual in MRAM applications. However, there are two other factors that can be problematic when using this PSA-based reference layer:

1) The resulting stray field of the PSA reference layer must be compensated in the free layer element.

2) Between the reference layer and the free layer, an interlayer coupling effect can occur, which is detrimental to device operation.

The following two Sections 4.2.1 and 4.2.3 provide solutions to these specific challenges .

In Section 4.2.2 we perform micromagnetic simulations of the reversal of the All-PSA MTJ structure.

4.2.1 Macrospin calculations: thermal stability & stray field.

As in the case of a double MgO based p-MTJ, a three-layer PSA-STT-MRAM must be designed so that the free layer has sufficient thermal stability and the bottom and top polarizer layers can be set antiparallel to each other to ensure a double STT contribution during the writing operation.

In our case, the antiparallel alignment is used not only to provide double STT, but also to compensate for the stray field of both polarizers in the free layer, since we do not use a SAF structure.

We performed macroscopin calculations of the thermal stability of each element of the three-layers All-PSA structure and their mutual interactions. The analytical expression for calculating the demagnetizing energy of a parallelepiped-shaped magnetic element was previously described [185]. The model is based on a coulombian representation of the magnetostatic interactions. The magnet poles are considered as surface distributions of magnetic charges of opposite charge value. Several integrations with logarithmic and arc tangent functions are performed.

$$E_{\parallel} = \frac{J \cdot J'_{\parallel}}{4\pi\mu_0} \sum_{i=0}^{1} \sum_{j=0}^{1} \sum_{k=0}^{1} \sum_{l=0}^{1} \sum_{p=0}^{1} \sum_{q=0}^{1} (-1)^{i+j+k+l+p+q} \Psi_{\parallel}(U_{ij}, V_{kl}, W_{pq}, r) \tag{4.3}$$

with

$$\Psi_{\parallel}(U,V,W,r) = \frac{U(V^2 - W^2)}{2} ln(r-U) + \frac{V(U^2 - W^2)}{2} ln(r-V) + UVW \cdot tg^{-1}(\frac{UV}{rW}) + \frac{r}{6}(U^2 + V^2 - 2W^2) \tag{4.4}$$

and for the perpendicular polarization case:

$$E_{\perp} = \frac{J \cdot J'_{\perp}}{4\pi\mu_0} \sum_{i=0}^{1} \sum_{j=0}^{1} \sum_{k=0}^{1} \sum_{l=0}^{1} \sum_{p=0}^{1} \sum_{q=0}^{1} (-1)^{i+j+k+l+p+q} \Psi_{\perp}(U_{ij}, V_{kl}, W_{pq}, r) \tag{4.5}$$

with

$$\begin{aligned} \Psi_{\perp}(U,V,W,r) = & \frac{V(V^2 - 3U^2)}{6} ln(W + r) + \frac{W(W^2 - 3U^2)}{6} ln(V + r) + \\ & + UVW \cdot ln(-U + r) + \frac{U}{6}(3V^2 tg^{-1}(\frac{UW}{V \cdot r}) + \\ & + 3W^2 tg^{-}1(\frac{UV}{W \cdot r}) + U^2 tg^{-1}(\frac{VW}{U \cdot r})) + \frac{V \cdot W \cdot r}{3} \end{aligned} \tag{4.6}$$

being in both cases

$$\begin{aligned} U_{ij} &= \alpha + (-1)^j A - (-1)^i a \\ V_{kl} &= \beta + (-1)^l B - (-1)^k b \\ W_{pq} &= \gamma + (-1)^q C - (-1)^p c \\ r &= \sqrt{U_{ij}^2 + V_{kl}^2 + W_{pq}^2} \end{aligned} \tag{4.7}$$

where 2a, 2b and 2c are the dimensions of the first magnet along the x, y and z direction respectively, as in Figure 4.3 a. Similarly 2A, 2B and 2C are the dimensions of the second magnet along the x, y and z direction respectively. α, β and γ define the distance between the origin of the two magnetic bodies (OO'), along x, y and z directions. In our case, as both bodies are positioned one on top of each other, only $\gamma \neq 0$, while $\alpha = 0$ and $\beta = 0$.

The thermal stability factor can then be calculated as the difference in energy between the parallel and perpendicular cases, divided by $k_B \cdot T$:

$$\Delta = \frac{\Delta E}{k_B \cdot T} = \frac{E_\perp - E_\parallel}{k_B \cdot T} \tag{4.8}$$

For the free layer element, a thermal stability factor between 60 and 100 is usually desired to ensure a sufficiently long retention time. Figure 4.3 b shows thermal stability as a function of thickness and diameter for a FeCoB element (Ms = 1MA/m), such as the one in Figure 4.3 a.

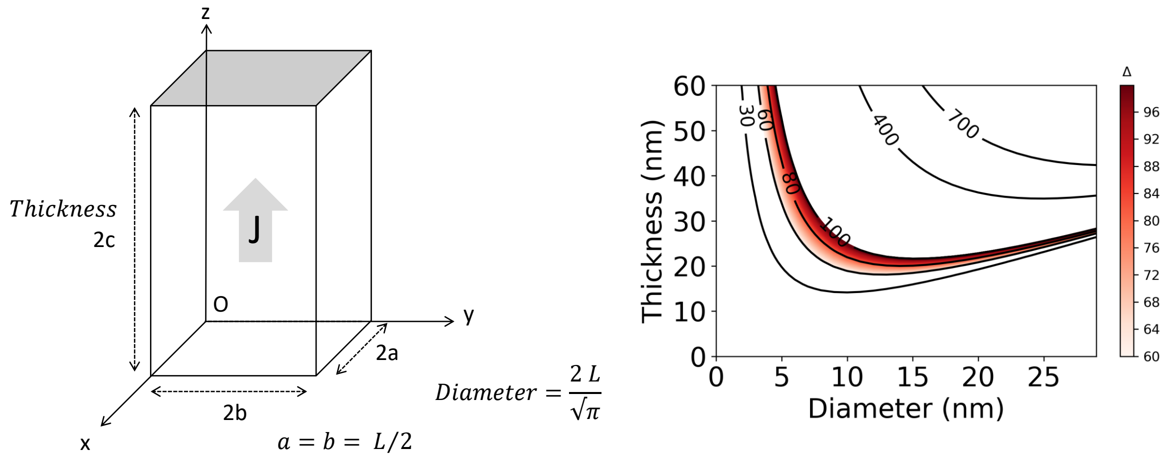

(a)

(b)

Fig. 4.3: Scheme of the magnetic element dimensions (a). Thermal stability factor as a function of the magnetic element dimensions for the case of FeCoB, Ms=1 MA/m (b).

The red colormap highlights the target region of thermal stability between 60 and 100. Figure 4.3 shows that by using a 20 nm thick free layer, a sufficiently high thermal stability is guaranteed down to 10 nm nodes.

However, to design the All-STT-MRAM, it is necessary to take into account the effect of the free layer on the polarizers and vice versa.

Normally, the desired stability hierarchy is as follows: $\Delta_{\text{Bottom polarizer}} > \Delta_{\text{Top polarizer}} > \Delta_{\text{Free layer}}$.

The free layer element is chosen to be the element with the smallest Δ since it is the one that will switch between the binary memory states 'P' and 'AP'. Indeed, it is optimal for the free layer element to be sandwiched between the two polarizers, since it will be subjected to a double spin transfer torque, thus reducing the switching current. However, this double STT will only work if the two polarizers are placed antiparallel to each other, a necessary condition to compensate the stray field also in the free layer element. This 'setting operation' requires that the top polarizer has a lower thermal stability than the lower reference polarizer, so that it can be adjusted antiparallel to the latter without affecting its magnetic configuration.

In addition, during operation, the thermal stability of the top polarizer will be affected by the state of the free layer. Therefore, when the free layer is in a state antiparallel to the top polarizer (up/up/down), the top polarizer will decrease its thermal stability due to the Zeeman energy contribution from the neighboring free layer, $\Delta_{\text{Top polarizer}}$ (Δ^{-}). Also the free layer parallel to the bottom polarizer experiences a slight increase in thermal stability if the Zeeman energy contribution of the bottom polarizer, which favors this parallel alignment, is stronger than the counteracting Zeeman energy contribution of the antiparallel top polarizer $\Delta_{\text{Free layer}}$ (Δ^{+}). Therefore, in such a critical situation, the hierarchy will be affected in such a way that:
$\Delta_{\text{Bottom polarizer}}$ $(\Delta^{+}) > \Delta_{\text{Top polarizer}}$ $(\Delta^{-}) > \Delta_{\text{Free layer}}$ (Δ^{+})

The risk in such a situation is that the top polarizer layer could reduce its thermal stability too much so that it is lower than that of the free layer, breaking the antiparallel configuration with the bottom polarizer, and thus the optimal performance of the device.

Stray field compensation

The thermal stability of each magnetic element is proportional to its saturation magnetization (Ms), as seen in Equation 4.1. Therefore, a logical choice would be, at first, to use an Ms hierarchy among the three PSA elements. However, in order to have a better compensation of the stray field in the free-layer element, it is more convenient that the lower and top polarizers are made of the same material. Figure 4.4 a shows a schematic of the All-PSA stack, where the Ms of the bottom polarizer is set to that of FeCoB (1 MA/m) and its thickness to 40 nm. The free layer element consists of a 20 nm thick FeCoB layer.

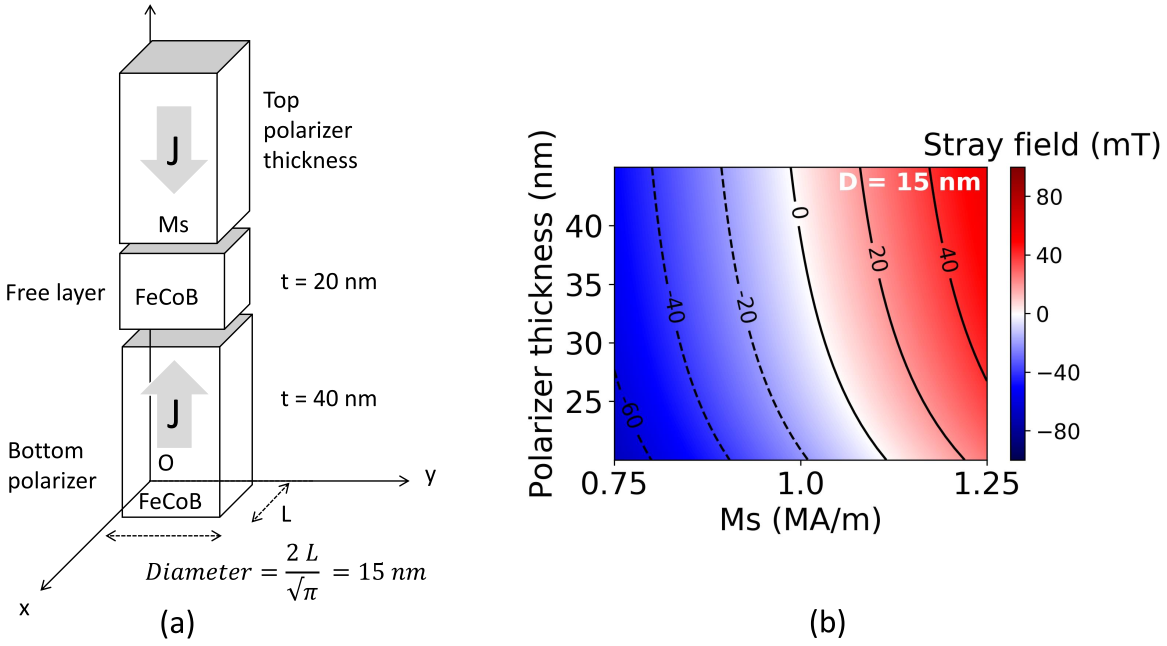

Fig. 4.4: Schematic of the magnetic elements of the system with a top polarizer of variable thickness and Ms (a). Resulting stray field in the free-layer element for a bottom polarizer with 40 nm thick FeCoB as in (a) and varying the thickness of the top polarizer and Ms (b).

Figure 4.4 b shows the resulting mean stray field in the PSA 20 nm FeCoB free layer as a function of Ms and top polarizer thickness. Full compensation is achieved when the thickness of the top polarizer and Ms is the same as that of the bottom polarizer (Ms=1MA/m, t=40nm), given an antiparallel configuration between the two. As already mentioned, varying the Ms of the top polarizer to modify its thermal stability is not an optimal strategy, since the resulting stray field is very sensitive to such a change. For example, for a top polarizer of 40 nm, if the material is chosen to be NiFe, with Ms of 0.756 MA/m, it is seen in Figure 4.4 b that the resulting stray field would be shifted to values greater than -40mT. These stray field values are too large and could hinder the bistability of the parallel and antiparallel states of the free layer. Resulting stray fields smaller than 20 mT are more convenient. However, it is possible to tune the thermal stability of the polarizers by varying their thickness, as seen previously in Figure 4.3 b. Such thickness variation will have a much smaller effect on the stray field compensation. Figure 4.4 b shows that by varying the polarizer thickness (y-axis), the stray field is much less affected and the compensation can be maintained. The thickness of the top polarizer can be changed from 40 nm to 30 nm keeping the stray field very close to 0 and therefore an optimal compensation.

The diagram shown here shows the resulting stray field for an MTJ diameter of 15 nm, but the same conclusions can be extrapolated for smaller diameters.

We conclude then that the two polarizers must be made of the same material, and that the stability hierarchy must be achieved by varying the aspect ratio of the two elements. For the free layer, a material with lower Ms can be selected, since the stray field produced in the two neighboring polarizers will be identical, and will help to achieve the desired hierarchy in thermal stability.

The Co/FeCoB/Co system therefore appears to be a good alternative. Other systems that respect the Ms hierarchy we are looking for could be Co/NiFe/Co or FeCoB/NiFe/FeCoB. However, in these systems, the Ms of at least one element is reduced. A higher Ms allows for similar thermal stability values with a lower aspect ratio, which is preferred in the nanofabrication process. Since the aspect ratio of each layer must be close to or greater than one to maintain PSA, the total thickness of the nanopillar will be quite large. A very large overall thickness is not desirable, as the pillars could tilt or fall if the final aspect ratio is too high. Therefore, a system with a large Ms in each of the three components will keep the overall aspect ratio smaller.

Thermal stability hierarchy

Next, we investigated the optimal setting and working conditions of the All-PSA-STT-MRAM. We consider the Zeeman field required to overcome the energy barrier between the parallel and perpendicular magnetization state of each element. First, an external field is required to saturate the three elements in the same direction, and a second opposing field of smaller amplitude will establish the antiparallel state between the two polarizers. Therefore, during this setting step, the lower reference polarizer is required to have a sufficiently high switching field to remain in the same initial orientation.

The free layer increases its stability in this first saturation condition, since it is sandwiched between the two parallel oriented polarizers, and it may be that the top polarizer switches even before the free layer. For this first initial adjustment step, the hierarchy can be modified and the stability of the free layer can be higher than that of the top polarizer for certain geometries. Nonetheless, it is not important, since once the top polarizer is switched to the antiparallel configuration, the compensation (or almost full compensation, depending on the thickness of the top polarizer, as seen in Figure 4.4 b), will be achieved. In that state of compensation, the free layer will again be the layer with the least stability thus having a switchable magnetization.

First, we evaluate the Zeeman field required to overcome the energy barrier for the three elements during the setting operation, when the three layers are oriented parallel as depicted in Figure 4.5 a. In this case, it is required that the top polarizer can be switched without switching the bottom polarizer. Figure 4.4 b shows the Zeeman field required to overcome the energy barrier to switch the upper or bottom polarizer (since both are Co), as a function of thickness and diameter. The stray field of the neighboring free layer is also taken into account. A field difference of 25mT can be found at low diameters, such as 10 nm, for the case of setting the bottom polarizer thickness to 40 nm and reducing the top polarizer to 30 nm, as seen in Figure 4.5 b. This difference should be sufficient to establish the antiparallel configuration. However, larger thresholds can be achieved by increasing the thickness of the top polarizer, as seen in Figure 4.5 c, from red to blue. Figure 4.5 c shows the field difference as a function of MTJ diameter for a fixed 30 nm thick top polarizer and a variable thickness bottom polarizer. The difference can be increased from 25 mT to 40 mT by increasing the thickness of the bottom polarizer from 40 nm (red line) to 50 nm (orange line). Furthermore, as explained above, such an increase in thickness of the bottom layer would not have a large effect on the stray field compensation, as seen in Figure 4.4 b. However, the main reason why we decided to maintain a smaller margin is that the total thickness of the pillar should not be too large, in order to facilitate the manufacturing process.

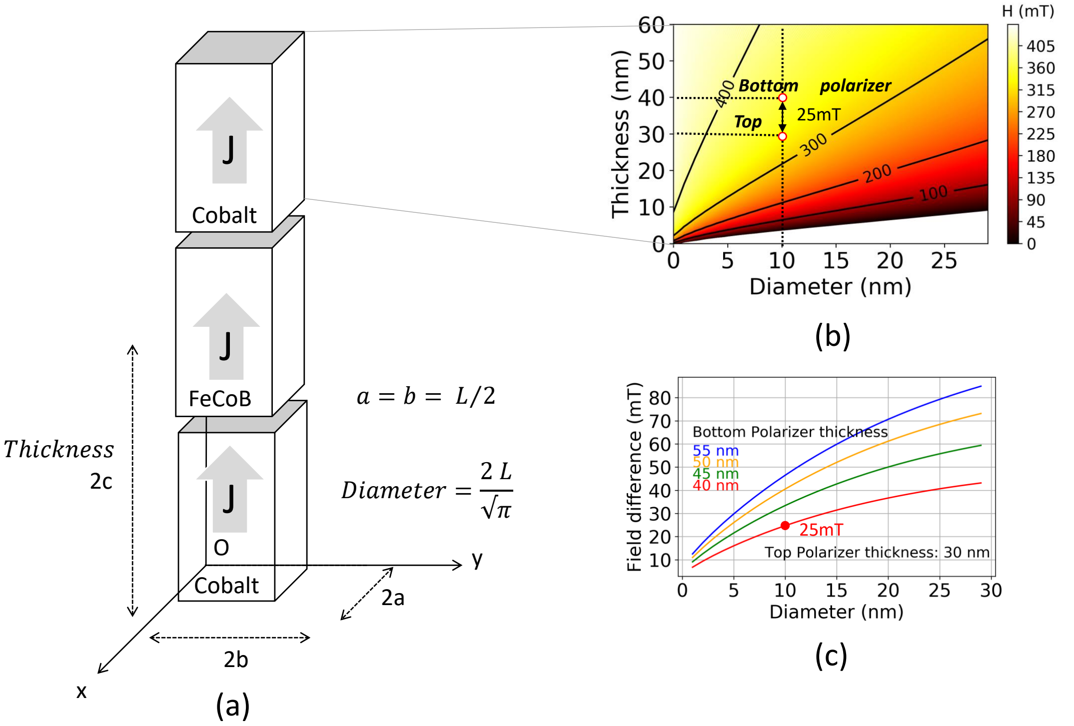

Fig. 4.5: Schematic of the magnetic elements of the system (a). Zeeman field required to overcome the energy barrier of the polarizing elements as a function of their thickness and diameter (b). The diagram of (b) is identical for both lower and top polarizers, since the stray field of the storage layer is the same. Difference of the critical fields between both polarizers, as a function of the thickness of the bottom polarizer, for a constant thickness of the top polarizer of 30 nm (c).

Once the top polarizer has been set antiparallel to the bottom polarizer, as shown in Figure 4.6 a, we evaluate the Zeeman fields for the top polarizer and the free layer, again taking into account the stray field contributions of each component.

In the operating mode, there are two possible settings for the bottom polarizer, the free layer and the top polarizer, respectively: ↑/↑/↓ and ↑/↓/↓. Between the two configurations, only the free layer element should change its orientation. Therefore, the challenge is to switch the free layer element without switching the top polarizer, which is the less stable of the two polarizers. The first configuration is the most critical, since the top polarizer, which we have chosen to be the polarizer with smaller stability, is antiparallel to the free layer. In such an antiparallel configuration, its thermal stability is reduced due to the stray field from the free layer. In the second configuration, ↑/↓/↓, it is the bottom polarizer that is subjected to the opposing stray field of the free layer, disfavouring its ‘up’ configuration. However, the magnitude of this stray field in the bottom polarizer will be identical to that of the first configuration in the top polarizer. This means that if in the first case, the top polarizer was stable enough during the operation of the free layer, the bottom polarizer will also be stable in the second case. An evaluation of the fields for the top polarizer in Figure 4.6 b and the free layer in Figure 4.6 c, show us that for 10 nm diameter, if we keep a free layer thickness of 20 nm (I) and a top polarizer thickness of 30 nm, a difference of 65 mT can be obtained. This difference should be sufficient to switch the free layer magnetization without affecting the top polarizer. In addition, during the write operation, the free layer element will be subjected to a double STT effect from both MgO barriers, while the top polarizing element will only be subjected to STT from electrons passing through the second oxide barrier. Therefore, the torque exerted on the free layer must be substantially higher, ensuring a wide operating range.

Another possible strategy to increase the margin between the stability of the free layer and the stability of the top polarizer is to create a free layer with a larger diameter than that of the polarizers, its anisotropy being decreased, but still large enough to remain perpendicular. It is observed in Figure 4.6 c that by increasing the diameter of the free layer by 10 nm, the margin increases by 100 mT.

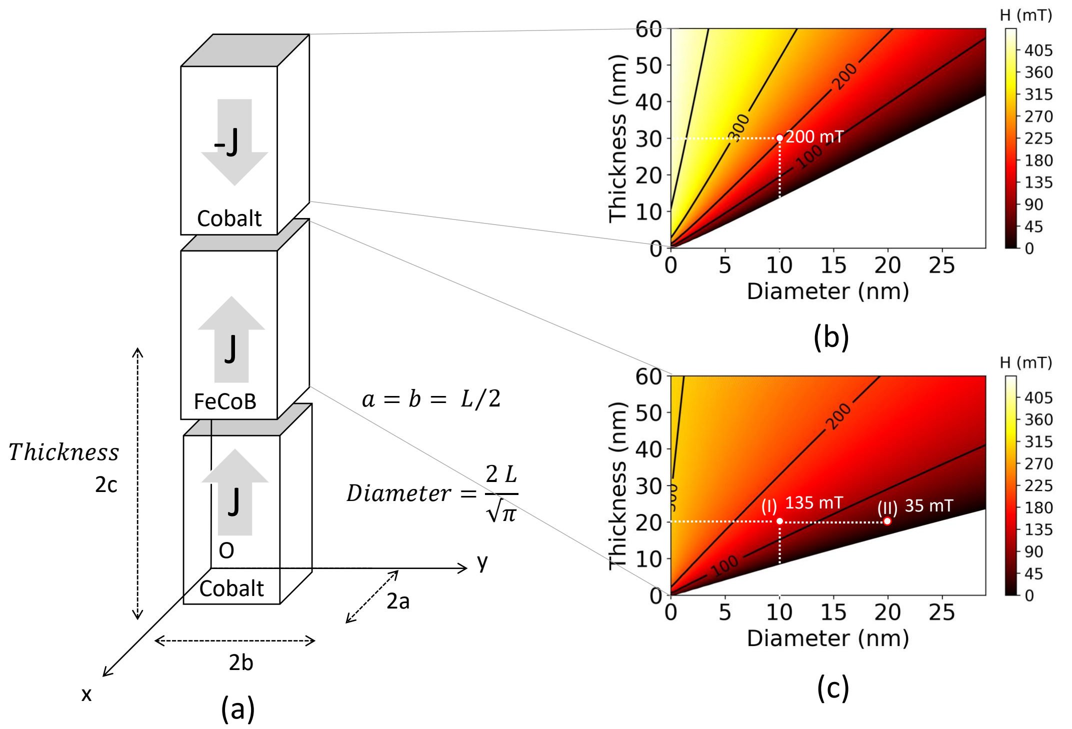

Fig. 4.6: Schematic of the magnetic elements of the system (a). Zeeman field required to overcome the energy barrier of the polarizing elements as a function of their thickness and diameter (b). Zeeman field required to overcome the energy barrier of the free layer element as a function of its thickness and diameter (c).

In the next section, we show electron holography results of this structure with a free layer of elongated diameter.

We conclude in this section that a system made of Co 40 nm / FeCoB 20 nm / Co 30 nm, where the thickness of each layer is indicated, could be an optimal candidate for the fabrication of the All-PSA-STT-MRAM.

Macroscopic calculation of the stray field distribution from the polarizers

We have seen that the total stray field in the free layer element can be compensated by using a reference layer and an oppositely magnetized top polarizer with the same saturation magnetization, as in Figure 4.4 a.

However, the amplitude of the stray field varies largely in space, as seen in Figure 4.7 for the case of a magnetic element 10 nm in diameter and 40 nm thick, schematically depicted in Figure 4.7 a. Figure 4.7 b shows the resulting y-component of the stray field, while Figure 4.7 c shows the z-component.

It is observed that the stray field is very large near the interface but strongly decreases in space. In addition, the horizontal (y) component of the demagnetizing field is strong at the edges of the body, which stabilizes what is known as the micromagnetic "flower state" in elongated bodies [186, 187]. Consequently, the magnetization, which is aligned towards the long axis of the element, is slightly inclined radially towards the edges in the upper and lower regions.

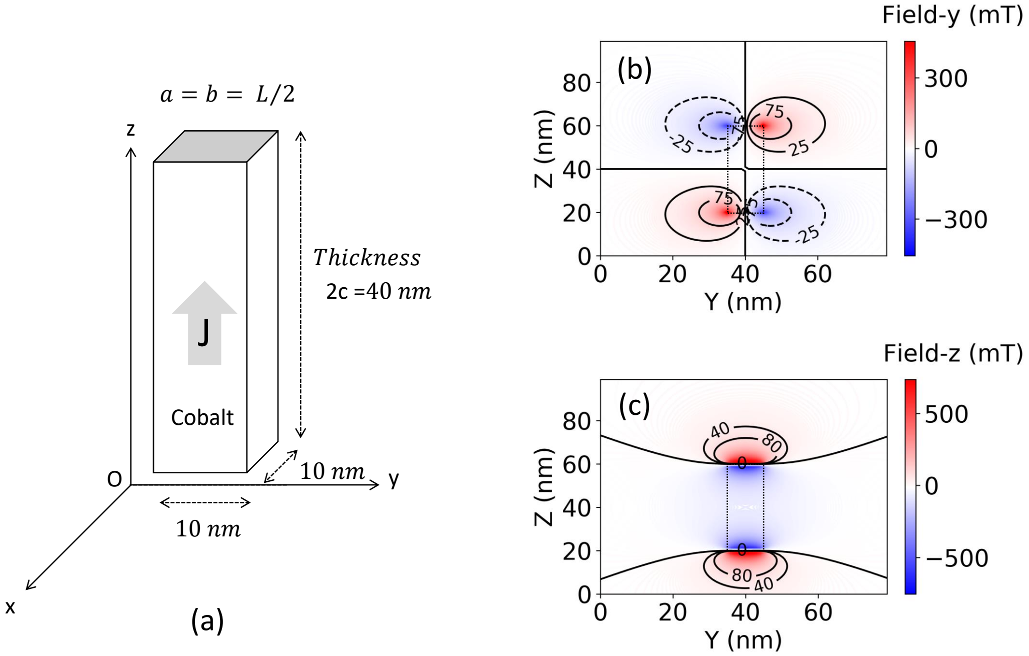

Fig. 4.7: Schematic view of a perpendicularly magnetized ferromagnetic element. The distributions of H_y and H_z in a plane at the center of the element, x=0, are shown in (b) and (c), respectively.

When two oppositely magnetized elements are facing each other, as in Figure 4.8 a, and in the case of the All-PSA-STT-MRAM, the stray field increases the 'flower state', due to the local stray field distribution shown in Figure 4.8 b. The amplitude of the lateral stray field is observed to increase at the antiparallel interface (at Z=60 nm).

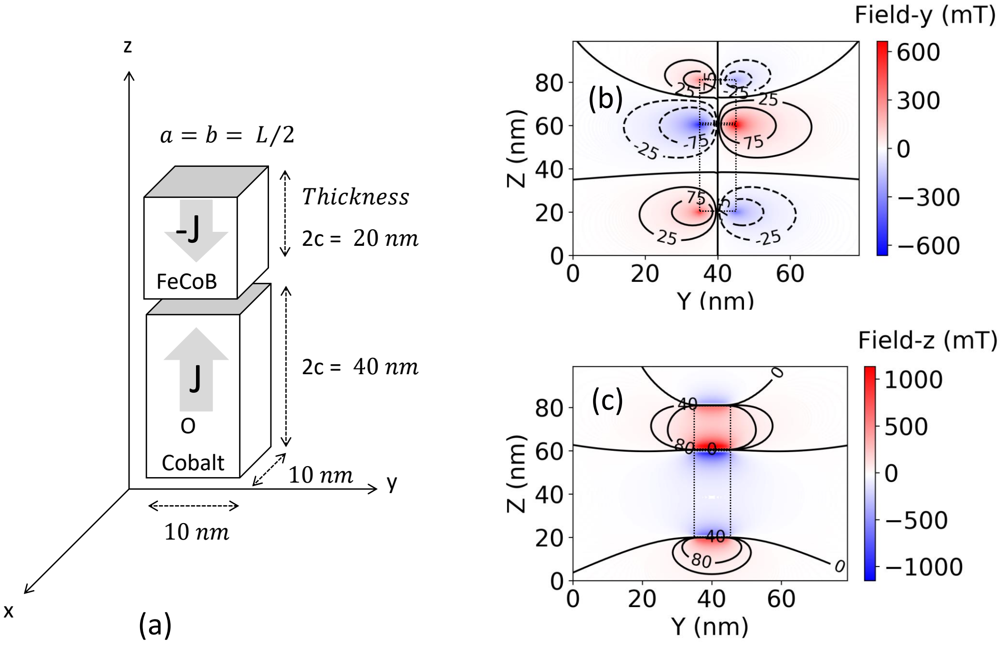

Fig. 4.8: Schematic view of two perpendicularly magnetized ferromagnetic elements with antiparallel orientations. The distributions of H_y and H_z on a plane at the center of the element, x=0, are (b) and (c), respectively.

Consequently, it is interesting to perform a micromagnetic study on the importance of such an enhancement of the flower state. In the next section, the influence of such magnetostatic interaction during the switching of two facing PSA elements is studied in comparison with a single element in which there is no stray field acting on it.

4.2.2 Micromagnetic simulations: influence of magnetization distorsions on switching time

Micromagnetic simulations were performed using MuMax3 [188]. It allows the calculation of space and time-dependent magnetization dynamics in nanometer-sized ferromagnets using a finite difference discretization.

Relaxation: flower state enhancement at the AP interface

First, we observe an increase in the flower state magnetization distortion when two PSA elements, with Ms = 1MA/m and exchange stiffness coefficient A_{ex}= 10 pJ/m, face each other in an antiparallel configuration as seen in Figure 4.9 a, in the relaxed state. The damping is set to α=1 during the relaxation process.

Figure 4.9 a shows a snapshot of the micromagnetic configuration of the two 20 nm thick and 10 nm diameter magnetic elements in antiparallel configuration. During the simulation, the magnetization evolution is observed in three different 2 nm thick regions of the bottom element (with Mz>0): the upper antiparallel interface (blue box), the central region (green box) and the bottom region (orange box).

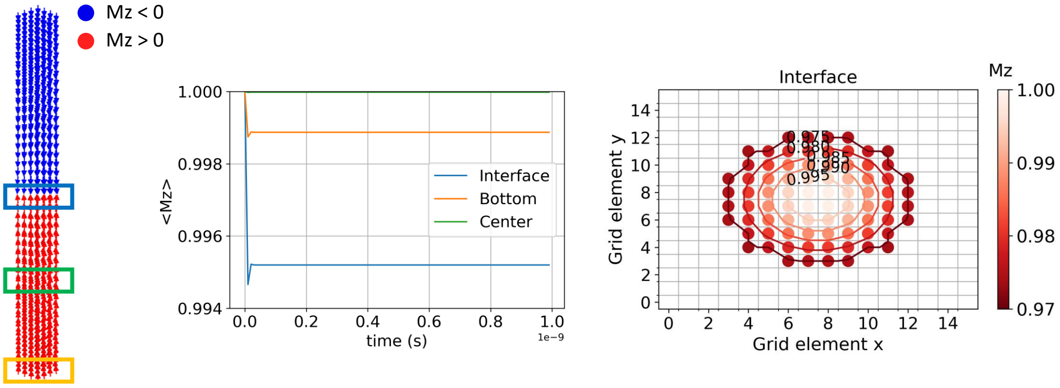

(a) (b) (c)

Fig. 4.9: Micromagnetic configuration of two ferromagnetic elements 10 nm in diameter and 20 nm thick in an antiparallel configuration. The insets indicate a 2 nm thick region of the bottom element (with Mz>0) on the top surface (blue), the intermediate region (green) and the bottom region (orange) (a). The corresponding perpendicular magnetization value, Mz, of those regions, during the relaxation process, from an initial state in which the ferromagnetic element is set with Mz=1, is shown (b). Mz distribution of the elementary cells corresponding to the upper interface shown in (a) as a blue box (c).

Figure 4.9 b shows the $\mathrm{M_z}$ value of the three different regions described above, top (blue line), middle (green line) and bottom (orange line), during the relaxation process. It can be seen how the value of $\mathrm{M_z}$ is reduced at the AP interface (blue), due to the stray field of the upper element, which enhances the flower state compared to the lower region (orange).

Figure 4.9 c shows the $\mathrm{M_z}$ value of each individual cell of 1 nm size in x and y, of the interfacial region. It can be seen how the value of $\mathrm{M_z}$ decreases radially.

The typical flower state observed in elongated magnetic elements is enhanced at the interface between the two magnetic bodies due to the magnetostatic interactions between the two elements, as seen above in Figure 4.8.

Switching dynamics under magnetic field: PSA vs All-PSA-MTJ

We performed micromagnetic simulations of the reversal of a 20 nm thick, 10 nm diameter PSA storage layer element, and for the MTJ All-PSA case, with and without the effect of interfacial anisotropy. Figure 4.10 a shows the evolution of the magnetization M_z of the three different regions of the free layer element, as described above (blue-top, green-middle and orange-bottom), under a step of applied field of 1T in the opposite direction to the free layer magnetization. For the All-PSA-MTJ case, we set the saturation magnetization of the upper and bottom polarizers at 1.4 MA/m as for Co and the Ms of the free layer at 1MA/m. In addition, we use the thicknesses previously calculated in Section 4.2.1: 40 nm / 20 nm / 30 nm, for the reference, free layer and top polarizer respectively. The exchange stiffness coefficient is still A_{ex}= 10 pJ/m but the damping is set to α=0.1 for the observation of the switching dynamics. For the case of including the interfacial anisotropy, the constant $K_s = 1.4mJm^{-2}$ for both interfaces.

Figure 4.10 a shows that for the case of the free PSA layer alone, the time to start reversing the magnetic layer is longer.

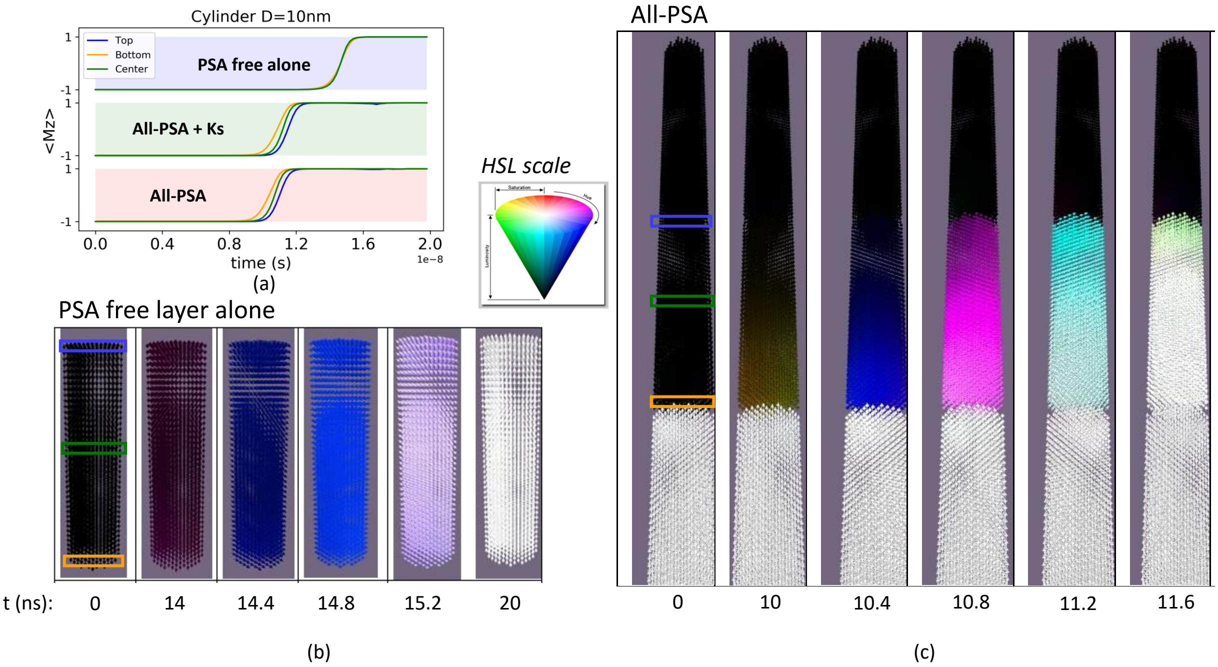

Fig. 4.10: Evolution of Mz with time under a step of applied external field of 1T in the positive z-direction, for the three different 2 nm thick regions: top (blue line), middle (green line) and bottom (orange line) of the PSA free layer for the case of a single PSA element, or the All-PSA structure with and without surface anisotropy at the bottom and top interfaces (a). The PSA free layer has D= 10 nm and t = 20 nm. Snapshots of the magnetization of the single PSA free layer during the reversal process (b). Snapshots of the magnetization during the reversal process for the All-PSA-STT-MRAM (c). We use an HSL color scale for which black (white) represents the magnetization aligned in the direction of the negative (positive) longitudinal axis.

For the case of All-PSA MTJ, the nucleation of the reversal takes place earlier, making even the effect of interfacial anisotropy negligible. Moreover, the reversal starts at the AP interface, as seen in the orange line in Figure 4.10 a and finally at the top interface, where the free layer configuration is parallel to the top polarizer. The reversal order is determined by the initial flower state magnetization distortion, as seen in 4.11. An enhanced flower state triggers a faster magnetization reversal. For the case of the All-PSA-MTJ, the flower state is enhanced at the AP interface (lower region of the free layer, represented by an inverted triangle), while it decreases at the parallel interface (upper region, upper triangle).

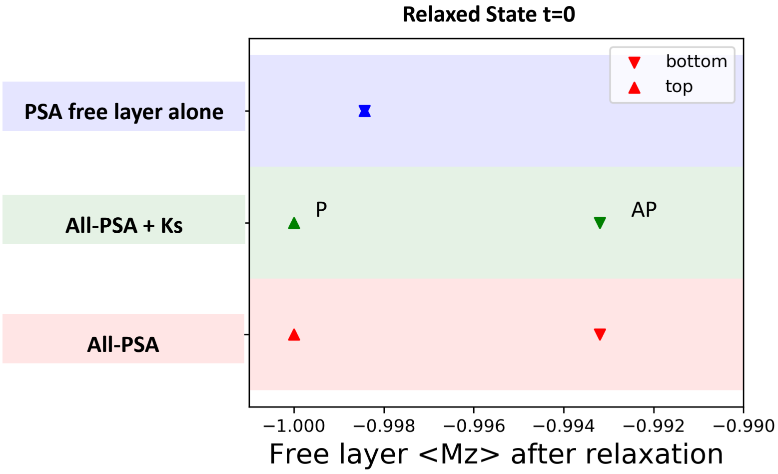

Fig. 4.11: Mz value of the upper (△) and lower (▽) 2 nm thick region, depicted in Figure 4.10 b and c (blue and orange boxes), for the case of PSA alone and the All-PSA structure, respectively.

We have seen that the use of two antiparallel oriented polarizers can be beneficial for the switching dynamics of the free layer element. However, the growth of the MgO barrier over a reference layer element of PSA thickness can give rise to an effect known as Neel coupling. In the next section, we explain the origin of such an effect and investigate how to avoid its presence in All-PSA-MTJs.

4.2.3 Neel coupling reduction due to the insertion of Ta laminations

A magnetostatic interlayer coupling, known as Neel coupling[3], arises between ferromagnetic layers separated by a thin spacer layer in the presence of a correlated roughness [189, 190]. Figure 4.12 shows a representation of such interlayer coupling.

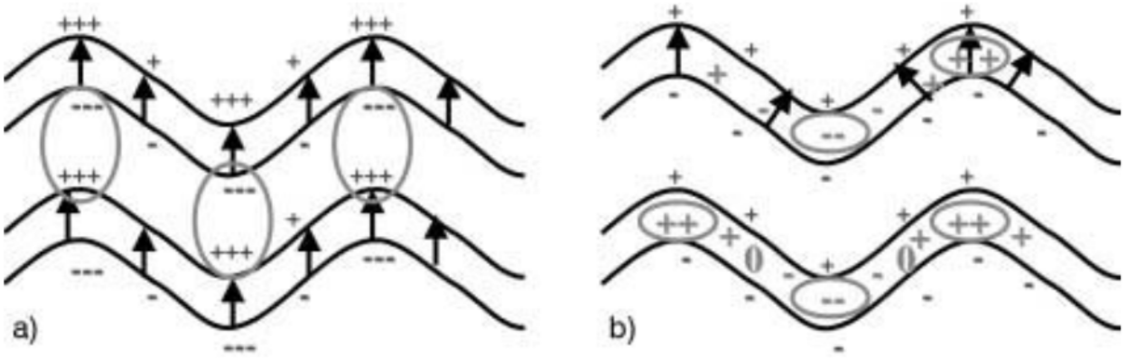

Fig. 4.12: Representative image of the configuration of magnetic moments in an MTJ with interface waviness, in the case of low anisotropy (a) and large anisotropy (b) From Moritz et al. [190]

In thick layers such large roughness can appear and it is often caused by grain growth. The resulting Neel coupling is undesirable if it exists between the reference layer and the free layer of the All-PSA-MTJ structure, as it will affect the switching of the free layer, favoring one particular orientation.

To limit grain growth, we proposed a solution based on laminating the thick reference layer with thin Ta laminations that stop grain growth [191]. Several samples were prepared with one or more Ta laminations in thick ferromagnetic (FM) layers of crystalline Co or amorphous FeCoB in MTJs of the form: Ta 3nm / FM (Co or FeCoB 20nm) / Ta 0.2nm / FeCoB 2.5nm / MgO 1.2nm / FeCoB 2.5 nm / Ta 0.2nm / Co 2nm / IrMn 8 nm / Pt 2 nm. The interlayer coupling across the MgO barrier was measured to observe the effect of varying the number of Ta insertions.

Figure 4.13 a shows the initial structure in which a Ta buffer is first deposited, followed by the 20 nm FM PSA layer and a 0.2 nm Ta lamination that is required prior to the FeCoB layer interfacial with the MgO barrier, as explained during the introductory Chapter 1.2, to break the texture of the bottom layer and absorb the boron that migrates out of the FeCoB layer upon annealing. In the other samples, a higher number of laminations was used, with a maximum of 4 laminations as in Figure 4.13 j, but always maintaining the same total FM element thickness of 20 nm.

Atomic force microscopy (AFM) measurements show that in all cases the RMS roughness increases between the as-deposited state (Figure 4.13 b-e) and, the annealed state (Figure 4.13 f-i). However, for the case of Co, the lowest roughness is observed for the case of four Ta insertions. A decrease in roughness is observed with the number of laminations, as depicted in Figure 4.14 a, along with the results in a FeCoB FM layer. For the case of FeCoB, the RMS roughness did not show a decrease with increasing Ta laminations after the annealing process. This trend could be explained by the amorphous nature of FeCoB, as its crystallinity arises after the annealing process.

---

[3] Also known as orange peel coupling.

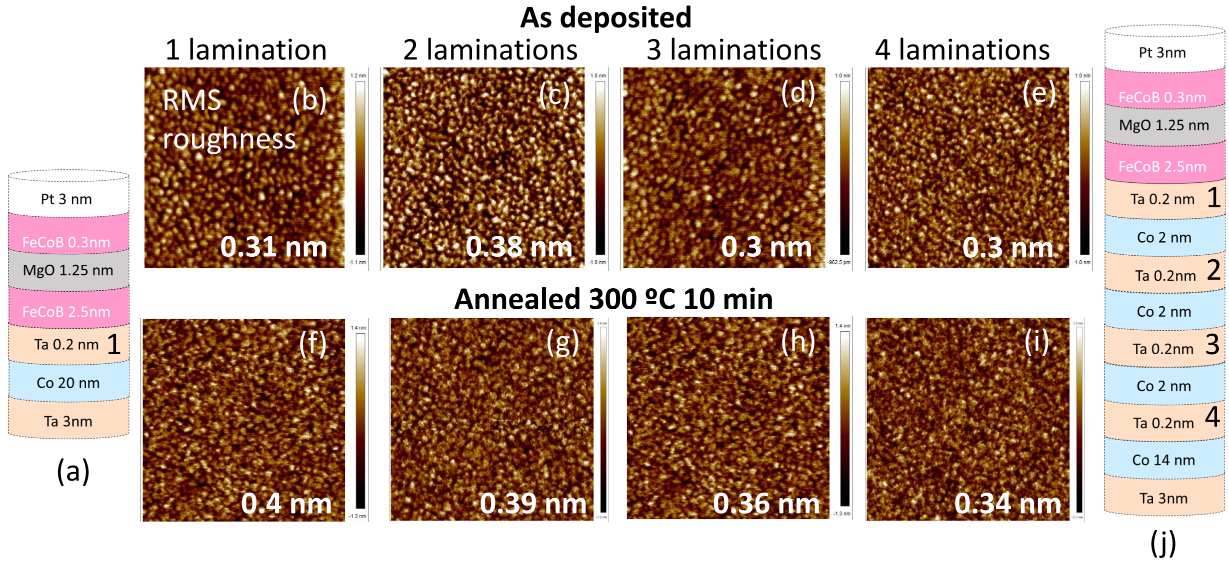

Fig. 4.13: AFM measurements of RMS roughness for samples with a variable number of Ta texture-breaking laminations, from one as represented in (a) to four (j) in the thick Co PSA layer, for the as-deposited state (b,c,d,e) and after annealing at 300°C for 10 minutes (f,g,h,i).

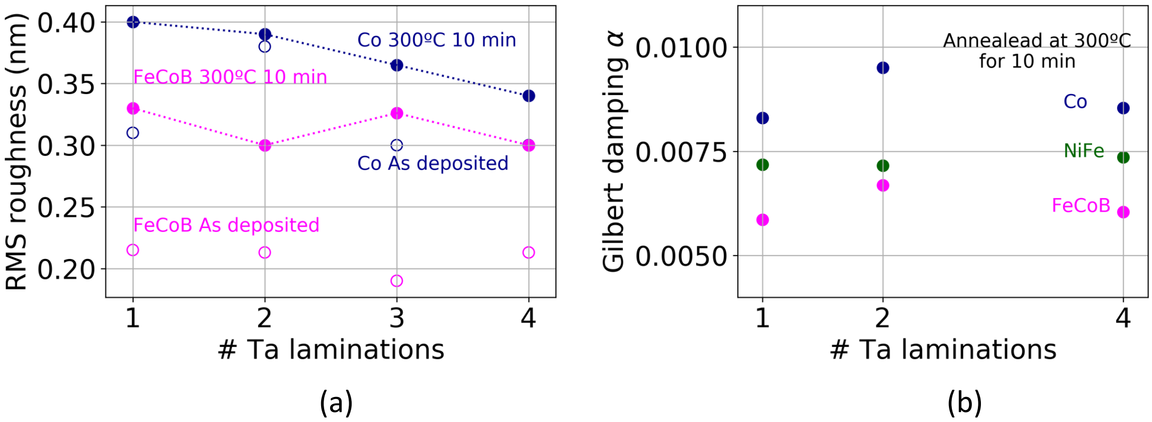

Fig. 4.14: AFM measurements of RMS roughness for samples with varying number of Ta texture-breaking laminations in the thick PSA layer, for the deposited state (open circles) and after annealing at 300°C for 10 min (filled circles) (a). Gilbert damping measured by ferromagnetic resonance (VNA-FMR) as a function of the number of Ta laminations for Co (blue), FeCoB (magenta) and NiFe (green) after annealing at 300°C for 10 min (b).

Another important factor to consider when introducing Ta insertions is the Gilbert damping, α. As spin-orbital coupling is more pronounced in heavy elements such as Ta, damping is expected to increase with the content of Ta diluted in the FM layer affecting the switching dynamics.

As can be observed from the LLG Equation 4.9 for the magnetization dynamics, the increase in the damping α has an effect on the relaxation term.

$$\frac{\partial \vec{m}}{\partial t} = -\mu_0 \gamma \vec{m} \times \vec{H}_{eff} - \alpha \mu_0 \gamma \vec{m} \times (\vec{m} \times \vec{H}_{eff}) \tag{4.9}$$

In addition, an increase in damping leads to an increase in the critical switching current I_{C0}, as seen in the Equation 4.10, in the macrospin approximation [75]:

$$I_{C0} = \frac{4 \cdot e}{\hbar} \frac{\alpha \cdot k_B \cdot T}{\eta} \Delta \tag{4.10}$$

where η is the amplitude of the spin polarization, $\hbar$ is the reduced Plank constant, k_B is the Boltzmann's constant, and T is the absolute temperature.

A higher α could increase the stability of the reference layer. However, we intend to laminate also the PSA free layer to avoid Neel coupling across the second MgO barrier, between the top polarizer and the free layer. Therefore, an increase of α is not desirable, as it would increase the critical switching current of the free layer.

The experimentally measured damping values by VNA-FMR in Figure 4.14 b shows that there is not direct relationship between α and the number of Ta laminations. Damping values of about α =0.006 were obtained, similar to those of Sabino et al. [192] for a p-MTJ with double MgO and a 0.3 nm Ta insertion in a FeCoB-free layer. Sabino et al. [192] observed that for MTJs with double MgO layers, the damping tends to increase with the number of Ta laminations, with α around 0.006 for one lamination to 0.008 with two Ta laminations. However, in their case, a thin free FeCoB layer with a maximum thickness of 2.5 nm was used. They also observed a decrease in α with increasing t_{eff}, effective thickness. This observation could explain the fact that in our case we did not observe an increase in α with the number of insertions, due to the large thickness of the ferromagnetic material used in our study. Since the ratio of ferromagnetic material to tantalum is an order of magnitude larger in our case, the effect of Ta inserts on damping could be negligible.

In addition, we performed Vibrating-sample-magnetometer (VSM) measurements to check the interlayer coupling with the introduction of Ta laminations (0.2 nm) into the thick FM layer.

The structure of the samples studied was as follows:

- S1: Ta 3nm/**(Co or FeCoB 20nm)/Ta 0.2nm/FeCoB 2.5nm** /MgO 1.2nm/FeCoB 2.5 nm/ Ta 0.2nm/ Co 2nm/IrMn 8 nm/Pt 2 nm. As in Figure 4.15 c.
- S2 : Ta 3nm/**FM (Co or FeCoB 18nm)/Ta 0.2nm/FM 2nm/Ta0.2nm/FeCoB 2.5nm** /MgO 1.2nm/FeCoB 2.5 nm/ Ta 0.2nm/ Co 2nm/IrMn 8 nm/Pt 2 nm. As in Figure 4.15 d.
- S3 : Ta 3nm/**FM (Co or FeCoB 14nm)/3x(Ta 0.2nm/FM 2nm)/Ta0.2nm/FeCoB 2.5nm** /MgO 1.2nm/FeCoB 2.5 nm/ Ta 0.2nm/ Co 2nm/IrMn 8 nm/Pt 2 nm. As in Figure 4.15 e.

All samples were annealed at 300°C for 30 minutes under an applied external field of 3kOe in an in-plane direction to establish the direction of magnetization of the antiferromagnetic IrMn layer.

As a result, an exchange bias appears in the upper Co 2nm layer interfacial with IrMn, as the -90 Oe observed in the blue curve of Figure 4.15 a. The loop with the largest magnetization amplitude, closer to H=0 corresponds to the PSA layer below the MgO tunneling barrier. In the absence of interlayer coupling, this loop should be center at zero field. Nonetheless, it is observed how for the case of 1 lamination (black line), it is shifted to negative field values. Nonetheless, this shift is decreased by increasing the number of Ta laminations, which indicates a reduction of the interlayer coupling.

Figure 4.15 a also shows that the exchange bias decreases when fewer laminations are used, indicating increased interlayer coupling (or Neel coupling) across the MgO barrier due to higher roughness.

Similarly, for the FeCoB case, a reduction of the shift of the PSA hysteresis loop and a increase in the exchange bias in the Co layer hysteresis loop is observed in Figure 4.15 b, from 1 to 4 Ta laminations.

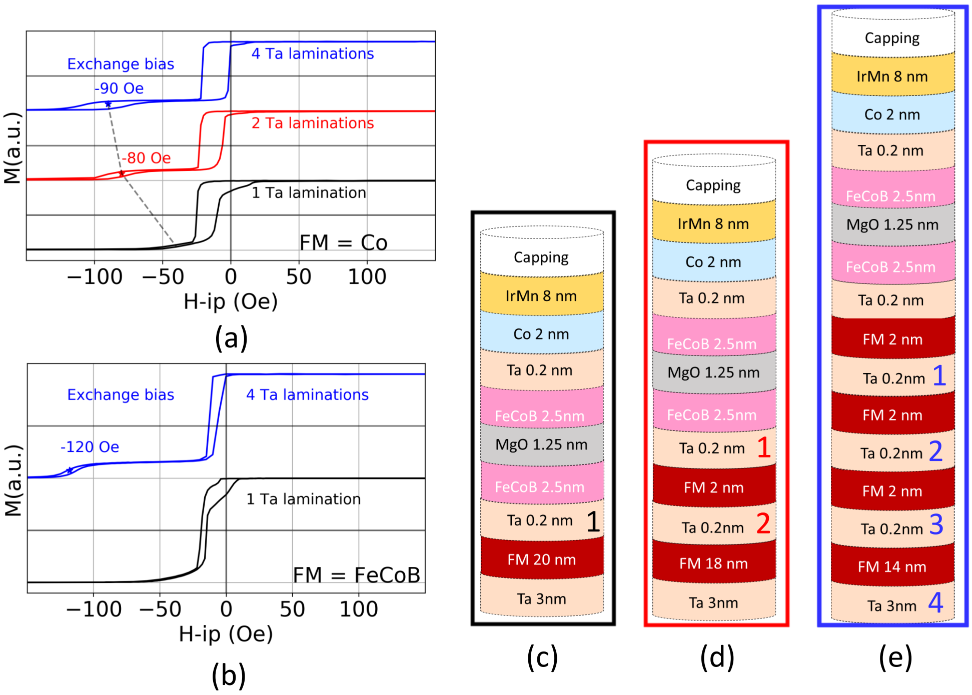

Fig. 4.15: VSM measurements of three stacks with 1 (black) Ta texture break lamination as shown in (b), 2 (red) as shown in c and 4 as in c (blue) in the PSA layer respectively (a).

As a conclusion, it is shown that the insertion of Ta laminations into the thick PSA reference thick layer of the All-PSA-STT-MRAM can help to reduce a possible orange peel coupling through the tunneling barrier. In addition, the laminations can also be used for the storage layer to avoid Neel coupling with the top polarizer, as we have seen that Gilbert damping is not affected by the introduction of thin Ta laminations.

4.3 Fabrication of PSA-STT-MRAM at small nodes

In Chapter 3, we explained the whole fabrication process of MTJs. However, for the case of PSA-MTJs, an additional challenge is to pattern MTJs at small diameters below 20 nm.

To reduce the diameter of the MTJs after the etching process, ion milling is performed at grazing incidence (10° with respect to the wafer plane).

During the IBE process, the substrate is rotated at 20 rpm to ensure the homogeneity of the trimming. Figure 4.16 a-c shows a schematic of the process, which is usually performed in several steps.

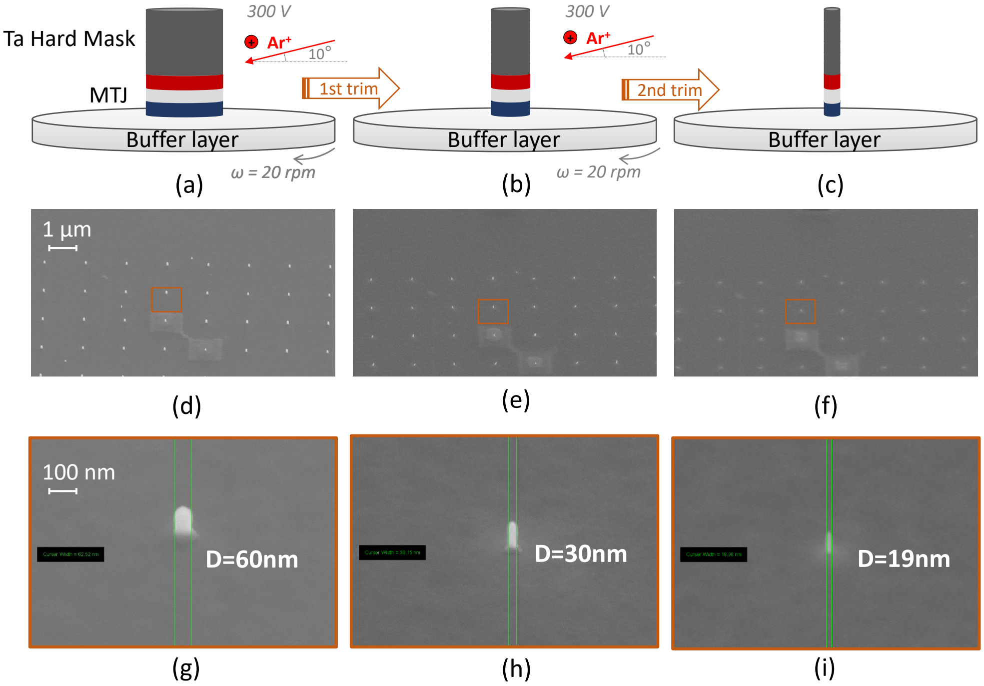

Fig. 4.16: Schematic of a PSA-STT-MRAM MTJ cell before trimming by IBE at grazing incidence (10°) (a) after a first trimming (b) and a second trimming at diameters sub 20 nm (c), with respective SEM observations for several MTJs (d-f) and individual MTJs (g-i) respectively.

Figures 4.16 d-f show an array of control MTJs used for observation after the etching process.

As seen in Figure 4.16 g, the initial diameter after IBE, can be relatively large, such as 60 nm (even 100 nm observed, if the free layer thickness is large), and contains the redepositions that arise after the MTJ IBE process. Therefore, a lateral trimming is performed that allows to remove redepositions and further reduce the diameter of the MTJ to the target of less than 20 nm, as in Figure 4.16 i.

Trimming is performed in several steps to have a better control of the etching speed, as the plasma conditions are usually not identical.

Using this procedure, we were able to fabricate ultra-small pillars like the one in Figure 4.17 a, only 10 nm in diameter.

Figure 4.17 a shows a MTJ with an 11 nm thick FeCoB PSA free layer, in which we inserted 0.2nm Ta laminations, which can be distinguished in the high-angle annular dark-field ring scanning transmission electron microscopy (HAADF-STEM) observation. In the following section, the preparation of the samples for TEM observation is explained in more details.

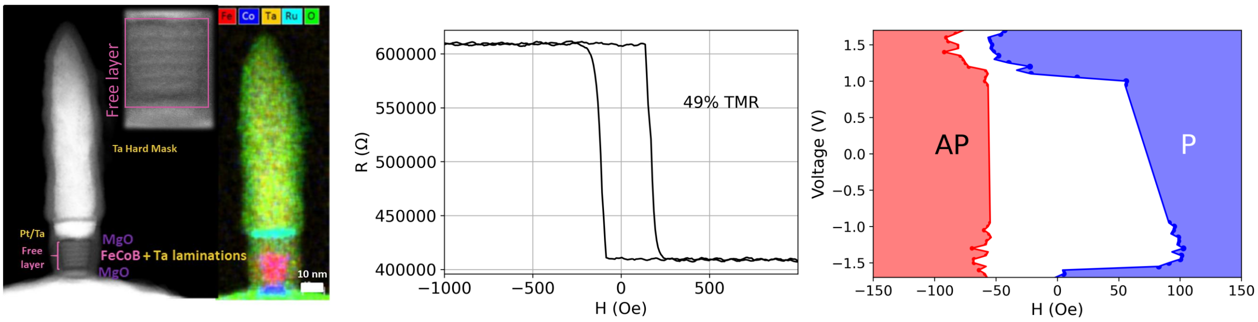

(a) (b) (c)

Fig. 4.17: HAADF (left) and EDX (right) observation of a MTJ with a free PSA FeCoB layer (in red) of 10 nm diameter (a). The inset shows a zoom of the laminated free layer element. R-H loop of a PSA-STT-MRAM device (b). Phase diagram of the switching of a PSA-STT-MRAM device (c).

Figure 4.17 b shows a R-H loop of a sample with the structure of Figure 4.17 a, with a free PSA layer laminated FeCoB and a conventional SAF structure in the reference layer. Figure 4.17 c shows the (H,V) stability diagram of this structure. STT switching is observed in these PSA free layers, albeit at large voltage values, due to the large junction resistance.

4.4 Characterization of All-PSA-STT-MRAM

In this section, the characterization of the All-PSA-STT-MRAM is reported. First by HAADF, energy dispersive X-ray spectroscopy (EDX) and off-axis electron holography to observe the magnetization of the fabricated pillars. Finally we show the results of the electrical characterization of the nanopatterned MTJs.

4.4.1 HAADF, EDX and off-axis electron holography of the All-PSA patterned structure

We have patterned the MTJs with 3-PSA Co/FeCoB/Co layers, as indicated in the previous section. To confirm their perpendicular anisotropy, we observed these structures by off-axis electron holography. Off-axis electron holography (EH) is a technique sensitive to the phase of the electron beam passing through the sample and is therefore used to image nanoscale magnetism. The electron wave phase shift is used to provide information on local variations of magnetic induction and electrostatic potential [193].

The images shown here were taken by Dr. Trevor Almeida at CEA-LETI. TEM samples were prepared by etching the pillars using the process described in Chapter 3 and Section 4.3, followed by deposition of a protective layer (approximately 1 µm) of organic resin before deposition of a Pt protective layer by focused ion beam (FIB). Cross-sectional TEM lamellae were then transferred to Omniprobe copper slots and thinned using conventional FIB methods. The protective resin layer was removed by plasma etching and the remaining Pt layer was broken with the micromanipulator. A probe-Cs-corrected Thermo Fisher Titan TEM at 200kV was used for the STEM imaging. Off-axis electron holograms were acquired at remanescence in Lorentz mode on a Gatan OneView 4K camera using a Thermo Fisher Titan TEM equipped with an image-CS corrector and an electron biprism.

Figure 4.18 shows an energy dispersive X-ray spectroscopy (EDX) map of a pillar with such a 3-PSA layers structure. The MTJ elements can be distinguished from each other because each element has its own type of X-ray spectrum that they emit after interacting with electrons.

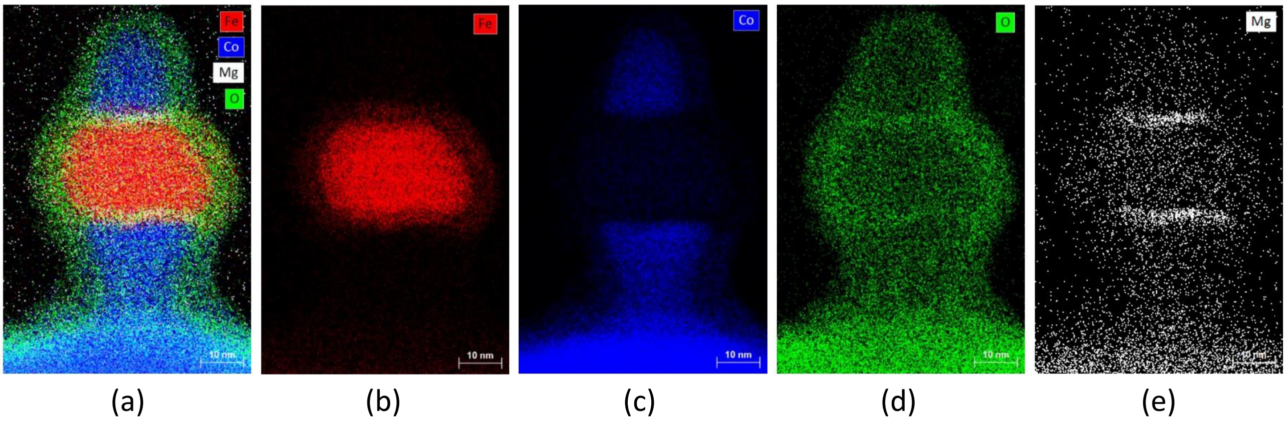

(a) (b) (c) (d) (e)

Fig. 4.18: EDX chemical maps of a MTJ with three PSA components. Iron (Fe) is indicated in red, cobalt (Co) in blue, oxygen (O) in green and magnesium (Mg) in white.

The two polarizer layers are made of cobalt, as seen in blue, in Figures 4.6 a and c. They have been etched with a reduced diameter to increase their shape anisotropy with respect to the free layer. The free layer is made of FeCoB, as seen in red in Figures 4.6 a, b. The free layer is etched with a larger diameter that would allow a larger margin during the operation process, as explained above in the discussion of Figure 4.6 c. The position of the two MgO barriers can also be seen in Figure 4.6 e. A thin oxide layer has formed around the pillar, colored green in Figures 4.6 a and d. This oxide layer is not desirable for the optimal functioning of the MRAM device, as it will increase the overall resistance. However, it is understandable since in our manufacturing process the pillars are not directly encapsulated after the ion beam etching (IBE) process. However, in state of the art tools, such encapsulation can be performed in situ after the etching process, which avoids such oxide formation. Figure 4.19 shows a High-angle annular dark-field scanning transmission electron microscopy (HAADF-STEM) image of the same MTJ. Using this technique, it is possible to identify the 0.2 nm Ta laminations that we used in order to avoid the possible Neel coupling effect as explained in Section 4.2.3. In HAADF, the intensity depends on the atomic number of the elements [194]. The Ta laminations in the free layer and reference layer show up with higher contrast due to the larger mass of these atoms.

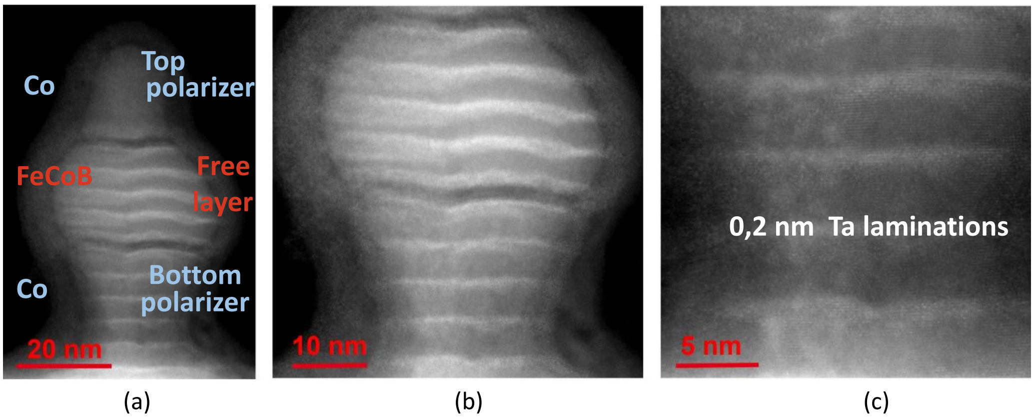

Fig. 4.19: HAADF of a MTJ with three PSA components.

Finally, observation by off-axis electron holography of the structure with three PSA layers allows us to confirm that the MTJ shows perpendicular shape anisotropy at zero field after saturation. The magnetic flux lines in yellow indicate that the magnetization is oriented in the vertical direction along the axis of the MTJ structure, and in the second case still in the same direction but in the opposite direction.

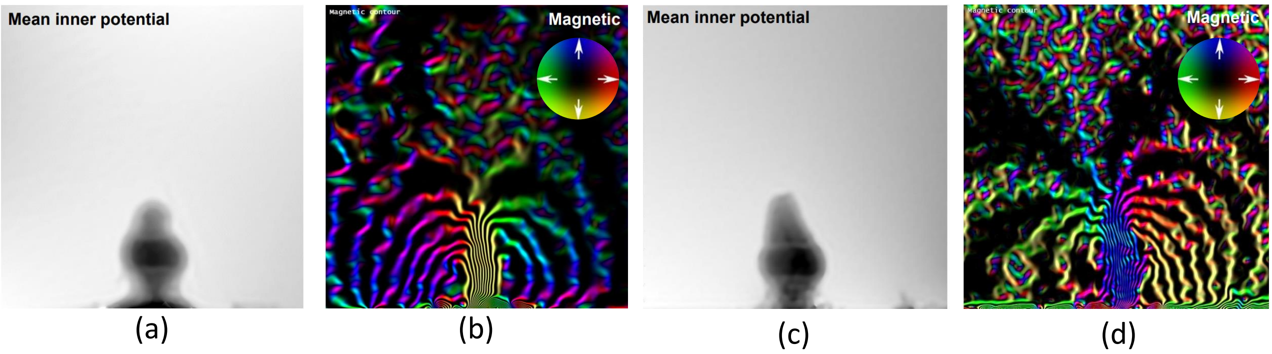

Fig. 4.20: Electron holography of a MTJ with three PSA components (Co 40nm / FeCoB 20nm / Co 30nm. Magnetic induction maps (b,d) reveal perpendicular shape anisotropy of the All-PSA structure.

These results confirm that perpendicular shape anisotropy is achieved in the All-PSA-STT-MRAM device. We continue to fabricate MTJs, now creating a top contact to proceed with their electrical characterization. The results are discussed in the next section.

4.4.2 Electrical characterization of one layer, two layers and three layers PSA devices

In Figure 4.21 a, the stack structure of the fabricated devices is shown. As explained in section 4.2.1, we fabricated the structure with the same material in the upper and bottom polarizer to achieve a better compensation of the stray field in the free layer element. The selected structure is 40 nm Co bottom polarizer / 20 nm FeCoB free layer / 30 nm Co top polarizer. In both polarizers, we have included a thin 1.2 nm FeCoB layer coupled to the PSA layer. These FeCoB layers are necessary to have good TMR and transport properties as explained in the introductory part.

As shown above in Section 4.2.3, the PSA layers are laminated with Ta insertions, as in Figure 4.19 to reduce possible Neel coupling arising between the magnetic layers.

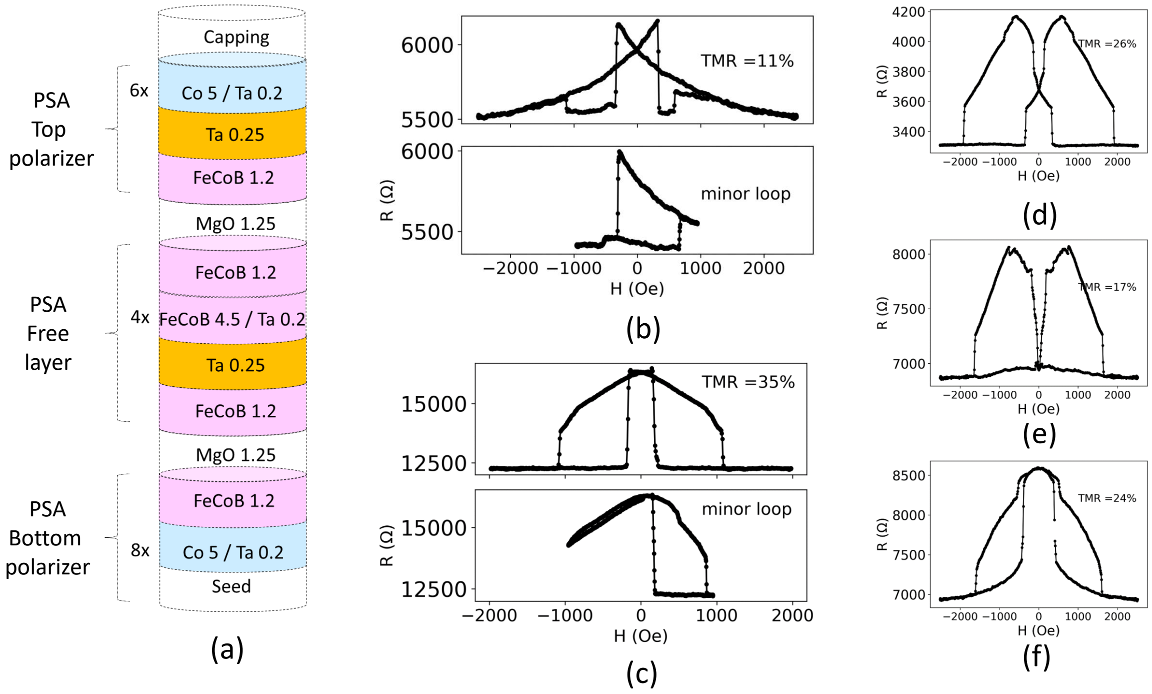

Fig. 4.21: Stack structure of the fabricated All-PSA-STT-MRAM devices (a). Different types of R-H loops obtained on the fabricated devices (b-f). The field is applied out-of-plane.

What the electrical results in Figure 4.21 b-f show is that the magnetic layers of the fabricated stack do not have a completely uniform perpendicular magnetization. It is possible that the free layer element does not exhibit sufficient perpendicular shape anisotropy. However, just the fact that the free layer exhibits in-plane magnetization does not explain the R-H response observed in Figure 4.21 b-f.

We performed micromagnetic simulations of the switching of a PSA free layer of 20 nm thickness, as the free layer used in the experimental results of Figure 4.21 a. Figure 4.22 a shows that for low diameters, D=20 nm, the reversal occurs between two uniform perpendicularly magnetized states. However, for larger diameters, D=30 nm, as in Figure 4.22 b, a micromagnetic vortex state can be formed during the reversal process.

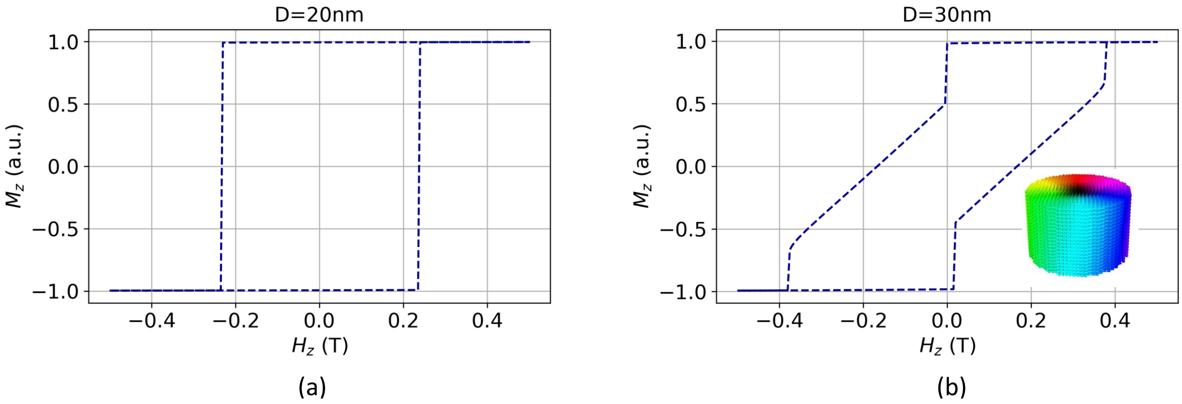

(a)

(b)

Fig. 4.22: M-H loop of a PSA free layer reversal of t=20 nm, A_{ex}=10 pJ/m, α=0.01, M_s=1MA/m, D=20 nm (a) and D= 30 nm (b) obtained by micromagnetic simulations. The field is applied out of plane. The snapshot in (b) shows a micromagnetic vortex state of the PSA free layer.

Such vortex state in one of the layers of the All-PSA structure can explain the linear R-H response observed in the devices of Figure 4.21.

Moreover, we performed micromagnetic simulations of the reversal of the All-PSA-MTJ structure. In this case we used a 40 nm thick Co (M_s=1.44 MA/m) / 20 nm FeCoB (M_s=1 MA/m) / 30 nm Co (M_s=1.44 MA/m) layers structure. The diameter used was D=30 nm.

Figure 4.23 a shows that during the reversal process, for the case of the three PSA layer structure, the reference layer and top polarizer present a vortex state at zero field. In order to mimic the R-H experimental results of Figure 4.21, we plot the product (-1) · sgn $(M_{z,free}) \cdot M_{z,ref}$. This expression can be used since in this case the free layer switches between uniformly magnetized states, so the sgn function is used, while the (-1) factor accounts for the fact that the resistance is minimal when the magnetization of the free layer and reference are oriented in a parallel configuration.

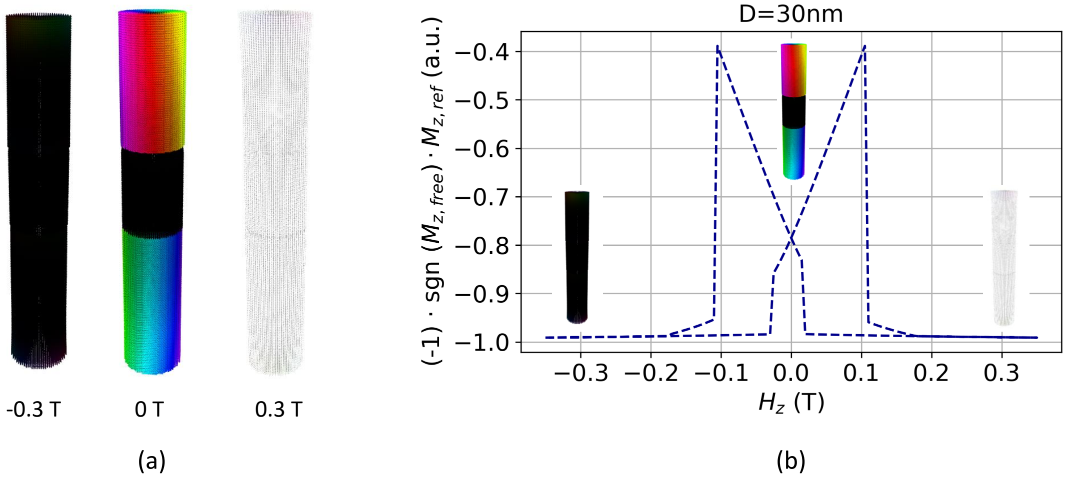

(a)

(b)

Fig. 4.23: Snapshots of the three layer structure (t in nm): Co 40nm/ FeCoB 20 nm / Co 30 nm and A_{ex}=10 pJ/m, α=0.01 D=30 nm, at different fields (a) (-1) · sgn $(M_{z,free}) \cdot M_{z,ref}$ - H loop. The field is applied out of plane. sgn is the sign function, as the free layer commutes between M_z=+1 and M_z=-1 in this case. The factor (-1) is used to mimic the resistance response.

The polarizer magnetization is omitted since during the fabrication, the $R \times A$ product of the top MgO barrier is lowered ($\approx 1\Omega\mu m^2$) so that the main resistance response is given by the bottom MgO barrier of larger $R \times A \approx 10\Omega\mu m^2$. The optimization of the $R \times A$ values can be done by varying the oxidation pressure and time during MgO deposition, as given in Appendix B.

Figure 4.23 b shows the same response as for the device in Figure 4.21 d. Similarly, the antiparallel alignment at zero field for 4.21 c and f can be explained by such vortex formation.

To simplify our analysis, we fabricated structures with only 2 PSA layers and a stack with a PSA reference layer and a conventional free layer.

The stack fabricated with a PSA polarizer layer and a PSA free layer is shown in Figure 4.24 a. R-H loops of devices with such a structure are shown in Figure 4.24 b and c. Figure 4.24 d and e, show MTJ pillars with 20 nm diameter at the bottom of the pillar where the MTJ is located, which should be sufficient to ensure PSA in the fabricated MTJ. The loop observed in Figure 4.24 b could indicate the presence of a flower state at zero field that slightly increases the resistance with respect to the values at the saturation fields, for which the flower state is overcome by the external applied field. Therefore, at low field values the first PSA layer switches, in this case the FeCoB free layer with lower thickness, followed by the reversal of the Co bottom layer at larger field values. Nonetheless, the reversal by STT does not take place, even up to large V values of more than 1V (not shown).

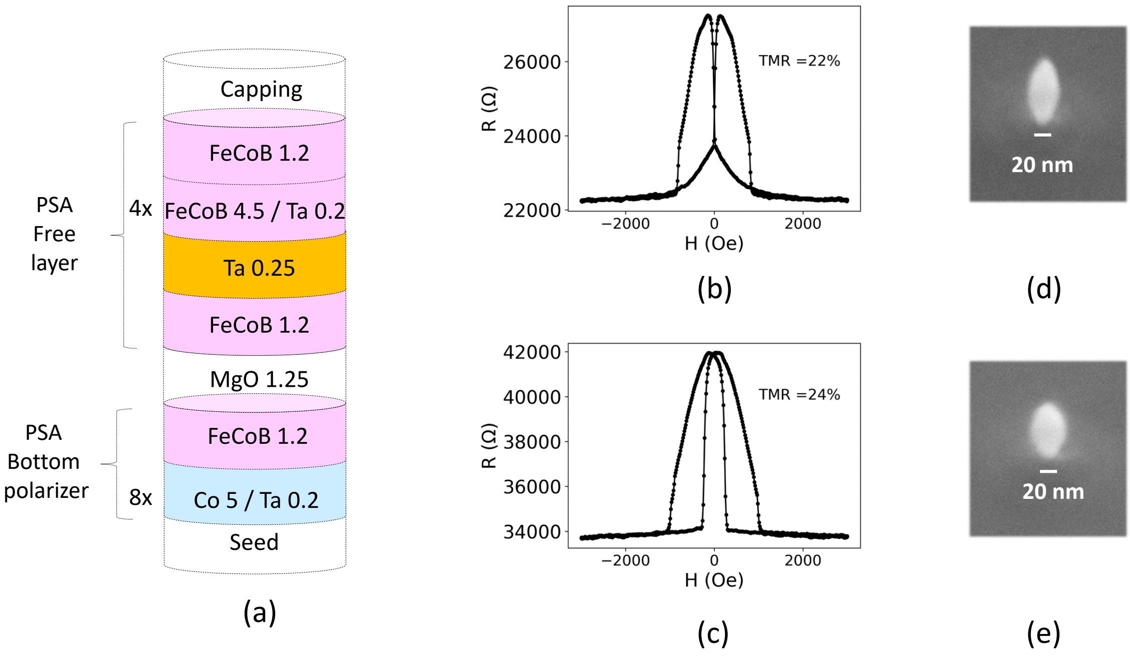

Fig. 4.24: Stack structure of the fabricated devices of the 2-PSA-STT-MRAM (a). R-H loops of patterned devices (b,c). The field is applied out-of-plane. SEM observation of the pillars after IBE and trimming down to diameters below 20 nm (d,e).

Figure 4.24 c shows a different behavior that can be understood by the previously given micromagnetic simulations that show a vortex formation in PSA layers. Indeed, in this case the large resistance state at zero field can be again explained by a vortex state in one of the layers, as in Figure 4.23.

In addition, we have fabricated MTJs with a single layer of PSA combined with a conventional free layer with i-PMA, as shown in Figure 4.25 a.

For small MTJ diameters, down to 20 nm, the PSA layer aspect ratio close to one might still stabilize a vortex state. Nonetheless, as the i-PMA free layer have a very small coercivity at this small diameters, the switching takes place at values very close to zero field, what explains the symmetric R-H response with respect to applied field observed in Figure 4.25 b. The linear response is related to the vortex magnetization reversal.

For large diameters, as shown in Figure 4.25 e, the free layer with i-PMA still retains a strong PMA, therefore, the switching takes place at larger fields as observed by the straight resistance variations in Figure 4.25 c. The 20 nm thick PSA layer stabilizes a vortex configuration at these large 50 nm diameters, as indicated by the linear response in Figure 4.25 c.

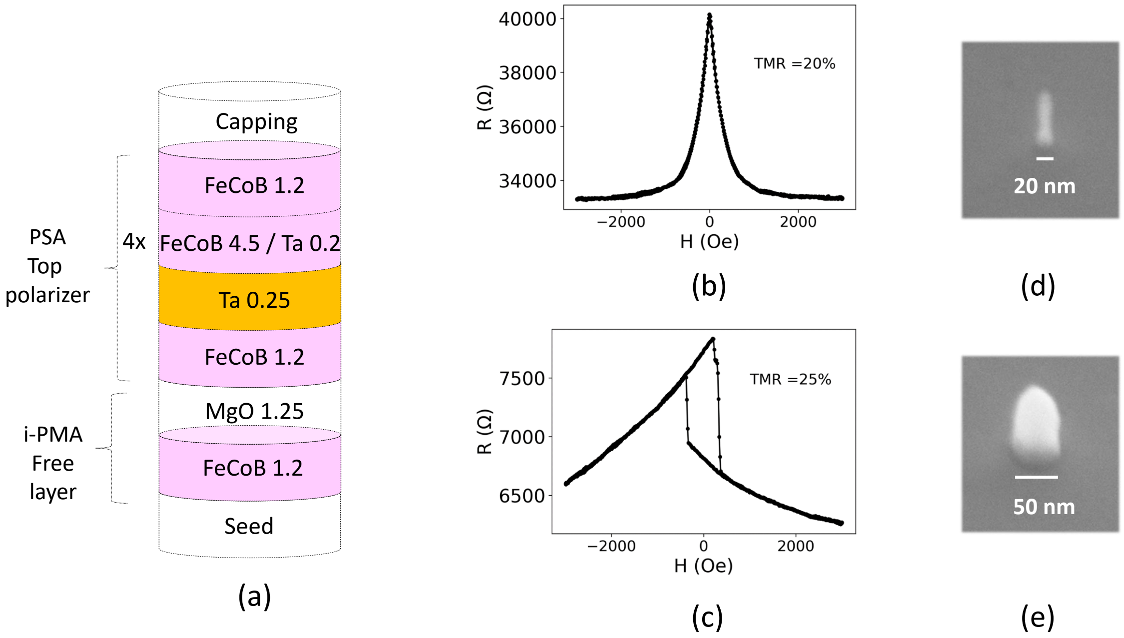

Fig. 4.25: Stack structure of devices fabricated from the 1-PSA-STT-MRAM (a). R-H loops of the patterned devices (b,c). The field is applied out-of-plane. SEM observation of the pillars after IBE and trimming down to diameters below 20 nm (d), and larger diameters where the conventional free layer should have large PMA (e).

4.5 Conclusions

In this Chapter, we have performed first macrospin simulations in order to find the optimal conditions for the fabrication of the All-PSA-STT-MRAM structure that completely avoids the use of PGMs. Micromagnetic simulations at small diameters showed that the switching dynamics can be improved in this All-PSA-STT-MRAM structure due to an enhanced flower state at the AP interfaces. In addition, we have seen that the insertion of Ta laminates can reduce a possible interlayer coupling due to correlated roughness in thick PSA layers, without affecting the Gilbert damping. Off-axis electron holography results confirm that this structure can exhibit PSA. However, during the electrical characterization of the patterned devices, a more complex response is observed which is attributed to the formation of a vortex state in some of the PSA layers. This hypothesis is confirmed by micromagnetic simulations and serves as motivation for the development of a new sensor device concept discussed in Chapter 6.

Chapter 5

Alternative sources of PMA for the reference layer of p-MRAM

In this chapter, we first investigate the possibility of reducing the number of Co/Pt multilayers in the SAF structure. In a second approach, we use Co/Ni multilayers that have the advantage of using non-critical nickel instead of platinum. As seen in Chapter 2, Ni production is much more diversified, which avoids the high supply risk of using Pt in the SAF structure. Finally, we discuss the use of a Co/Ni reference layer for stochastic computing or cybersecurity applications.

5.1 Co/Pt reduced SAF

One possibility to reduce the amount of platinum contained in the SAF of p-STT-MRAM is to make a simpler SAF. Such structure contains only Co/Pt multilayers in the lower part of the SAF. The upper structure is directly the polarizer FeCoB reference layer in contact with the tunneling barrier. With this approach, a 55% reduction in Pt usage is achieved compared to more conventional SAFs with, for example, nine Pt laminations.

5.1.1 RKKY strength as a function of Ta spacer thickness

As described previously in Chapter 1, a thin layer of Ta (or W or Mo) is usually required to break the texture of the Co/Pt multilayers and absorb the boron present in the amorphous FeCoB polarizer layer after annealing. In this section, we study the influence of the Ta spacer thickness on the coupling between the Co/Pt multilayers and the FeCoB polarizer through the composite Ru/Ta spacer layer.

The stack structure used is shown in Figure 5.1 a. An evaluation of the switching field of the reference layer as function of the Ta thickness is performed by nanoMOKE, after annealing at 300°C for 10 minutes. Figure 5.1 b shows that increasing the Ta thickness decreases the RKKY antiferromagnetic coupling through the Ru/Ta composite spacer layer between the lower SAF structure and the upper FeCoB reference layer. This decrease in RKKY coupling strength is observed especially for the 0.35nm and 0.39nm Ta thickness cases. For 0.39 nm of Ta spacer (in blue), the reference layer becomes antiparallel to the Co/Pt multilayers only at field values close to the free layer switch, as highlighted with a red circle, from negative saturation.

In addition, an increase of the reference layer switching field from 887 Oe to 1569 Oe is observed in Figure 5.1 b (dashed dots) by reducing the thickness of the Ta layer from 0.39 nm to 0.23 nm. This increase is explained by the fact that the antiferromagnetic coupling between the two SAF components through the composite Ru/Ta spacer is higher, confirming the benefit of using a thinner Ta layer.

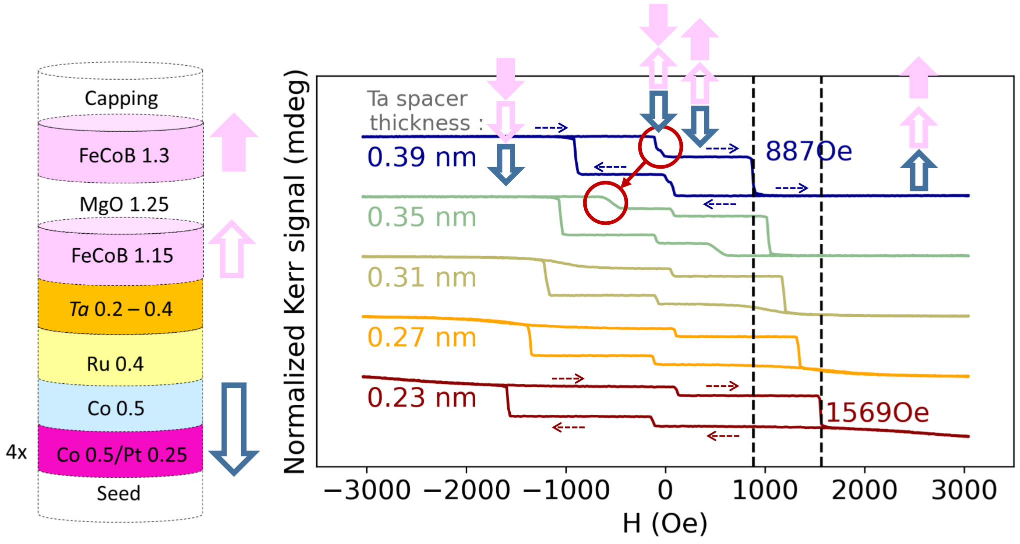

(a) (b)

Fig. 5.1: MTJ structure with a simplified SAF as reference layer (thickness in nm): Ta 25 / FeCoB 2 / Pt 3 / 4x[Co 0.5/Pt 0.25] / Co 0.5 / Ru 0.4 / Ta 0.2-0.4 / FeCoB 1.15 / MgO 1.25 / FeCoB 1.3 / Capping. The Ta spacer thickness is varied between 0.2 and 0.4nm (a). NanoMOKE hysteresis loops under external perpendicular field for different Ta spacer thicknesses (b).

5.1.2 Electrical results in patterned devices with Co/Pt reduced SAF

Once the MTJ was characterized at the thin film level, we proceeded to pattern the memory devices following the process explained in Chapter 3.

The stack structure of the devices is as follows: Ta25 / FeCoB 2 / Pt 3 / 4x[Co0.5/Pt0.25] / Co0.5 / Ru0.4 / Ta0.25 / FeCoB1.2 / MgO1.25 / FeCoB(1.0-1.7) / Capping. The stability of the reference layer was confirmed in the previous Section 5.1.1 for a thin spacer layer thickness of around 0.25 nm at thin film level.

In the sample we fabricated, we also introduced a free layer with variable thickness (1-1.7nm) to study the transition regions between in-plane and out-of-plane magnetization and maximum TMR. Characterization was performed after thermal annealing at 300°C for 10 minutes.

Prior to the nanofabrication, the NanoMOKE thin film characterization in Figure 5.2 a reveals the transition of the free layer magnetization from a paramagnetic, to an in-plane regime, passing through the out-of-plane configuration, for which the coercive field is larger.

Figure 5.2 b shows the coercivity (Hc) of the free layer after the patterning process. The trend observed before patterning is also revealed after the device nanofabrication.

The paramagnetic region (III) in Figure 5.2 b shows a very low coercivity after patterning. For large thicknesses for which the free layer was in-plane at thin film level (II), as in Figure 5.2 a, an out-of-plane configuration is recovered, as seen by the increase in the coercivity values in Figure 5.2 b. This phenomenon can be explained by the contribution of shape anisotropy after the patterning of the devices, now being a less unfavorable out-of-plane configuration than at the blanket level.

Even if only a wedge has been used in the free layer thickness in the Y direction, a certain trend in the coercive field in the X direction can also be observed. At the edges of the wafer, it is evident that the coercive field is larger than in the central region. The deposition is largely homogeneous in the central 50 mm but the homogeneity begins to decrease at the edges, slightly reducing the deposited thickness. Therefore, a tunneling barrier with a slightly smaller Mg content will be more oxidized, leading to such an increase in the Hc of the FeCoB free layer, due to a resulting larger PMA. In addition, a smaller free layer thickness can also increase Hc. This effect is also observed in the NanoMOKE mapping of Figure 5.2 a.

As a result, the apparent drop in coercivity of the central region of Figure 5.2 b is actually due

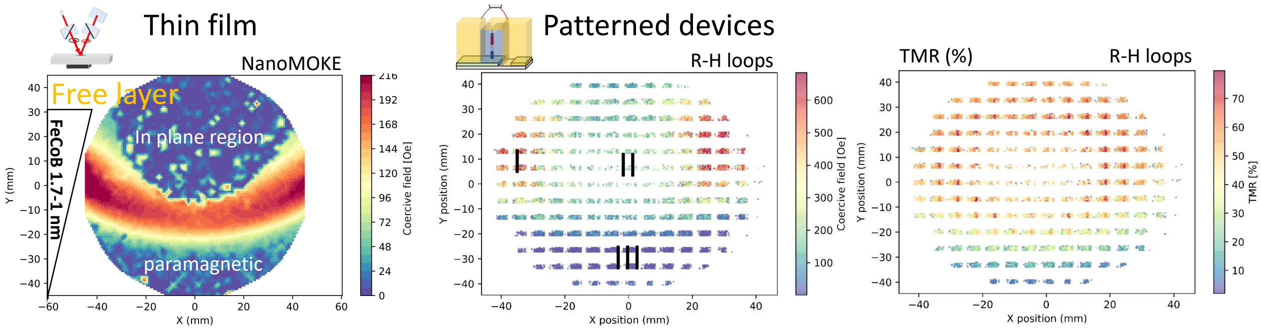

(a) (b) (c)

Fig. 5.2: Mapping of free layer coercive field values for the entire 100mm wafer measured by NanoMOKE before patterning (a). Coercive field of the free layer after the nanofabrication process (b). Tunneling magnetoresistance (TMR) mapping of the patterned devices (d).

to the reversal of the reference layer. In Figure 5.3, the hysteresis loops of patterned devices in these different regions are observed: stable reference layer (I), reference layer reversal (II) and paramagnetic free layer (III).

The fact that the reference layer is more stable at the edges than in the central zone of the wafer can be attributed to the same effect as for the free layer, a more oxidized barrier and a smaller reference layer thickness.

Figure 5.2 d shows the TMR distribution across all devices on the 4” wafer. Typically, the spin polarization increases with electrode thickness, resulting in larger TMR values, until it saturates with the full spin polarization [195]. The tunneling magnetoresistance results shown in Figure 5.2 d show how, in this case, above the paramagnetic free layer region, the TMR distribution is fairly constant.

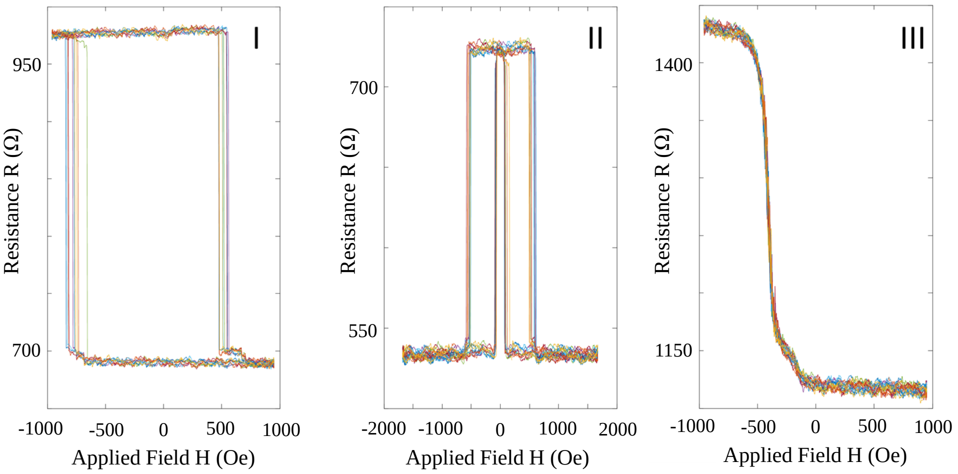

Fig. 5.3: R-H loops for devices in the regions I, II,III displayed in Figure 5.2 b.

Finally, Figure 5.4 shows the values of TMR versus resistance for STT-MRAM cells with thin-SAF and different nominal diameters, ranging from 20 nm to 150 nm.

In this case, a buffer layer with the composition: Ta 25 nm/ FeCoB 2nm/ Pt 3nm was used to reduce the use of platinum. In principle, such Ta buffer layer could introduce some large unwanted serial resistance. However, this would appear, for devices with the same nominal diameter, as a decrease in TMR with higher resistance values, which is not seen in Figure 5.4. Only for the case of small nominal diameters can this behavior be slightly observed. However, such series resistance can be attributed to an unwanted tapered shape in the Ta hard mask during the RIE process, as seen in the inset of Figure 5.4, which shows SEM images after the IBE process of pillars with nominal diameters

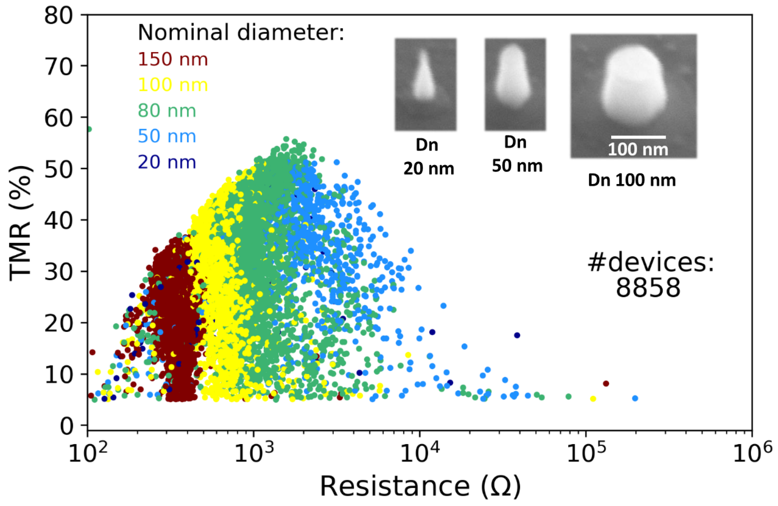

Fig. 5.4: TMR vs. resistance of the patterned devices corresponding to the previous stack. Different colors correspond to devices with different nominal diameters, being 20nm, 50nm, 80nm, 100nm and 150nm. The inset shows SEM images after the IBE process. A conical shape is observed in the Ta hard mask at small diameters, leading to some serial resistance.

(Dn) 20 nm, 50 nm and 100 nm. Due to the conical shape of the hard mask after the RIE process, most devices with nominal diameters of 20 nm were not contacted, while those with 50 nm show some series resistance. However, devices with a larger nominal diameter, whose shape is more cylindrical, do not present series or parallel resistance indices, as inferred from the vertical distribution of TMR shown in Figure 5.4 for devices with 80, 100 and 150 nm.

Finally, we tested the stability of the Co/Pt thin film against the STT writing process. Figure 5.5 a shows a voltage field switching phase diagram for a device with reduced SAF, for voltage pulses of 100 ns. The red and blue areas represent antiparallel (AP) and parallel (P) configuration of the magnetization of the storage layer with respect to the magnetization of the reference layer. The white area is a bi-stable region, where both the P and AP configurations can be stabilized.

The switching voltage of fabricated devices is quite small, as seen in the H-V phase diagram in Figure 5.5 a, slightly larger than 0.2 V for a device with a nominal diameter of 100 nm, 42% TMR and thermal stability of 30 k_BT.

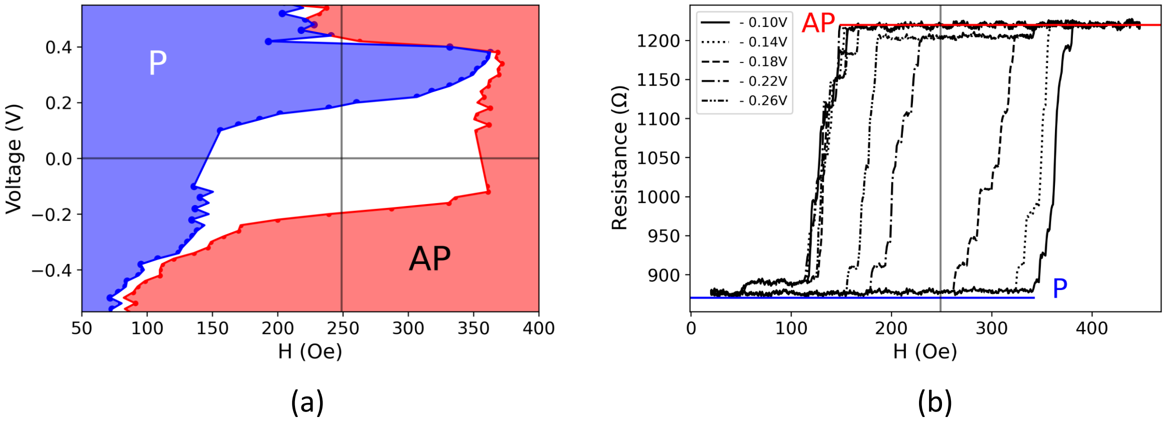

Fig. 5.5: Voltage-field switching phase diagram for a device with thin SAF (a) Resistance vs. voltage loop with varying 100 ns negative voltage pulses

Even if it is shown here that such a thin-SAF may be stable enough for free-layer switching operation, we observe that the reference layer reverses at field values slightly above 1 kOe for most devices (not shown here). Even if further optimization of the thin-SAF structure for a larger reference stability could be investigated, Chatterjee et al. already reported about such structure [196]. STT-MRAM cells with reference layer stability against applied write voltage pulses of up to 1V have been reported. However, such thin-SAF, although it reduces the amount of Pt used in the MTJ, does not completely suppress the use of Pt, so the supply risk is still present. Therefore, an alternative SAF structure based on a non-critical combination of cobalt with nickel is investigated in the next section.

5.2 Co/Ni based SAF as an alternative to Co/Pt

Other material systems instead of multilayers of Co/Pt can provide perpendicular magnetic anisotropy (PMA). Other multilayers such as Co/Pd, Co/Ni or Co/Ir are well known for providing large PMA values. Also other materials like CoPt, CoPd, FePt, FePd ordered alloys or rare earth transition alloys like TbFe or TbCo exhibit strong PMA. However, in most of the systems mentioned, platinum group metals or rare earths are included, except in the case of Co/Ni multilayers. Therefore, these latter systems are advantageous in terms of criticality of the materials. The perpendicular magnetic anisotropy of Co/Ni multilayers has already been studied but the obtained properties were so far not reaching the specifications required for use in the reference layer of MRAM [197, 198, 199, 200, 201].

A key requirement to achieve strong PMA in Co/Ni multilayers is to promote good (111) texture in these multilayers. It was previously reported that the selected seed layer strongly influences the magnetic properties of Co/Ni multilayers [126, 200]. Jan et al. [126] concluded that NiCr, NiFeCr, Hf or a seed layer composed of those materials yields the best texture to induce PMA in Co/Ni multilayers. In the case of Liu et al. [200], they studied the PMA of Co/Ni multilayers grown on four different seed layers: NiCr, Pt, Ta or Ru as seen in Figure 5.6.

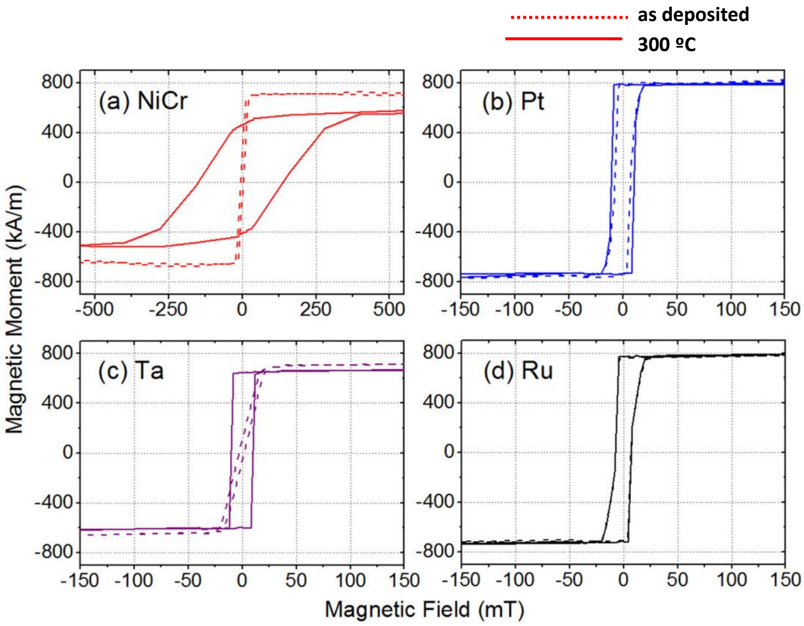

Fig. 5.6: VSM magnetization loops under external perpendicular field of Co/Ni multilayers, as deposited (dotted lines) and after 300ºC annealing (solid lines) for different seed layer materials. Figure from [200].

A NiCr seed layer resulted in the highest PMA in the Co/Ni multilayers after annealing at 400 °C. Pt or Ta seeds provided intermediate PMA values while for Ru the resulting PMA was low.

Bloomen et al. used a 50 nm copper (Cu) seed layer to induce PMA in Co/Ni multilayers [197]. Chen et al. used a complex structure made of Cr 1.5nm/Cu 100nm/Pt 20nm/Cu 10nm, where a thick layer of Cu is also present [201]. Other authors also studied the PMA of Co/Ni multilayers in seed systems using Cu and Ta, as Ta 3nm/Cu 2.8nm for Wang et al. [198] or Ta 1nm/Ti 3nm/Cu 3nm for Zhang et al. [199]. Zhang et al. also reported several methods to improve PMA, such as plasma treatment or the use of an oxygen surfactant coating.

The aforementioned studies were limited to Co/Ni multilayers, but did not extend to the synthetic antiferromagnetic (SAF) structure that is normally used for the reference layer of p-STT-MRAM. For the case of spin valves, Arora et al. reported coercive values for the SAF structure of 2 kOe when grown on a 3 nm Cu seed layer [202]. However, as shown below, a spin valve structure could be less challenging for the integration of a Co/Ni-based SAF than for the case of a MTJ.

A diverse number of elements make up the structure of a MTJ that can migrate to the SAF and alter its magnetic properties after the annealing process. MTJs implementing a SAF based on Co/Ni multilayers have been reported [124, 125, 203]. In Kar et al., a NiCr/Hf/Ta seed layer was used, leading to switching fields values of the reference layer around 1.5 kOe [124]. Tomczack et al. developed a thin-SAF structure based on Co/Ni multilayers with a NiCr/Hf seed layer [125]. For them, the reference layer switching field ranged between around 2 and 5 kOe depending on the thickness of the CoFeB polarizer used (1 nm and 0.4 nm respectively), after annealing at 300°C, for a CoFeBTa spacer. We can notice that even if the switching field of the reference layer can be increased by reducing the CoFeB polarizer thickness, there is a negative effect on the TMR amplitude since the spin polarization also depends on the polarizer thickness. In their study, they observed an abrupt decrease of the reference layer switching field after annealing at 400°C. Finally, Devolder et al. reported the thermal stability of MTJs with Co/Ni based thin-SAF [203], very similar to the structure used by Tomczack et al. The main difference is the use of $Fe_{60}Co_{20}B_{20}$ instead of CoFeB for the reference and storage layer electrodes and the co-sputtered composite spacer layer made in this case of $Fe_{60}Co_{20}B_{20}$ and Ta instead of CoFeBTa. Furthermore, Tomczack et al. used a Co 3Å /Ni 6Å ratio, while the inverse Co 6Å /Ni 3Å was used by Devolder et al. Devolder et al. obtained the reference layer switching at 3 kOe after annealing at 400 °C, showing a priori that STT-MRAM cells can be fabricated without Pt or Pd-based SAFs. However, results of patterned devices were not given.

Moreover, they identified the thin 6 Å Co layer used on top of the Ru layer to provide high antiferromagnetic RKKY coupling as the main weakness of their structure after high-temperature annealing.

In our case, a SAF structure with non-critical Cu as seed layer material has been developed. Our study also extends to high annealing temperatures of up to 400°C in patterned devices. We show how, unlike what Devolder et al. reported, in our case the decrease in the switching field of the reference layer stems from a migration of elements from the FeCoB polarizing layer. We observe that for a single SAF structure, not integrated in a MTJ, high switching fields are maintained even after 400°C anneal. However, by adding the SAF structure in a MTJ, the reference layer switching field starts to decrease at high annealing temperatures. We therefore conclude that texture-breaking layers playing the role of diffusion barrier during annealing could be the key to better BEOL compatibility.

5.2.1 Optimization of Co/Ni multilayers magnetic properties

In this section, we begin the material optimization at thin-film level by looking at the effect of Cu seed layer thickness on the coercivity of Co/Ni multilayers. Once an optimum Cu thickness has been chosen, the effect of different annealing temperatures is studied. Furthermore, we studied the evolution of the magnetic properties as a function of the number of Co/Ni repeats. We optimized the Co/Ni ratio to achieve the highest coercive field (Hc). A synthetic antiferromagnetic structure (SAF) is required to avoid a large stray field in the free layer. The optimum thickness of the ruthenium layer providing antiferromagnetic coupling was found to be 9Å. Having optimized the magnetic properties at the thin film level, a comparison with a Co/Pt-based SAF is given in the next section.

Seed layer optimization

As a first step, we have developed a Ta buffer layer with a low surface roughness of 0.25 nm, already introduced in Chapter 3.5, to constitute the basis of the subsequent Cu seed layer.

Copper (Cu) is an ideal candidate for the growth of Co/Ni multilayers, considering the fcc (111) texture required for high PMA in Co/Ni multilayers. In addition, Cu is classified as a non-critical metal and is produced by a large number of countries [109]. Shawn et al. observed an increase in the coercivity (Hc) of Co/Ni multilayers when thick Cu seed layers were used [204]. We have also observed such an effect, as shown in Figure 5.7 a and b.

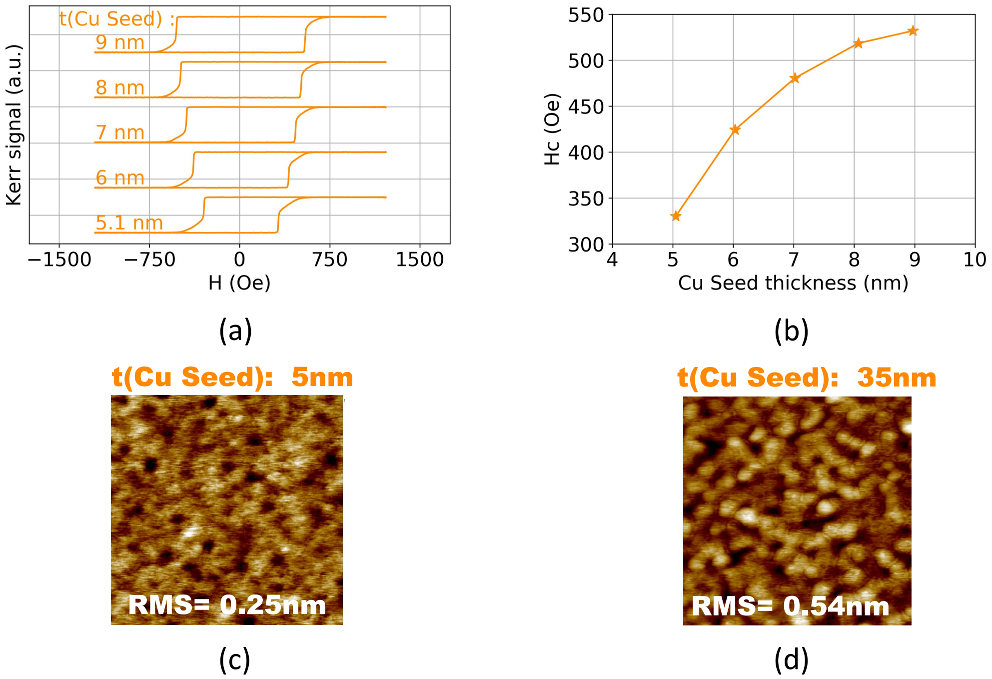

(a) (b)

(c) (d)

Fig. 5.7: Hysteresis loops of 8 x (Co 0.2nm/Ni 0.4nm) multilayers at wafer level as a function of Cu seed layer thickness characterized by magneto-optical Kerr effect under a perpendicular applied field. (a). Evolution of the coercivity with the thickness of the Cu seed layer (b). 500 nm x 500 nm AFM scans of a Cu seed layer with a thickness of 5 nm (c) and 35 nm (d), leading to an RMS surface roughness of 0.25 nm and 0.54 nm, respectively.

Figure 5.7 a shows the hysteresis loops measured by magneto-optical Kerr effect (MOKE) versus Cu seed thickness in the as-deposited state of a stack comprising 8x(Co/Ni) repeats of composition as follows: Ta 3nm / Cu t / 8x[Co 0.2nm/Ni 0.4nm] / Co 0.2nm / Cu 3nm / Ta 3nm. Figure 5.7 a shows that the coercive field (Hc) of the multilayers increases with the thickness of the Cu seed layer, as plotted in Figure 5.7 b. However, as the thickness of the seed Cu layer increases, the surface roughness also increases. Increased roughness is not desirable due to its detrimental impact on the properties of the tunnel barrier. For this reason, a balance has to be found in terms of Cu thickness to induce the required fcc (111) texture, while maintaining a low surface roughness.

Figure 5.7 c and d show atomic force microscopy (AFM) scans of a 5 and 35 nm Cu seed layer respectively, for a 500 x 500 nm scan section. Figure 5.7 d shows that a 35 nm Cu seed has a RMS roughness of 0.54 nm, while for a 5 nm Cu seed layer a much smoother RMS roughness of 0.25 nm is obtained, as seen in Figure 5.7 c. Therefore, a 5 nm thick Cu seed layer will ensure adequate low roughness while maintaining a sufficiently large coercive field, as we will see in the next section, coercivity increases after the annealing process.

Effect of annealing on the magnetic properties of Co/Ni multilayers

In the previous subsection, we have shown that the coercive field increases with the thickness of the Cu seed layer, as previously reported by Arora et al. [202]. They reported an increase in coercivity from 100 Oe to 400 Oe when growing the 8x [0.21 nm Co/Ni 0.57 nm] multilayers on 2 nm Cu or 30 nm Cu seeds respectively. This increase in coercivity is due to an enhancement of the fcc(111) texture with the larger thickness of the Cu seed layer, as indicated by their x-ray diffraction (XRD) results [202].

After the annealing process necessary for the crystallisation of the MgO barrier and of the surrounding FeCoB electrodes, the coercivity of the Co/Ni multilayers increases dramatically, reducing the need to use a much larger Cu seed layer thickness. MOKE hysteresis loops under perpendicular applied field in Figure 5.8 b, show such a large increase in Hc, for a Co/Ni multilayer stack of composition: Ta 3 /Cu 3 / 8x[Co 0.2/Ni 0.4] / Co 0.2 / Cu 3 / Ta 3 nm, as illustrated in Figure 5.8 a.

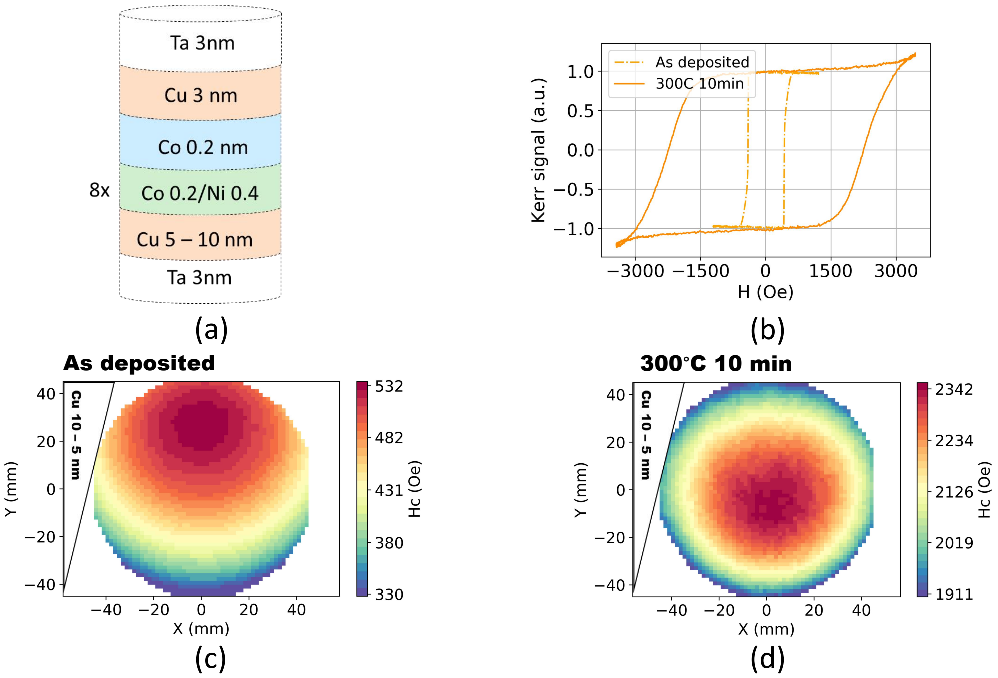

Fig. 5.8: Stack composition: Ta 3 / Cu 3 / 8x[Co 0.2/Ni 0.4] / Co 0.2 / Cu 3 / Ta 3 nm (a). MOKE hysteresis loop under an out-of-plane field, as deposited (dashed lines) and after annealing at 300°C for 10 minutes (solid lines). The coercivity abruptly increases after annealing (b). Wafer mapping of the coercive field of the sample, where the wedge in the Y-axis corresponding to a variation of the Cu seed layer thickness results in a gradient in the coercive field in the as deposited state (c). After annealing at 300°C for 10 minutes, the dependence of Hc on the thickness of the seed layer is no longer observed (d).

A pronounced increase in coercivity is observed after annealing at 300°C for 10 minutes, as also observed previously by Coutts et al. [205]. This increase in Hc is optimal for the application of such layers as a reference layer.

Interestingly, the coercivity dependence on the Cu seed layer thickness (Y-axis) observed in the as-deposit state in Figure 5.8 c, is not conserved after the annealing process, as observed in Figure 5.8 d. The small radially symmetric gradient in coercivity observed in Figure 5.8 d, comes from the inhomogeneity of the deposition between the center and the outer region of the wafer, as explained in Chapter 3.1.

To achieve BEOL compatibility with CMOS integration, the PMA of the reference layer must be preserved after exposure to temperatures up to 400°C. Figure 5.9 shows the VSM hysteresis loops of a stack with 8 Co/Ni repeats demonstrating that PMA can be maintained up to 400°C annealing (red). At 500°C (dark red), the magnetization is strongly reduced and PMA is lost due to inter-diffusion of Cu and Ta with the (Co/Ni) multilayers.

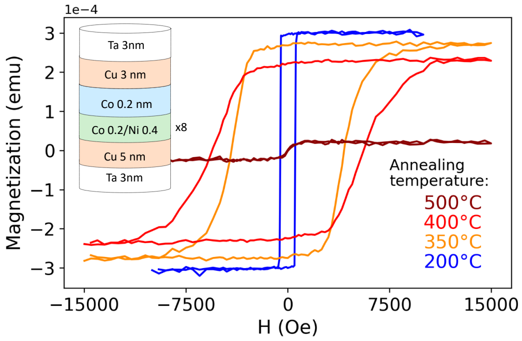

Fig. 5.9: VSM hysteresis loops under a perpendicular applied field of the sample shown in the inset with a 5 nm Cu seed layer and 8 Co/Ni repeats for different annealing temperatures: 200°C (blue), 350°C (orange), 400°C (red) and 500°C (dark red) for 10 minutes.

Influence of the number of Co/Ni repeats

The influence of the number of repeats on the magnetic properties of Co/Ni multilayers is shown in Figure 5.10. In both cases, the Cu seed layer has a Y-axis wedge ranging from 5 to 10 nm. The hysteresis loops in Figure 5.10 a show that for 18 Co/Ni repeats (in orange), the reversal is more gradual than for the case of 8 repeats (in red).

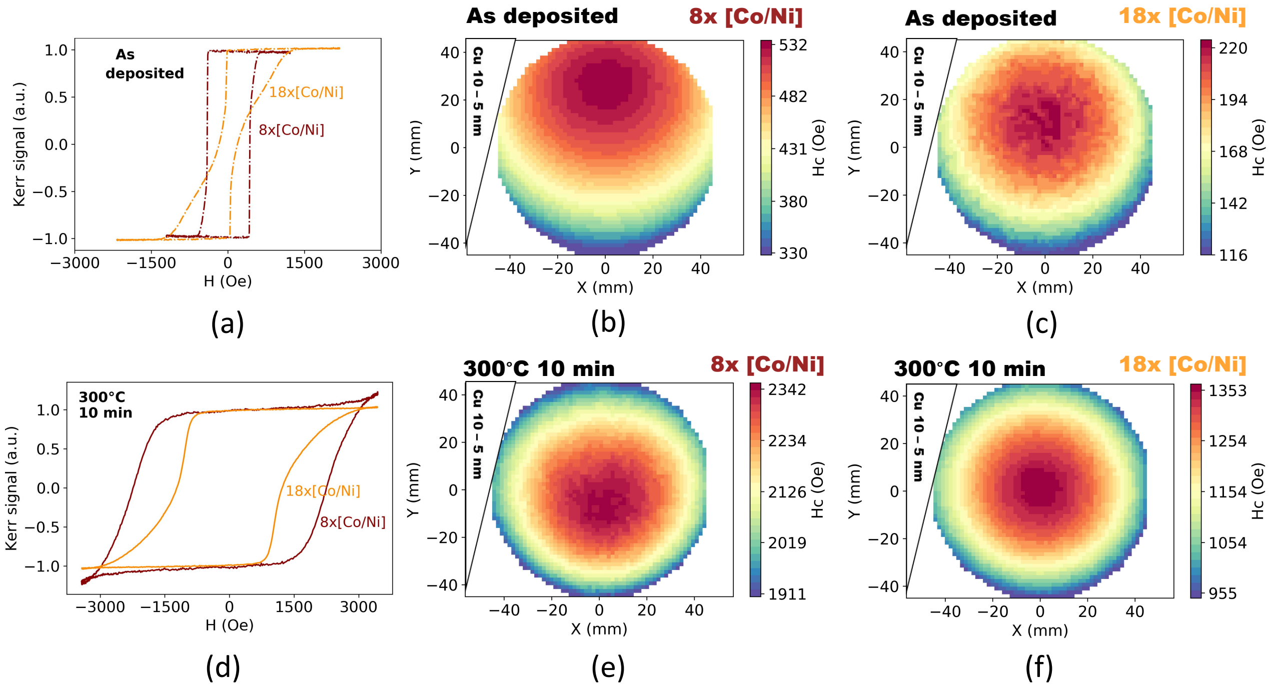

Fig. 5.10: NanoMOKE hysteresis loops under perpendicular field for Ta 3 / Cu 6 / N x [Co 0.2/Ni 0.4] / Co 0.2 / Cu 3 / Ta 3 nm, for the cases of N=8 (red) and N=18 (orange) in the as deposited state (a) and after 300°C annealing for 10 minutes (d). MOKE mappings of Hc for N=8 (b) and N=18 repeats (c) in the as deposited state, and after 300°C annealing for 10 minutes (e) and (f) respectively.

Previous work by A. Al Subhi and R. Sbiaa [206] showed that for a larger number of Co/Ni multilayers, smaller magnetic domains are formed, as seen in the MFM and OOMMF simulations for a variable number of repeats, from N=4 to N=12, in Figure 5.11.

The presence of smaller domains with a larger number of repeats explains the gradual reversal observed in Figure 5.10 a and d for the case of 18 Co/Ni repeats.

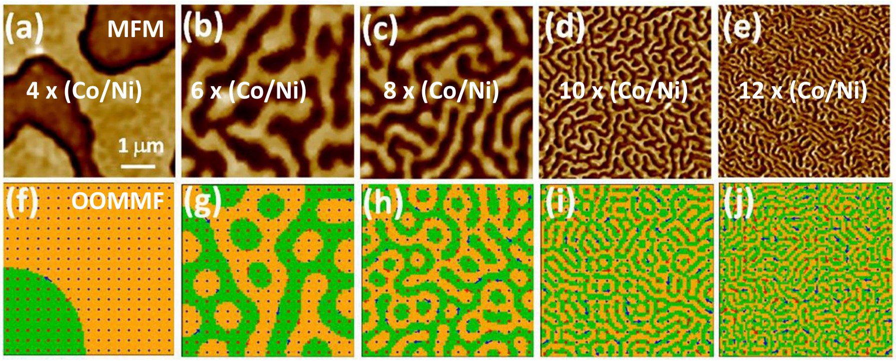

Fig. 5.11: Magnetic force microscopy (MFM) (top) and Object Oriented MicroMagnetic Framework (OOMMF) simulations (bottom) for Co/Ni multilayers with a varying number of N repeats: 4 (a,f), 6 (b,g), 8 (c,h) ,10 (d,i) and 12 (e,j). From [206].

They calculated a domain size reduction from 4.7 µm, for 4 bilayers, to 0.1 µm, for the case of 12 bilayers.

This is a very general phenomenon in out of plane magnetized systems: up to a certain thickness, the domain size reduces with the thickness of the PMA material. This was largely documented in ordered FePd or FePt alloys too [207, 208].

These smaller magnetic domains that form for a larger number of multilayers explain the gradual magnetic switching observed in Figure 5.10 a and d, for 18 Co/Ni bilayers. As in the case of A. Al Subhi and R. Sbiaa [206], the coercivity is reduced with more than 8 bilayers.

The MOKE mappings shown in Figure 5.10 b and c show that for a higher Cu seed layer thickness (y-axis) a higher coercivity is obtained, for 8 and 18 repeats respectively. However, as explained in the previous section, the coercivity loses its dependence on the seed layer thickness after annealing, as shown in Figure 5.10 e and f for 8 and 18 repeats respectively, due to an improvement of the texture after the annealing process at 300°C for 10 minutes, which also leads to higher coercivity values. The maximum coercivity goes from about 500 Oe to more than 2kOe for the case of eight Co/Ni repeats.

In the previous Figure 5.9, higher Hc values are observed for annealing at 350°C and 400°C, as Hc of the Co/Ni multilayers increases with annealing temperature. However, as we will see later, large annealing temperatures make the integration of Co/Ni multilayers into the MTJ structure more difficult.

Co/Ni content ratio optimization

Different Co/Ni content ratios for multilayers have been reported in the literature. We have studied the evolution of the magnetic properties of a stack with eight repeats, varying the ratio of Co to Ni. We studied two stacks with the following composition:

- S1: Ta 3nm/Cu 3nm /8x[***Co 0.14-0.26 nm/Ni 0.3-0.5 nm***]/Co 0.2nm/Cu 3nm/Ta 3nm
- S2 : Ta 3nm/Cu 3nm /8x[***Co 0.14-0.26 nm/Ni 0.45-0.75 nm***]/Co 0.2nm/Cu 3nm/Ta 3nm

The maximum coervicity is obtained for Co 0.2 nm / Ni 0.55 nm in the as deposited state as shown in Figures 5.12 a and d. Ni thickness has a strong influence on the magnetic response of the multilayers, while Co thickness has a weak effect. The remanence plots in Figures 5.12 b and e show that for low Ni thicknesses below 0.37 nm the PMA starts to decrease, which can also be seen in the corresponding hysteresis loops in Figures 5.12 c and f.

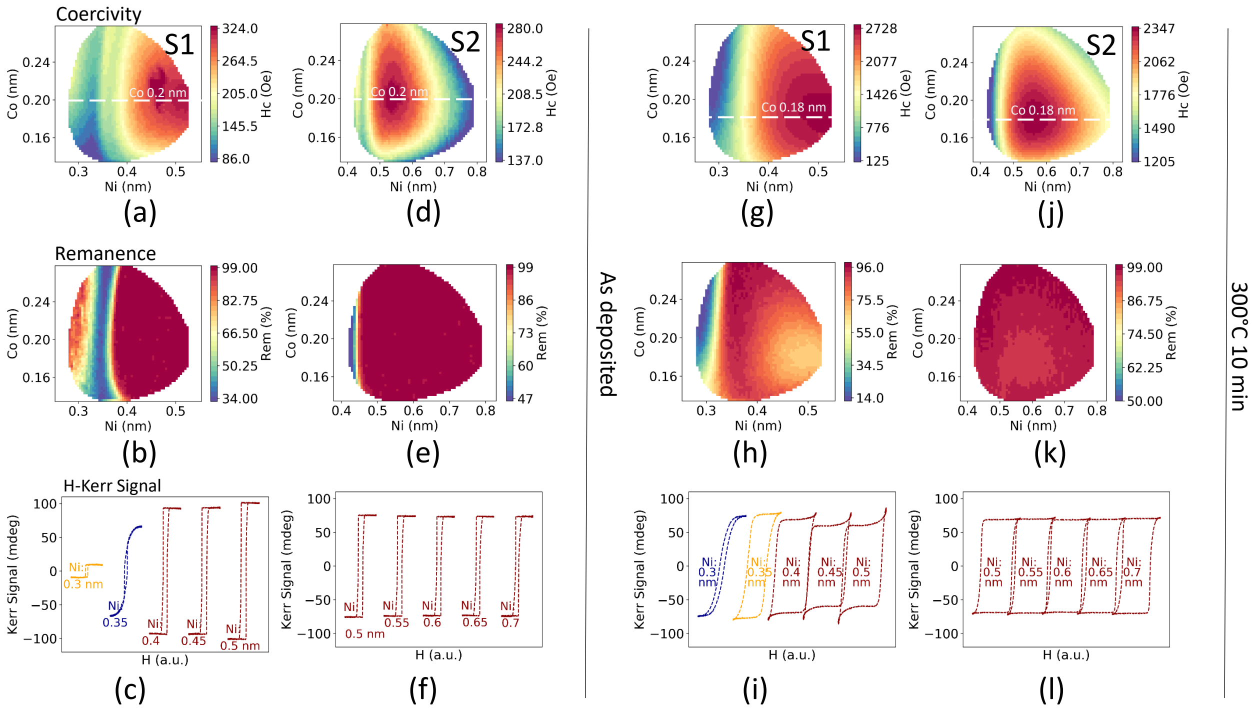

Fig. 5.12: NanoMOKE mappings of coercivity and remanence for two stacks, labelled S1 and S2. In the case of S1, Co thickness varies between 0.14 nm and 0.26 nm (y-axis) and Ni thickness varies between 0.3 nm and 0.5 nm (x-axis). S2 maintains the same Co variation as S1 but the Ni thickness varies to higher values, between 0.45 nm and 0.75 nm (x-axis). Coercive field mapping (a), remanence mapping (b) and corresponding hysteresis loops for a constant Co thickness at 0.2nm (c) for S1 in the as-deposited state, and after annealing at 300°C for 10 minutes (g,h,i) respectively. Coercive field mapping (d), remanence mapping (e) and corresponding hysteresis loops for a constant Co thickness at 0.2nm (f) for S2 in the as-deposited state, and after annealing at 300°C for 10 minutes (j,k,l) respectively.

After annealing at 300°C for 10 minutes, the coercivity increases strongly. In addition, the region of maximum Hc has shifted to Co thickness values of 0.18 nm, as shown in Figures 5.12 g and j. The remanence mappings in Figures 5.12 h and k reveal that the PMA degradation region now takes place at slightly lower Ni thickness values, around 0.32 nm. We determine that the region of highest coercivity in our system corresponds to Co 0.18nm / Ni 0.55 nm as seen in Figure 5.12 j.

RKKY antiferromagnetic coupling optimization

The synthetic antiferromagnetic structure used in p-STT-MRAM is often constructed using a Ru spacer layer due to its large interlayer exchange coupling strength [209]. The RRKY interaction can result in the two magnetic layers being configured in either a ferromagnetic (parallel to each other) or antiferromagnetic (antiparallel) state depending depending on the thickness of the non magnetic spacer. The thickness of the non magnetic layer also influences the coupling strength [210, 211].

Figure 5.13 a shows VSM hysteresis loops of a Co/Ni SAF structure with a varying Ru spacer thickness, between 7.5 and 11 Å.

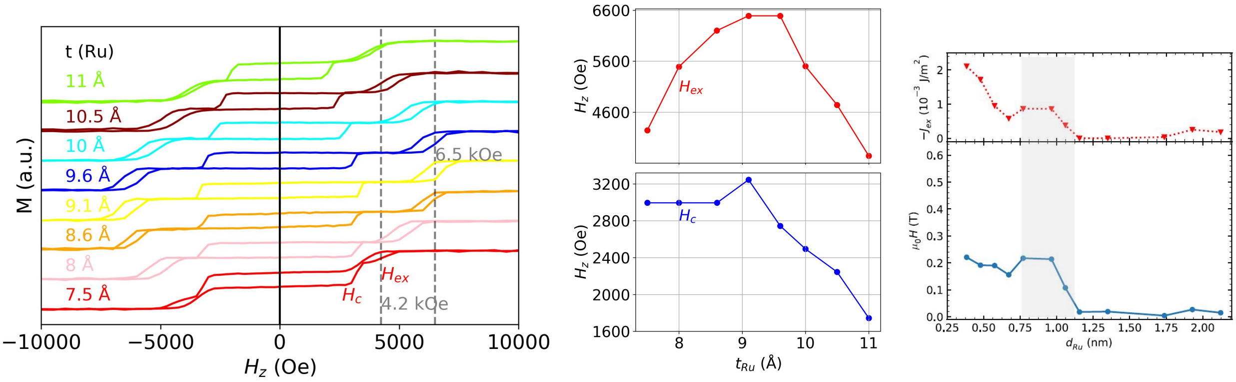

(a) (b) (c)

Fig. 5.13: VSM hysteresis loops of a sample with the following stack structure: Ta 3nm / Cu 5nm / 4x[Co 0.2 nm/Ni0.4 nm]/ Co 0.5 nm /Ru t / Co 0.5 nm / 3x[Ni 0.4 nm / Co 0.2 nm]/ Cu 3nm/ Ta 3nm (a) The switching field of the SAF (H_c) (blue) and the exchange field (H_{ex}) (red) are plotted (b). Coercive field (blue) and exchange coupling (red) for a similar Co/Ni SAF structure, as a function of Ru thickness from [202] (c).

The highest values of the coercive field and exchange field are obtained for a Ru thickness of 9 Å (yellow hysteresis), as seen in Figure 5.13 b as well. The switching field of the SAF is as large as 3.2 kOe with an exchange field of 6.5 kOe, after which the antiferromagnetic coupling is overcome by the external field. Figure 5.13 b shows the oscillatory behaviour of the RRKY exchange coupling strength with Ru thickness [54, 210]. A similar trend showing oscillations with an overall decay in both H_c and H_{ex} with increasing Ru thickness was reported by Arora et al. [202], as seen in Figure 5.13 c.

5.2.2 Co/Pt vs Co/Ni at thin film level

In this section, we compare the magnetic properties of two MTJs with different SAF, one based on Co/Pt multilayers (S1) and the second on Co/Ni multilayers (S2) at thin film level. The stack structure of both samples is as follows, with the thickness indicated in nm:

- **S1**: Ta3 / Pt25 / 6x[Co0.5/Pt0.25] / Co0.5 / Ru0.9 / 3x[Co0.5/Pt0.25] / Co0.5 / Ta0.2 / FeCoB1.2 / MgO0.75 / Ox(30s) / MgO0.5 / FeCoB1.5 / Capping layer

- **S2**: Ta22 / FeCoB0.8 / Ta3 / Cu3 / 6x[Co0.2/Ni0.4] / Co0.5 / Ru0.9 / Co0.5 / 3x[Co0.2/Ni0.4]/ Ta0.2 / FeCoB1.2 / MgO0.75 / Ox (30s) / MgO0.5 / FeCoB1.5 / Capping layer

Figure 5.14 a shows a comparison between the magnetic properties of the two samples with Co/Ni (green) or Co/Pt (magenta) SAF structure. Both samples were annealed at 300ºC for 10 minutes.

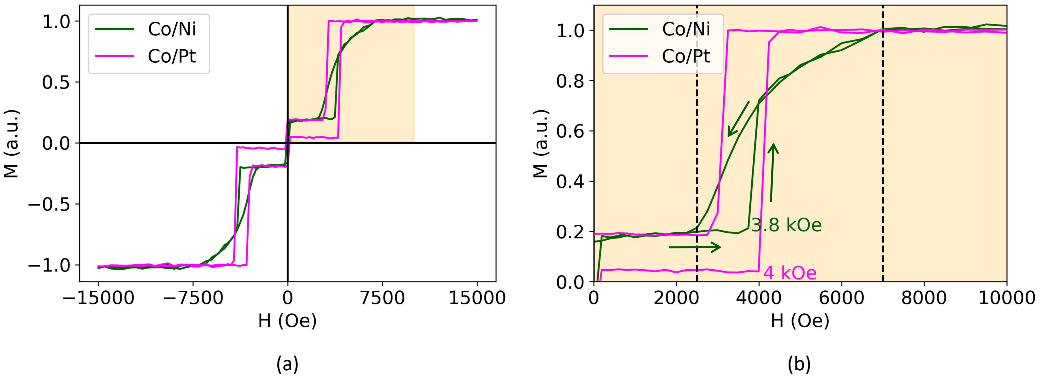

Fig. 5.14: VSM hysteresis loops under out of plane applied field at thin film level of a MTJ with a Co/Ni (green) or Co/Pt (magenta) SAF as part of the reference layer after annealing at 300ºC for 10 minutes (a). Zoom of the VSM hysteresis loop shown in (a) for which the sense of the field scan is indicated by green arrows (b).

The large switching field of 3.8 kOe of the reference layer with Co/Ni based SAF is almost as high as the 4 kOe obtained for the Co/Pt SAF case, as seen in the zoom of Figure 5.14 b. These results indicate that the Co/Ni multilayer based SAF can be sufficiently stable even after device patterning. In the next section, we show the electrical results of patterned devices with a Co/Ni SAF in the reference layer.

5.2.3 Electrical results in patterned devices with Co/Ni SAF

This section shows the STT switching of MTJs comprising a reference layer with a synthetic antiferromagnet based on Co/Ni multilayers. The MTJs were patterned down to 40 nm diameter lateral dimensions and measured under applied voltage pulses. The resistance was recorded at low bias after each applied voltage pulse of 100 ns of increasing amplitude. The V-R loop measurements are plotted in Figure 5.15 a for a single device. The fabricated tunnel junctions incorporate the smooth buffer layer shown in Section 3.5 and a 3 nm Cu seed layer. The composition of the stack is as follows: Ta 22 / FeCoB 0.8 / Ta 3 / Cu 3 / 6x[Co 0.2/ Ni 0.4] / Co 0.5 / Ru 0.9 / Co 0.5 / 3x[Ni 0.4/Co 0.2] / Ta 0.3 / FeCoB 1.2 / MgO 1.2 / FeCoB 1.5 / Capping. The stack was annealed at 300°C for 10 minutes after deposition.

Figure 5.15 a shows the R-V loop of a MTJ with Co/Ni based SAF. The reference layer is perfectly stable under the STT writing operation. Figure 5.15 b is a SEM image after the ion beam etching of a 40 nm diameter junction. The switching probability of the free layer, in Figure 5.15 c, reaches 50% for voltage pulses below 0.5 V, and the thermal stability value extracted based on the switching voltage dispersion is about 39 k_BT. This was achieved with a FeCoB free layer of 1.5 nm, a thickness value close to the threshold thickness between perpendicular and in-plane magnetization. The value

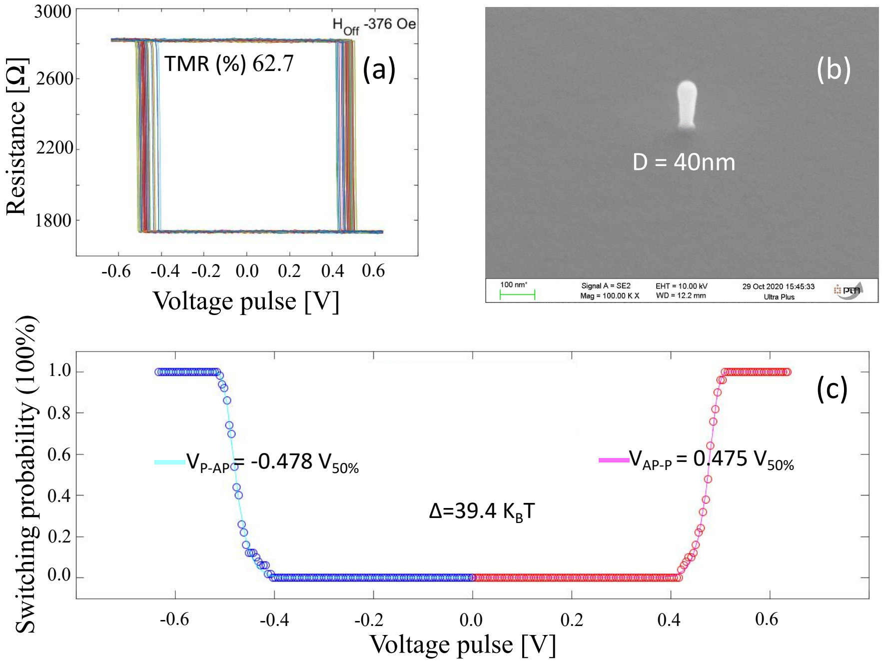

Fig. 5.15: Voltage-pulse resistance loop under an external field equivalent to the offset field (a). SEM image of the MTJ after ion beam etching (IBE) (b). Switching probability after applied voltage pulse for 50 events (c).

of thermal stability can be further enhanced by using composite storage layers [212] and an MgO top capping, which have not yet been included in this study.

In any case, what Figure 5.15 shows is that the Co/Ni-based SAF used for the reference layer is perfectly stable after the MTJ write operation.

However, an undesirable feature observed in our MTJs was a large stray field from the reference layer as observed in Figure 5.16 a for devices with varying diameter. SEM observations of the pillars with varying diameters between 40 and 75 nm are given in Figure 5.16 b-d, after the IBE process.

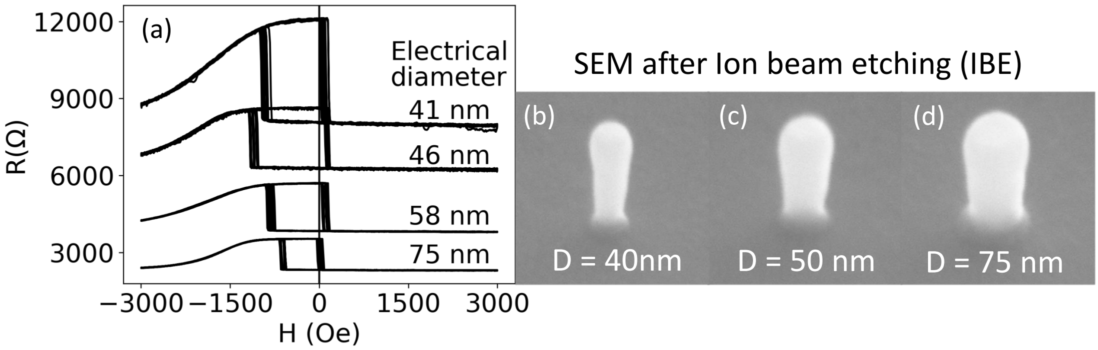

Fig. 5.16: R-H loops of MTJs display a large stray field, in the limit of the bistability region of both parallel and antiparallel states. SEM observations for pillars with increasing diameters : 40nm (b), 50 nm (c) and 75 nm (d) after IBE.

It is observed in the R-H loops in Figure 5.16 a that the reference layer tilts after increasing negative fields in the high-resistance, antiparallel configuration. However, the reference layer recovers its full anti-parallel configuration at zero field, so that such tilting does not hinder the bistability of the bit magnetic element.

The MTJs shown here are bistable at zero field, which means that both parallel and antiparallel states are possible in the absence of applied external field. However, it would be optimal to reduce the stray field. This is possible by varying the number of multilayers composing the SAF, as shown in the next subsection, using macrospin calculations.

5.2.4 Macrospin calculations: towards the compensation of stray field from the Co/Ni based SAF

We performed macrospin calculations of the stray field of the Co/Ni based SAF structure into the free magnetic layer by using a Coulombian model as in Chapter 4.2.1.

Calculations have been performed for 3 upper Co/Ni bilayers and a variable number of lower bilayers, N, in the form N x (Co/Ni) / Ru / 3x(Co/Ni). Figure 5.17 shows that the experimental results of the fabricated MTJs represented as dark red stars (from Figure 5.16 a) closely match the stray field predicted in the calculations. However, the resulting stray field is in between 250-500 Oe, being relatively large values. If the coercive field of the free layer is not large enough, such a large stray field would hinder the parallel and antiparallel bistable states of the free layer. Therefore, as observed in the calculations, the number of bottom repeats could be increased to reduce the stray field at intermediate diameters (40-80nm). An increase to ten bottom (Co/Ni) repeats (orange line) would be sufficient to ensure a lower stray field in the free layer.

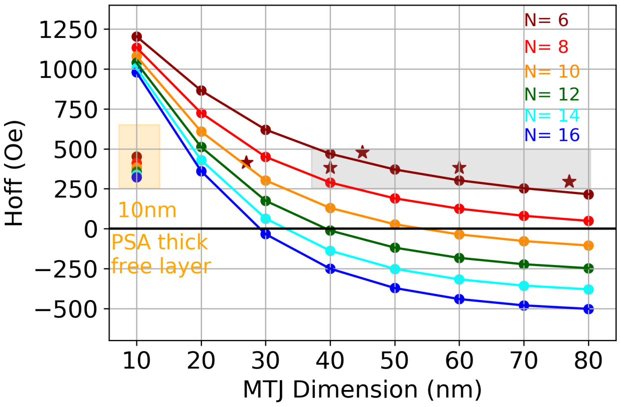

Fig. 5.17: Simulated stray field of Co/Ni SAF into the free magnetic layer of an MTJ as a function of the number of repeats comprising the bottom SAF structure: N x ([Co 0.18/Ni 0.55])/Co 0.5/Ru 0.9 /Co 0.5/3 x ([Co 0.18/Ni 0.55]) /Ta 0.3 /FeCoB 1.2/MgO 1.2/FeCoB 1.5 (thickness in nm). Experimental data corresponding to Figure 5.16 a is represented by a dark red star symbol.

Figure 5.17 also shows that for small diameters, below 20nm, the variation of the number of bottom repeats might not be sufficient to compensate the stray field from the top part. However, at such small diameters, the thermal stability of the free layer is strongly reduced. Therefore, in order to obtain acceptable retention at such small nodes, one possible option is to use strategies such as a PSA free layer [41, 42]. For such a thicker free layer, the average stray field will be reduced due to the larger volume of the magnetic free layer, as shown in the orange inbox of Figure 5.17, where the volume of the free layer has been changed to that of a PSA with 10 nm thickness.

Another possibility would be to use a reduced SAF structure for which the Co/Ni multilayers are present only in the bottom part of the SAF. As previously mentioned, such a structure has already been proposed by Chatterjee et al. [196] with a Co/Pt based SAF. Low stray fields at low diameters can be obtained by avoiding the use of Co/Ni multilayers at the top of the SAF, as in Devolder et al. [203]. Increasing the number of repeats in the bottom thin SAF can lead to low stray fields at diameters below 20 nm, as shown by the macrospin calculations in Figure 5.18 a.

To obtain a better compensated free layer at 10 nm diameters, the number of bottom repeats can be increased up to 12, as shown by the dashed green line in Figure 5.18 a.

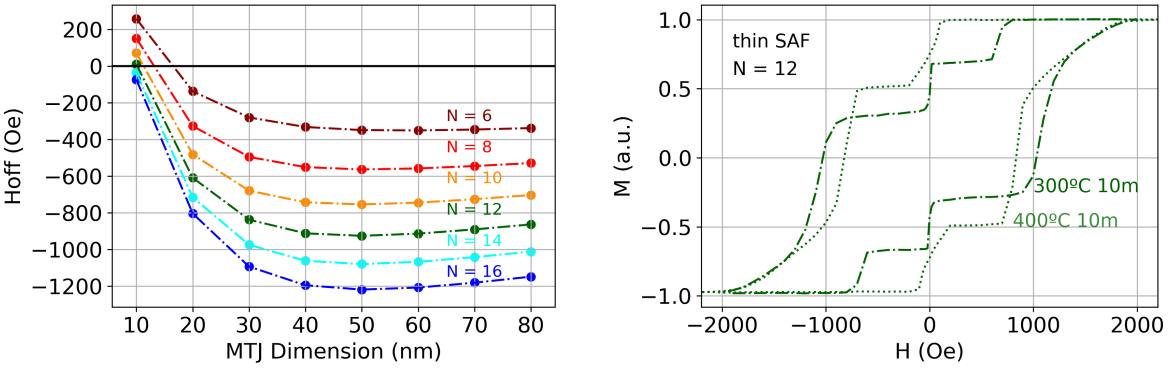

(a)

(b)

Fig. 5.18: Simulated stray field of a thin SAF: N x [(Co0.18/Ni0.55)] / Co 0.5 / Ru 0.9 / Co 0.5/ Ta 0.3 / FeCoB 1.2/ MgO 1.25 reference layer into 1.5 nm FeCoB free layer (thickness in nm) (a). VSM measurements of a thin SAF structure with N = 12 bilayers: Ta 22 / FeCoB 0.8 / Ta 3 / Cu 5 / 12x(Co 0.18/Ni 0.55) / Co 0.5 / Ru 0.9 / Co 0.5 / Ta 0.3 / FeCoB 1.2 / MgO 1.25 / FeCo B1 / Ta 0.2 / FeCoB 0.8 / MgO 1.25 / FeCoB 0.4 / Ta 3 / Capping, under perpendicular applied field after 300°C anneal for 10 minutes (dashed) and 400°C (dotted) (b).

We performed VSM measurements of such a SAF structure with 12 bottom repeats as seen in Figure 5.18 b. The reference layer still retains its PMA. However, the switching field of the reference layer is slightly below 1kOe at the thin film level after annealing at 300°C for 10 minutes (dashed lines). This might not be sufficient to guarantee the stability of the reference layer after patterning. In addition, the switching field decreases further to 750 Oe after annealing at 400°C (dotted lines). Therefore, the above alternative of combining a conventional SAF based on Co/Ni multilayers with a large-volume PSA-free layer, as in Figure 5.17 is more attractive at small nodes.

5.2.5 Annealing tolerance: towards BEOL compatibility

In the previous section 5.2.3, we have shown that the reference layer with a Co/Ni multilayer based SAF is sufficiently stable after annealing the MTJ at 300°C for 10 minutes.

However, preserving perpendicular magnetic anisotropy (PMA) during back end-of-line (BEOL[1]) complementary metal oxide semiconductor (CMOS) processing up to 400°C [213] is a more difficult task. At such high temperatures, interdiffusion of elements in the different layers begins to occur, which is detrimental to the overall performance of the MTJ, unless properly engineered. It can be observed in Figure 5.19 b that the reference layer switches at 3.8 kOe at blanket film level after 300°C annealing, and its switching field abruptly drops to 500 Oe after 400°C annealing, as seen in Figure 5.19 c.

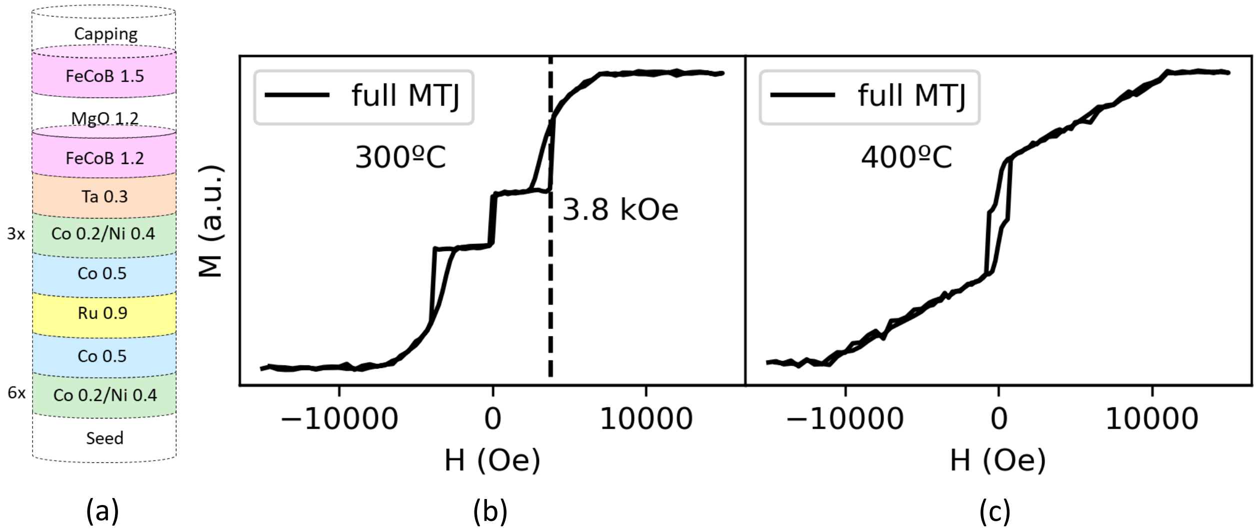

Fig. 5.19: VSM measurements under out-of-plane magnetic field of a standard MTJ with the structure shown in (a) after annealing at 300°C for 10 minutes(b) and 400°C respectively (c).

The deterioration of the switching field of the reference layer after annealing at high temperatures could be explained by a weaker RKKY coupling through the Ru layer or by a deterioration of the PMA of the multilayers alone.
We have characterized by VSM the magnetic response of the Co/Ni-based SAF alone, as in Figure 5.20 a, without the FeCoB polarizer on top, with two different capping materials:

- S1: Ta 3 / Cu 5 / 6x ([Co 0.2/Ni 0.4]) / Co 0.5 / Ru 0.9 / Co 0.5 / 3 x ([Co 0.2/Ni 0.4]) /**Cu 3**
- S2: Ta 3 / Cu 5 / 6x ([Co 0.2/Ni 0.4]) / Co 0.5 / Ru 0.9 / Co 0.5 / 3 x ([Co 0.2/Ni 0.4]) / **Ta 2**

Figure 5.20 b and c shows that the magnetic properties of the SAF structure alone are not substantially degraded after annealing at 400°C, regardless of the capping material used. The switching field remains larger than 3 kOe using both a Cu or Ta capping layer. A small amount of deterioration is observed using a Ta capping, as in Figure 5.20 c. However, it does not explain the strong reduction in Hc observed for the case of a full MTJ in Figure 5.19 c.

---

[1] The back end of line (BEOL) is the second stage of IC fabrication, where the interconnects are formed.

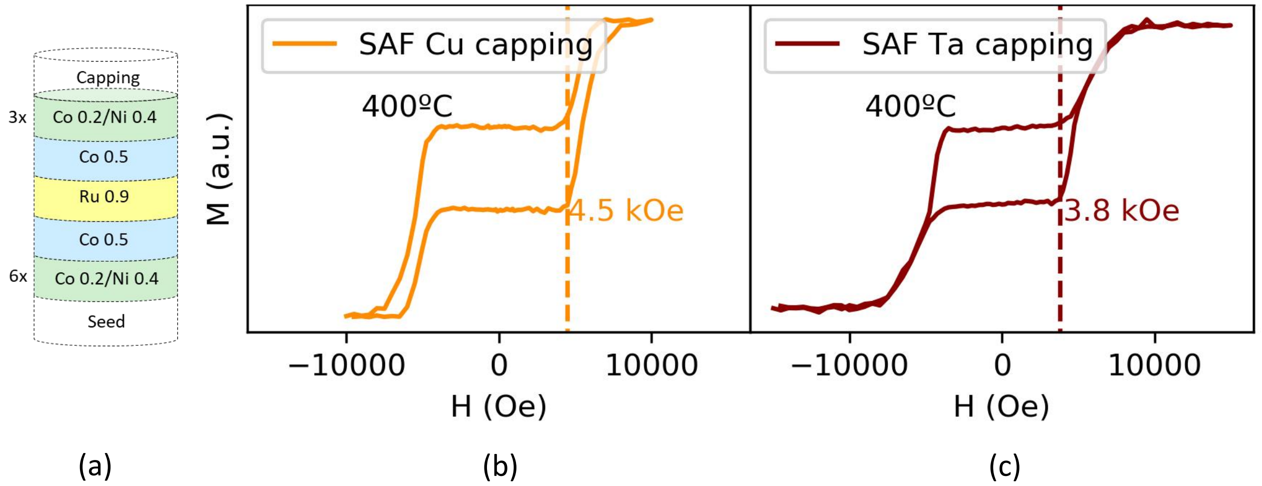

Fig. 5.20: VSM measurements under out-of-plane magnetic field of the SAF structure shown in (a) after annealing at 400°C for 10 minutes with a Cu capping (b) and a Ta capping (c).

The results shown in Figure 5.20 rule out the possibility that Ta diffusion into the multilayers is responsible for the large PMA loss, as the SAF with a Ta capping still maintains a large Hc. Therefore, it is most likely that it is the diffusion of Fe or B from the FeCoB reference layer into the multilayers that deteriorates the PMA of the SAF at high annealing temperatures. To simplify the analysis, we characterized Co/Ni multilayers coupled through a thin Ta layer of varying thickness to a 1.2nm FeCoB reference layer as shown in Figure 5.21 a.

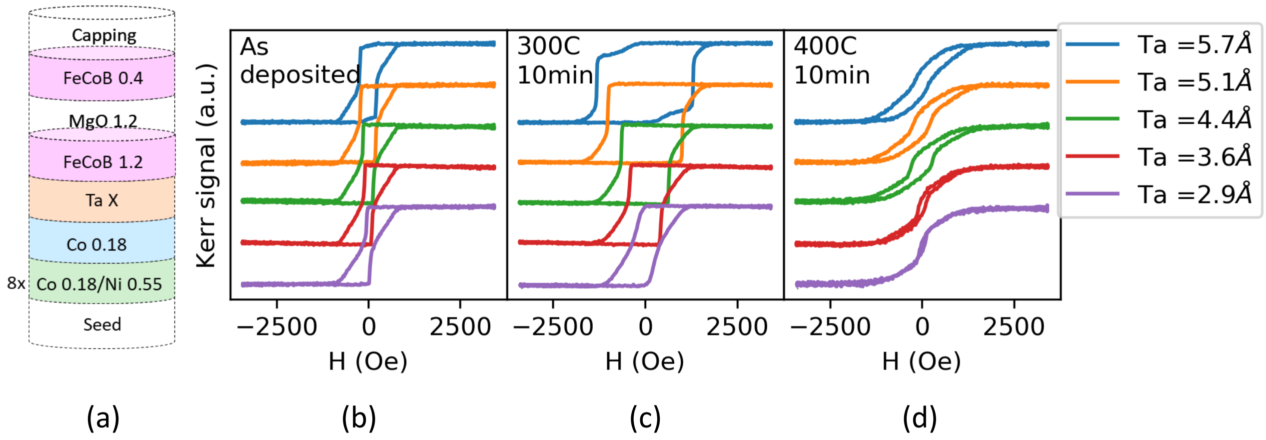

Fig. 5.21: Magneto-optical kerr effect (MOKE) measurements under an out-of-plane magnetic field of the reference layer structure depicted in (a) as deposited (b), after a 10 min annealing at 300°C (c) and 400°C (d) respectively. The colors show the dependence of the magnetic properties on the thickness of the Ta texture breaking layer between the FeCoB polarizer and the Co/Ni multilayers.

Figure 5.21 shows that the coercive field of the Co/Ni multilayers coupled with the reference layer increases from the as deposited state (b) after annealing at 300°C (c). The effect becomes more important when the thickness of the Ta layer acting as a boron getter is larger. We can observe in Figure 5.21 c that at 5.1Å (orange line), the Hc increase is maximum while the coupling is maintained, while moving towards 5.7Å (blue line), the FeCoB layer and the Co/Ni multilayers get decoupled.

Figure 5.21 d shows that the PMA is lost under 400°C annealing and the switching field becomes very low.

The results shown in Figure 5.21 confirm that the degradation of magnetic properties after annealing at 400°C takes place for the complete MTJ structure. However, this was not the case for SAF alone, as shown in Figure 5.20. Figure 5.21 also suggests that increasing the Ta layer thickness could be beneficial for the coercivity of Co/Ni multilayers, but the coupling with the FeCoB polarizer may excessively reduce at large thicknesses. Therefore, a compromise has to be found.

To improve the magnetic properties of the multilayers and at the same time have a sufficiently large coupling across the Ta texture breaking layer, we have developed a Ta/Co/Ta composite texture breaking layer as shown in Figure 5.22 a.

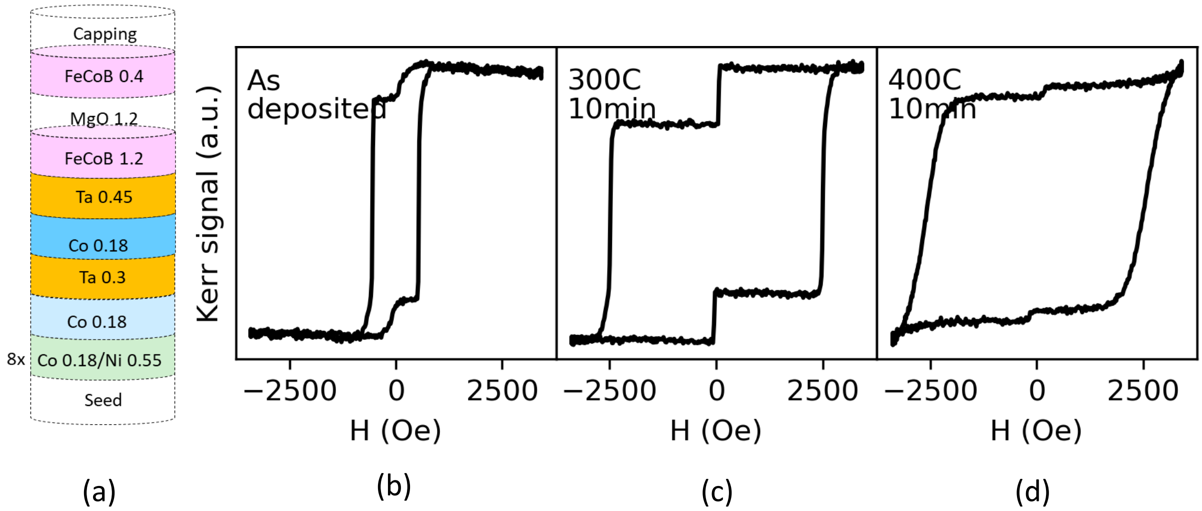

Fig. 5.22: Magneto optical kerr effect (MOKE) measurements under out of plane magnetic field of the reference layer structure depicted in (a) with composite Ta/Co/Ta texture breaking layer as deposited (b), after annealing for 10 minutes at 300°C (c) and 400°C respectively (d).

Figure shows 5.22 that in the as deposited state (b) and after annealing at 300°C (c), the FeCoB and Co/Ni reference layers are decoupled. Furthermore, we observe that the coercivity of the Co/Ni multilayers is strongly increased after 300ºC annealing with respect to the previous structure shown in Figure 5.21 c, where a single Ta layer was used as a diffusion barrier between the FeCoB reference layer and the Co/Ni multilayers. This structure would not be suitable due to the decoupling between the two parts of the reference layer. However, after annealing at 400°C, an intermixing effect occurs in the Ta/Co/Ta layer which makes the coupling stronger, as shown in Figure 5.22 d.

We incorporated this Ta/Co/Ta boron getter layer into a full MTJ stack with a complete SAF structure composed of Co/Ni multilayers, as shown in Figure 5.23 g. Figure 5.23 a shows an MTJ with a conventional 0.3 nm Ta getter for comparison, and the respective VSM H-M loops under perpendicular field are shown for different annealing temperatures 300ºC (b), 325ºC (c), 350ºC (d), 375ºC (e) and 400ºC (f). The switching field of the reference layer gradually decreases with increasing annealing temperature until a sharp reduction after 400°C annealing (f). However, it is observed that for the case of using a composite boron getter layer (Ta/Co/Ta) as shown in Figure 5.23 g, the resulting switching field remains large and even increases with increasing annealing temperature (h-l).

Figure 5.23 g shows that the SAF switching field with Ta/Co/Ta spacer remains large even after 400°C annealing, while for the case of a single Ta layer, as in Figure 5.23 f, a strong reduction occurs.

The switching fields of the SAF at different annealing temperatures in Figure 5.23 b-f (in black) and h-l (in green) are shown in Figure 5.24 respectively.

It is shown here that the main source of Hc decay in the complete MTJ structure is the migration of elements from the FeCoB layer into the SAF. The use of a thicker diffusion barrier, such as (Ta/Co/Ta), allows maintaining a high Hc after annealing at 400°C, as seen in Figure 5.24. However, the coupling between the FeCoB reference and the SAF could be compromised due to the large thickness of this barrier.

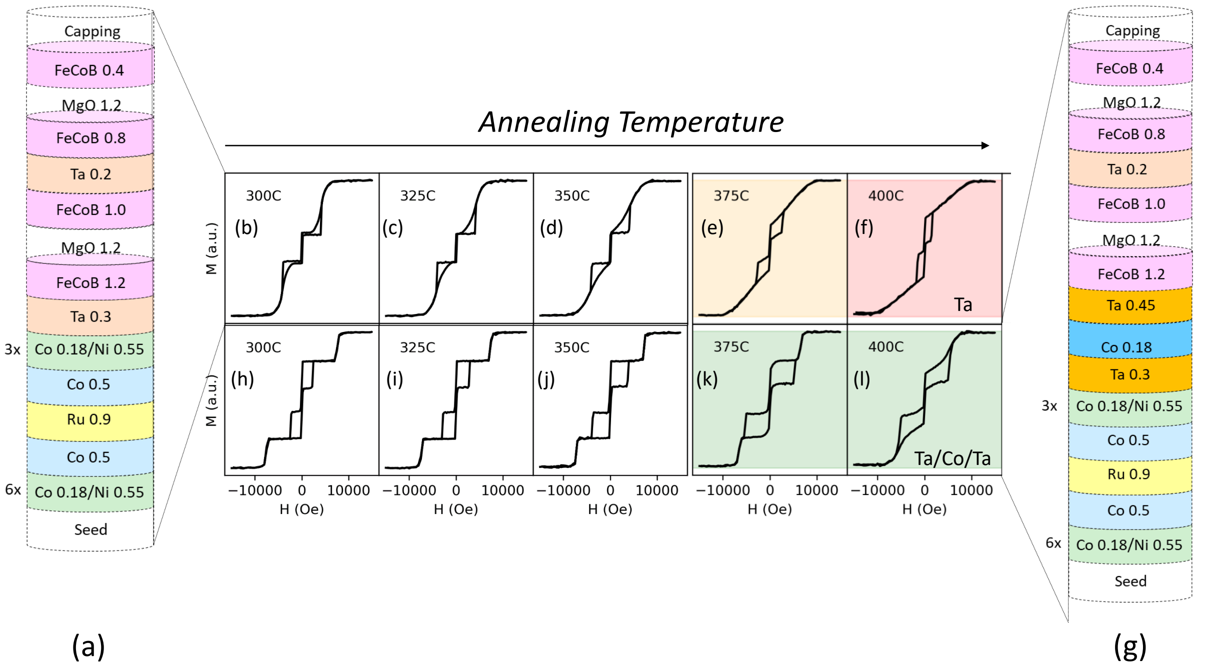

Fig. 5.23: Magneto-optical kerr effect (MOKE) measurements under an out-of-plane magnetic field of the reference layer structure depicted in (a) with a single Ta insertion or (b) with a composite Ta/Co/Ta insertion layer. The M-H loops show the dependence of the magnetic properties for different annealing temperatures (300°C, 325°C, 350°C, 375°C and 400°C). The upper graphs (b-f) correspond to the structure of (a), while the lower graphs (h-l) correspond to the structure of (b).

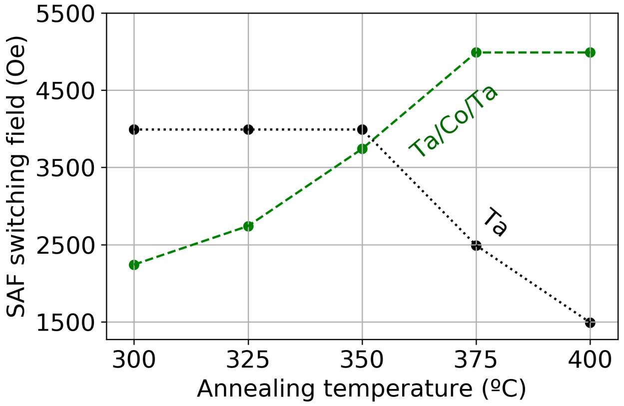

Fig. 5.24: Switching field of the Co/Ni SAF at different annealing temperatures of the VSM hysteresis loops shown in Figure 5.23, for the case of a single boron getter Ta layer, as in Figure 5.23 a (in black) and a composite Ta/Co/Ta layer, as in Figure 5.23 g (in green).

5.2.6 Electrical results of Co/Ni based SAF with high annealing tolerance

Finally, we patterned MTJs with the Co/Ni based SAF after annealing at 400°C with the previously developed Ta/Co/Ta trilayer structure. As explained above, this composite layer acts as a boron getter and diffusion barrier, protecting the SAF while maintaining some coupling with the FeCoB reference layer after annealing. Figure 5.25 a shows such a structure.

The R-H loops of this type of device, shown in Figures 5.25 b and c, show that the reference layer still maintains its PMA even after annealing at 400°C.

The R-H minor loop in Figure 5.25 b shows a stray field of 250 Oe, in agreement with the calculations in Figure 5.17. The free layer writing operation can still be performed, even after this high annealing temperature (400°C). The stray field of the reference layer in the free layer is relatively high and makes the free layer only stable in the parallel state at zero field. However, the stray field compensation can be further optimized by varying the number of Co/Ni repeats, as explained in Section 5.2.4.

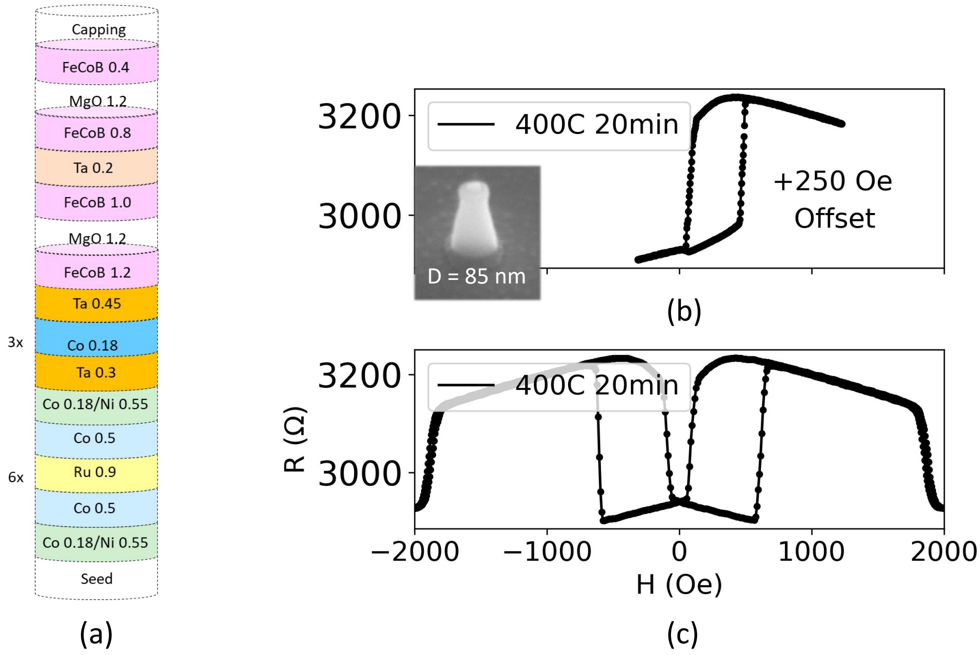

Fig. 5.25: Stack structure of the fabricated devices (a). R-H loops of the patterned MTJs at diameters below 100 nm under perpendicularly applied field (b,c). The MTJs were annealed at 400°C for 20 minutes. The inset in (b) shows an SEM image of a pillar after the IBE process.

To further optimize the Co/Ni based SAF for high annealing temperature tolerance, the insertion of a thinner W- or Mo-based boron getter would be highly appropriate. It has previously been reported that W or Mo have lower interdiffusion than Ta at high annealing temperatures, without requiring large thicknesses. In the previous section, we have shown that the interdiffusion of elements from the FeCoB reference layer is mainly responsible for the degradation of the SAF properties. Therefore, the combination of such W or Mo getter layers with the Co/Ni based SAF, which shows good magnetic properties at high annealing temperatures as shown in Figure 5.20, could be an ideal solution for BEOL process compatibility. Devolder et al. reached a similar conclusion for the case of a thin SAF at thin film level [203].

5.2.7 Real time measurements: reference back-hopping for stochastic computing or cybersecurity applications

Superparamagnetic MTJs are used to generate random telegraph noise (RTN) for stochastic computing or cybersecurity applications[214, 215]. Recently, it has been reported that in-plane MTJs can be advantageous as they can result in faster RTN [216, 217]. Dwell times as low as 2-8 ns were reported, 5 order shorter than for the perpendicular case [214, 218], as seen in Figure 5.26 a and b, for the perpendicular and in-plane case respectively. Note the different time scale on the x-axis.

In contrast to previous observations, we have observed that RTN, with short dwell times, can also be obtained in p-MTJs with a Co/Ni-based SAF. We performed real-time resistance measurements of a MTJ with a Co/Ni reference layer, with the following stack composition: Ta 22 / FeCoB 0.8 / Ta 3 / Cu 3 / 6x[Co 0.2/ Ni 0.4] / Co 0.5 / Ru 0.9 / Co 0.5 / 3x[Ni 0.4/Co 0.2] / Ta 0.3 / FeCoB 1.2 / MgO 1.2 / FeCoB 1.5 / Capping. The stack was annealed at 300ºC for 10 minutes. The measurements were performed by Dr. Bruno Texeira using an existing set-up that he optimized. Details of the set-up can be found in Appendix C. .

The hysteresis loop was measured in the setup as a first step, ramping the external field and taking the resistance value, as seen in Figure 5.26 c. The offset field experienced by the magnetic free layer is thus determined and compensated during the measurement. The coil generating the field is controlled by an applied voltage, while the exact value of the field is not measured in situ. A rough estimate, based on a previous calibration, puts the compensation field at 177 Oe.

Next, the resistance state of the MTJ is observed in real time for increasing voltages, from 423 mV to 800 mV, as seen in Figure 5.26 d. Figure 5.26d shows that for a pulse of 585 mV (pink trace) a single switching event occurs. However, as the voltage increases, the back-hopping phenomenon is observed, as for 638 mV (dark green trace). As the voltage is further increased, as in the case of 692 mV (orange trace), a higher number of transitions is observed, showing that the number of transitions between both resistance states can be controlled by the applied voltage.

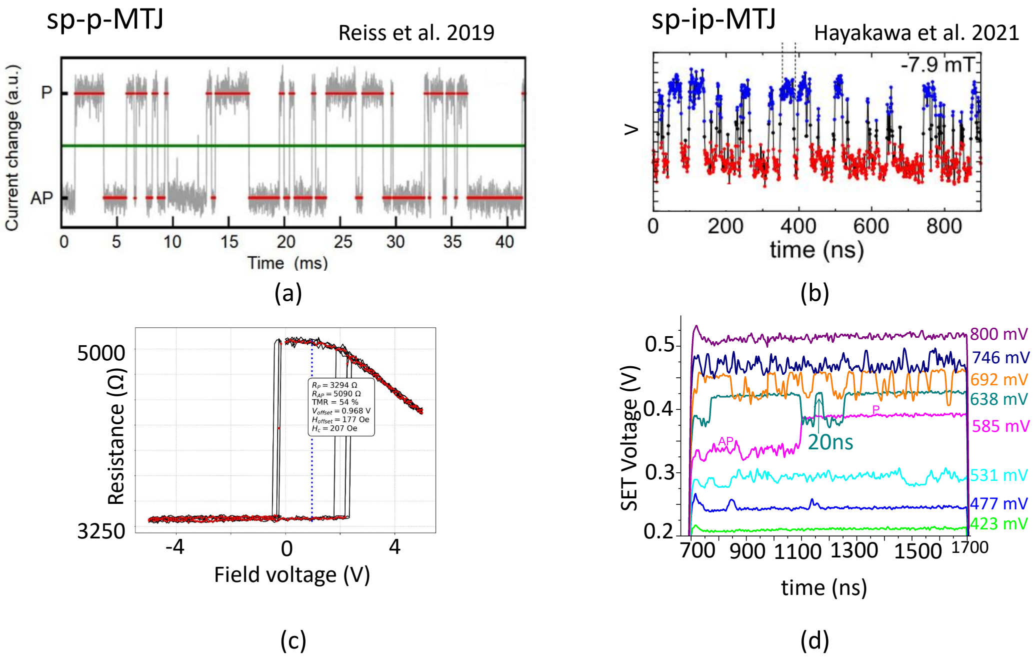

(a) (b) (c) (d)

Fig. 5.26: Real time signals of a superparamagnetic p-MTJ (a) [214] and in-plane MTJ (b) [216]. Hysteresis loop of our p-MTJ device (c). Real-time signal of our p-MTJ, for increasing applied voltages (in different colors) (d).

The main advantage that we observe in our junctions, as seen in Figure 5.26 d, is that dwell times can be as low as 20 ns, in the same ns range as for in-plane superparamagnetic MTJs, while still using a perpendicular configuration. In this case, we associate the telegraphic noise with the backhopping of the reference layer. Previous studies reported the use of an unstable reference layer for building all spin artificial neural networks [219]. The device presented here has the same characteristics, with the advantage of shorter dwell times.

The RTN shown here is ascribed to the spin-flop transitions occurring within the SAF/reference layer as in Figure 1.26 c. Furthermore, Figure 5.26 d shows that the amplitude of the resistance fluctuations decreases with applied voltage, as can be observed at 800 mV (purple trace). This decrease in TMR is a characteristic of Joule heating, due to the large applied voltage for 1000 ns, which may explain the decrease in stability of the reference layer and the observed RTN.

We note from the R-V results in Figure 5.15, for which conventional shorter pulse times of 100 ns were used, that the spin flop that appears when applying an external perpendicular field should not affect the performance of the MTJ as a memory element. However, more write error rate (WER) measurements should be performed to check the stability of the reference layer under a large number of write cycles.

5.3 Conclusions

In this chapter, we studied first the use of a Co/Pt reduced SAF. However, we have seen that its stability is not sufficient and reducing the amount of critical Pt does not solve the problem of its high supply risk. Therefore, we investigated an alternative Co/Ni based SAF. The use of non-critical Cu as seed layer enabled large Co/Ni multilayers coercive field values due to its fcc (111) texture that promotes a large PMA in Co/Ni multilayers. Patterned MTJs with a Co/Ni based SAF have demonstrated the reference layer stability under applied fields up to 3kOe and STT switching of the free layer. However, at large annealing temperatures, up to 400ºC, the intermixing of elements from the reference layer deteriorate the Co/Ni SAF stability. The use of thicker Ta layers between the reference layer and SAF structure improves the stability but deteriorates the coupling. A structure composing a Ta/Co/Ta spacer has been proposed with promising results, but the use of thinner layers with more robust elements as W or Mo is expected to demonstrate the BEOL compatibility of the Co/Ni SAF. Finally, we have shown an interesting RTN in MTJs showing a spin-flop transition within the SAF/Reference layer element, with short dwell times, which is attractive for stochastic computing or cybersecurity applications.

Chapter 6

Vortex magnetic sensor sensitive to out-of-plane field

Magnetic tunnel junctions and spin valves are widely used as magnetic sensors due to their high field sensitivity, compact size, low power consumption, compatibility with CMOS integration, and low cost [92]. Various automotive applications, such as wheel speed and current sensing, require a long magnetic field range sensor with linear operation without hysteresis. Vortex-based sensors have been proven to be good candidates for such applications, due to their linear response with low magnetic noise [94, 95, 96].

In this chapter, we develop a vortex-based magnetic sensor sensitive to an out-of-plane field with a very large linear operating range, at smaller diameters than conventional vortex-based sensors.

As for materials, previous vortex-based sensors typically use a few nanometers of an antiferromagnetic layer, $Ir_{20}Mn_{80}$ or $Pt_{50}Mn50$, to fix the in-plane magnetized reference layer in a certain direction by exchange bias [96, 95, 220, 221]. The high criticality of platinum has already been discussed extensively in Chapter 2. Nonetheless, iridium is also a critical material, scarcer even than platinum and more expensive [222]. Very high price volatility has been observed for Ir in the last years, as seen in Figure 6.1 a, with a price peak approaching 200€/g due to processing disruptions in South Africa [223]. Iridium is a co-product of the mining production of platinum (Pt) and palladium (Pd) and its global production is still quite small compared to the other two, as seen in Figure 6.1 b, which makes its substitution very attractive.

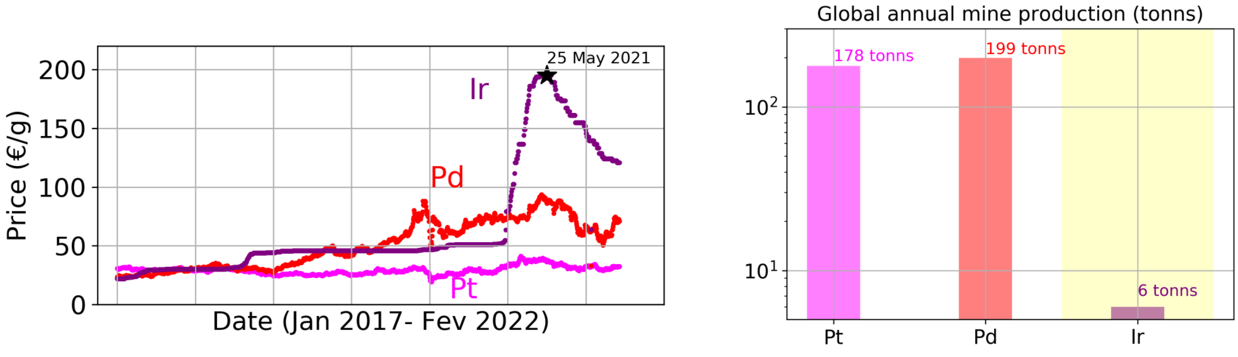

(a) (b)

Fig. 6.1: Evolution of Pt, Pd and Ir prices from January 2017 to February 2022. Data from [224] (a). World annual mining production of these metals for the period 2012-2016. Data from [127]

.

Research is underway to use alternative antiferromagnetic materials to iridium such as Heusler alloys for spintronic devices [222]. In the innovative vortex-based magnetic sensor proposed in this chapter, an out-of-plane magnetized reference layer is used. This allows to use a synthetic antiferromagnetic structure as the one developed in Chapter 4, based on Co/Ni multilayers, without Pt and without Ir. In the results shown here, a Co/Pt-based SAF was used due to the unavailability of Ni in the tool at the time of the study. However, similar results can be predicted using a Co/Ni based SAF. Furthermore, the proposed device features several other advantages such as smaller diameters and larger linear range compared to conventional vortex-based magnetic sensors.

6.1 Working method: large thickness/diameter aspect ratio

Conventional vortex based sensor have a low thickness to diameter ratio (t/D), as the sensing layer thickness is usually an order of magnitude smaller than the diameter, often being the later in the micrometer range.

The vortex structure is stable for certain geometries due to a minimization of the total energy of the system which includes the exchange energy arising from the non-uniformity of the vortex structure, the magneto-static energy from dipolar interactions, the magneto-crystalline anisotropy energy and the Zeeman energy if an external field is applied [225]. In such geometries, magnetostatic energy dominates the exchange energy, resulting in the formation of a vortex configuration that corresponds to an in-plane curling of the magnetic moments allowing an in-plane flux closure while the vortex core is out-of-plane magnetized. For low thickness to diameter ratios (t/D), the diameter of the core is given by the exchange length, $l_{ex} = \sqrt{\frac{A}{\frac{1}{2}\mu_0 M_s^2}}$, around 5 nm for conventional ferromagnetic materials such as Permalloy or Co.

The transfer-curve of those conventional sensors under an in-plane applied field is seen in Figure 6.2 b. The linear variation of the MTJ resistance comes from the displacement of the out of the plane magnetized vortex core of the sensing layer in a direction perpendicular to the in-plane applied field.

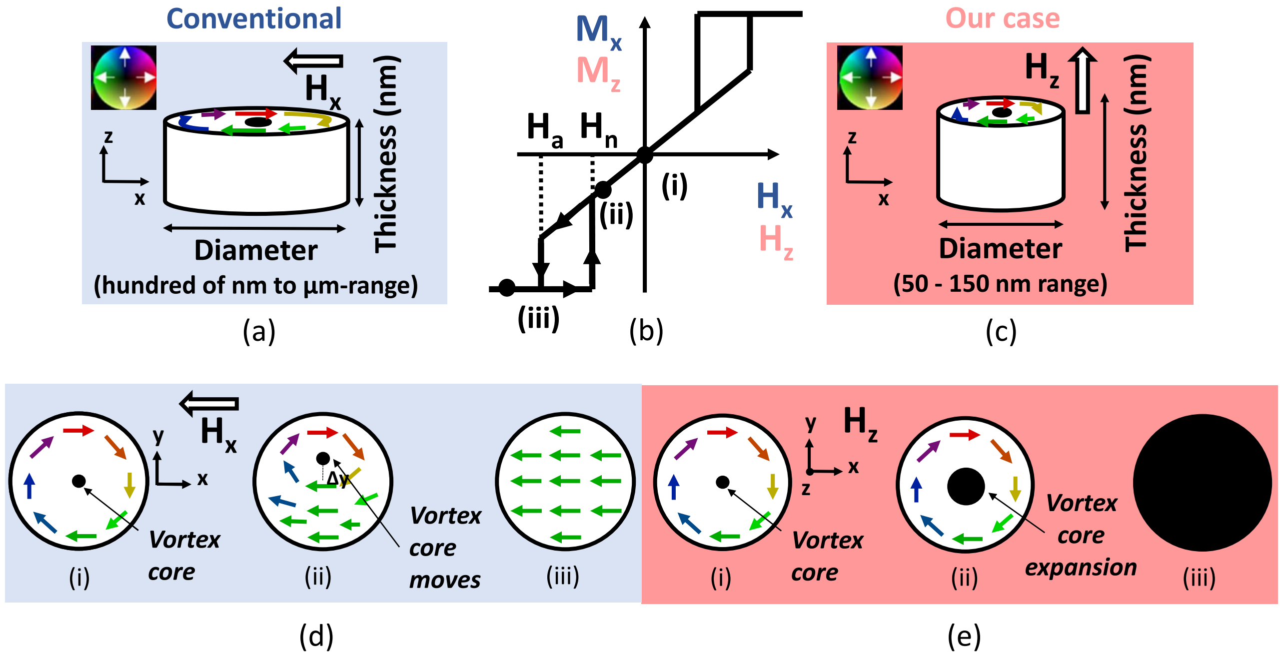

Fig. 6.2: Schematic representation of a conventional in-plane field-sensitive vortex-based sensor (a) and our proposed device, an out-of-plane field-sensitive vortex-based sensor (c). The theoretical transfer curve of both vortex-based sensors under the action of an in-plane magnetic field (Hx) or an out-of plane magnetic field (Hz) respectively (b). For both cases, the vortex stabilizes at zero field, with its core magnetization (represented in black) perpendicular to the plane (d(i) and e(i)). For the conventional case, the core of the vortex moves in a direction perpendicular to the applied magnetic field in the plane (d(ii)), until it annihilates at saturation (d(iii)). For the out-of-plane field-sensitive vortex-based sensor, the linear variation in resistance comes from the expansion of the vortex core (e(ii)), until it completely annihilates (e(iii)) in a single perpendicular domain.

At zero field, a flux-closure vortex state stabilizes in the sensing layer, as seen in Figure 6.2 d(i).

Under an external magnetic field in the plane, the vortex is displaced in a direction orthogonal to the applied field. As seen in Figure 6.2 d(ii), the core of the vortex moves in the y direction while the magnetic field is applied in the x direction. Finally, at a certain field, known as the annihilation field (Ha), the vortex annihilates and a single magnetic domain oriented in the direction of the applied field stabilizes, as seen in Figure 6.2 d(iii). When the magnetic field decreases, the vortex re-nucleates at a certain magnetic field known as the nucleation field (Hn). The mechanism of vortex re-nucleation under an applied in-plane field has been recently studied by Wurft et al. [226]. They see how for low thickness to diameter (t/D) ratios, vortex nucleation is initiated by buckling, which induces smaller nucleation and annihilation fields and therefore smaller linear operation range. For larger t/D, the buckling is almost avoided and the nucleation takes place via double vortex formation. However, the study covered geometries down to 300 nm in diameter, remaining in a regime $t/D < 0.1$.

We propose a device that makes use of an alternative operating mechanism. Our device has a smaller diameter and larger t/D aspect ratio than conventional vortex-based sensors as schematically seen in Figure 6.2 c. By reducing the diameter of our MTJs to achieve an aspect ratio (t/D) close to 1, the in-plane demagnetizing energy is reduced. Under the application of an out-of-plane magnetic field, the transfer curve shows a resistance variation in the MTJ due to the broadening or shrinking of the vortex core, rather than its translation. The vortex state is stable at remanence, as shown in Figure 6.2 e(i), as in the previous case. However, applying a perpendicular field, Hz, the perpendicularly magnetized vortex core expands, as in Figure 6.2 e(ii), until it is completely annihilated as seen in Figure 6.2 e(iii). Micromagnetic simulations of the sensing layer reversal are shown in the next section.

The advantage of such a device, in terms of materials, is that the use of Ir or Pt is no longer required, as only a stable perpendicular reference layer is needed. As we saw in Section 5.2, a SAF based on Co/Ni could be an ideal candidate for such an application.

6.1.1 Tolerance to defects or local anisotropy fluctuations

In conventional vortex-based sensors sensitive to an applied in-plane field, the core of the vortex can be trapped during its motion due to local anisotropy variations or structural defects at the interface between the oxide barrier and the sensing layer, as seen in Figure 6.3 a.

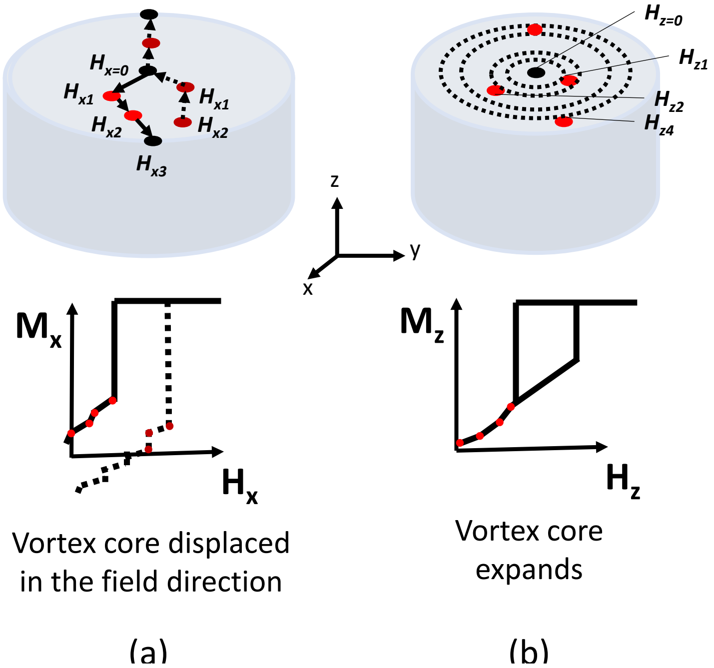

Fig. 6.3: Vortex core displacement path in conventional vortex sensors in the presence of defects (red circles) and its respective effect on the transfer curve (a) vortex expansion path in the presence of defects for the out-of-plane vortex sensor (b).

Such difference in anisotropy can arise due to different local concentrations of oxygen, boron, or other elements present in the MTJ that can diffuse, which generates noise, equivalent to Barkhausen noise in domain wall propagation.

The randomly distributed defects can modify the vortex core displacement path, leading to different resistance values at each applied field value [227] as seen in the M-H response schematically shown in Figure 6.3 a.

However, for the case of the out-of-plane sensitive vortex sensor, the vortex core is a much bigger object which expands or contracts depending on the field to be sensed. Due to its larger size, the local fluctuations of anisotropy are averaged on a larger area so that in its expansion/contraction, the pinning is much less effective than for in-plane vortex sensor. This is illustrated in Figure 6.3 b, yielding a more reproducible R(H) transfer curve. Therefore, the proposed sensor can exhibit a significant noise reduction compared to conventional in-plane vortex sensor.

6.2 Micromagnetic simulations for sensing range optimization

In this section, the effect of the diameter and saturation magnetization of the sensing layer on the amplitude of the linear range of the sensor transfer curve is studied. The simulations have been carried out using MuMax3 [188]. It allows to calculate the space and time dependent magnetization dynamics in nanometer sized ferromagnets, using a finite difference discretization.

6.2.1 Linear range dependence on diameter

The reversal of a sensing layer with a thickness of 60 nm and saturation magnetization, M_s= 0.8e-6 A/m, as for $Ni_{80}Fe_{20}$ has been simulated. Figure 6.4 a shows the M-H loops resulting from the magnetization reversal process for different diameters under a perpendicular applied field.

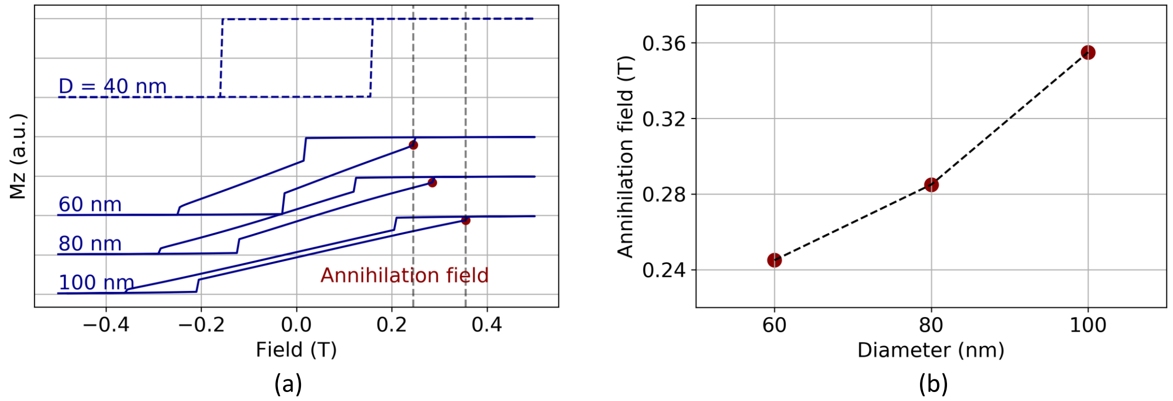

Fig. 6.4: Simulated M-H loops under external perpendicular field along the thickness axis for different diameters (a). Vortex annihilation field versus sensing layer diameter is plotted (b). The material parameters used for the sensing layer are as follows: M_s= 0.8e6 (A/m), A_{ex}= 13e-12 (J/m), α = 0.01

Figure 6.4 a shows that the reversal between two stable states occurs abruptly at low diameters, as 40 nm (dashed line), for which the shape anisotropy is large enough to make the magnetization align parallel to the long axis (i.e. the vertical direction). However, at diameters of 60 nm or larger, the magnetostatic energy favors a flux closure vortex state at zero field (solid lines).

Figure 6.4 b shows that the annihilation fields increased when increasing the diameter. The tunability of the nucleation and annihilation fields with the diameter is interesting for sensor applications, since the linear range of the transfer curve and sensitivity can be controlled for the desired application. Similar geometrical dependence was reported for vortex sensors based on the vortex core motion under an in plane applied field [228].

The micromagnetic configurations of the sensing element during the reversal process are shown in Figure 6.5 a, for different magnitudes of perpendicular applied field. The corresponding M-H loop is given in Figure 6.5 b. Figure 6.5 a shows how starting from negative saturation (i) the vortex state is stable at zero field (ii) with negative core polarity and how increasing the field reduces the diameter of its core (iii).

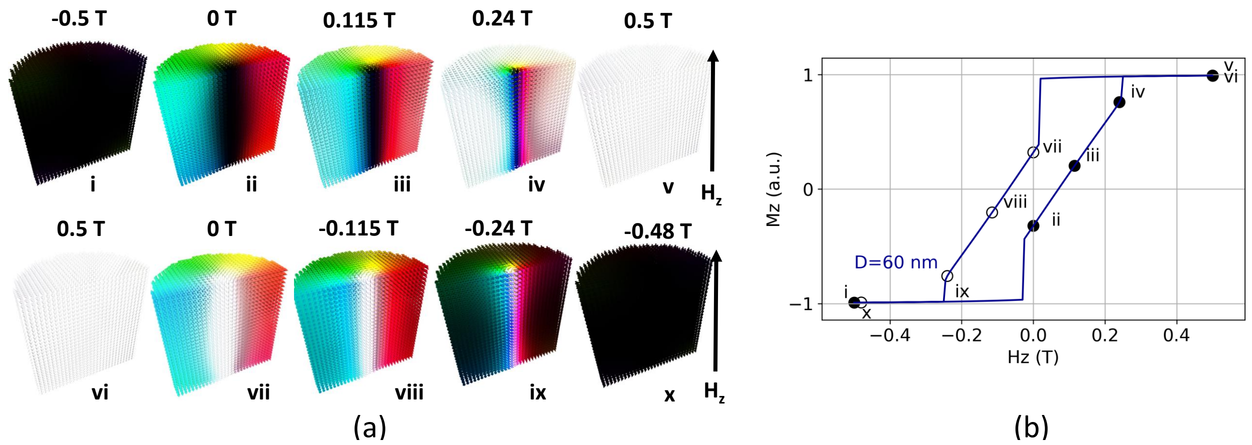

Fig. 6.5: Snapshots of the longitudinal cross section of the magnetization during the reversal of the sensing layer with D= 60 nm t = 60nm and M_s = 0.8 MA/m (a), with its respective simulated M-H loop (b).

Eventually, the vortex is annihilated as the magnetization of the outer core region rotates coherently in the same direction as the applied external field (iv) until total annihilation of the vortex core occurs (v). If the external perpendicular field decreases from positive saturation (vi), the vortex nucleates with an opposite polarity (vii), now positive. Such a change in polarity of the vortex core results in the magnetization difference observed in Figure 6.5 b, between (ii) and (vii). This vortex polarity change in the out-of-plane field-sensitive vortex-based sensor could lead to an undesired magnetoresistance difference if the device is exposed to annihilation fields in opposite directions. Some details and ways to get around these problems are given in the experimental Section 6.4.3.

6.2.2 Linear range dependence on saturation magnetization

We have seen that the nucleation and annihilation fields can be controlled by varying the diameter of the MTJ. By modifying the saturation magnetization (M_s) of the sensing layer the linear regime of the sensor is also affected as seen in Figure 6.6 a.

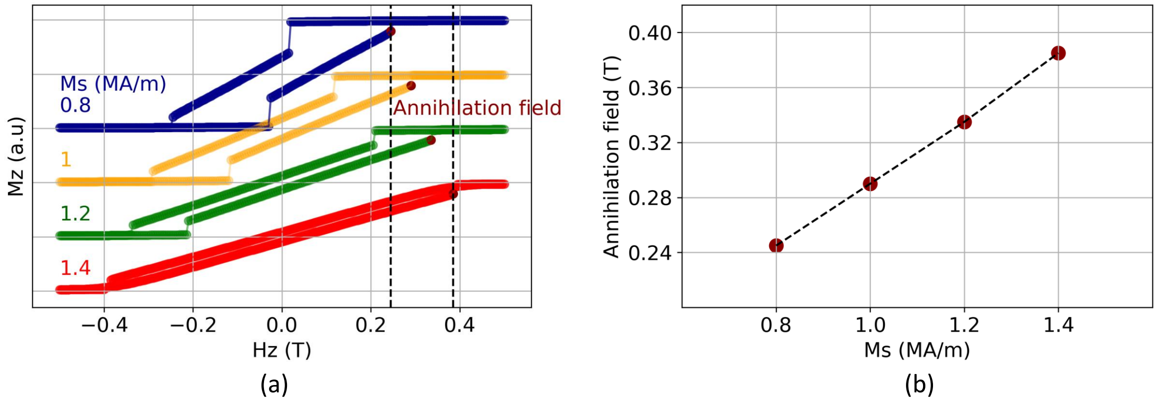

Fig. 6.6: Simulated M-H loops under external perpendicular field for different saturation magnetization values of the sensing layer, for an element with D = 60nm and thickness = 60nm.

Larger magnetic saturation values lead to larger annihilation fields, as seen in Figure 6.6 b. For the case of M_s = 0.8 MA/m, as for NiFe, the simulated annihilation field is 0.24 T, and it increases to 0.38 T using a material with M_s = 1.4 MA/m, close to that of cobalt.

6.3 Imaging the vortex state by off-axis electron holography

Off-axis electron holography enables imaging of magnetization within nanoscale materials. Vortex states have been observed in ferrite nanoparticles using this technique [229], or the PSA-STT-MRAM free layer stability has been tested under a wide temperature range up to 250ºC [184, 230].

The images shown here were made by Dr. Tevor Almeida at CEA-LETI. TEM samples were prepared by etching the pillars using the process described in Chapter 3, followed by deposition of a protective layer (about 1 µm) of organic resin before depositing a protective layer of Pt by focused ion beam (FIB). Cross-sectional TEM lamellae were then transferred to Omniprobe copper slots and thinned using conventional FIB methods. The protective resin layer was removed by plasma etching and the remaining Pt layer was broken with the micromanipulator. A probe-Cs-corrected Thermo Fisher Titan TEM at 200kV was used for the STEM imaging. Off-axis electron holograms were acquired at remanescence in Lorentz mode on a Gatan OneView 4K camera using a Thermo Fisher Titan TEM equipped with an image-CS corrector and an electron biprism.

Figure 6.7 a shows a chemical map obtained by Energy Dispersive X-Ray Spectroscopy (EDX) of the MTJ pillar with a 58 nm thick NiFe sensing layer, indicated by the red and blue dots.

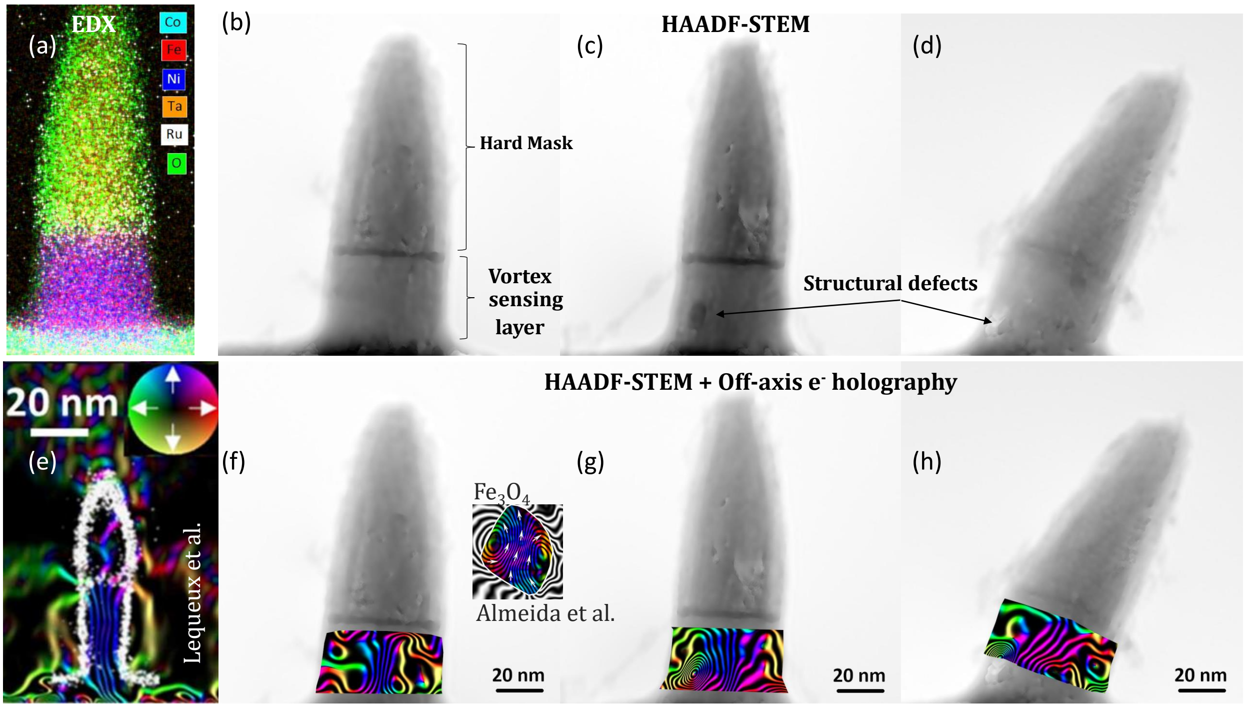

Fig. 6.7: Energy Dispersive X-Ray Spectroscopy (EDX) observation of a nanopillar revealing the chemical composition of the permalloy sensing layer, based on Ni (blue) and Fe (red) atoms. The Ta hard mask on top is covered by an oxide layer due to the exposure to atmosphere prior to the observation (a). High-angle annular dark-field scanning transmission electron microscopy (HAADF-STEM) observation of the nanopillars reveals some structural defects related to the ion beam etching process at grazing incidence (b-d). Magnetic induction maps reconstructed from holograms for a MTJ with 58nm NiFe free layer at remanence after saturation in the out-of-plane direction. The remanent magnetization state is uniform for low diameters below 20 nm (e), from [231]. At larger diameters, around 50-60 nm, only an out-of-plane magnetized core is observed (f-h). The inset of (f) shows the magnetic induction map of a ferrite nanoparticle showing a vortex state for comparison [229].

The Ta hard mask on top exhibits a surrounding oxide layer, highlighted in green, due to sample exposure to the atmosphere after the etching process and some residual resin remaining during preparation for STEM observation. Figures 6.7 b, c and d show high-angle annular dark-field scanning transmission electron microscopy images of three different pillars, where some structural defects appear in (c) and (d), attributed to grazing incidence ion beam etching used to slightly reduce the diameter of the pillars. The diameter of the MTJs is set between 50 and 60 nm, which corresponds to the region where a vortex state must be stabilized in the sensing layer, as seen earlier in the micromagnetic simulations of Figure 6.5 a(ii).

For small diameters, as in Figure 6.7 e, the magnetic induction map reveals a uniform stable state at zero field magnetized in the long axis direction. However, when the diameter increases, the magnetization is no longer uniform, and only the central core region of the sensing layer is magnetized in the perpendicular direction, as seen in the Figures 6.5 f, g and h. Structural defects result in some artifacts during holography observation, as seen by the rippling in Figures 6.5 g and h, at the position of the structural defects seen in Figures 6.5 c and d. However, the induction maps reveal a flux-closure vortex state, similar to that previously observed in the Fe_3O_4 nanoparticles in the inset of Figure 6.5 f.

6.4 Electrical results on patterned devices

As explained in the micromagnetic simulations section, the linear response field range of the vortex based sensor devices will depend on both the diameter and the material used for the free layer in the MTJ. In this section, we demonstrate the trends already predicted by the simulations. We also find means to avoid the vortex polarity change during the sensor operation.

6.4.1 Linear range dependence on diameter

First, we fabricated MTJs with a NiFe sensing layer with varying diameters. The micromagnetic simulations predicted an increase in linear range with MTJ diameter as seen in Figure 6.8 a. The experimental resistance response to the applied out-of-plane field showed a very similar transfer curve predicted by micromagnetic simulations as seen in Figure 6.8 b. MTJs were fabricated with a variable diameter, from around 65 nm to 120 nm, as seen in Figure 6.8 c. Both experimental results and micromagnetic simulations followed the same trend in that the annihilation field was increased for larger MTJ diameters. In MTJs with lower resistance (larger diameter), the annihilation takes place at larger external applied field values. A comparison between both simulated and experimental annihilation field values is given in Figure 6.8 d. The difference between the two is explained by the fact that for the micromagnetic simulations thermal fluctuations were neglected, whereas the core magnetization reversal and vortex annihilation/nucleation fields are thermally activated phenomena.

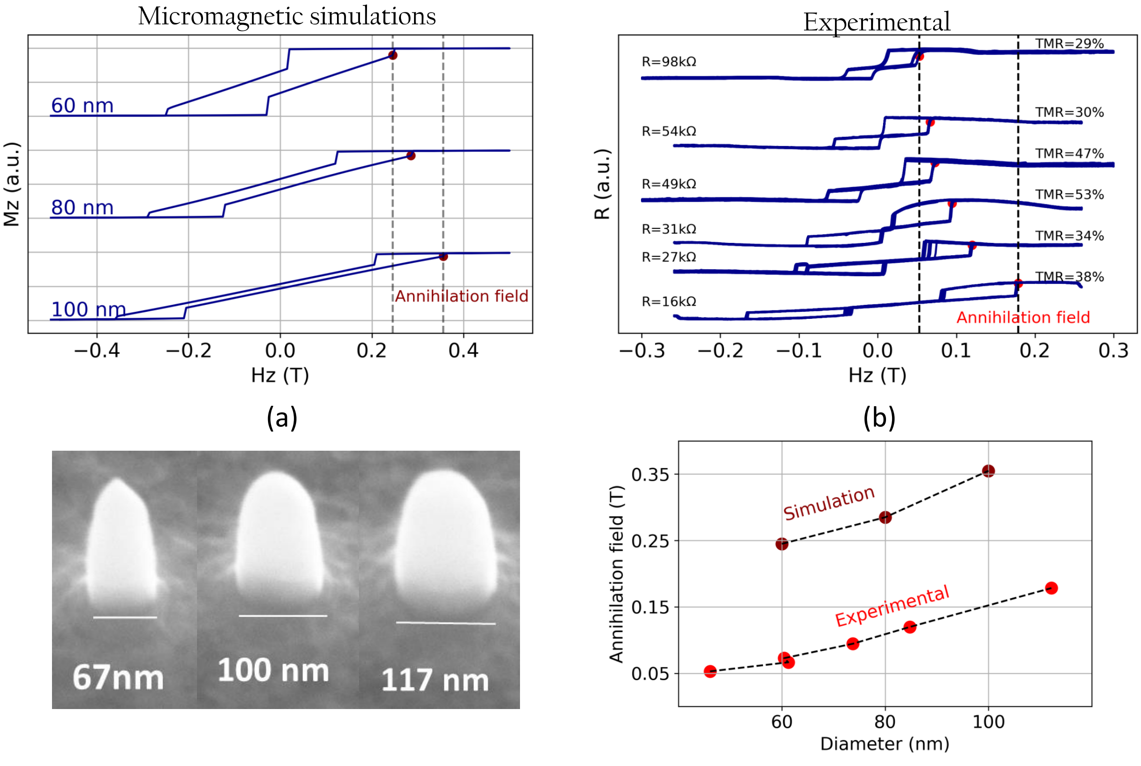

(a) (b)

(c) (d)

Fig. 6.8: Simulated M-H loops under external perpendicular field for different diameters: 60, 80 and 100 nm, for a sensing layer with M_s=0.8MA/m (a). Experimental R-H loops for MTJs with a NiFe sensing layer, with the following structure: Seed/4x[Co 0.5/Pt0.25]/Co 0.5/Ru 0.9/Co 0.5/3x[Co 0.5/Pt0.25]/Ta 0.2/FeCoB 1.1/MgO 1.2/ FeCoB 1.4/Ta 0.2/NiFe 58/Capping (b). The diameter is varied between ≈ 65 nm and 120 nm as observed in the scanning electron microscopy (SEM) images of the MTJs after the IBE etching process of the pillars (c). Comparison between the annihilation fields predicted by the simulations and the experimentally measured values (d).

6.4.2 Linear range dependence on saturation magnetization

To test the dependency of the linear range with the material of the sensing layer, we also fabricated MTJs with a cobalt sensing layer. It can be seen in Figure 6.9 that even before patterning, the magnetic response of both cobalt and permalloy is substantially different, NiFe being a softer material than Co.

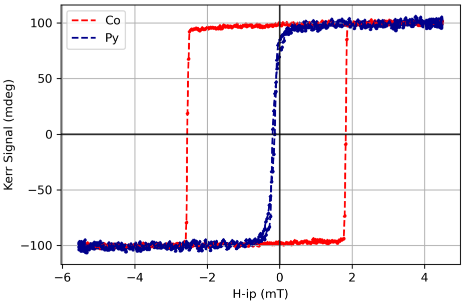

Fig. 6.9: NanoMOKE measurements of MTJ stacks with Co (red) or NiFe (blue) as free layers under an applied in-plane field at blanket level.

Figure 6.10 a-d shows SEM images of MTJs fabricated with a cobalt sensing layer with varying diameters.

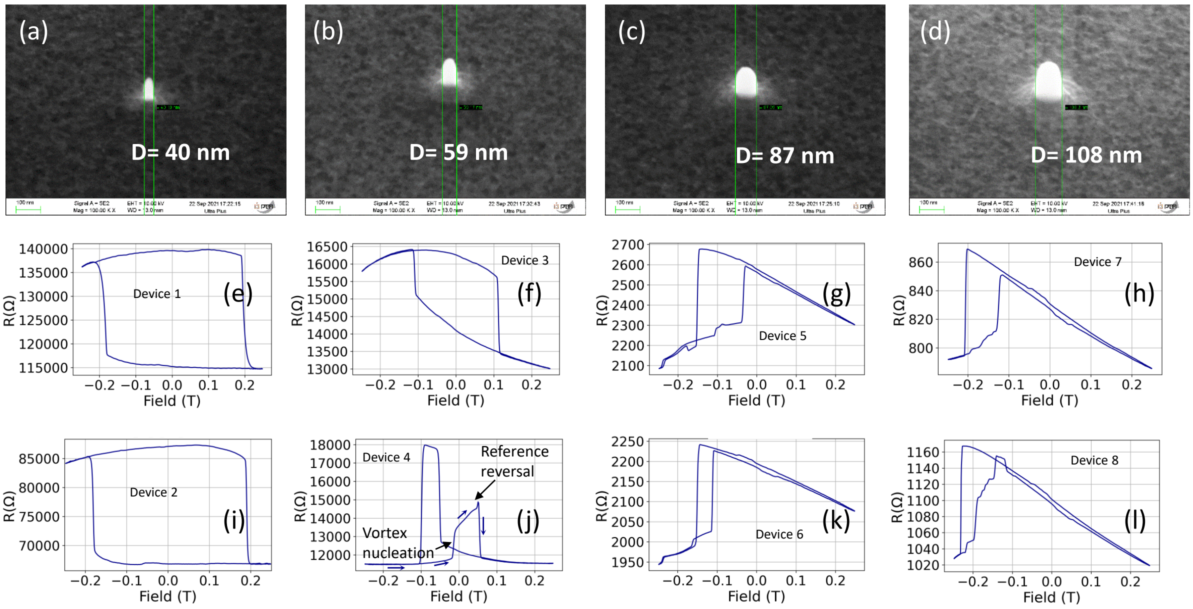

Fig. 6.10: SEM observation of fabricated MTJs with diameters ranging from ≈ 40 nm to 110 nm (a-d). Experimental R-H loops for MTJs with a Co sensing layer, with the following structure: Seed/6x[Co 0.5/Pt0.25]/Co 0.5/Ru 0.9/Co 0.5/3x[Co 0.5/Pt0.25]/Ta 0.2/FeCoB 1.0/MgO 1.2/ FeCoB 1.4/Ta 0.2/Co 58/Capping, at different diameters, corresponding to the SEM figure at the top of each figure column respectively (e-l).

The electrical results show that for low diameters, an abrupt reversal is observed, as seen in Figure 6.10 e and i, in line with the previous electron holography observations. These types of R(H) characteristics with high remanence are suitable for binary memory application. For for larger diameters, at values above 60 nm, we begin to observe a linear response characteristic of the vortex core expansion/shrinking which gets even more evident as the device diameter increases (Figure 6.10 g, 6.10 h, 6.10 k, 6.10 l), in Figure 6.10 j. In Figure 6.10 j, starting from negative saturation, it is observed that the vortex nucleates near zero field, but the reference layer reverses before annihilation of the vortex occurs. For larger diameter devices, Figures 6.10 g, h, k, l, the reference layer is also unstable and reverses before vortex nucleation and annihilation can be observed.

By limiting the measurement field range, we were able to observe the characteristic transfer curve of the vortex sensor before the reference layer reversed in some devices, as seen in Figure 6.11.

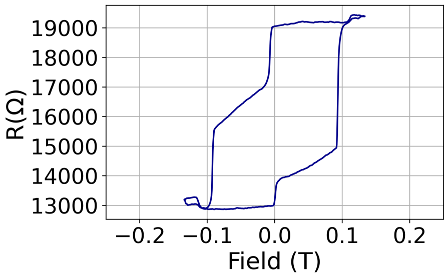

Fig. 6.11: R-H loop for a MTJ with field scan limited to 0.13 T, over which the reference layer is not reversed.

In addition, we were able to perform electrical measurements of the devices in a set-up developed by Hprobe [232] with a magnetic head providing larger perpendicular fields, resulting in the R-H response seen in Figure 6.12.

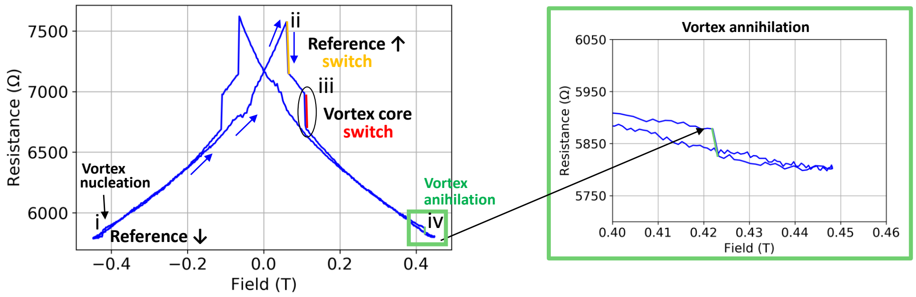

(a) (b)

Fig. 6.12: R-H loop for a MTJ with Co sensing layer with field scan up to 0.45 T, where the reference layer reversal is observed along with the vortex state nucleation and annihilation.

In Figure 6.12 a, it can be seen that starting from negative saturation and decreasing the field in absolute value, the vortex state nucleates (i), resulting in a linear variation of the resistance with the decrease of the field amplitude, due to the reduction in core diameter. After a certain positive field, the reference layer reverses (ii), highlighted in yellow, and the core of the vortex reverses in the positive perpendicular direction (iii), highlighted in red. Then, as the field keeps on increasing, the core of the vortex expands, aligned in the same direction as the reference layer, decreasing resistance, until finally it is annihilated at large fields (iv), greater than 0.4 T. Figure 6.12 b shows a zoom of the resistance variation due to vortex annihilation.

We improved the stability of the reference layer by reducing the thickness of the FeCoB polarizer, as seen in the VSM measurements of Figure 6.13. Reducing the thickness from 1.2 nm (black) to 0.8 nm (red) allowed the switching field to be slightly increased.

We fabricated devices with reference layer of enhanced coercivity and then could not observe any switching of the reference layer over a wide field range of more than 0.2 T, as seen in Figure 6.14 d.

Reference layer optimization allowed us to compare the linear range of devices with Co and NiFe sensing layers with similar diameters.

Patterned devices show that the linear range increases for junctions with a detection layer with larger M_s (Co-red, NiFe-blue), for similar diameters, as seen in Figure 6.15 b. Therefore, as predicted by the simulations, shown in Figure 6.15 a, we demonstrate that the nucleation and annihilation fields increase with the M_s of the sensing layer.

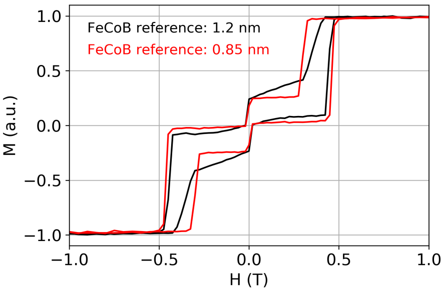

Fig. 6.13: VSM magnetic response of a MTJ with FeCoB polarizer in the reference layer varying from 0.85 to 1.2 nm at thin film level.

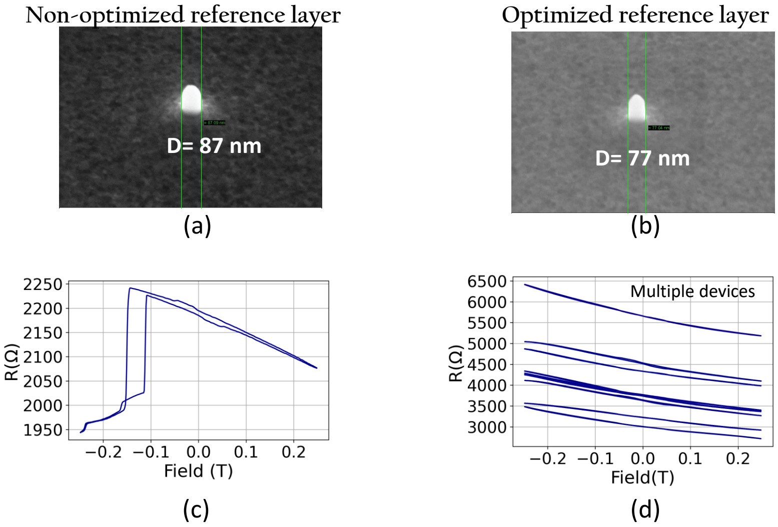

Fig. 6.14: SEM observation of MTJs after IBE etching with diameters of 87 and 77 nm, for the non-optimized (a) and optimized (b) reference layer cases. The R-H responses show the reference layer reversal (c) for FeCoB reference layer thicknesses of 1 nm, while the reference remains stable up to more than 0.2 T when the FeCoB thickness is reduced to 0.9 nm (d).

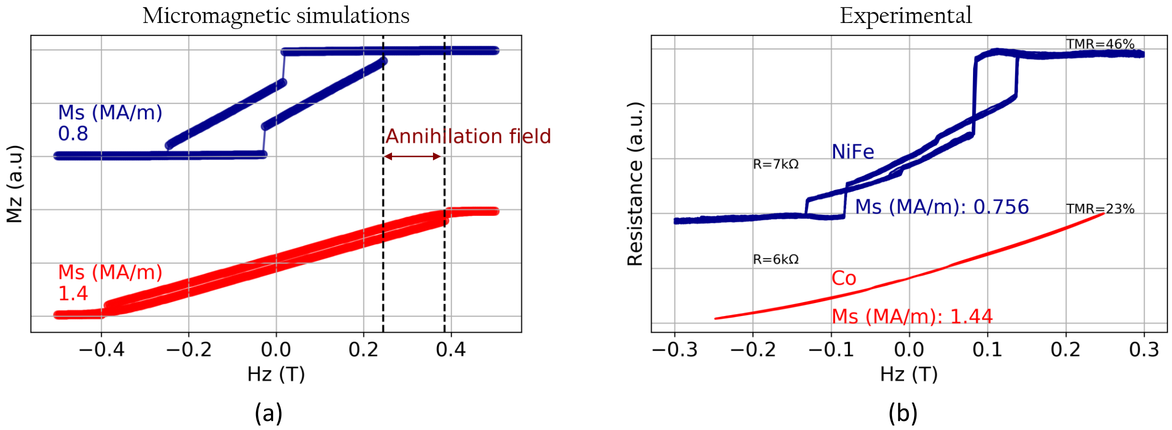

Fig. 6.15: M-H loops obtained by micromagnetic simulations for the reversal of a sensing layer with 60 nm diameter and thickness, for a different saturation magnetization value of 0.8 MA/m (blue) and 1.4 MA/m (red) (a). The R-H loops of patterned MTJs under an out-of-plane external field show the difference in linear range for both materials (Co in red, NiFe in blue).

6.4.3 Vortex polarity variation

One possible challenge that we need to overcome, already observed during the simulated reversal process in Figure 6.5, is the polarity change of the vortex core if the sensor is exposed to field values greater than the annihilation field in opposite direction.

A plausible solution would be to use an antiferromagnetic layer to provide an out-of-plane exchange bias to the core of the vortex, to stabilize it always in the same direction. However, as in the case of planar field-sensitive vortex-based sensors, this would require the use of IrMn or PtMn alloys containing the undesired critical PGM materials that we wish to avoid due to their high supply risk.

Figure 6.16 a and b shows that for devices whose nucleation fields (Hn) are rather symmetric, the vortex core polarity reversal takes place. The vortex core polarity reversal results in a shift in the resistance variation between the two linear regimes depending of the saturation direction. If the field is only scanned between values lower than the annihilation field at negative fields, as in Figure 6.16 c, the vortex core polarity remains always positive and a single linear response is observed.

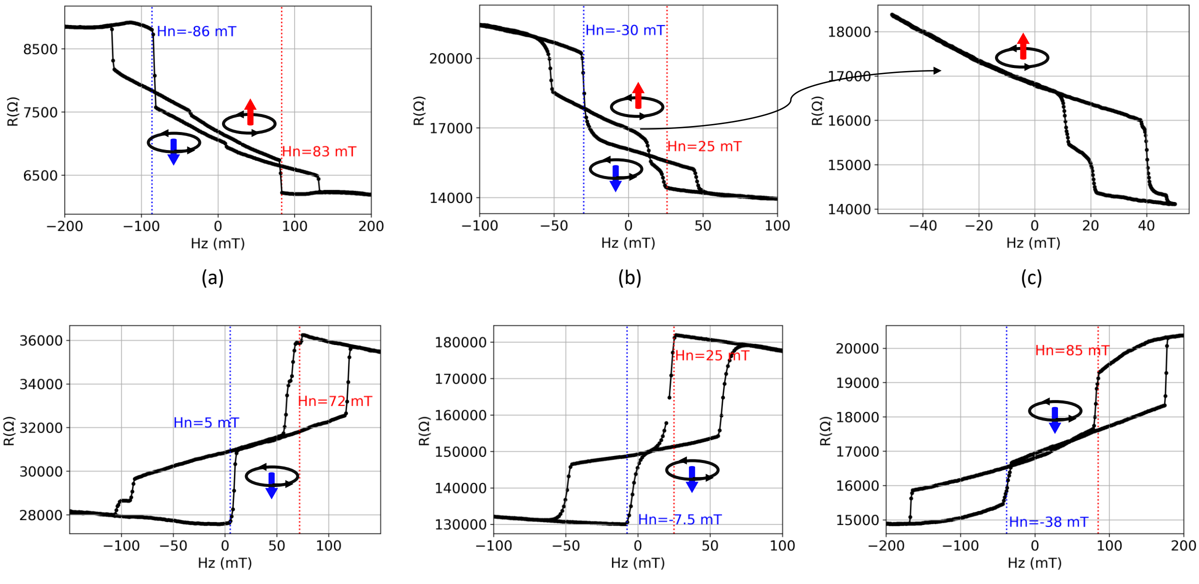

(a) (b) (c)

(d) (e) (f)

Fig. 6.16: R-H loops for NiFe 58nm sensing layer. The devices that show similar values for nucleation fields in both negative and positive field directions (Hn in blue and red respectively) (a,b) exhibit a difference in their resistance at remanence, as for both vortex polarities. A minor loop of the device shown in (b) demonstrates that avoiding the annihilation at negative fields, the vortex polarity remains always positive, which leads to no hysteresis formation (c). Devices with strong asymmetry in the nucleation fields between both polarities (d,e,f) show a single linear response before annihilation, corresponding to one vortex core polarity state. This can be attributed to a stronger stray field from the reference layer.

However, devices that show rather asymmetric nucleation fields, as in Figure 6.16 d, e and f, do not show such resistance difference and it is apparent that the vortex polarity remains unchanged independently of the annihilation field direction. The effect can be understood due to a stabilization of the vortex core in one direction due to residual stray field from an uncompensated reference layer. The unbalanced stray field is apparent in the asymmetry of the nucleation fields but in any case, it does not strongly affect the annihilation fields, so a large linear range regime is still maintained.

The results shown here indicate that a reference layer with high PMA could be valid without the requirement of a synthetic antiferromagnetic (SAF), since some residual stray field is beneficial for the proper functioning of the device. A particular advantage of such configuration is that the use of critical ruthenium, which provides RKKY antiferromagnetic coupling, can also be avoided, resulting in a completely PGM-free sensor structure.

6.4.4 Sensor parameters

Sensitivity

A statistical comparison of the sensitivity of the devices, as the slope $d(\Delta R/R)/dH$ is shown in Figure 6.17a, for the case of a 58 nm thick NiFe sensing layer. It is observed that the sensitivity decreases for larger diameters. This drop in sensitivity is attributed to an increase in the linear field range, as the total TMR amplitude is distributed over a larger field range.

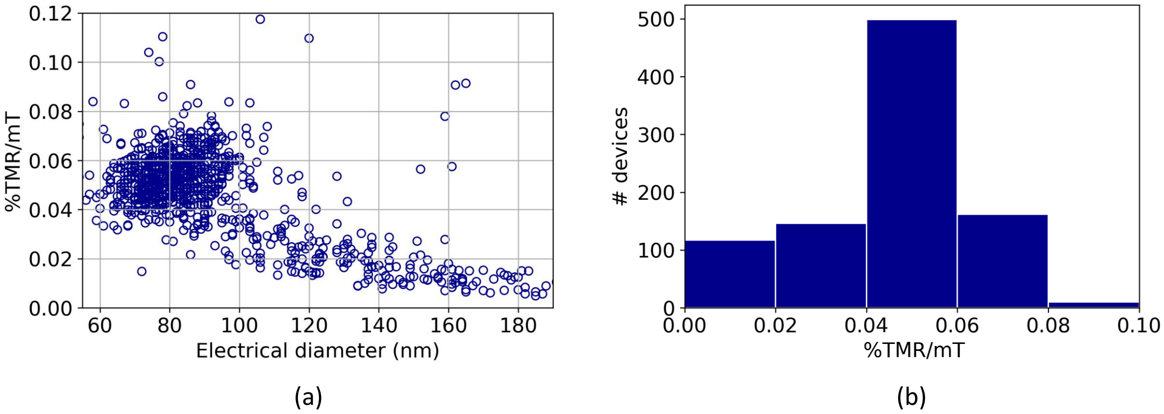

(a)

(b)

Fig. 6.17: Sensitivity values of a MTJ with 58 nm NiFe sensing layer for different electrical diameters (a). Histogram of sensitivity values (b). The stack structure is as follows: Seed / SAF / Reference / MgO 1.2 nm / FeCoB 1.4 nm / W 0.2nm / NiFe 58 nm / Capping.

Figure 6.17 b shows that most devices show a sensitivity between 0.04 and 0.06%/mT, with a mean sensitivity value of 0.05%/mT, slightly above the previously reported GMR sensors of Suess et al. [96] but below the 0.3-0.6 %/mT for TMR vortex-based sensors reported by Weitensfelder et al [95].

The relatively low sensitivity results from the low TMR observed in our devices (between 10-25%), which can be attributed to some deterioration of the barrier quality during processing. Nonetheless, with state of the art MTJs, TMR values of 150-200% can be achieved. With such a large TMR, we might expect an increase in sensitivity of almost an order of magnitude.

A second sample showed larger TMR values, up to 50%, leading to higher sensitivity values, up to 0.17%/mT, as seen in figure 6.18.

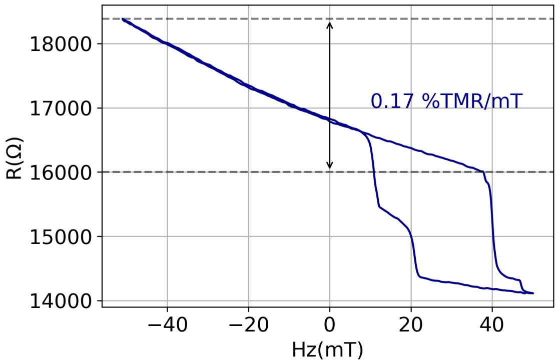

Fig. 6.18: R-H loop of a device with same stack structure as in Figure 6.17 a, but in this case with higher TMR.

Unfortunately, the yield of devices of that sample was too small to provide statistical analysis. Nonetheless, we can see that a sensitivity three times higher is obtained compared to the devices in Figure 6.17 a, which confirms our previous hypothesis.

Signal to noise ratio (SNR)

We also characterized the signal-to-noise ratio (SNR) of our perpendicular field-sensitive vortex-based sensors. It is calculated as follows:

First, a third-order polynomial fit of the resistance is performed.

$$R_{fit}(H) = a + bH + cH^2 + dH^3 \tag{6.1}$$

The root mean square (RMS) is calculated as in equation 6.4.4:

$$RMS(H) = \sqrt{\frac{1}{N}\sum_{i=1}^{N}[R(H_i - R_{fit}(H_i)]^2} \tag{6.2}$$

Finally, the SNR is given by equation 6.4.4,

$$SNR = \frac{R_{fit}}{RMS} \tag{6.3}$$

The SNR is commonly expressed in dB scale as SNR(dB)= 20 log(SNR). Figure 6.19 a shows a plot of SNR(dB) values for a set of devices.

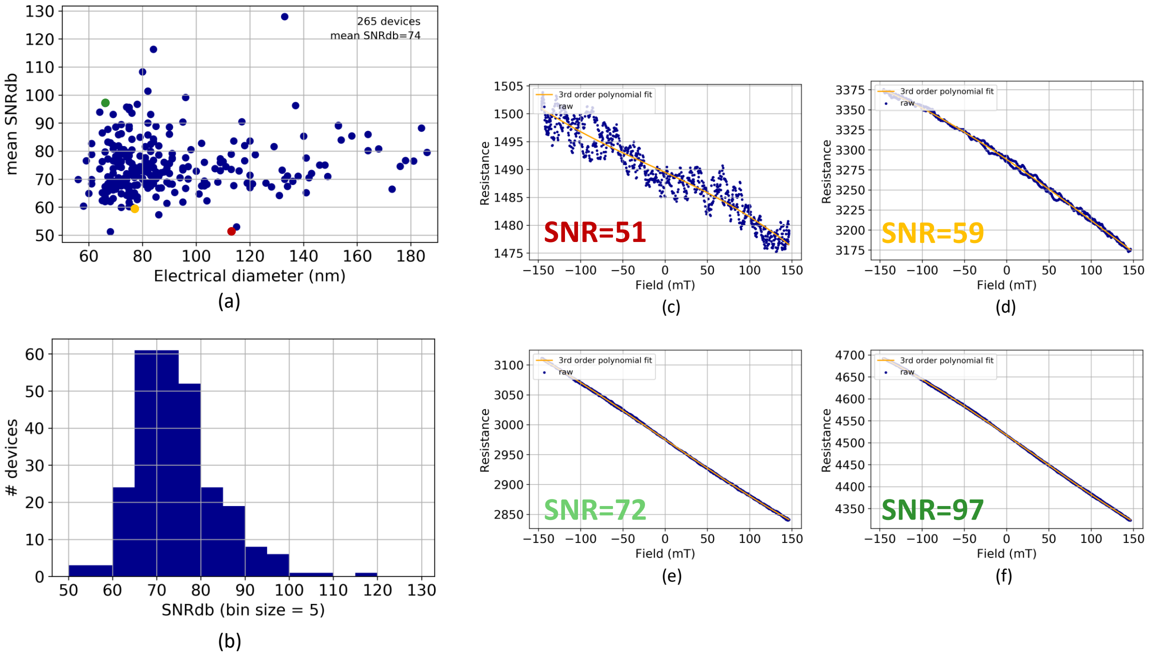

Fig. 6.19: Sensitivity values of a MTJ with 58 nm NiFe sensing layer for different electrical diameters (a). Histogram of SNR(dB) (b). R-H loops of selected devices with low (c,d), average (e) and large (f) SNR(dB) values. The 3th order polynomial fit use for calculating the RMS is plotted in yellow.

The histogram in Figure 6.19b shows that most devices have an SNR of around 70, with a mean SNR value of 74. Figures 6.19 c and d show that the magneto-resistance response of devices with SNR less than 60 show a relatively large dispersion of resistance values. However, devices within the mean SNR value as in Figure 6.19 e show a good linear response with little noise.

6.5 Comparison with other vortex based sensors and conclusions

A comparison with other conventional vortex-based sensing devices [95, 96] is provided in the Table 6.1.

	Weitensfelder et al. (2018)[95]	**Suess et al. (2018)[96]**	**Our sensor**
Diameter	1-2 µm	2 µm	60-120 nm
Sensitivity	0.3-0.6%/mT	0.04%/mT	0.03-0.5*%/mT
Linear range	Up to 40-80 mT	40 mT	>200mT
Mechanism	In-plane motion of vortex core		Diameter variation of vortex core
Field direction	In-plane		Out-of-plane

Table 6.1: Typical characteristics of conventional vortex-based sensors compared to our device based on the expansion and contraction of the vortex core under a perpendicular field. *Assuming a MTJ with state-of-the-art TMR values of up to 150-200%.

An advantage of our sensor devices is their high down-size scalability which goes with reduced power consumption. For other vortex-based sensors based on in-plane motion of the vortex core, micrometer-sized junctions have typically been reported. In our case, we report MTJs with diameter less than 100 nm showing good linear electrical response for sensor requirements.

The sensitivity is highly dependent on the TMR of the junctions, and we have seen that it was increased to 0.17%/mT for junctions with about 50%TMR, which anticipates the possibility of sensitivity values close to 0.5 % /mT for MTJs with state-of-the-art TMR values of 150-200%.

In addition, the linear range of the transfer curve is greatly increased compared to the other two cases, up to values of more than 200 mT. Both the simulations and the experimental results showed that the nucleation and annihilation fields can be controlled by adjusting the junction diameter and the material used for the sensing layer.

Finally, the sensitivity to perpendicular fields allows the use of a perpendicularly magnetized reference layer, avoiding the use of a critical antiferromagnetic layer that provides exchange bias.

Further research is required to test the possibility of using a completely PGM-free reference layer, as we have seen that the use of a SAF structure may not be required. However, the results reported in this chapter show encouraging prospects for such a proposal and open the possibility of an innovative magnetic detection method.

Perspectives

Perpendicular shape anisotropy for the reference layer of STT-MRAM

Despite having presented important results showing the perpendicular shape anisotropy of All-PSA-STT-MRAM by off-axis electron holography, the electrical results and micromagnetic simulations showed that a vortex configuration can appear in some components of the three layer structure. One possible approach to avoid such vortex formation would be to simply use a free layer element based on i-PMA, and use only PSA for the bottom reference layer and top polarizer. By following this approach, PGMs are still avoided and fabrication is facilitated, as the pillar aspect ratio is reduced.

Alternative sources of PMA for the reference layer of p-MRAM

We demonstrate that Co/Ni multilayers can provide sufficient stability to the reference layer of p-MTJs after annealing at 300°C. However, after annealing at 400°C, the mixing of elements deteriorates the properties of the SAF. We have seen how increasing the thickness of the Ta laminate between the FeCoB reference layer and the SAF, or using a Ta/Co/Ta composite structure, improves the annealing tolerance. Nonetheless, the coupling between the reference layer and SAF is compromised if large thicknesses of the Ta layer are used. More robust elements, such as W or Mo, will potentially allow smaller thicknesses to be used while retaining high coupling, improving the overall BEOL compatibility.

Vortex magnetic sensor sensitive to out-of-plane field

In this chapter, we propose a new concept of magnetic sensor comprising a vortex in the sensing layer that responds to an applied out-of-plane field. The proposed device can potentially avoid the use of iridium or platinum, but also has other advantages such as a large linear range that can be controlled by the aspect ratio of the sensing layer and the saturation magnetization. In the future, an interesting study would be to use a Wheatstone bridge configuration. This configuration is often used to reduce noise in magnetic sensors. However, one of the challenges is that half of the MTJs must have an opposite response to the other two MTJs, which is difficult since the magnetization direction of the reference layer is given by the AF pinning layer, defined during the annealing process at wafer level. In our case, by combining the use of Joule heating under an applied current and an applied external field, the magnetization of the reference and vortex core of two of the MTJs composing the Wheatstone bridge can be reversed individually, since the stability of the reference layer strongly decreases with temperature. Therefore, a future study of the reference layer switching under these conditions in MTJs with a large resistance area product (R × A) is of interest.

Appendix A

Evaluation of the impact of Pt substitution: data sources

The data for the calculation of the parameters in Figure 2.14 is given in Table A.1.

	Pt	Ni	Co	Silicon wafer
Energy (MJ/kg)	20000 [233]	200 [234]	2100 [233]	691.2 [143]
GWP (kg.eq/kg)	12500 [141]	6.5 [141]	8.3 [141]	130 kg_{CO_2-eq}/m^2 [146]
Price (euro/kg)	25000 [115]	12 [235]	24 [235]	0,76 dollar/in^2 in 2015 [236]

Table A.1: Energy, global warming potential (GWP) and price of Pt, Ni, Co and a 300mm Si wafer used for the calculation of the bar plot given in Figure 2.14

The electricity requirements for Si wafer fabrication have been converted to energy for direct comparison with the other raw materials requirements (3.6 MJ/kWh). Losses related to power plants efficiency have been neglected. The energy has been considered up to sc-Si ingot but not that related to wafer dicing. Assuming a 72.5% losses during sputtering deposition and for 300mm wafers. For the case of Co/Pt SAF, 9 layers of 0.25 nm of Pt were assumed. For the case of Co/Ni SAF, 9 layers of 0.4 nm of Ni were assumed. For the case of PSA substitution, two thick layers made of Co of 40 nm and 30 nm were assumed below and above the free layer respectively. For the Si wafer requirements calculations, we assumed a 300 mm Si wafer.

Appendix B

$R \times A$ values

The different values of TMR and resulting $R \times A$ measured by current-in-plane-tunneling (CIPT) [237] as a function of oxidation time and pressure are given in Table B.1. A CIPTech M200 of CAPRES was used for the measurements.

	$3 \times 10^{-2} mbar$		$1 \times^{-2} mbar$		$3 \times^{-3} mbar$	
	TMR (%)	$R \times A(\Omega \mu m^2)$	TMR (%)	$R \times A(\Omega \mu m^2)$	TMR (%)	$R \times A(\Omega \mu m^2)$
30s	78	9.8	35.9	4.8	39.5	3.2
10s	38	5.4	36.2	4.1	25.8	2.3
5s	66	4.8	33.6	3.0	31.8	2.3
1s	56	3.6	38.7	3.0	27.3	1.2

Table B.1: TMR and $R \times A$ values measured by CIPTMR for different values of oxidation pressure and time for a total Mg thickness of 1.2nm.

Table B.1 shows that it is possible to increase the $R \times A$ product by increasing the oxidation pressure and time after Mg deposition.

Appendix C

Real-time measurements

Notes on the set-up:

An experimental setup dedicated to the measurement of the dynamic magnetoresistance was used for measuring the switching probability and the time resolved switching during voltage pulse application.

In this setup, the output of a pulse generator (Agilent 81130A) is connected to the device under test via an RF probe with four leads (GSSG), in transmission mode, i.e. the current flows from the bottom (top) to the top (bottom) electrode of the MTJ - that are connected to the inner signal leads of the probe - while the ground leads contact a metal line encircling the pads of the MTJ in a dedicated RF layout. In this arrangement, the current that is transmitted through the MTJ travels through the 50Ω internal resistance of a digital oscilloscope (Lecroy HDO6000, bandwith of 500 MHz) with the resulting voltage being registered in real time.

There is an inherently high impedance mismatch given that the usual resistance of the MTJ ($\mathrm{Z_{MTJ}}$) is much larger than the circuitry's $\mathrm{Z_0} = 50\ \Omega$. As a result most of the power is reflected instead of transmitted. For that reason, the small output voltage is normally amplified and the measured voltage is

$$V_{measured} = G_{amp}(\frac{2Z_0}{2Z_0 + Z_{MTJ}})V_{in} \tag{C.1}$$

with G_{amp} the amplifier gain.

Looking at the equation it is clear that, without amplification, $\mathrm{V_{measured}} \ll \mathrm{V_{in}}$ but that $\mathrm{V_{measured}}$ is very sensitive to variations of $\mathrm{Z_{MTJ}}$

The small output voltage requires the use of an RF amplifier (SRS SR445A, bandwith of 350 MHz)

Bibliography

[1] Nevill Francis Mott and Ralph Howard Fowler. "The electrical conductivity of transition metals". In: *Proceedings of the Royal Society of London. Series A - Mathematical and Physical Sciences* 153.880 (1936), pp. 699–717. DOI: 10.1098/rspa.1936.0031. URL: https://royalsocietypublishing.org/doi/abs/10.1098/rspa.1936.0031.

[2] Safa Kasap. "Magnetic Properties and Superconductivity". In: *Principles of electronic materials and Devices 3rd edition*. McGraw-Hill, 2006, pp. 685–773.

[3] Fert, A. and Campbell, I. A. "Transport properties of ferromagnetic transition metals". In: *J. Phys. Colloques* 32 (1971), pp. C1-46-C1–50. DOI: 10.1051/jphyscol:1971109. URL: https://doi.org/10.1051/jphyscol:1971109.

[4] N. Locatelli and V. Cros. "Basic spintronic transport phenomena". In: *B. Dieny, R.B. Goldfarb and K. Lee (eds) Introduction to Magnetic Random-Access Memory*. John Wiley Sons, Hoboken, NJ 101–164, 2016, pp. 1–27. ISBN: 9781119079415. URL: https://doi.org/10.1002/.

[5] M. N. Baibich et al. "Giant Magnetoresistance of (001)Fe/(001)Cr Magnetic Superlattices". In: *Phys. Rev. Lett.* 61 (21 Nov. 1988), pp. 2472–2475. DOI: 10.1103/PhysRevLett.61.2472. URL: https://link.aps.org/doi/10.1103/PhysRevLett.61.2472.

[6] G. Binasch et al. "Enhanced magnetoresistance in layered magnetic structures with antiferromagnetic interlayer exchange". In: *Phys. Rev. B* 39 (7 Mar. 1989), pp. 4828–4830. DOI: 10.1103/PhysRevB.39.4828. URL: https://link.aps.org/doi/10.1103/PhysRevB.39.4828.

[7] B. Dieny et al. "Giant magnetoresistive in soft ferromagnetic multilayers". In: *Phys. Rev. B* 43 (1 Jan. 1991), pp. 1297–1300. DOI: 10.1103/PhysRevB.43.1297. URL: https://link.aps.org/doi/10.1103/PhysRevB.43.1297.

[8] R. L. Comstock. "Review Modern magnetic materials in data storage". In: *Journal of Materials Science: Materials in Electronics* 13 (9 2002), pp. 509–523. DOI: 10.1023/A:1019642215245. URL: https://doi.org/10.1023/A:1019642215245.

[9] M. Julliere. "Tunneling between ferromagnetic films". In: *Physics Letters A* 54.3 (1975), pp. 225–226. ISSN: 0375-9601. DOI: https://doi.org/10.1016/0375-9601(75)90174-7. URL: https://www.sciencedirect.com/science/article/pii/0375960175901747.

[10] J. S. Moodera et al. "Large Magnetoresistance at Room Temperature in Ferromagnetic Thin Film Tunnel Junctions". In: *Phys. Rev. Lett.* 74 (16 Apr. 1995), pp. 3273–3276. DOI: 10.1103/PhysRevLett.74.3273. URL: https://link.aps.org/doi/10.1103/PhysRevLett.74.3273.

[11] T. Miyazaki and N. Tezuka. "Giant magnetic tunneling effect in Fe/Al2O3/Fe junction". In: *Journal of Magnetism and Magnetic Materials* 139.3 (1995), pp. L231–L234. ISSN: 0304-8853. DOI: https://doi.org/10.1016/0304-8853(95)90001-2. URL: https://www.sciencedirect.com/science/article/pii/0304885395900012.

[12] W. H. Butler et al. "Spin-dependent tunneling conductance of Fe|MgO|Fe sandwiches". In: *Phys. Rev. B* 63 (5 Jan. 2001), p. 054416. DOI: 10.1103/PhysRevB.63.054416. URL: https://link.aps.org/doi/10.1103/PhysRevB.63.054416.

[13] J. Mathon and A. Umerski. "Theory of tunneling magnetoresistance of an epitaxial Fe/MgO/Fe(001) junction". In: *Phys. Rev. B* 63 (22 May 2001), p. 220403. DOI: 10.1103/PhysRevB.63.220403. URL: https://link.aps.org/doi/10.1103/PhysRevB.63.220403.

[14] Stuart S. P. Parkin et al. “Giant Tunnelling Magnetoresistance at Room Temperature with MgO (100) Tunnel Barriers”. In: *Nature Materials* 3 (2004), pp. 862–867. DOI: 10.1038/nmat1256. URL: https://www.nature.com/articles/nmat1256 (visited on 04/08/2020).

[15] Shinji Yuasa et al. “Giant Room-Temperature Magnetoresistance in Single-Crystal Fe/MgO/Fe Magnetic Tunnel Junctions”. In: *Nature Materials* 3 (2004), pp. 868–871. DOI: 10.1038/nmat1257. URL: https://www.nature.com/articles/nmat1257 (visited on 04/09/2020).

[16] S. Ikeda et al. “Tunnel magnetoresistance of 604% at 300K by suppression of Ta diffusion in CoFeBMgOCoFeB pseudo-spin-valves annealed at high temperature”. In: *Applied Physics Letters* 93.8 (2008), p. 082508. DOI: 10.1063/1.2976435. URL: https://doi.org/10.1063/1.2976435.

[17] P. G. Mather, J. C. Read, and R. A. Buhrman. “Disorder, defects, and band gaps in ultrathin (001) MgO tunnel barrier layers”. In: *Phys. Rev. B* 73 (20 May 2006), p. 205412. DOI: 10.1103/PhysRevB.73.205412. URL: https://link.aps.org/doi/10.1103/PhysRevB.73.205412.

[18] S Yuasa and D D Djayaprawira. “Giant tunnel magnetoresistance in magnetic tunnel junctions with a crystalline MgO(0 0 1) barrier”. In: *Journal of Physics D: Applied Physics* 40.21 (Oct. 2007), R337–R354. DOI: 10.1088/0022-3727/40/21/r01. URL: https://doi.org/10.1088/0022-3727/40/21/r01.

[19] H. X. Wei et al. “80% tunneling magnetoresistance at room temperature for thin Al–O barrier magnetic tunnel junction with CoFeB as free and reference layers”. In: *Journal of Applied Physics* 101.9 (2007), 09B501. DOI: 10.1063/1.2696590. eprint: https://doi.org/10.1063/1.2696590. URL: https://doi.org/10.1063/1.2696590.

[20] J.C. Slonczewski. “Current-Driven Excitation of Magnetic Multilayers”. In: *Journal of Magnetism and Magnetic Materials* 159 (1996), pp. L1–L7. DOI: 10.1016/0304-8853(96)00062-5. URL: https://linkinghub.elsevier.com/retrieve/pii/0304885396000625 (visited on 01/31/2020).

[21] L. Berger. “Emission of Spin Waves by a Magnetic Multilayer Traversed by a Current”. In: *Physical Review B* 54 (1996), pp. 9353–9358. DOI: 10.1103/PhysRevB.54.9353. URL: https://link.aps.org/doi/10.1103/PhysRevB.54.9353 (visited on 04/14/2020).

[22] M. Tsoi et al. “Excitation of a Magnetic Multilayer by an Electric Current”. In: *Phys. Rev. Lett.* 80 (19 May 1998), pp. 4281–4284. DOI: 10.1103/PhysRevLett.80.4281. URL: https://link.aps.org/doi/10.1103/PhysRevLett.80.4281.

[23] J. A. Katine et al. “Current-Driven Magnetization Reversal and Spin-Wave Excitations in Co /Cu /Co Pillars”. In: *Phys. Rev. Lett.* 84 (14 Apr. 2000), pp. 3149–3152. DOI: 10.1103/PhysRevLett.84.3149. URL: https://link.aps.org/doi/10.1103/PhysRevLett.84.3149.

[24] Yiming Huai et al. “Observation of spin-transfer switching in deep submicron-sized and low-resistance magnetic tunnel junctions”. In: *Applied Physics Letters* 84.16 (2004), pp. 3118–3120. DOI: 10.1063/1.1707228. eprint: https://doi.org/10.1063/1.1707228. URL: https://doi.org/10.1063/1.1707228.

[25] Zhitao Diao et al. “Spin Transfer Switching and Spin Polarization in Magnetic Tunnel Junctions with MgO and AlOx Barriers”. In: *Applied Physics Letters* 87 (2005), p. 232502. DOI: 10.1063/1.2139849. URL: https://aip.scitation.org/doi/10.1063/1.2139849 (visited on 04/14/2020).

[26] Hitoshi Kubota et al. “Evaluation of Spin-Transfer Switching in CoFeB/MgO/CoFeB Magnetic Tunnel Junctions”. In: *Japanese Journal of Applied Physics* 44 (2005), p. L1237. DOI: 10.1143/JJAP.44.L1237. URL: https://iopscience.iop.org/article/10.1143/JJAP.44.L1237/meta (visited on 04/14/2020).

[27] Jun Hayakawa et al. “Current-Driven Magnetization Switching in CoFeB/MgO/CoFeB Magnetic Tunnel Junctions”. In: *Japanese Journal of Applied Physics* 44 (2005), p. L1267. DOI: 10.1143/JJAP.44.L1267. URL: https://iopscience.iop.org/article/10.1143/JJAP.44.L1267/meta (visited on 04/14/2020).

[28] H. Jaffrès et al. "Angular dependence of the tunnel magnetoresistance in transition-metal-based junctions". In: *Phys. Rev. B* 64 (6 July 2001), p. 064427. DOI: 10.1103/PhysRevB.64.064427. URL: https://link.aps.org/doi/10.1103/PhysRevB.64.064427.

[29] M.D Stiles and J. Miltat. "Spin-Transfer Torque and Dynamics". In: *Hillebrands B., Thiaville A. (eds) Spin Dynamics in Confined Magnetic Structures III*. Topics in Applied Physics. Springer, Berlin, Heidelberg, 2006, pp. 225–308. URL: https://doi.org/10.1007/10938171_7.

[30] R. Meservey and P.M. Tedrow. "Spin-polarized electron tunneling". In: *Physics Reports* 238.4 (1994), pp. 173–243. ISSN: 0370-1573. DOI: https://doi.org/10.1016/0370-1573(94)90105-8. URL: https://www.sciencedirect.com/science/article/pii/0370157394901058.

[31] Jack C. Sankey et al. "Measurement of the spin-transfer-torque vector in Magnetic Tunnel junctions". In: *Nature Physics* 4.1 (2008), pp. 67–71. DOI: 10.1038/nphys783.

[32] Hitoshi Kubota et al. "Quantitative measurement of voltage dependence of spin-transfer torque in MGO-based magnetic tunnel junctions". In: *Nature Physics* 4.1 (2007), pp. 37–41. DOI: 10.1038/nphys784.

[33] Alina M. Deac et al. "Bias-driven high-power microwave emission from mgo-based tunnel magnetoresistance devices". In: *Nature Physics* 4.10 (2008), pp. 803–809. DOI: 10.1038/nphys1036.

[34] Z. Li et al. "Perpendicular Spin Torques in Magnetic Tunnel Junctions". In: *Physical Review Letters* 100 (2008), p. 246602. DOI: 10.1103/PhysRevLett.100.246602. URL: https://link.aps.org/doi/10.1103/PhysRevLett.100.246602 (visited on 04/14/2020).

[35] Se-Chung Oh et al. "Bias-voltage dependence of perpendicular spin-transfer torque in asymmetric mgo-based magnetic tunnel junctions". In: *Nature Physics* 5.12 (2009), pp. 898–902. DOI: 10.1038/nphys1427.

[36] A. A. Timopheev et al. "Respective Influence of In-Plane and out-of-Plane Spin-Transfer Torques in Magnetization Switching of Perpendicular Magnetic Tunnel Junctions". In: *Physical Review B* 92 (2015), p. 104430. DOI: 10.1103/PhysRevB.92.104430. URL: https://link.aps.org/doi/10.1103/PhysRevB.92.104430 (visited on 01/31/2020).

[37] Ioan Mihai Miron et al. "Perpendicular switching of a single ferromagnetic layer induced by in-plane current injection". In: *Nature* 476.7359 (2011), pp. 189–193. DOI: 10.1038/nature10309.

[38] Yu. A. Bychkov and É. I. Rashba. "Properties of a 2D electron gas with lifted spectral degeneracy". In: *Soviet Journal of Experimental and Theoretical Physics Letters* 39 (Jan. 1984), p. 78.

[39] V.M. Edelstein. "Spin polarization of conduction electrons induced by electric current in two-dimensional asymmetric electron systems". In: *Solid State Communications* 73.3 (1990), pp. 233–235. ISSN: 0038-1098. DOI: https://doi.org/10.1016/0038-1098(90)90963-C. URL: https://www.sciencedirect.com/science/article/pii/003810989090963C.

[40] Kevin Garello et al. "Symmetry and magnitude of spin–orbit torques in ferromagnetic heterostructures". In: *Nature Nanotechnology* 8.8 (2013), pp. 587–593. DOI: 10.1038/nnano.2013.145.

[41] N. Perrissin et al. "A highly thermally stable sub-20 nm magnetic random-access memory based on perpendicular shape anisotropy". In: *Nanoscale* 10 (25 2018), pp. 12187–12195. DOI: 10.1039/C8NR01365A. URL: http://dx.doi.org/10.1039/C8NR01365A.

[42] K. Watanabe et al. "Shape anisotropy revisited in single-digit nanometer magnetic tunnel junctions". In: *Nature Communications* 9.1 (Feb. 2018), p. 663. ISSN: 2041-1723. DOI: 10.1038/s41467-018-03003-7. URL: https://doi.org/10.1038/s41467-018-03003-7.

[43] N Perrissin et al. "Perpendicular shape anisotropy spin transfer torque magnetic random-access memory: towards sub-10 nm devices". In: *Journal of Physics D: Applied Physics* 52.23 (Mar. 2019), p. 234001. DOI: 10.1088/1361-6463/ab0de4. URL: https://doi.org/10.1088/1361-6463/ab0de4.

[44] S. Lequeux et al. “Thermal robustness of magnetic tunnel junctions with perpendicular shape anisotropy”. In: *Nanoscale* 12 (11 2020), pp. 6378–6384. DOI: `10.1039/C9NR10366J`. URL: `http://dx.doi.org/10.1039/C9NR10366J`.

[45] L. Buda-Prejbeanu. “Micromagnetism Applied To Magnetic Nanostructures”. In: *B. Dieny, R.B. Goldfarb and K. Lee (eds) Introduction to Magnetic Random-Access Memory.* John Wiley Sons, Hoboken, NJ 101–164, 2016, pp. 55–79. ISBN: 9781119079415. URL: `https://doi.org/10.1002/`.

[46] S. Mader and A. S. Nowick. “METASTABLE Co–Au ALLOYS: EXAMPLE OF AN AMORPHOUS FERROMAGNET”. In: *Applied Physics Letters* 7.3 (1965), pp. 57–59. DOI: `10.1063/1.1754298`. eprint: `https://doi.org/10.1063/1.1754298`. URL: `https://doi.org/10.1063/1.1754298`.

[47] B. Dieny and M. Chshiev. “Perpendicular magnetic anisotropy at transition metal/oxide interfaces and applications”. In: *Rev. Mod. Phys.* 89 (2 June 2017), p. 025008. DOI: `10.1103/RevModPhys.89.025008`. URL: `https://link.aps.org/doi/10.1103/RevModPhys.89.025008`.

[48] A. Hubert and R. Schäfer. “Domain Theory”. In: *Magnetic Domains: The Analysis of Magnetic Microstructures.* Springer, 1998. ISBN: 9783540641087. URL: `https://books.google.fr/books?id=pBE42lLYs-MC`.

[49] Amikam Aharoni. “Demagnetizing Factors for Rectangular Ferromagnetic Prisms”. In: *Journal of Applied Physics* 83 (1998), pp. 3432–3434. DOI: `10.1063/1.367113`. URL: `https://aip.scitation.org/doi/10.1063/1.367113` (visited on 04/07/2020).

[50] Tomohiro Taniguchi. “An analytical computation of magnetic field generated from a cylinder ferromagnet”. In: *Journal of Magnetism and Magnetic Materials* 452 (Apr. 2018), pp. 464–472. DOI: `10.1016/j.jmmm.2017.11.078`. URL: `https://doi.org/10.1016%2Fj.jmmm.2017.11.078`.

[51] R P Cowburn. “Property variation with shape in magnetic nanoelements”. In: *Journal of Physics D: Applied Physics* 33.1 (Dec. 1999), R1–R16. DOI: `10.1088/0022-3727/33/1/201`. URL: `https://doi.org/10.1088/0022-3727/33/1/201`.

[52] W. H. Meiklejohn and C. P. Bean. “New Magnetic Anisotropy”. In: *Phys. Rev.* 105 (3 Feb. 1957), pp. 904–913. DOI: `10.1103/PhysRev.105.904`. URL: `https://link.aps.org/doi/10.1103/PhysRev.105.904`.

[53] J Nogués and Ivan K Schuller. “Exchange bias”. In: *Journal of Magnetism and Magnetic Materials* 192.2 (1999), pp. 203–232. ISSN: 0304-8853. DOI: `https://doi.org/10.1016/S0304-8853(98)00266-2`. URL: `https://www.sciencedirect.com/science/article/pii/S0304885398002662`.

[54] S. S. P. Parkin, N. More, and K. P. Roche. “Oscillations in Exchange Coupling and Magnetoresistance in Metallic Superlattice Structures: Co/Ru, Co/Cr, and Fe/Cr”. In: *Physical Review Letters* 64 (1990), pp. 2304–2307. DOI: `10.1103/PhysRevLett.64.2304`. URL: `https://link.aps.org/doi/10.1103/PhysRevLett.64.2304` (visited on 01/31/2020).

[55] J. Unguris et al. “Sempa Studies of Oscillatory Exchange Coupling”. In: *Farrow R.F.C., Dieny B., Donath M., Fert A., Hermsmeier B.D. (eds) Magnetism and Structure in Systems of Reduced Dimension.* NATO ASI Series (Series B: Physics). Springer, 1993. URL: `https://doi.org/10.1007/978-1-4899-1519-1_10`.

[56] A. D. Kent, B. Özyilmaz, and E. del Barco. “Spin-transfer-induced precessional magnetization reversal”. In: *Applied Physics Letters* 84.19 (2004), pp. 3897–3899. DOI: `10.1063/1.1739271`. eprint: `https://doi.org/10.1063/1.1739271`. URL: `https://doi.org/10.1063/1.1739271`.

[57] P. Khalili Amiri et al. “Switching current reduction using perpendicular anisotropy in CoFeB–MgO magnetic tunnel junctions”. In: *Applied Physics Letters* 98.11 (2011), p. 112507. DOI: `10.1063/1.3567780`. eprint: `https://doi.org/10.1063/1.3567780`. URL: `https://doi.org/10.1063/1.3567780`.

[58] S. Ikeda, K. Miura, and H. et al. Yamamoto. “A perpendicular-anisotropy CoFeB–MgO magnetic tunnel junction”. In: *Nature Mater* 9 (2010), pp. 721–724.

[59] S. Monso et al. “Crossover from in-plane to perpendicular anisotropy in Pt/CoFe/AlOx sandwiches as a function of Al oxidation: A very accurate control of the oxidation of tunnel barriers”. In: *Applied Physics Letters* 80.22 (2002), pp. 4157–4159. DOI: `10.1063/1.1483122`. eprint: `https://doi.org/10.1063/1.1483122`. URL: `https://doi.org/10.1063/1.1483122`.

[60] D. C. Worledge et al. “Spin Torque Switching of Perpendicular Ta|CoFeB|MgO-Based Magnetic Tunnel Junctions”. In: *Applied Physics Letters* 98 (2011), p. 022501. DOI: `10.1063/1.3536482`. URL: `https://aip.scitation.org/doi/10.1063/1.3536482` (visited on 04/29/2020).

[61] Lavinia Elena Nistor et al. “Correlation Between Perpendicular Anisotropy and Magnetoresistance in Magnetic Tunnel Junctions”. In: *IEEE Transactions on Magnetics* 46.6 (2010), pp. 1412–1415. DOI: `10.1109/TMAG.2010.2045641`.

[62] Daniele Ielmini and Stefano Ambrogio. “Emerging neuromorphic devices”. In: *Nanotechnology* 31.9 (Dec. 2019), p. 092001. DOI: `10.1088/1361-6528/ab554b`. URL: `https://doi.org/10.1088/1361-6528/ab554b`.

[63] B. Dieny, I.L. Prejbeanu, and K. et al. Garello. “Opportunities and challenges for spintronics in the microelectronics industry”. In: *Nature Nanotechnology* 3 (2020), pp. 446–459. DOI: `https://doi.org/10.1038/s41928-020-0461-5`.

[64] S. Jung, H. Lee, and S. et al. Myung. “A crossbar array of magnetoresistive memory devices for in-memory computing”. In: *Nature* 601 (2022), pp. 211–216. URL: `https://doi.org/10.1038/s41586-021-04196-6`.

[65] Mengxing Wang et al. “Field-free switching of a perpendicular magnetic tunnel junction through the interplay of spin–orbit and spin-transfer torques”. In: *Nature Electronics* 1 (Nov. 2018). DOI: `10.1038/s41928-018-0160-7`.

[66] Noriyuki Sato et al. “Two-terminal spin–orbit torque magnetoresistive random access memory”. In: *Nature Electronics* 1 (Sept. 2018), pp. 508–511. DOI: `10.1038/s41928-018-0131-z`.

[67] H. Yoda et al. “Voltage-control spintronics memory (VoCSM) having potentials of ultra-low energy-consumption and high-density”. English. In: *2016 IEEE International Electron Devices Meeting, IEDM 2016*. Technical Digest - International Electron Devices Meeting, IEDM. 62nd IEEE International Electron Devices Meeting, IEDM 2016 ; Conference date: 03-12-2016 Through 07-12-2016. Institute of Electrical and Electronics Engineers Inc., Jan. 2017, pp. 27.6.1–27.6.4. DOI: `10.1109/IEDM.2016.7838495`.

[68] S. Tehrani et al. “Magnetoresistive Random Access Memory Using Magnetic Tunnel Junctions”. In: *Proceedings of the IEEE* 91 (2003), pp. 703–714. DOI: `10.1109/JPROC.2003.811804`.

[69] Leonid Savtchenko et al. “Method of Writing to Scalable Magnetoresistance Random Access Memory Element”. 2003. URL: `https://patents.google.com/patent/US20030072174A1/en` (visited on 04/29/2020).

[70] *4-Mbit Device Is First Commercially Available MRAM*. 2006. URL: `https://www.electronicdesign.com/technologies/dsps/article/21776170/4mbit-device-is-first-commercially-available-mram` (visited on 04/29/2020).

[71] B.N. Engel et al. “A 4-Mb Toggle MRAM Based on a Novel Bit and Switching Method”. In: *IEEE Transactions on Magnetics* 41 (2005), pp. 132–136. DOI: `10.1109/TMAG.2004.840847`.

[72] T.W. Andre et al. “A 4-Mb 0.18-/Spl Mu/m 1T1MTJ Toggle MRAM with Balanced Three Input Sensing Scheme and Locally Mirrored Unidirectional Write Drivers”. In: *IEEE Journal of Solid-State Circuits* 40 (2005), pp. 301–309. DOI: `10.1109/JSSC.2004.837962`.

[73] B. Dieny and Redon.O. “Magnetic device with magnetic tunnel junction, memory array and read/write methods using said device”. US6950335 (B2). 2005.

[74] I.L. Prejbeanu et al. “Thermally Assisted Switching in Exchange-Biased Storage Layer Magnetic Tunnel Junctions”. In: *IEEE Transactions on Magnetics* 40 (2004), pp. 2625–2627. DOI: 10.1109/TMAG.2004.830395.

[75] B. Dieny and I.L. Prejbeanu. “Magnetic Random Access Memory”. In: *B. Dieny, R.B. Goldfarb and K. Lee (eds) Introduction to Magnetic Random-Access Memory.* John Wiley Sons, Hoboken, NJ 101–164, 2016, pp. 101–165. ISBN: 9781119079415. URL: https://doi.org/10.1002/.

[76] G. Hu et al. “STT-MRAM with double magnetic tunnel junctions”. In: *2015 IEEE International Electron Devices Meeting (IEDM)*. 2015, pp. 26.3.1–26.3.4. DOI: 10.1109/IEDM.2015.7409772.

[77] Zhitao Diao et al. “Spin transfer switching in dual MgO magnetic tunnel junctions”. In: *Applied Physics Letters* 90.13 (2007), p. 132508. DOI: 10.1063/1.2717556. eprint: https://doi.org/10.1063/1.2717556. URL: https://doi.org/10.1063/1.2717556.

[78] G. Gaudin et al. “A writable magnetic memory element”. US-8416618-B2. 2013.

[79] Murat Cubukcu et al. “Spin-orbit torque magnetization switching of a three-terminal perpendicular magnetic tunnel junction”. In: *Applied Physics Letters* 104.4 (2014), p. 042406. DOI: 10.1063/1.4863407. eprint: https://doi.org/10.1063/1.4863407. URL: https://doi.org/10.1063/1.4863407.

[80] K. Garello et al. “SOT-MRAM 300MM Integration for Low Power and Ultrafast Embedded Memories”. In: *2018 IEEE Symposium on VLSI Circuits* (June 2018). DOI: 10.1109/vlsic.2018.8502269. URL: http://dx.doi.org/10.1109/VLSIC.2018.8502269.

[81] S. Fukami, T. Anekawa, and C. et al. Zhang. “A spin–orbit torque switching scheme with collinear magnetic easy axis and current configuration”. In: *Nature Nanotech* 11 (2016), pp. 621–625. DOI: https://doi.org/10.1038/nnano.2016.29.

[82] Luqiao Liu et al. “Spin-Torque Switching with the Giant Spin Hall Effect of Tantalum”. In: *Science* 336.6081 (2012), pp. 555–558. DOI: 10.1126/science.1218197. eprint: https://www.science.org/doi/pdf/10.1126/science.1218197. URL: https://www.science.org/doi/abs/10.1126/science.1218197.

[83] Chi-Feng Pai et al. “Spin transfer torque devices utilizing the giant spin Hall effect of tungsten”. In: *Applied Physics Letters* 101.12 (2012), p. 122404. DOI: 10.1063/1.4753947. eprint: https://doi.org/10.1063/1.4753947. URL: https://doi.org/10.1063/1.4753947.

[84] K. Garello et al. “Manufacturable 300mm platform solution for Field-Free Switching SOT-MRAM”. In: *2019 Symposium on VLSI Technology* (June 2019). DOI: 10.23919/vlsit.2019.8776537. URL: http://dx.doi.org/10.23919/VLSIT.2019.8776537.

[85] Noriyuki Sato et al. “CMOS Compatible Process Integration of SOT-MRAM with Heavy-Metal Bi-Layer Bottom Electrode and 10ns Field-Free SOT Switching with STT Assist”. In: *2020 IEEE Symposium on VLSI Technology*. 2020, pp. 1–2. DOI: 10.1109/VLSITechnology18217.2020.9265028.

[86] Law W.C. and Wong S.D.W. “Spin Transfer Torque Magnetoresistive Random Access Memory.” In: *Lew W.S., Lim G.J., Dananjaya P.A. (eds) Emerging Non-volatile Memory Technologies.* Springer, Singapore, 2021. URL: https://doi.org/10.1007/978-981-15-6912-8_2.

[87] C. Nail et al. “Understanding RRAM endurance, retention and window margin trade-off using experimental results and simulations”. In: *2016 IEEE International Electron Devices Meeting (IEDM)*. 2016, pp. 4.5.1–4.5.4. DOI: 10.1109/IEDM.2016.7838346.

[88] S. Aggarwal et al. “Demonstration of a Reliable 1 Gb Standalone Spin-Transfer Torque MRAM For Industrial Applications”. In: *2019 IEEE International Electron Devices Meeting (IEDM)*. 2019, pp. 2.1.1–2.1.4. DOI: 10.1109/IEDM19573.2019.8993516.

[89] *Catching Up on the Latest Developments in MRAM.* URL: https://www.electronicdesign.com/industrial-automation/article/21126158/catching-up-on-the-latest-developments-in-mram (visited on 02/04/2022).

[90] Paulo P. Freitas, Ricardo Ferreira, and Susana Cardoso. “Spintronic Sensors”. In: *Proceedings of the IEEE* 104.10 (2016), pp. 1894–1918. DOI: `10.1109/JPROC.2016.2578303`.

[91] Chloé Chopin et al. “Magnetoresistive Sensor in Two-Dimension on a 25 m Thick Silicon Substrate for In Vivo Neuronal Measurements”. In: *ACS Sensors* 5.11 (2020). PMID: 33108725, pp. 3493–3500. DOI: `10.1021/acssensors.0c01578`. eprint: `https://doi.org/10.1021/acssensors.0c01578`. URL: `https://doi.org/10.1021/acssensors.0c01578`.

[92] Xuyang Liu et al. “Overview of Spintronic Sensors With Internet of Things for Smart Living”. In: *IEEE Transactions on Magnetics* 55.11 (2019), pp. 1–22. DOI: `10.1109/TMAG.2019.2927457`.

[93] Silva, Ana V. et al. “Linearization strategies for high sensitivity magnetoresistive sensors”. In: *Eur. Phys. J. Appl. Phys.* 72.1 (2015), p. 10601. DOI: `10.1051/epjap/2015150214`. URL: `https://doi.org/10.1051/epjap/2015150214`.

[94] Lukas Wetterau et al. “Micromagnetic Simulations of Submicron Vortex Structures for the Detection of Superparamagnetic Labels”. In: *Sensors* 20.20 (2020). ISSN: 1424-8220. DOI: `10.3390/s20205819`. URL: `https://www.mdpi.com/1424-8220/20/20/5819`.

[95] Herbert Weitensfelder et al. “Comparison of Sensitivity and Low-Frequency Noise Contributions in Giant-Magnetoresistive and Tunneling-Magnetoresistive Spin-Valve Sensors with a Vortex-State Free Layer”. In: *Phys. Rev. Applied* 10 (5 Nov. 2018), p. 054056. DOI: `10.1103/PhysRevApplied.10.054056`. URL: `https://link.aps.org/doi/10.1103/PhysRevApplied.10.054056`.

[96] Dieter Suess et al. “Topologically protected vortex structures for low-noise magnetic sensors with high linear range”. In: *Nature Electronics* 1.6 (June 2018), pp. 362–370. ISSN: 2520-1131. DOI: `10.1038/s41928-018-0084-2`. URL: `https://doi.org/10.1038/s41928-018-0084-2`.

[97] Giovanni Andrea Blengini et al. “Methodology for Establishing the EU List of Critical Raw Materials - Guidelines”. In: *European Commission* (2017). DOI: `10.2873/769526`. URL: `https://op.europa.eu/en/publication-detail/-/publication/2d43b7e2-66ac-11e7-b2f2-01aa75ed71a1`.

[98] Anders S. G. Andrae and Tomas Edler. “On Global Electricity Usage of Communication Technology: Trends to 2030”. In: *Challenges* 6.1 (2015), pp. 117–157. ISSN: 2078-1547. DOI: `10.3390/challe6010117`. URL: `https://www.mdpi.com/2078-1547/6/1/117`.

[99] D.Reinsel, J.Gantz, and J.Rydning. “The Digitization of the World From Edge to Core”. In: *IDC White Paper – US44413318* (2018). URL: `https://www.seagate.com/files/www-content/our-story/trends/files/idc-seagate-dataage-whitepaper.pdf`.

[100] Lotfi Belkhir and Ahmed Elmeligi. “Assessing ICT global emissions footprint: Trends to 2040 recommendations”. In: *Journal of Cleaner Production* 177 (2018), pp. 448–463. ISSN: 0959-6526. DOI: `https://doi.org/10.1016/j.jclepro.2017.12.239`. URL: `https://www.sciencedirect.com/science/article/pii/S095965261733233X`.

[101] Sophiane Senni et al. “Non-Volatile Processor Based on MRAM for Ultra-Low-Power IoT Devices”. In: *J. Emerg. Technol. Comput. Syst.* 13.2 (Dec. 2016). ISSN: 1550-4832. DOI: `10.1145/3001936`. URL: `https://doi.org/10.1145/3001936`.

[102] Dmytro Apalkov, Bernard Dieny, and J. M. Slaughter. “Magnetoresistive Random Access Memory”. In: *Proceedings of the IEEE* 104.10 (2016), pp. 1796–1830. DOI: `10.1109/JPROC.2016.2590142`.

[103] G. Pitron. *La guerre des métaux rares: La face cachée de la transition énergétique et numérique.* Éditions Les Liens qui libèrent, 2018. ISBN: 979-10-209-0574-1.

[104] European Commission. “Critical Materials for Strategic Technologies and Sectors in the EU - A Foresight Study”. In: (2020). DOI: `https://doi.org/10.2873/58081.`.

[105] Anthony Y. Ku. "Anticipating critical materials implications from the Internet of Things (IOT): Potential stress on future supply chains from emerging data storage technologies". In: *Sustainable Materials and Technologies* 15 (2018), pp. 27–32. ISSN: 2214-9937. DOI: https://doi.org/10.1016/j.susmat.2017.10.001. URL: https://www.sciencedirect.com/science/article/pii/S2214993717301252.

[106] B. Dieny, R.B. Goldfarb, and K. Lee. *Introduction to Magnetic Random-Access Memory*. John Wiley Sons, Hoboken, NJ 101–164, 2016. ISBN: 9781119079415. URL: https://doi.org/10.1002/.

[107] A. Chapman et al. "Study on Critical Raw Materials at EU Level: Final Report". In: (2013). URL: http://ec.europa.eu/DocsRoom/documents/5605/attachments/1/translations.

[108] European Commission. "Study on the Review of the List of Critical Raw Materials - Critical Raw Materials Factsheets European Commission". In: (2017). DOI: https://doi.org/10.2873/398823.

[109] European Commission. "Study on the Review of the List of Critical Raw Materials - Non Critical Raw Materials Factsheets European Commission". In: (2017). DOI: https://doi.org/10.2873/49178.

[110] Christian Hagelüken. "Recycling the Platinum Group Metals: A European Perspective". In: *Platinum Metals Review* 56.1 (2012), pp. 29–35. ISSN: 0032-1400. DOI: doi:10.1595/147106712X611733. URL: https://www.ingentaconnect.com/content/matthey/pmr/2012/00000056/00000001/art00004.

[111] T. Raymond and B. Clifford. "Low Supply Growth from Recycled Platinum Will Not Offset Lower Mine Supply in 2020". In: *Platinum Perspectives, World Platinum Investment Council* (2019). URL: https://platinuminvestment.com/files/422346/WPIC_Platinum_Perspectives_November_2019.pdf..

[112] C. Hagelüken and C.W. Corti. "Recycling of gold from electronics: Cost-effective use through 'Design for Recycling'". In: *Gold Bull* 43 (2010), pp. 209–220. DOI: https://doi.org/10.1007/BF03214988.

[113] P.G.M. Johnson Matthey. In: *Market Report* (2014). URL: http://www.platinum.matthey.com/documents/market-data-tables/platinum/pdf-2004-to-2013.pdf.

[114] P.G.M. Johnson Matthey. In: *Market Report* (2014). URL: http://www.platinum.matthey.com/documents/new-item/pgm-market-reports/pgm-market-report-may-2020.pdf.

[115] Johnson Matthey. In: *Price Charts* (2022). URL: http://www.platinum.matthey.com/prices/price-charts.

[116] UKERC. "Materials Availability for Low-Carbon Technologies: An Assessment of the Evidence". In: (2014). URL: http://www.ukerc.ac.uk/asset/34D2BFC5%5C%2D9C0D%5C%2D4C07%5C%2DBA6CD6D15BDE549A/..

[117] Daniel Behn. "The Potential Problem with Dual Gas Pricing Practices at the WTO". In: (2007). DOI: http://dx.doi.org/10.2139/ssrn.1151553.

[118] *Ukrainian Invasion Adds to Chaos for Global Supply Chains*. URL: https://www.nytimes.com/2022/03/01/business/economy/ukraine-russia-supply-chains.html (visited on 03/15/2022).

[119] *Russia's Palladium Exports Face Disruption From Flight Bans*. URL: https://www.bloomberg.com/news/articles/2022-02-28/russia-s-palladium-exports-face-disruption-from-flight-bans (visited on 03/17/2022).

[120] *Russia / Ukraine update - Maersk*. URL: https://www.maersk.com/news/articles/2022/02/24/russia-ukraine-situation-update (visited on 03/17/2022).

[121] *World's largest shipping companies suspend bookings to and from Russia*. URL: cnbc.com/2022/03/03/russia-shipping-giants-maersk-msc-and-cma-cgm-suspend-bookings.html (visited on 03/17/2022).

[122] U.S. Geological Survey. “Mineral commodity summaries 2019”. In: *Mineral commodity summaries* (2019). DOI: https://doi.org/10.3133/70202434.

[123] Pia Sinisalo and Mari Lundström. “Refining Approaches in the Platinum Group Metal Processing Value Chain—A Review”. In: *Metals* 8.4 (2018). ISSN: 2075-4701. DOI: 10.3390/met8040203. URL: https://www.mdpi.com/2075-4701/8/4/203.

[124] G. S. Kar et al. “Co/Ni based p-MTJ stack for sub-20nm high density stand alone and high performance embedded memory application”. In: *2014 IEEE International Electron Devices Meeting*. 2014, pp. 19.1.1–19.1.4. DOI: 10.1109/IEDM.2014.7047080.

[125] Yoann Tomczak et al. “Influence of the Reference Layer Composition on the Back-End-of-Line Compatibility of Co/Ni-Based Perpendicular Magnetic Tunnel Junction Stacks”. In: *IEEE Transactions on Magnetics* 52.7 (2016), pp. 1–4. DOI: 10.1109/TMAG.2016.2515109.

[126] G. Jan, W. Kula, and J.Wang Y. Tong. “Co/Ni Multilayers with Improved Out-of-plane Anisotropy for Magnetic Device Applications”. US Patent No. 9,478,733 B2. Headway Technologies. Mar. 24, 2015.

[127] European Commission. “Study on the EU’s list of Critical Raw Materials, Factsheets on Critical Raw Materials”. In: (2020). DOI: doi:10.2873/92480.

[128] S Cole and CJ Ferron. “A review of the beneficiation and extractive metallurgy of the platinum-group elements, highlighting recent process innovations”. In: *SGS Minerals Services Technical Paper* 3 (2002), pp. 1–43.

[129] M. Junior Mabiza, Charles Mbohwa, and Michael Mutingi. “Life cycle inventory analysis and equivalent carbon dioxide emissions calculation of the mining and ore concentration processes of PGM at the anglo American Platinum Ltd, South Africa”. In: *2014 IEEE International Conference on Industrial Engineering and Engineering Management* (2014), pp. 1018–1022.

[130] R.T. Jones. “An overview of Southern African PGM smelting”. In: *Nickel and Cobalt 2005, Challenges in Extraction and Production* (2005), pp. 147–178.

[131] Fouad S. M. Rashed and Satyendra Nath. “Recovery of Copper from Industrial Waste Water by Foam Flotation Process : A Review”. In: 2016.

[132] Frank Crundwell et al. *Extractive metallurgy of nickel, cobalt and platinum group metals*. Elsevier, 2011.

[133] G.J. Hodges et al. “Stillwater Mining Co.’s Precious Metals Smelter: from Pilot to Production.” In: *Mining Engineering* (July 1991), pp. 724–727.

[134] Keith Liddell et al. “Energy consumption for Kell hydrometallurgical refining versus conventional pyrometallurgical smelting and refining of PGM concentrates”. In: *Journal of the Southern African Institute of Mining and Metallurgy* 111 (Feb. 2011), pp. 127–132.

[135] John Rankin. “Energy Use in Metal Production”. In: *4th Annual High Temperature Processing Symposium 2012* (), pp. 7–9. URL: http://hdl.handle.net/102.100.100/101541?index=1.

[136] T.E. Norgate and R.R. Lovel. “Sustainable water use in minerals and metal production”. In: *Australasian Institute of Mining and Metallurgy Publication Series*. 2006, pp. 133–141. ISBN: 978-1-920806-45-3.

[137] Eric D. Williams, Robert U. Ayres, and Miriam Heller. “The 1.7 Kilogram Microchip: Energy and Material Use in the Production of Semiconductor Devices”. In: *Environmental Science & Technology* 36.24 (Dec. 1, 2002). Publisher: American Chemical Society, pp. 5504–5510. ISSN: 0013-936X. DOI: 10.1021/es025643o. URL: https://doi.org/10.1021/es025643o.

[138] H. Walter et al. “Focusing Magnetron Sputtering Apparatus”. US Patent No. 4,472,259. Tokyo Electron Ltd. 1984.

[139] A.C. Tolcin. “Indium”. In: *Minerals Yearbook* (2008). URL: http://minerals.usgs.gov/minerals/pubs/commodity/indium/myb1-2008-indiu.pdf..

[140] Stephen Rossnagel. “8 - Sputtering and Sputter Deposition”. In: *Handbook of Thin Film Deposition Processes and Techniques (Second Edition)*. Ed. by Krisna Seshan. Second Edition. Norwich, NY: William Andrew Publishing, 2001, pp. 319–348. ISBN: 978-0-8155-1442-8. DOI: https://doi.org/10.1016/B978-081551442-8.50013-4. URL: https://www.sciencedirect.com/science/article/pii/B9780815514428500134.

[141] Philip Nuss and Matthew J. Eckelman. “Life Cycle Assessment of Metals: A Scientific Synthesis”. In: *PLOS ONE* 9.7 (July 2014). Publisher: Public Library of Science, pp. 1–1. DOI: 10.1371/journal.pone.0101298. URL: https://doi.org/10.1371/journal.pone.0101298.

[142] Sarah B. Boyd. *Life-Cycle Assessment of Semiconductors*. New York, NY: Springer New York, 2012. ISBN: 978-1-4419-9987-0 978-1-4419-9988-7. DOI: 10.1007/978-1-4419-9988-7. URL: http://link.springer.com/10.1007/978-1-4419-9988-7 (visited on 08/12/2021).

[143] Hiroaki Takiguchi. “Global Flow Analysis of Crystalline Silicon”. In: *Crystalline Silicon - Properties and Uses*. 2011. DOI: 10.5772/23573. URL: https://app.dimensions.ai/details/publication/pub.1047930728.

[144] Michael F. Ashby. “Chapter 6 - Eco-data: Values, sources, precision”. In: *Materials and the Environment (Second Edition)*. Ed. by Michael F. Ashby. Second Edition. Boston: Butterworth-Heinemann, 2013, pp. 119–174. ISBN: 978-0-12-385971-6. DOI: https://doi.org/10.1016/B978-0-12-385971-6.00006-3. URL: https://www.sciencedirect.com/science/article/pii/B9780123859716000063.

[145] A. Palomino et al. “Evaluating critical metals contained in spintronic memory with a particular focus on Pt substitution for improved sustainability”. In: *Sustainable Materials and Technologies* 28 (2021), e00270. ISSN: 2214-9937. DOI: https://doi.org/10.1016/j.susmat.2021.e00270. URL: https://www.sciencedirect.com/science/article/pii/S2214993721000257.

[146] M. Schmidt, H. Hottenroth, and M. et al. Schottler. “Life cycle assessment of silicon wafer processing for microelectronic chips and solar cells”. In: *Int J Life Cycle Assess* 17 (2012), pp. 126–144. DOI: https://doi.org/10.1007/s11367-011-0351-1.

[147] B. Buijs and H. Sievers. “Resource Security Risks in Perspective: Complexity and Nuance, Clingendael International Energy Programme, The Hague”. In: (2011). (briefing paper), p. 42. URL: https://www.clingendaelenergy.com/inc/upload/files/Resource_security_risks.pdf..

[148] “Critical Imported Materials, Study of Ad Hoc Group Established by NSSM 197/ CIEPSM 33, US Government (Nixon Administration), Available at the US Bureau of Public Affairs, Office of the Historian, ‘Foreign Relations of the United States, 1969–1976, Volume XXXI, Foreign Economic Policy, 1973–1976’.” In: (July 1974). URL: http://history.state.gov/historicaldocuments/frus1969-76v31.

[149] Leena Grandell et al. “Role of critical metals in the future markets of clean energy technologies”. In: *Renewable Energy* 95 (2016), pp. 53–62. ISSN: 0960-1481. DOI: https://doi.org/10.1016/j.renene.2016.03.102. URL: https://www.sciencedirect.com/science/article/pii/S0960148116302816.

[150] Alicia Valero et al. “Material bottlenecks in the future development of green technologies”. In: *Renewable and Sustainable Energy Reviews* 93 (2018), pp. 178–200. ISSN: 1364-0321. DOI: https://doi.org/10.1016/j.rser.2018.05.041. URL: https://www.sciencedirect.com/science/article/pii/S1364032118303861.

[151] U.S. Geological Survey. “Mineral commodity summaries 2019”. In: *Mineral commodity summaries* (2018). URL: https://minerals.usgs.gov/minerals/pubs/mcs/.

[152] Michael L. Zientek et al. *Platinum-group elements*. English. Report 1802N. Reston, VA, 2017, p. 106. DOI: 10.3133/pp1802N. URL: http://pubs.er.usgs.gov/publication/pp1802N.

[153] Gavin M. Mudd. "Key trends in the resource sustainability of platinum group elements". In: *Ore Geology Reviews* 46 (2012), pp. 106–117. ISSN: 0169-1368. DOI: `https://doi.org/10.1016/j.oregeorev.2012.02.005`. URL: `https://www.sciencedirect.com/science/article/pii/S0169136812000273`.

[154] World Platinum Investment Council . Q1 Last accessed 05/10/2020. In: (2020). URL: `https://platinuminvestment.com/files/186857/WPIC_Platinum_Quarterly_Q1_2020.pdf`.

[155] Global Wafer Capacity Last accessed 05/10/2020. In: (2020-2024). URL: `https://www.icinsights.com/services/global-wafer-capacity/pricing-order-forms`.

[156] E.D. Gemechu, G. Sonnemann, and S.B. Young. "Geopolitical-related supply risk assessment as a complement to environmental impact assessment: the case of electric vehicles." In: *Int J Life Cycle Assess* 22 (2017), pp. 31–39. URL: `https://doi.org/10.1007/s11367-015-0917-4`.

[157] European Commission. "EU's new Conflict Minerals Regulation". In: (2020). URL: `https://ec.europa.eu/trade/policy/in-focus/conflict-minerals-regulation/regulation-explained/`.

[158] Jyotirmoy Chatterjee et al. "Enhanced annealing stability and perpendicular magnetic anisotropy in perpendicular magnetic tunnel junctions using W layer". In: *Applied Physics Letters* 110.20 (2017), p. 202401. DOI: `10.1063/1.4983159`. eprint: `https://doi.org/10.1063/1.4983159`. URL: `https://doi.org/10.1063/1.4983159`.

[159] Blandine Ageron, Angappa Gunasekaran, and Alain Spalanzani. "Sustainable supply management: An empirical study". In: *International Journal of Production Economics* 140.1 (2012). Sustainable Development of Manufacturing and Services, pp. 168–182. ISSN: 0925-5273. DOI: `https://doi.org/10.1016/j.ijpe.2011.04.007`. URL: `https://www.sciencedirect.com/science/article/pii/S092552731100171X`.

[160] *PTA — Upstream Technological Platform*. URL: `http://pta-grenoble.com/` (visited on 01/10/2022).

[161] Stuart S. P. Parkin et al. "Giant tunnelling magnetoresistance at room temperature with MgO (100) tunnel barriers". In: *Nature Materials* 3.12 (Dec. 2004), pp. 862–867. ISSN: 1476-4660. DOI: `10.1038/nmat1256`. URL: `https://doi.org/10.1038/nmat1256`.

[162] David D. Djayaprawira et al. "230% room-temperature magnetoresistance in CoFeBMgOCoFeB magnetic tunnel junctions". In: *Applied Physics Letters* 86.9 (2005), p. 092502. DOI: `10.1063/1.1871344`. eprint: `https://doi.org/10.1063/1.1871344`. URL: `https://doi.org/10.1063/1.1871344`.

[163] G. Binnig, C. F. Quate, and Ch. Gerber. "Atomic Force Microscope". In: *Phys. Rev. Lett.* 56 (9 Mar. 1986), pp. 930–933. DOI: `10.1103/PhysRevLett.56.930`. URL: `https://link.aps.org/doi/10.1103/PhysRevLett.56.930`.

[164] S. B. Kaemmer. "Application Note # 133 Introduction to Bruker ' s ScanAsyst and PeakForce Tapping AFM Technology, 2011". In.

[165] Simon Foner. "Versatile and Sensitive Vibrating-Sample Magnetometer". In: *Review of Scientific Instruments* 30.7 (1959), pp. 548–557. DOI: `10.1063/1.1716679`. eprint: `https://doi.org/10.1063/1.1716679`. URL: `https://doi.org/10.1063/1.1716679`.

[166] "Experimental Methods". In: *Introduction to Magnetic Materials*. John Wiley Sons, Ltd, 2008. Chap. 2, pp. 23–86. ISBN: 9780470386323. DOI: `https://doi.org/10.1002/9780470386323.ch2`. eprint: `https://onlinelibrary.wiley.com/doi/pdf/10.1002/9780470386323.ch2`. URL: `https://onlinelibrary.wiley.com/doi/abs/10.1002/9780470386323.ch2`.

[167] John Kerr LL.D. "XLIII. On rotation of the plane of polarization by reflection from the pole of a magnet". In: *The London, Edinburgh, and Dublin Philosophical Magazine and Journal of Science* 3.19 (1877), pp. 321–343. DOI: `10.1080/14786447708639245`. eprint: `https://doi.org/10.1080/14786447708639245`. URL: `https://doi.org/10.1080/14786447708639245`.

[168] Rob Legtenberg et al. "Anisotropic Reactive Ion Etching of Silicon Using SF 6 / O 2 / CHF 3 Gas Mixtures". In: *Journal of The Electrochemical Society* 142.6 (June 1995), pp. 2020–2028. DOI: 10.1149/1.2044234. URL: https://doi.org/10.1149/1.2044234.

[169] Michael Shearn et al. "Advanced Plasma Processing: Etching, Deposition, and Wafer Bonding Techniques for Semiconductor Applications". In: *Semiconductor Technologies*. Ed. by Jan Grym. Rijeka: IntechOpen, 2010. Chap. 5. DOI: 10.5772/8564. URL: https://doi.org/10.5772/8564.

[170] *ACCUFLO® Technical Data Sheets*. URL: http://www.matweb.com/search/GetMatlsByTradename.aspx?navletter=A%5C&tn=ACCUFLO%5C%C2%5C%AE (visited on 02/12/2022).

[171] S. L. Tang et al. "Scanning tunneling microscopy of Pt/Co multilayers on Pt buffer layers". In: *Applied Physics Letters* 59.22 (1991), pp. 2898–2900. DOI: 10.1063/1.105845. eprint: https://doi.org/10.1063/1.105845. URL: https://doi.org/10.1063/1.105845.

[172] Lavinia Elena NISTOR. "Magnetic tunnel junctions with perpendicular magnetization: anisotropy, magnetoresistance, magnetic coupling and spin transfer torque switching". PhD thesis. Université de Grenoble, 2011.

[173] P. Chowdhury et al. "Effect of coherent to incoherent structural transition on magnetic anisotropy in Co/Pt multilayers". In: *Journal of Applied Physics* 112.2 (2012), p. 023912. DOI: 10.1063/1.4739284. eprint: https://doi.org/10.1063/1.4739284. URL: https://doi.org/10.1063/1.4739284.

[174] V. Boureau et al. "An electron holography study of perpendicular magnetic tunnel junctions nanostructured by deposition on pre-patterned conducting pillars". In: *Nanoscale* 12 (33 2020), pp. 17312–17318. DOI: 10.1039/D0NR03353G. URL: http://dx.doi.org/10.1039/D0NR03353G.

[175] Svante Arrhenius. "Über die Dissociationswärme und den Einfluss der Temperatur auf den Dissociationsgrad der Elektrolyte". In: *Zeitschrift für Physikalische Chemie* 4U.1 (1889), pp. 96–116. DOI: doi:10.1515/zpch-1889-0408. URL: https://doi.org/10.1515/zpch-1889-0408.

[176] Daniel Sanchez Hazen et al. "Double magnetic tunnel junctions with a switchable assistance layer for improved spin transfer torque magnetic memory performance". In: *Nanoscale* 13 (33 2021), pp. 14096–14109. DOI: 10.1039/D1NR01656C. URL: http://dx.doi.org/10.1039/D1NR01656C.

[177] D. Sanchez Hazen et al. "Real time investigation of double magnetic tunnel junction with a switchable assistance layer for high efficiency STT-MRAM". In: *APL Materials* 10.3 (2022), p. 031104. DOI: 10.1063/5.0080335. eprint: https://doi.org/10.1063/5.0080335. URL: https://doi.org/10.1063/5.0080335.

[178] K. Nishioka et al. "Novel Quad interface MTJ technology and its first demonstration with high thermal stability and switching efficiency for STT-MRAM beyond 2Xnm". In: *2019 Symposium on VLSI Technology*. 2019, T120–T121. DOI: 10.23919/VLSIT.2019.8776499.

[179] Sadahiko Miura et al. "Scalability of Quad Interface p-MTJ for 1X nm STT-MRAM With 10-ns Low Power Write Operation, 10 Years Retention and Endurance gt; 10^{11}". In: *IEEE Transactions on Electron Devices* 67.12 (2020), pp. 5368–5373. DOI: 10.1109/TED.2020.3025749.

[180] H. Sato et al. "Properties of magnetic tunnel junctions with a MgO/CoFeB/Ta/CoFeB/MgO recording structure down to junction diameter of 11nm". In: *Applied Physics Letters* 105.6 (2014), p. 062403. DOI: 10.1063/1.4892924. eprint: https://doi.org/10.1063/1.4892924. URL: https://doi.org/10.1063/1.4892924.

[181] M. Sato and Y. Ishii. "Simple and approximate expressions of demagnetizing factors of uniformly magnetized rectangular rod and cylinder". In: *Journal of Applied Physics* 66.2 (1989), pp. 983–985. DOI: 10.1063/1.343481. eprint: https://doi.org/10.1063/1.343481. URL: https://doi.org/10.1063/1.343481.

[182] B. Jinnai et al. "High-Performance Shape-Anisotropy Magnetic Tunnel Junctions down to 2.3 nm". In: *2020 IEEE International Electron Devices Meeting (IEDM)*. 2020, pp. 24.6.1–24.6.4.

[183] Junta Igarashi et al. “Temperature dependence of the energy barrier in X/1X nm shape-anisotropy magnetic tunnel junctions”. In: *Applied Physics Letters* 118.1 (2021), p. 012409. DOI: 10.1063/5.0029031. eprint: https://doi.org/10.1063/5.0029031. URL: https://doi.org/10.1063/5.0029031.

[184] Trevor Almeida et al. “Direct observation of the perpendicular shape anisotropy and thermal stability of STT-MRAM nano-pillars examined by off-axis electron holography”. In: *Microscopy and Microanalysis* 27.S1 (2021), pp. 2170–2172. DOI: 10.1017/S1431927621007819.

[185] Hicham Allag et al. “Coulombian Model for 3D Analytical Calculation of the Torque Exerted on Cuboidal Permanent Magnets with Arbitrarly Oriented Polarizations”. In: *LDIA 2011 (8th International Conference on Linear Drives for Industry Applications)*. Eindhoven, Netherlands, July 2011. URL: https://hal.archives-ouvertes.fr/hal-00608059.

[186] N.A. Usov and S.E. Peschany. “Flower state micromagnetic structure in fine cylindrical particles”. In: *Journal of Magnetism and Magnetic Materials* 130.1 (1994), pp. 275–287. ISSN: 0304-8853. DOI: https://doi.org/10.1016/0304-8853(94)90684-X. URL: https://www.sciencedirect.com/science/article/pii/030488539490684X.

[187] C. A. Ross et al. “Micromagnetic behavior of electrodeposited cylinder arrays”. In: *Phys. Rev. B* 65 (14 Mar. 2002), p. 144417. DOI: 10.1103/PhysRevB.65.144417. URL: https://link.aps.org/doi/10.1103/PhysRevB.65.144417.

[188] Arne Vansteenkiste et al. “The design and verification of MuMax3”. In: *AIP Advances* 4.10 (2014), p. 107133. DOI: 10.1063/1.4899186. eprint: https://doi.org/10.1063/1.4899186. URL: https://doi.org/10.1063/1.4899186.

[189] B. D. Schrag et al. “Néel “orange-peel” coupling in magnetic tunneling junction devices”. In: *Applied Physics Letters* 77.15 (2000), pp. 2373–2375. DOI: 10.1063/1.1315633.

[190] J Moritz et al. “Orange peel coupling in multilayers with perpendicular magnetic anisotropy: Application to (Co/Pt)-based exchange-biased spin-valves”. In: *Europhysics Letters (EPL)* 65.1 (2004), pp. 123–129. DOI: 10.1209/epl/i2003-10063-9.

[191] Léa Cuchet et al. “Influence of a Ta spacer on the magnetic and transport properties of perpendicular magnetic tunnel junctions”. In: *Applied Physics Letters* 103.5 (2013), p. 052402. DOI: 10.1063/1.4816968.

[192] Maria Patricia Rouelli Sabino, Sze Ter Lim, and Michael Tran. “Influence of Ta insertions on the magnetic properties of MgO/CoFeB/MgO films probed by ferromagnetic resonance”. In: *Applied Physics Express* 7.9 (Aug. 2014), p. 093002. DOI: 10.7567/apex.7.093002. URL: https://doi.org/10.7567/apex.7.093002.

[193] Rafal Dunin-Borkowski, Takeshi Kasama, and Richard Harrison. “CHAPTER 5: Electron holography of nanostructured materials”. In: Jan. 2015, pp. 158–210. ISBN: 978-1-84973-805-7. DOI: 10.1039/9781782621867-00158.

[194] “High-Resolution STEM Imaging”. In: *Transmission Electron Microscopy and Diffractometry of Materials*. Berlin, Heidelberg: Springer Berlin Heidelberg, 2008, pp. 583–609. ISBN: 978-3-540-73886-2. DOI: 10.1007/978-3-540-73886-2_11. URL: https://doi.org/10.1007/978-3-540-73886-2_11.

[195] Léa Cuchet et al. “Influence of magnetic electrodes thicknesses on the transport properties of magnetic tunnel junctions with perpendicular anisotropy”. In: *Appl. Phys. Lett.* 105.052408 (2014). DOI: https://doi.org/10.1063/1.4892450.

[196] Jyotirmoy Chatterjee et al. “Novel multifunctional RKKY coupling layer for ultrathin perpendicular synthetic antiferromagnet”. In: *Scientific Reports* 8.1 (Aug. 2018), p. 11724. ISSN: 2045-2322. DOI: 10.1038/s41598-018-29913-6. URL: https://doi.org/10.1038/s41598-018-29913-6.

[197] P. J. H. Bloemen, W. J. M. de Jonge, and F. J. A. den Broeder. "Magnetic anisotropies in Co/Ni(111) multilayers". In: *Journal of Applied Physics* 72.10 (1992), pp. 4840–4844. DOI: 10.1063/1.352048. eprint: https://doi.org/10.1063/1.352048. URL: https://doi.org/10.1063/1.352048.

[198] Guangzhong Wang et al. "Magnetic anisotropy and thermal stability study of perpendicular Co/Ni multilayers". In: *Journal of Applied Physics* 113.17 (2013), p. 17C111. DOI: 10.1063/1.4799524. eprint: https://doi.org/10.1063/1.4799524. URL: https://doi.org/10.1063/1.4799524.

[199] K. Zhang, M. Li, and Y. Zhou. "Multilayer Structure with High Perpendicular Anisotropy for Device Applications". US Patent No. 8,920,947 B2. Headway Technologies. 2014.

[200] Enlong Liu et al. "Seed layer impact on structural and magnetic properties of [Co/Ni] multilayers with perpendicular magnetic anisotropy". In: *Journal of Applied Physics* 121.4 (2017), p. 043905. DOI: 10.1063/1.4974885. eprint: https://doi.org/10.1063/1.4974885. URL: https://doi.org/10.1063/1.4974885.

[201] W. Chen et al. "Spin-torque driven ferromagnetic resonance of CoNi synthetic layers in spin valves". In: *Applied Physics Letters* 92.1 (2008), p. 012507. DOI: 10.1063/1.2827570. eprint: https://aip.scitation.org/doi/pdf/10.1063/1.2827570. URL: https://aip.scitation.org/doi/abs/10.1063/1.2827570.

[202] Arora M. et al. "Magnetic properties of Co/Ni multilayer structures for use in STT-RAM". In: *J. Phys. D: Appl. Phys.* 50 (Nov. 2017), p. 505003. DOI: 10.1088/1361-6463/aa97fa. URL: https://doi.org/10.1088/1361-6463/aa97fa.

[203] T. Devolder et al. "Annealing stability of magnetic tunnel junctions based on dual MgO free layers and [Co/Ni] based thin synthetic antiferromagnet fixed system". In: *Journal of Applied Physics* 121.11 (2017), p. 113904. DOI: 10.1063/1.4978633. eprint: https://doi.org/10.1063/1.4978633. URL: https://doi.org/10.1063/1.4978633.

[204] Justin M. Shaw, Hans T. Nembach, and T. J. Silva. "Roughness induced magnetic inhomogeneity in Co/Ni multilayers: Ferromagnetic resonance and switching properties in nanostructures". In: *Journal of Applied Physics* 108.9 (2010), p. 093922. DOI: 10.1063/1.3506688. eprint: https://doi.org/10.1063/1.3506688. URL: https://doi.org/10.1063/1.3506688.

[205] Chris Coutts et al. "Magnetic properties of Co/Ni grain boundaries after annealing". In: *AIP Advances* 8.5 (2018), p. 056318. DOI: 10.1063/1.5007689. eprint: https://doi.org/10.1063/1.5007689. URL: https://doi.org/10.1063/1.5007689.

[206] A. Al Subhi and R. Sbiaa. "Control of magnetization reversal and domain structure in (Co/Ni) multilayers". In: *Journal of Magnetism and Magnetic Materials* 489 (2019), p. 165460. ISSN: 0304-8853. DOI: https://doi.org/10.1016/j.jmmm.2019.165460. URL: https://www.sciencedirect.com/science/article/pii/S0304885319315422.

[207] V. Gehanno et al. "Magnetic susceptibility and magnetic domain configuration as a function of the layer thickness in epitaxial FePd(0 0 1) thin films ordered in the L1o structure". In: *Journal of Magnetism and Magnetic Materials* 172.1 (1997), pp. 26–40. ISSN: 0304-8853. DOI: https://doi.org/10.1016/S0304-8853(97)00089-9. URL: https://www.sciencedirect.com/science/article/pii/S0304885397000899.

[208] P. R. Aitchison et al. "High resolution measurement and modelling of magnetic domain structures in epitaxial FePd (001) L10 films with perpendicular magnetisation". In: *Journal of Magnetism and Magnetic Materials* 223 (2001), pp. 138–146.

[209] S. S. P. Parkin. "Systematic variation of the strength and oscillation period of indirect magnetic exchange coupling through the 3d, 4d, and 5d transition metals". In: *Phys. Rev. Lett.* 67 (25 Dec. 1991), pp. 3598–3601. DOI: 10.1103/PhysRevLett.67.3598. URL: https://link.aps.org/doi/10.1103/PhysRevLett.67.3598.

[210] P. Bruno and C. Chappert. “Oscillatory coupling between ferromagnetic layers separated by a nonmagnetic metal spacer”. In: *Phys. Rev. Lett.* 67 (12 Sept. 1991), pp. 1602–1605. DOI: 10.1103/PhysRevLett.67.1602. URL: https://link.aps.org/doi/10.1103/PhysRevLett.67.1602.

[211] L. Cuchet, B. Rodmacq, and S. et al. Auffret. “Perpendicular magnetic tunnel junctions with a synthetic storage or reference layer: A new route towards Pt- and Pd-free junctions”. In: *Sci Rep* 6 (2016). URL: https://doi.org/10.1038/srep21246.

[212] Jyotirmoy Chatterjee et al. “Reduced Thermal Variation of Perpendicular Magnetic Anisotropy in Magnetically Stiffened Dual-W Composite Storage Layer for Spin-Transfer-Torque Magnetic Random-Access Memory”. In: *Phys. Rev. Applied* 12 (4 Oct. 2019), p. 044043. DOI: 10.1103/PhysRevApplied.12.044043. URL: https://link.aps.org/doi/10.1103/PhysRevApplied.12.044043.

[213] S.H. Kang and K. Lee. “Emerging materials and devices in spintronic integrated circuits for energy-smart mobile computing and connectivity”. In: *Acta Materialia* 61.3 (2013). The Diamond Jubilee Issue, pp. 952–973. ISSN: 1359-6454. DOI: https://doi.org/10.1016/j.actamat.2012.10.036. URL: https://www.sciencedirect.com/science/article/pii/S1359645412007835.

[214] Borders WA et al. “Integer factorization using stochastic magnetic tunnel junctions”. In: *Nature* 573 (7774 2019), pp. 390–393. DOI: doi:10.1038/s41586-019-1557-9.

[215] Swaroop Ghosh. “Spintronics and Security: Prospects, Vulnerabilities, Attack Models, and Preventions”. In: *Proceedings of the IEEE* 104.10 (2016), pp. 1864–1893. DOI: 10.1109/JPROC.2016.2583419.

[216] K. Hayakawa et al. “Nanosecond Random Telegraph Noise in In-Plane Magnetic Tunnel Junctions”. In: *Phys. Rev. Lett.* 126 (11 Mar. 2021), p. 117202. DOI: 10.1103/PhysRevLett.126.117202. URL: https://link.aps.org/doi/10.1103/PhysRevLett.126.117202.

[217] Christopher Safranski et al. “Demonstration of Nanosecond Operation in Stochastic Magnetic Tunnel Junctions”. In: *Nano Letters* 21 (Feb. 2021). DOI: 10.1021/acs.nanolett.0c04652.

[218] Jana Ludwig, Karsten Rott, and Guenter Reiss. “Superparamagnetic dwell times and tuning of switching rates in perpendicular CoFeB/MgO/CoFeB tunnel junctions.” In: *arXiv: Mesoscale and Nanoscale Physics* (2019).

[219] Ming-Hung Wu et al. “Extremely Compact Integrate-and-Fire STT-MRAM Neuron: A Pathway toward All-Spin Artificial Deep Neural Network”. In: *2019 Symposium on VLSI Technology* (2019), T34–T35.

[220] Mafalda Jotta Garcia et al. “Spin–torque dynamics for noise reduction in vortex-based sensors”. In: *Applied Physics Letters* 118.12 (2021), p. 122401. DOI: 10.1063/5.0040874. eprint: https://doi.org/10.1063/5.0040874. URL: https://doi.org/10.1063/5.0040874.

[221] Motoki Endo et al. “Control of sensitivity in vortex-type magnetic tunnel junction magnetometer sensors by the pinned layer geometry”. In: *Journal of Physics D: Applied Physics* 55.19 (Feb. 2022), p. 195001. DOI: 10.1088/1361-6463/ac5080. URL: https://doi.org/10.1088/1361-6463/ac5080.

[222] Atsufumi Hirohata et al. “Development of antiferromagnetic Heusler alloys for the replacement of iridium as a critically raw material”. In: *Journal of Physics D: Applied Physics* 50.44 (Sept. 2017), p. 443001. DOI: 10.1088/1361-6463/aa88f4. URL: https://doi.org/10.1088/1361-6463/aa88f4.

[223] P.G.M. Johnson Matthey. In: *Market Report* (2021). URL: https://matthey.com/-/media/files/pgm-market-report/jm-pgm-market-report-may-2021.pdf.

[224] Johnson Matthey. In: *Price Charts* (2021). URL: http://www.platinum.matthey.com/prices/price-charts.

[225] Konstantin L Metlov and Konstantin Yu Guslienko. “Stability of magnetic vortex in soft magnetic nano-sized circular cylinder”. In: *Journal of Magnetism and Magnetic Materials* 242-245 (2002). Proceedings of the Joint European Magnetic Symposia (JEMS'01), pp. 1015–1017. ISSN: 0304-8853. DOI: `https://doi.org/10.1016/S0304-8853(01)01360-9`. URL: `https://www.sciencedirect.com/science/article/pii/S0304885301013609`.

[226] T. Wurft et al. “Evolution of magnetic vortex formation in micron-sized disks”. In: *Applied Physics Letters* 115.13 (2019), p. 132407. DOI: `10.1063/1.5116299`. eprint: `https://doi.org/10.1063/1.5116299`. URL: `https://doi.org/10.1063/1.5116299`.

[227] Salim Dounia, Claire Baraduc, and Bernard Dieny. “Magnetic element having an improved measurement range.” EP. Patent No.19315026.5. 2020. URL: `https://data.epo.org/publication-server/document?iDocId=6380261&iFormat=0` (visited on 02/10/2022).

[228] Valenty Novosad and Kristen Buchanan. “Method for the detection of a magnetic field utilizing a magnetic vortex”. US Patent No. 7,697.243 B1. The United States of America as represented by the United States Department of Energy. 2010.

[229] Trevor P. Almeida et al. “Direct visualization of the thermomagnetic behavior of pseudo–single-domain magnetite particles”. In: *Science Advances* 2.4 (2016), e1501801. DOI: `10.1126/sciadv.1501801`. eprint: `https://www.science.org/doi/pdf/10.1126/sciadv.1501801`. URL: `https://www.science.org/doi/abs/10.1126/sciadv.1501801`.

[230] Trevor P. Almeida et al. “Direct observation of the perpendicular shape anisotropy and thermal stability of p-STT-MRAM nano-pillars”. working paper or preprint. Feb. 2022. URL: `https://hal.archives-ouvertes.fr/hal-03553914`.

[231] Steven Lequeux et al. “PSA-STT-MRAM solution for extended temperature stability”. In: *2021 IEEE International Memory Workshop (IMW)*. 2021, pp. 1–4. DOI: `10.1109/IMW51353.2021.9439609`.

[232] *HPROBE*. URL: `https://www.hprobe.com/products/` (visited on 01/22/2022).

[233] European Commission et al. *Report on critical raw materials and the circular economy*. Publications Office, 2018. DOI: `doi/10.2873/331561`.

[234] Timothy G. Gutowski et al. “The energy required to produce materials: constraints on energy-intensity improvements, parameters of demand”. In: *Philosophical Transactions of the Royal Society A: Mathematical, Physical and Engineering Sciences* 371.1986 (2013), p. 20120003. DOI: `10.1098/rsta.2012.0003`. eprint: `https://royalsocietypublishing.org/doi/pdf/10.1098/rsta.2012.0003`. URL: `https://royalsocietypublishing.org/doi/abs/10.1098/rsta.2012.0003`.

[235] *Daily Metal Prices*. URL: `www.dailymetalprice.com` (visited on 01/10/2021).

[236] Wynand Lambrechts et al. “The Economics of Semiconductor Scaling”. In: *Extending Moore's Law through Advanced Semiconductor Design and Processing Techniques*. 1st. USA: CRC Press, Inc., 2018, pp. 33–67. ISBN: 0815370741. URL: `https://doi.org/10.1201/9781351248679`.

[237] D. C. Worledge and P. L. Trouilloud. “Magnetoresistance measurement of unpatterned magnetic tunnel junction wafers by current-in-plane tunneling”. In: *Applied Physics Letters* 83.1 (2003), pp. 84–86. DOI: `10.1063/1.1590740`. eprint: `https://doi.org/10.1063/1.1590740`. URL: `https://doi.org/10.1063/1.1590740`.